



ELECTROCHEMICALLY ENGINEERED ANODIC ALUMINA NANOTUBES: PHYSICO-CHEMICAL PROPERTIES AND APPLICATIONS

Jakub Domagalski

ADVERTIMENT. L'accés als continguts d'aquesta tesi doctoral i la seva utilització ha de respectar els drets de la persona autora. Pot ser utilitzada per a consulta o estudi personal, així com en activitats o materials d'investigació i docència en els termes establerts a l'art. 32 del Text Refós de la Llei de Propietat Intel·lectual (RDL 1/1996). Per altres utilitzacions es requereix l'autorització prèvia i expressa de la persona autora. En qualsevol cas, en la utilització dels seus continguts caldrà indicar de forma clara el nom i cognoms de la persona autora i el títol de la tesi doctoral. No s'autoritza la seva reproducció o altres formes d'explotació efectuades amb finalitats de lucre ni la seva comunicació pública des d'un lloc aliè al servei TDX. Tampoc s'autoritza la presentació del seu contingut en una finestra o marc aliè a TDX (framing). Aquesta reserva de drets afecta tant als continguts de la tesi com als seus resums i índexs.

ADVERTENCIA. El acceso a los contenidos de esta tesis doctoral y su utilización debe respetar los derechos de la persona autora. Puede ser utilizada para consulta o estudio personal, así como en actividades o materiales de investigación y docencia en los términos establecidos en el art. 32 del Texto Refundido de la Ley de Propiedad Intelectual (RDL 1/1996). Para otros usos se requiere la autorización previa y expresa de la persona autora. En cualquier caso, en la utilización de sus contenidos se deberá indicar de forma clara el nombre y apellidos de la persona autora y el título de la tesis doctoral. No se autoriza su reproducción u otras formas de explotación efectuadas con fines lucrativos ni su comunicación pública desde un sitio ajeno al servicio TDR. Tampoco se autoriza la presentación de su contenido en una ventana o marco ajeno a TDR (framing). Esta reserva de derechos afecta tanto al contenido de la tesis como a sus resúmenes e índices.

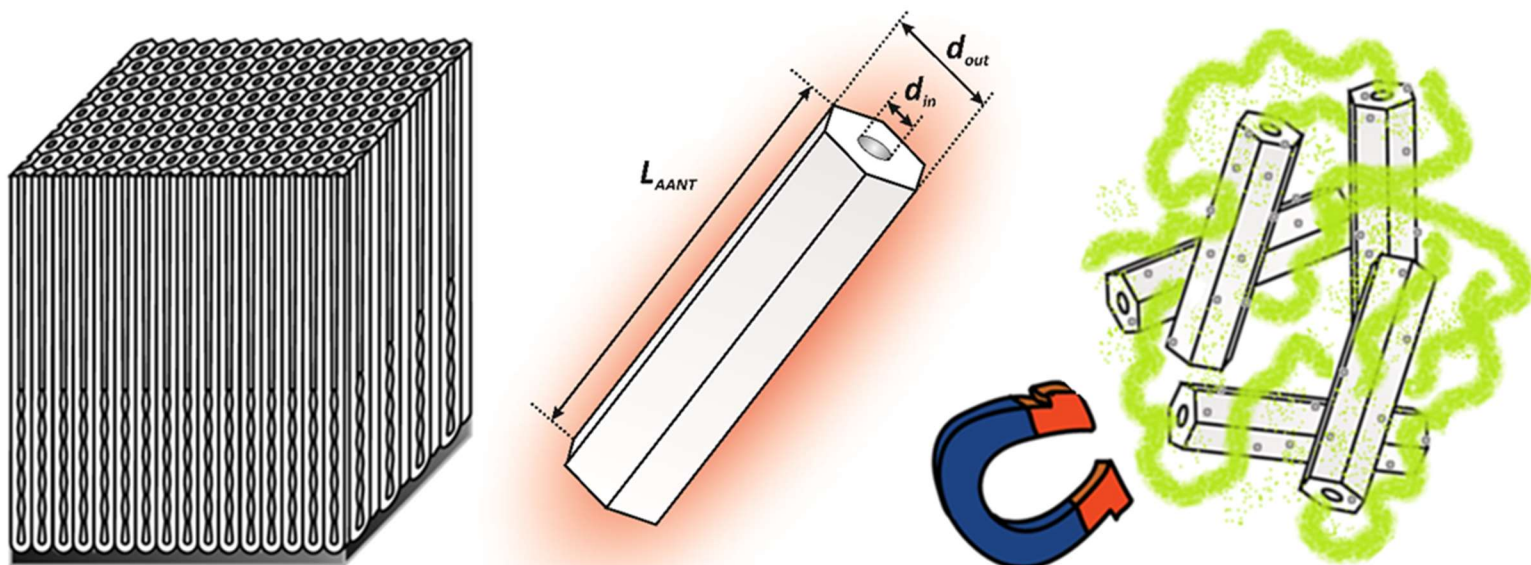
WARNING. Access to the contents of this doctoral thesis and its use must respect the rights of the author. It can be used for reference or private study, as well as research and learning activities or materials in the terms established by the 32nd article of the Spanish Consolidated Copyright Act (RDL 1/1996). Express and previous authorization of the author is required for any other uses. In any case, when using its content, full name of the author and title of the thesis must be clearly indicated. Reproduction or other forms of for profit use or public communication from outside TDX service is not allowed. Presentation of its content in a window or frame external to TDX (framing) is not authorized either. These rights affect both the content of the thesis and its abstracts and indexes.



UNIVERSITAT
ROVIRA I VIRGILI

ELECTROCHEMICALLY ENGINEERED ANODIC ALUMINA NANOTUBES: PHYSICO-CHEMICAL PROPERTIES AND APPLICATIONS

JAKUB TOMASZ DOMAGALSKI



TESI DOCTORAL – TESIS DOCTORAL- DOCTORAL THESIS
2021



UNIVERSITAT ROVIRA I VIRGILI

Jakub Tomasz Domagalski

**ELECTROCHEMICALLY ENGINEERED ANODIC ALUMINA
NANOTUBES: PHYSICO-CHEMICAL PROPERTIES AND
APPLICATIONS**

DOCTORAL THESIS

Supervised by
Prof. Lluís F. Marsal Garví
and
Dr. Elisabet Xifré-Pérez

Department of Electronic, Electric and Automatic Engineering



UNIVERSITAT ROVIRA I VIRGILI

Tarragona

2021



Escola Tècnica Superior d'Enginyeria

Departament d'Enginyeria Electrònica, Elèctrica i Automàtica

Av. Països Catalans 26

Campus Sescelades

43007 Tarragona

FAIG CONSTAR que aquest treball, titulat "**ELECTROCHEMICALLY ENGINEERED ANODIC ALUMINA NANOTUBES: PHYSICO-CHEMICAL PROPERTIES AND APPLICATIONS**", que presenta **Jakub Domagalski** per a l'obtenció del títol de Doctor, ha estat realitzat sota la meva direcció al Departament d'Enginyeria Electrònica, Elèctrica i Automàtica d'aquesta universitat.

HAGO CONSTAR que el presente trabajo, titulado "**ELECTROCHEMICALLY ENGINEERED ANODIC ALUMINA NANOTUBES: PHYSICO-CHEMICAL PROPERTIES AND APPLICATIONS**", que presenta **Jakub Domagalski** para la obtención del título de Doctor, ha sido realizado bajo mi dirección en el Departamento de Ingeniería Eléctrica, Electrónica y Automática de esta universidad.

I STATE that the present study, entitled "**ELECTROCHEMICALLY ENGINEERED ANODIC ALUMINA NANOTUBES: PHYSICO-CHEMICAL PROPERTIES AND APPLICATIONS**", presented by **Jakub Domagalski** for the award of the degree of Doctor, has been carried out under my supervision at the Department of Electronic, Electric and Automatic Engineering of this university.

Tarragona, 22/02/2021

Els directors de la tesi doctoral
Los directores de la tesis doctoral
Doctoral Thesis Supervisors

Lluís F. Marsal Garví

Elisabet Xifre Perez

Acknowledgments

I would like to thank my supervisor Prof. Dr. Lluís Francesc Marsal Garví for giving me the opportunity to work on my thesis in his department at Universitat Rovira i Virgili.

Special thanks go to my supervisor Dr. Elisabet Xifré-Pérez for the guidance during my work, the proof-reading of this work and all the support and suggestions. Thanks for the patience, dedication and for the enthusiasm during this work.

I am grateful to Dr. Josep Ferre-Borrull for coordination of the PhD program and valuable suggestions.

I am very thankful to all the friends who have worked with me at the NePhoS group: Lluís Francesc Marsal Garvi, Elisabet Xifre-Perez, Josep Ferre-Borrull, Josep Pallares Marzal, Aurelien Viterisi, Jose Guadalupe Sanchez Lopez, Laura Karen Acosta Capilla, Pilar Formentin, Francesc Berto-Rosello, Maria Pilar Montero-Rama, Laura Pol Pankaj Kapruwan, Anandapadmanabhan Ambily Rajendran, Alfonsina Abat Amelenan Torimtubun, Enas Moustafa Mohamed Abdelghafar.

I would like to thank Dr. Abel Santos from the University of Adelaide, for the valuable discussions, honesty and support that enabled to improve the quality of my work.

Furthermore, I would like to thank Dr. Mahmoud Amouzadeh Tabrizi, for his pragmatism, knowledge and inspiring talks during daily work.

I am very thankful to Dr. Rita Marimon Picó, Dr. Mercè Moncusí Mercadé, Dr. Mariana Stefanova Trifonova and all the staff of the Servei Center of the Universitat Rovira i Virgili, for the support and for the fruitful discussions, for helping me with the understanding of the method and common talks.

Furthermore, I would like to thank Dr. Sara Maria Aguilar Sierra from the Universidad Católica Luis Amigo, your support and our conversations were valuable to ensure me of the legitimacy of the undertaken path at the beginning of my PhD studies.

At last, I would like to express my gratitude to all my friends and family – for being with me and harboring the place I could always come back to, despite the outcome.

This work was supported in part by the Spanish Ministerio de Ciencia, Innovación y Universidades (MICINN/FEDER) RTI2018-094040-B-I00, by the Agency for Management of University and Research Grants (AGAUR) 2017-SGR-1527 and by the Catalan Institution for Research and Advanced Studies (ICREA) under the ICREA Academia Award. This project has received funding from the European Union's Horizon 2020 research and innovation program under the Marie Skłodowska-Curie grant agreement No. 713679 and from the Universitat Rovira i Virgili (URV).

TABLE OF CONTENTS

LIST OF PUBLICATIONS

LIST OF CONGRESSES

Chapter 1. Introduction

- 1.1. Background
- 1.2. Motivation
- 1.3 Hypothesis and objectives
- 1.4 Organization of the document
- 1.5 References

Chapter 2. State of the art. Recent Advances in Nanoporous Anodic Alumina: Principles, Engineering and Applications

Abstract

- 2.1. Introduction
- 2.2. Nanoporous anodic alumina (NAA): principles and formation mechanism of the porous oxide
 - 2.2.1. Electrolytic passivation of aluminum
 - 2.2.2. NAA pore growth mechanism and spatial ordering
 - 2.2.3. Electrolyte specific geometry
 - 2.2.3.1. Impact of temperature and additives
 - 2.2.4. Mild and hard anodization: two growth regimes
 - 2.2.5. Pore separation phenomenon
 - 2.2.6. Pre- and Post-anodization treatments
 - 2.2.6.1. Pre-anodization patterning of the aluminum surface
 - 2.2.6.2. Thermal annealing
- 2.3. Engineered NAA structures
 - 2.3.1. Structures based on the modulation of the anodization current
 - 2.3.2. Nanotubes
 - 2.3.3. Micro- and nanoparticles
 - 2.3.4. Funnel and inverted funnel structures
 - 2.3.5. Hierarchical pore structures

2.3.6. Three-dimensional interconnected nanoarchitectures

2.4. Examples of NAA applications

2.4.1. Photonic structures

2.4.2. Sensors

2.4.3. Templates

2.4.4. Membranes for filtering and separation

2.4.5. Biological monitoring and cell culture

2.4.6. Drug delivery

2.4.7. Functional layer for composites

2.5. Conclusions

2.6 References

Chapter 3. AA Nanotubes Fabrication System and Characterization methods

3.1. Introduction

3.2. Fabrication Setup

3.2.1. Electrochemical cell

3.2.2. Source for growth control

3.2.2.1. Voltage control

3.2.2.2. Current control

3.2.3. Control Program

3.3. Electrolytes

3.4. Preparation of Aluminum wafers

3.5. Fabrication Parameters

3.6. From AAN substrate to nanotubes

3.7. Characterization Techniques

3.7.1. Electron Microscopy

3.7.1.1. Environmental Scanning Electron Microscopy

3.7.1.2. Transmission Electron Microscopy

3.7.2. Confocal Microscopy

3.7.3. Dynamic Light Scattering and ζ -potential

3.7.4. Fourier Transform Infrared Spectroscopy

3.7.5. Spectrophotometry

3.7.6. X-ray Diffraction

3.8. Conclusions

3.9. References

Chapter 4. Tailor-engineered structural and physico-chemical properties of anodic alumina nanotubes by pulse anodization: A step forward.

Abstract

4.1. Introduction

4.2. Experimental

4.2.1. Materials

4.2.2. AANTs fabrication

4.2.3. Structural and physiochemical characterization of AANTs

4.2.4. Annealing and crystallographic characterization of AA and AANTs

4.3. Results

4.3.1. Structure of AA template and AANTs produced by pulse anodization

4.3.2. Evolution of current density/voltage profile during pulse anodization

4.3.3. Effect of hard anodization current density on the physical and chemical properties of AANTs

4.3.4. Effect of hard anodization pulse duration on the physical and chemical properties of AANTs

4.3.5. Post-treatment modification of AANTs produced by pulse anodization

4.3.5.1. Effect of sonication parameters on dispersity and separation of AANTs

4.3.5.2. Effect of annealing temperature on the crystallinity and physio-chemical properties of AANTs

4.4. Conclusions

4.5. Supplementary data

4.6. References

Chapter 5. Magnetic nanoparticle decorated anodic alumina nanotubes for fluorescent detection of cathepsin B.

Abstract

5.1. Introduction

5.2. Materials and methods

5.2.1. Materials

5.2.2. Characterization methods

5.3. Magnetic anodic alumina nanotubes (MAANTs)

5.3.1. Preparation of magnetic anodic alumina nanotubes

5.3.2. Characterization of magnetic anodic alumina nanotubes(MAANTs)

5.4. Stimuli-responsive release of MAANTs load for drug delivery and biosensing applications

5.4.1. Magnetic AANTs(FITC-BSA) fabrication and characterization

5.4.2. Interaction of MAANTs(FITC-BSA) with cathepsin B

5.5. Conclusions

5.6. Supplementary data

5.7. References

Chapter 6. Discussion and Conclusions

LIST OF PUBLICATIONS

J. T. Domagalski, E. Xifre-Perez and L. F. Marsal. Recent Advances in Nanoporous Anodic Alumina: Principles, Engineering and Applications. *Nanomaterials* 2021, 11, 430, DOI: 10.3390/nano11020430.

J. T. Domagalski, E. Xifre-Perez, M. A. Tabrizi, J. Ferre-Borrull and L. F. Marsal. Magnetic nanoparticle decorated anodic alumina nanotubes for fluorescent detection of cathepsin B. *J. Colloid Interface Sci.* 2021, 584, 236-245, DOI: 10.1016/j.jcis.2020.09.109.

J. T. Domagalski, E. Xifre-Perez, A. Santos, J. Ferre-Borrull, and L. F. Marsal. Tailor-engineered structural and physico-chemical properties of anodic alumina nanotubes by pulse anodization: A step forward. *Microporous Mesoporous Mater.* 2020, 303, 110264, DOI: 10.1016/j.micromeso.2020.110264.

LIST OF CONGRESSES

J.T. Domagalski, E. Xifre-Perez, J. Ferre-Borrull and L.F. Marsal. “Structural engineering of magnetic alumina nanotubes”. Porous Semiconductors – Science and Technology 2020 International Conference (PSST 2020), Lidio di Camaio, postponed due to Covid-19 outbreak to 2021 (talk).

J.T. Domagalski, E. Xifre-Perez, J. Ferre-Borrull and L.F. Marsal. “Engineering of magnetic nanotubes based on nanoporous anodic alumina”. Trends in Nanotechnology International Conference (TNT2019), San Sebastian 2019 (talk).

J.T. Domagalski, E. Xifre-Perez, J. Ferre-Borrull and L.F. Marsal. “Controlled fabrication of nanotubes from nanoporous anodic alumina”. NanoSpain2019, Barcelona 2019 (talk).

J.T. Domagalski, E. Xifre-Perez, L.K. Acosta and L.F. Marsal. “Study of physical and photonic properties of anodized alumina nanotubes”. Spanish Conference on Nanophotonics 2018 (CEN2018), San Sebastian 2018 (poster).

Chapter 1. Introduction

1.1. Background

Numerous metals and semiconductors are naturally covered by a native oxide layer that can be additionally developed through the process of anodic oxidation. During the process, the material is immersed in the electrolyte and current flow is introduced to the system. The material of interest serves in such setup as an anode, hence the term anodization. With this approach, it is possible to grow a layer of an amorphous oxide on the surface. Anodization is a process commonly used in industry where it serves as a robust, cost-effective approach to create a surface with better mechanical properties and higher chemical resistance as compared to native metals [1]. Moreover, the anodization of several metals such as aluminum [2], titanium [3], iron [4], zinc and tin [5] can lead to spontaneous formation of nanostructured pores. Not every porous layer provides sufficient benefits to find a niche in nanotechnology, however properties of some are remarkable, usually being intensively investigated or already applied in use [6]–[8]. Recent popularity of nanotechnology originates from the fact that such a small structures have unique properties as compared to a bulk material, and were also the first tool capable of directly affecting biosystems at a cellular level. Titanium oxide is one example of a porous material with multidisciplinary benefits. Anodic TiO₂ nanotubes are effectively immobilized on the titanium surface. Such setup seems promising for hydrogen sensors, since the conductivity of such TiO₂ layer increase by several orders of magnitude in presence of hydrogen at higher temperatures [9]. While anodization usually results in creation of amorphous oxide, it is possible to induce formation of crystalline phase during the process. Dental implants covered with layer of TiO₂ were found to improve osseointegration as compared to the bare metal [10]. Amongst other promising applications, anodic TiO₂ demonstrated its potential with photocatalytic performance [11] and as a component of the composite for anode in lithium-ion batteries [12]. Also porous structures derived from silicon anodization are worth noting, since structures made of mesoporous silica are well-known and may be considered a standard in the field of porous materials. Silica and organosilica fabrication process can be adjusted controlling size, geometry, morphology, composition and surface chemistry [13]. Inorganic nanoparticles have certain niche in drug delivery systems providing more robust architecture and limiting load over time leakage, as compared to fragile polymeric and liposomal structures. Enormous surface area and volume inside porous structures provide for impressive performance of mesoporous silica nanoparticles for drug and gene delivery applications. Porous structure – that can be specifically tailored – is also beneficial at mitigating degradation of more fragile molecules like DNA [14], [15]. Mesoporous silica nanoparticles biodegradability and clearance has been demonstrated in numerous studies and enables safe use in bioapplications [16]. But potential utility is not only limited to biomaterials as several different fields such as detection and selective binding of heavy ions

[17], [18], silica based anode and active filler for lithium-ion batteries [19], [20] or catalysis [21] are also examined.

Aluminum is the most frequently anodized metal. What is more, its anodization process is significantly safer than the fabrication of another highly valued material – mesoporous silica – that involves highly toxic and dangerous hydrofluoric acid [22], [23]. Fabrication of nanoporous anodic alumina is industrially scalable and cost-effective [24], [25]. Taking into account the level of spatial ordering and the high regularity of the structure, nanoporous anodic alumina (NAA) can be considered the most striking example of anodic metal oxide and also, a mesoporous silica competitor. Contrary to soft and flexible aluminum, created NAA layer is hard and brittle [26], [27], although it has been demonstrated that thinner walls of the pores correlate positively with its ductility [28]. In the nanotechnology field, limited versatility of methods is often a significant restriction regarding practical application of the material – needs may often be adjusted to the form/properties rather than otherwise. This aspect incentivize researchers to seek for alternative fabrication methods and materials. Such was the case of aluminum anodization as well. Initially simple yet robust surface coating approach turned into versatile nanofabrication tool. Currently, precise selection of conditions or smart combination of material preparation and post-processing enables to tailor-engineer whole spectrum of nanomaterials: highly ordered mesoporous membranes (10 nm average pore diameter) [29], complex 3D networks [30], nanospheres [31] and nanotubes [32]. Focus of this thesis was on the one particular variant amongst many: pulse anodization with high current pulses resulting in formation of nanotubes.

The method originates from pulse anodization, which was proposed as a mean to optimize the process of hard anodization – process occurring at high current densities resulting in limited control over the process and occasional destruction of the sample [33]. While pulse anodization may serve as an approach leading to high speed defect-free growth of anodic alumina under high current, under certain conditions connections between individual pores are weakened. This property, combined with carefully designed post-processing enabled to yield anodic alumina nanotubes for the first time [32]. First, sufficiently high current flow during anodization was needed to produce the structure with weaker connections between the cells. Second, acid etching step was introduced to exploit occurring discrepancy in the material susceptibility to acid. Third, this loose array of pores was sonicated in water resulting in separation of the structure into nanotubes – colloidal anodic alumina nanotubes were obtained. Anodic alumina nanotubes display many features valuable, especially as a biomaterial and drug nanocarrier. They are biologically inert and exhibit low nanotoxicity, which was supported by both, *in vitro* [34] and *in vivo* [35] studies. Moreover, they feature impressive drug-loading capacity due to intrinsic hollow architecture and can be easily modified through the silanization process [36]. After fabrication, they display low surface reactivity and lack catalyst contamination. These findings facilitated proof-of-concept cancer therapy experiments, in which drug loaded nanotubes were introduced into the cancer cells through targeting of cell signaling networks [37].

These reports already demonstrate potential benefits of anodic alumina nanotubes. However, nanotubes fabrication through pulse anodization is a relatively new discovery that still needs improvements. Aim of this thesis was to contribute to the research on the material: increase the understanding of the process, refine the manufacturing procedure and investigate new functionalization alternatives. The thesis contains detailed introduction to nanoporous anodic alumina in general, and may serve as a guidance when starting the work with the material. Equipment that constitute for fabrication setup and set of measurement techniques are described in detail. Further, formation mechanism and role of every fabrication parameters for creation of nanotubes is explained, providing a step-forward in the manufacturing technique. At last, novel functionalization methods are presented.

1.2. Motivation

The doctoral thesis is an outcome of the research pursued in the Department of Electronic, Electrical and Automation Engineering at the Universitat Rovira I Virgili. Complementary, part of the work was conducted in cooperation with School of Chemical Engineering and Advanced Materials at The University of Adelaide.

Work in the department along with the cooperation enabled to explore and refine a variant of aluminum anodization – hard anodization with pulses – designed to tailor-engineer nanotubes made of the anodic oxide. The process was investigated with aim to improve the overall process yield and precision in which the structure is created. Additionally, analysis of the formation mechanism was analyzed. Further, attempt to provide the material with additional functionalities was carried out. Anodic alumina nanotubes are biologically inert nanoparticles, that can be precisely tailored for required length and diameter. Due to bioavailability and its intrinsically hollow nature, they are attractive candidate when considering drug-delivery systems [36]. Anodic alumina nanotubes were already utilized in proof-of-concept experiments aimed at cancer treatment [37] and their compatibility with living organisms examined [35]. Development of this material, improved understanding of the technique and portfolio of functionalization possibilities may be of value in future experiments providing alternatives to already established solutions.

As a consequence of the research, refined fabrication of nanotubes through pulse anodization of aluminum was reported (see **section 4**). Work consist of analysis how the process parameters influence properties of the yield material. The parameters were associated with the change in morphology and properties, providing detailed guide how to tailor-engineer anodic alumina nanotubes. The improvement enables to yield the shortest so far alumina nanotubes with average length of 424 ± 92 nm. Additionally, dependence between hard anodization current density and diameters of nanotubes: inner and outer (thus, wall thickness) was provided. Apart from the anodization itself, also post-processing alternatives were investigated as well. Degradation of nanotubes under extended high temperature sonication was reported for the first time, highlighting importance of this part of the process as well. With the process refined, functionalization possibilities were investigated (see **section 5**). Charged character of these nanotubes in the suspension was utilized to prepare nanotube-maghemite nanoparticles composite. Positively charged nanotubes were decorated with 10 nm avg. diameter maghemite superparamagnetic nanoparticles. As result, nanotubes gained magnetic properties – which was demonstrated by movement of the suspension following the magnetic field. Another improvement was selective functionalization of inner walls of nanotubes. As the structure is initially similar to standard nanoporous anodic alumina template – outer walls of the pores are in isolated from the environment. Thus, prior to acid etching and sonication, the inner interface can be modified selectively. In our case, protein padding of bovine serum albumin modified with fluorescein isothiocyanate was introduced. After the modification, the nanotubes were liberated and their combined functionalities (protein padding inside + maghemite on the outer walls) examined.

1.3. Hypothesis and objectives

Nanotechnology that involves control over features in nanoscale is at the same time its virtue and a limitation. While ability to manipulate objects as small as components of living matter is a disruptive discovery, design, manufacturing and analysis are significant constraint. These objects, far smaller than the naked eye can perceive are difficult to observe – in fact until recently, not possible with light-based methods. Design of manufacturing processes are stories about taming and exceeding limitations of the known world. Nanotechnology is still about a compromise: how connect what we have and what we can do with what we can measure.

This work is a part of this process – focused on improvement of one of available fabrication techniques. Improvement followed by attempt to provide functionality – that could in the future serve as an application. So far there is no ultimate purpose or need – and scientists are attempting to unravel these many yet blank pages of the science.

Fabrication of nanotubes is a cost-effective nanofabrication tool. The material is biologically inert, can be tailor-engineered through the fabrication process and features impressively high regularity of the structure. The method is relatively new with first report discussing the fabrication process being published in 2008. Until now, several improvements have been introduced, along with detailed analysis of the properties and interactions with living matter explored. However, when compared to other alternative material featuring similar properties, many aspects regarding the material remains on the initial stage – yet to be explored.

With the purpose to alter the current state of the method, the objectives of this thesis have been:

1. Increase understanding of the anodic alumina nanotubes manufacturing process with regards to the mechanism and exact impact of each fabrication parameter.
2. Optimize the process leading to improved quality, i.e. more accurate engineering of nanotubes, increased separation and yield.
3. Explore the functionalization possibilities with aim to increase attractiveness of the method. Development of multi-functional nanotube-based platform with either biomedical or sensor application.

1.4. Organization of the document

This chapter serves as a general overview regarding scope of the work: brief introduction, motivation behind the work and objectives realized in this thesis. Cost-effective, precise nanofabrication is important purpose of continuous development conducted in research facilities. Anodization of aluminum is a method known for a long time, with many perspectives of practical applications. Nanotubes made of the material are still a recent discovery that may yet to gain some of its importance. Part of these efforts are presented in this thesis. At last, each section of the thesis is explained.

Chapter 2 is a journal article titled “Recent Advances in Nanoporous Anodic Alumina: Principles, Engineering, and Applications” published in *Nanomaterials*. It provides state of the art of the anodic alumina fabrication in general. In the first section of the chapter history of the material as well as its importance in material science and nanotechnology fields is presented. Second chapter contains background information with description of formation mechanism, influence of various fabrication parameters on properties and geometry of the structure along with different modifications of the manufacturing process are presented. Third chapter elaborates on complex structural features, that can be tailor-engineered using smart-design approach and formation of nanoparticles. Fourth chapter gathers the most recent applications of the material organized into categories: photonic structures, sensors, templates, membranes, biomaterials, drug delivery and composites. Fifth provides a short summary with a future lookout.

Chapter 3 explains materials and methods utilized in the work. First, each element of the fabrication setup is presented and its role indicated. Then, fabrication conditions are presented. In the next section materials and chemicals are presented and their preparation process explained. Fabrication description is presented in detail, in order to facilitate reproducibility. At last, theoretical background of all characterization techniques used during work on this thesis is provided, together with application of the method and specific model of the device indicated.

Chapter 4 is a journal article titled “Tailor-engineered structural and physico-chemical properties of anodic alumina nanotubes by pulse anodization: A step forward” published in *Microporous and Mesoporous Materials*. It provides description of research aimed at better understanding and optimization of the anodic alumina nanotubes process. At first, state of the art of the technique from before the report is described and motivation behind the project indicated. Second, modification to the fabrication process are presented with purpose behind each change explained. Third, results of these adjustments are presented and supported by detailed analysis of experimental and previously reported data. At last, impact of the work is explained in the summary.

Chapter 5 is a journal article titled “Magnetic nanoparticle decorated anodic alumina nanotubes for fluorescent detection of cathepsin B” published in *Journal of Colloid and Interface Science*. It presents functionalization possibilities on example of magnetically guided Fe₃O₄ NPs (AANTs) functional composite with stimuli-responsive release of protein fragments.

At first, introduction explaining motivation behind the work, materials and characterization methods are discussed. Second, development of magnetic anodic alumina nanotubes (MAANTs) is presented, along with the analysis of created composite. Third, functionalization with protein inside the nanotubes is explained. It follows by evaluation of created functionality – both magnetic and stimuli-responsive features of the material. Last, impact of the work and future suggestions are provided.

Chapter 6 is a summary. Results presented in the thesis are discussed and conclusions provided. Additionally, a recommendation with regards to future work on anodic alumina nanotubes is presented.

1.5. References

- [1] A. Michaelis. In *Electrochemical Surface Modification: Thin Films, Functionalization and Characterization*; Alkire R. C., Kolb D. M., Lipkowski J., Ross P. N., Eds; Willey-VCH, NY, USA, 2008; Chapter 1, p 1-106, DOI: 10.1002/9783527625307.ch1
- [2] W. Lee and S. J. Park. Porous anodic aluminum oxide: Anodization and templated synthesis of functional nanostructures. *Chem. Rev.* **2014**, 114, 7487-7556, doi: 10.1021/cr500002z
- [3] Y. Fu and A. Mo. A Review on the Electrochemically Self-organized Titania Nanotube Arrays: Synthesis, Modifications, and Biomedical Applications. *Nanoscale Res. Lett.* **2018**, 13, 187, doi: 10.1186/s11671-018-2597-z
- [4] M. Martín-González, R. Martínez-Moro, M. H. Aguirre, E. Flores, and O. Caballero-Calero. Unravelling nanoporous anodic iron oxide formation. *Electrochim. Acta* **2020**, 330, 135241, doi: 10.1016/j.electacta.2019.135241
- [5] L. Zaraska, M. Bobruk, and G. D. Sulka. Formation of Nanoporous Tin Oxide Layers on Different Substrates during Anodic Oxidation in Oxalic Acid Electrolyte. *Adv. Condens. Matter Phys.* **2015**, 2015, 302560, doi: 10.1155/2015/302560
- [6] L. Zhou, Y. Tan, J. Wang, W. Xu, W. Cai, S. Zhu & J. Zhu. 3D self-assembly of aluminium nanoparticles for plasmon-enhanced solar desalination. *Nat. Photonics.* **2016**, 10, 393-398, doi: 10.1038/nphoton.2016.75
- [7] M. H. Sun, S. Z. Huang, L. H. Chen, Y. Li, X. Y. Yang, Z. Y. Yuan and B. L. Su. Applications of hierarchically structured porous materials from energy storage and conversion, catalysis, photocatalysis, adsorption, separation, and sensing to biomedicine. *Chem. Soc. Rev.* **2016**, 45, 3479-3563, doi: 10.1039/c6cs00135a
- [8] Q. Wei, F. Xiong, S. Tan, L. Huang, E. H. Lan, B. Dunn and L. Mai. Porous One-Dimensional Nanomaterials: Design, Fabrication and Applications in Electrochemical Energy Storage. *Adv. Mater.* **2017**, 29, e1602300, doi: 10.1002/adma.201602300
- [9] O. K. Varghese, D. Gong, M. Paulose, K. G. Ong, E. C. Dickey, and C. A. Grimes. Extreme changes in the electrical resistance of titania nanotubes with hydrogen exposure. *Adv. Mater.* **2003**, 15, 624-627, doi: 10.1002/adma.200304586.
- [10] M. Pedferri. Titanium Anodic Oxidation: A Powerful Technique for Tailoring Surface Properties for Biomedical Applications. *TMS 2015 144th Annu. Meet. Exhib.* **2015**, pp. 515-520, doi: 10.1007/978-3-319-48127-2_65
- [11] X. Zhou, N. Liu, and P. Schmuki. Photocatalysis with TiO₂ Nanotubes: 'Colorful' Reactivity and Designing Site-Specific Photocatalytic Centers into TiO₂ Nanotubes. *ACS Catal.* **2017**, 7, 3210-3235, doi: 10.1021/acscatal.6b03709
- [12] D. Qi, S. Li, Y. Chen, and J. Huang. A hierarchical carbon@TiO₂@MoS₂ nanofibrous composite derived from cellulose substance as an anodic material for lithium-ion batteries. *J. Alloys Compd.* **2017**, 728, doi: 10.1016/j.jallcom.2017.09.018
- [13] J. G. Croissant, Y. Fatieiev, A. Almalik, and N. M. Khashab. Mesoporous Silica and Organosilica Nanoparticles: Physical Chemistry, Biosafety, Delivery Strategies, and Biomedical Applications. *Adv. Healthc. Mater.* **2018**, 7, 1-75, doi: 10.1002/adhm.201700831
- [14] Y. Zhou, G. Quan, Q. Wu, X. Zhang, B. Niu, B. Wu, Y. Huang, X. Pan and C. Wu. Mesoporous silica nanoparticles for drug and gene delivery. *Acta Pharm. Sin. B.* **2018**, 8, 165-177, doi: 10.1016/j.apsb.2018.01.007
- [15] D. Shao, M. Li, Z. Wang, X. Zheng, Y. H. Lao, Z. Chang, F. Zhang, M. Lu, J. Yue, H. Hu, H. Yan, L. Chen, W. Dong and K. W. Leong. Bioinspired Diselenide-Bridged Mesoporous Silica

- Nanoparticles for Dual-Responsive Protein Delivery. *Adv. Mater.* **2018**, 30, 1-8, doi: 10.1002/adma.201801198.
- [16] J. G. Croissant, Y. Fatieiev, and N. M. Khashab. Degradability and Clearance of Silicon, Organosilica, Silsesquioxane, Silica Mixed Oxide, and Mesoporous Silica Nanoparticles. *Adv. Mater.* **2017**, 29, e1604634, doi: 10.1002/adma.201604634
- [17] M. R. Awual, M. Khraisheh, N. H. Alharthi, M. Luqman, A. Islam, M. R. Karim, M. M. Rahman and M. A. Khaleque. Efficient detection and adsorption of cadmium(II) ions using innovative nano-composite materials. *Chem. Eng. J.* **2018**, 343, 118-127, doi: 10.1016/j.cej.2018.02.116
- [18] A. Shahat, H. M. A. Hassan, H. M. E. Azzazy, E. A. El-Sharkawy, H. M. Abdou, and M. R. Awual. Novel hierarchical composite adsorbent for selective lead(II) ions capturing from wastewater samples. *Chem. Eng. J.* **2018**, 332, 377-386, doi: 10.1016/j.cej.2017.09.040
- [19] W. An, B. Gao, S. Mei, B. Xiang, J. Fu, L. Wang, Q. Zhang, P. K. Chu & K. Huo. Scalable synthesis of ant-nest-like bulk porous silicon for high-performance lithium-ion battery anodes. *Nat. Commun.* **2019**, 10, 1-11, doi: 10.1038/s41467-019-09510-5
- [20] D. Lin, P. Y. Yuen, Y. Liu, W. Liu, N. Liu, R. H. Dauskardt and Y. Cui. A Silica-Aerogel-Reinforced Composite Polymer Electrolyte with High Ionic Conductivity and High Modulus. *Adv. Mater.* **2018**, 30, 1-8, doi: 10.1002/adma.201802661
- [21] M. Hu, Z. Xing, Y. Cao, Z. Li, X. Yan, Z. Xiu, T. Zhao, S. Yang and W. Zhou. Ti³⁺ self-doped mesoporous black TiO₂/SiO₂/g-C₃N₄ sheets heterojunctions as remarkable visible-lightdriven photocatalysts. *Applied Catalysis B: Environmental.* **2018**, 226, 499-508, doi: 10.1016/j.apcatb.2017.12.069
- [22] R. Herino, G. Bomchil, K. Barla, C. Bertrand, and J. L. Ginoux. Porosity and Pore Size Distributions of Porous Silicon Layers. *J. Electrochem. Soc.* **1987**, 134, 1994-2000, doi: 10.1149/1.2100805
- [23] H. Masuda and K. Fukuda. Ordered Metal Nanohole Arrays Made by a Two-Step Replication of Honeycomb Structures of Anodic Alumina. *Science.* **1995**, 268, 1466-1468, doi: 10.1126/science.268.5216.1466
- [24] R. Z. Valiev, A. A. Nazarov. In *Bulk Nanostructured Materials*; Zehetbauer M. J., Y. T. Zhu, Eds; Willey-VCH: NY, USA, 2009; Chapter 2, p 21-48, DOI: 10.1002/9783527626892.ch2
- [25] W. Lee. The anodization of aluminum for nanotechnology applications. *Jom.* **2010**, 62, 57-63, doi: 10.1007/s11837-010-0088-5
- [26] P. Gu, H. Miao, Z. T. Liu, X. P. Wu, and J. H. Zhao. Investigation of elastic modulus of nanoporous alumina membrane. *J. Mater. Sci.* **2004**, 39, 3369-2273, doi: 10.1023/B:JMISC.0000026938.59949.1f
- [27] L. Vojkuvka, A. Santos, J. Pallarès, J. Ferré-Borrull, L. F. Marsal, and J. P. Celis. On the mechanical properties of nanoporous anodized alumina by nanoindentation and sliding tests. *Surf. Coatings Technol.* **2012**, 206, 8-9, doi: 10.1016/j.surfcoat.2011.09.040
- [28] J. Dai, J. Singh, and N. Yamamoto. Nonbrittle nanopore deformation of anodic aluminum oxide membranes. *J. Am. Ceram. Soc.* **2018**, 101, 2170-2180, doi: 10.1111/jace.15367
- [29] O. Nishinaga, T. Kikuchi, S. Natsui, and R. O. Suzuki. Rapid fabrication of self-ordered porous alumina with 10-/sub-10-nm-scale nanostructures by selenic acid anodizing. *Sci. Rep.* **2013**, 3, 1-6, doi: 10.1038/srep02748
- [30] A. Ruiz-Clavijo, S. Ruiz-Gomez, O. Caballero-Calero, L. Perez, and M. Martin-Gonzalez. Tailoring Magnetic Anisotropy at Will in 3D Interconnected Nanowire Networks. *Phys. Status Solidi - Rapid Res. Lett.* **2019**, 13, 1900263, doi: 10.1002/pssr.201900263

- [31] T. Yanagishita, M. Imaizumi, T. Kondo, and H. Masuda. Formation of porous Al particles by anisotropic anodic etching. *Electrochem. commun.* **2017**, *78*, 26-28, doi: 10.1016/j.elecom.2017.03.019
- [32] W. Lee, R. Scholz, and U. Gösele. A continuous process for structurally well-defined Al₂O₃ nanotubes based on pulse anodization of aluminum. *Nano Lett.* **2008**, *8*, 2155-2160, doi: 10.1021/nl080280x
- [33] W. Lee, R. Ji, U. Gösele, and K. Nielsch. Fast fabrication of long-range ordered porous alumina membranes by hard anodization. *Nat. Mater.* **2006**, *5*, 741-747, doi: 10.1038/nmat1717
- [34] Y. Wang, G. Kaur, A. Zysk, V. Liapis, S. Hay, A. Santos, D. Losic and A. Evdokiou. Systematic invitro nanotoxicity study on anodic alumina nanotubes with engineered aspect ratio: Understanding nanotoxicity by a nanomaterial model. *Biomaterials* **2015**, *46*, 117-130, doi: 10.1016/j.biomaterials.2014.12.008
- [35] Y. Wang, I. Zinonos, A. Zysk, V. Panagopoulos, G. Kaur, A. Santos, D. Losic and A. Evdokiou. In vivo toxicological assessment of electrochemically engineered anodic alumina nanotubes: a study of biodistribution, subcutaneous implantation and intravenous injection. *J. Mater. Chem. B.* **2017**, *5*, 2511-2523, doi: 10.1039/C7TB00222J
- [36] Y. Wang, A. Santos, G. Kaur, A. Evdokiou, and D. Losic. Structurally engineered anodic alumina nanotubes as nano-carriers for delivery of anticancer therapeutics. *Biomaterials.* **2014**, *35*, 5517-5526, doi: 10.1016/j.biomaterials.2014.03.059
- [37] Y. Wang, G. Kaur, Y. Chen, A. Santos, D. Losic, and A. Evdokiou. Bioinert Anodic Alumina Nanotubes for Targeting of Endoplasmic Reticulum Stress and Autophagic Signaling: A Combinatorial Nanotube-Based Drug Delivery System for Enhancing Cancer Therapy. *ACS Appl. Mater. Interfaces* **2015**, *7*, 27140-27151, doi: 10.1021/acsami.5b07557

Chapter 2. State of the art. Recent Advances in Nanoporous Anodic Alumina: Principles, Engineering and Applications

Abstract

The development of aluminum anodization technology features many stages. With the story stretching for almost a century, rather straightforward—from current perspective—technology, raised into an iconic nanofabrication technique. The intrinsic properties of alumina porous structures constitute the vast utility in distinct fields. Nanoporous anodic alumina can be a starting point for: Templates, photonic structures, membranes, drug delivery platforms or nanoparticles, and more. Current state of the art would not be possible without decades of consecutive findings, during which, step by step, the technique was more understood. This review aims at providing an update regarding recent discoveries—improvements in the fabrication technology, a deeper understanding of the process, and a practical application of the material—providing a narrative supported with a proper background.

2.1. Introduction

In 2015, the nanotechnology worldwide market value amounted to \$14.7 billion. Based on the growth rate observed back then, the market was predicted to grow by 375% and reach \$55 billion in 2022 [1]. Three years before 2022—in 2019—market value of nanotechnology reached over \$64 billion, exceeding the prediction significantly. The scale is even more impressive taking into account that so far, the majority of commercially available nanomaterials in the market are currently at the initial stage of their product life cycle. What is more, since countries are often lacking precise regulations involving production, distribution, and use of nanomaterials, precautionary measures are applied that can potentially slow down the development [2]. For example, nanomaterials are excluded from the simplified authorization procedure [3]. We are still ahead of the rapid expansion to various branches of the industry [4]. Furthermore, this opinion is not alone. The European Committee proposed the term Key Enabling Technology (KET) defining the most promising technologies to secure strategic position and competitiveness of the European industry. Advanced materials, nanotechnology, nano and microelectronics, photonics, biotechnology, and advanced manufacturing have all been identified as KETs [5]. Although there are many materials/technologies that cover some of these aspects, only a few cover all of those mentioned. An example of such can be fabrication and utilization of nanoporous anodic alumina.

Aluminum is the most frequently anodized metal. During the process, material is immersed in the electrolyte and the current flow is introduced to the system. The material of interest serves in such setup as an anode, hence the term anodization. With this approach, it is possible to grow a layer of an amorphous oxide on the material surface. Anodization is a process commonly used in the industry where it serves as a robust, cost-effective approach to provide the surface with better mechanical properties and higher chemical resistance of metals [6]. However, under carefully adjusted conditions, the created structure is highly ordered. In combination with intrinsic chemical and physical properties, material has been considered to various applications [7–13]. Amongst other materials, it offers fabrication simplicity and tailor-engineering versatility combined with the unprecedented self-ordered regularity as compared to other nanoporous materials [14,15]. What is more, the anodization process is significantly safer than the fabrication of another highly valued material—mesoporous silica—that involves highly toxic and dangerous hydrofluoric acid [16,17]. Fabrication of nanoporous anodic alumina is an industrially scalable and cost-effective process [18,19]. Taking into account the level of spatial ordering and the high regularity of the structure, nanoporous anodic alumina (NAA) can be considered as the most striking example amongst anodic metal oxides and, also, a mesoporous silica competitor. Contrary to soft and flexible aluminum, the created NAA layer is hard and brittle [20,21], although it has been demonstrated that thinner walls of the pores correlate positively with its ductility [22].

Since its first introduction to the industrial scale in 1923, fabrication technology has changed greatly. Observation of new discoveries and the continuous development is a fascinating demonstration of how science carves its path towards excellence. The precise nanotechnology tool nanofabrication of NAA began as a robust protective coating method—back then, no one was aware of its nanostructured morphology. Although this review will not provide elaborate details about the material's fabrication development history, insight on particular milestones is provided. Instead, focus was laid on gathering the most crucial data about formation mechanism, its tailor-engineering, investigation of certain material properties, and the most recent applications. The aim was to provide a comprehensive review, convenient as a first step to work with nanoporous anodic alumina.

2.2. Nanoporous anodic alumina (NAA): principles and formation mechanism of the porous oxide

NAA is formed by the electrochemical anodization of pure aluminum wafers and consists of a parallel array of pores surrounded by hexagonal cells of aluminum oxide (alumina). Each cell is in a direct contact with six others forming a structure that resembles a honeycomb. The pores grow in depth perpendicularly to the metallic surface as the anodization advances. A standard NAA structure can be defined with three physical parameters: The pore diameter (d_p), the interpore distance (d_{int}), and the length of the pores (l_p). These geometrical features of NAA are shown in figure 2.1 [12].

The pore diameter can range from 8 to 500 nm for NAA structures and depends on the anodization process conditions such as the applied potential, the electrolyte, and its temperature [23–26].

The interpore distance d_{int} indicates the average distance between the centers of two consecutive pores. This is an important value to determine the porosity of the structure since higher interpore distance translates to a smaller density of pores per surface unit. Higher concentration of the electrolyte and temperature seems to reduce the resulting interpore distance, while the applied potential was found to be in a positive correlation [27]. NAA presents high pore densities between 10^8 – 10^{11} cm^{-2} and pore length ranging from a few nanometers up to millimeter scale [28].

The length of the pore l_p is proportional to the total current charge. During a standard anodization carried out under potentiostatic conditions, a brief initial rise and fall of the current precedes the stable plateau that enables to estimate thickness based on duration of the anodization [29,30]. Although the geometry of the pores remains constant during all the anodization process when the anodization parameters are kept invariant, it can be observed that pores tend to be wider close to the surface. It can be attributed to the longer exposure time, which causes slow oxide dissolution by the electrolyte. This may yield a certain degree of discrepancies as initial geometric features are determined by the process conditions. The dissolution rate of NAA in various acids is compared in the work of Poznyak et al. [31]. It was demonstrated to depend on the nature of the acid—the reactivity with respect to aluminum and the morphology of aluminum surface.

The influence of conditions that enable the precise tailoring of NAA's geometrical features such as the electrolyte, its temperature and additives, the anodization potential and current, and post-processing treatments are described in detail in the sections below.

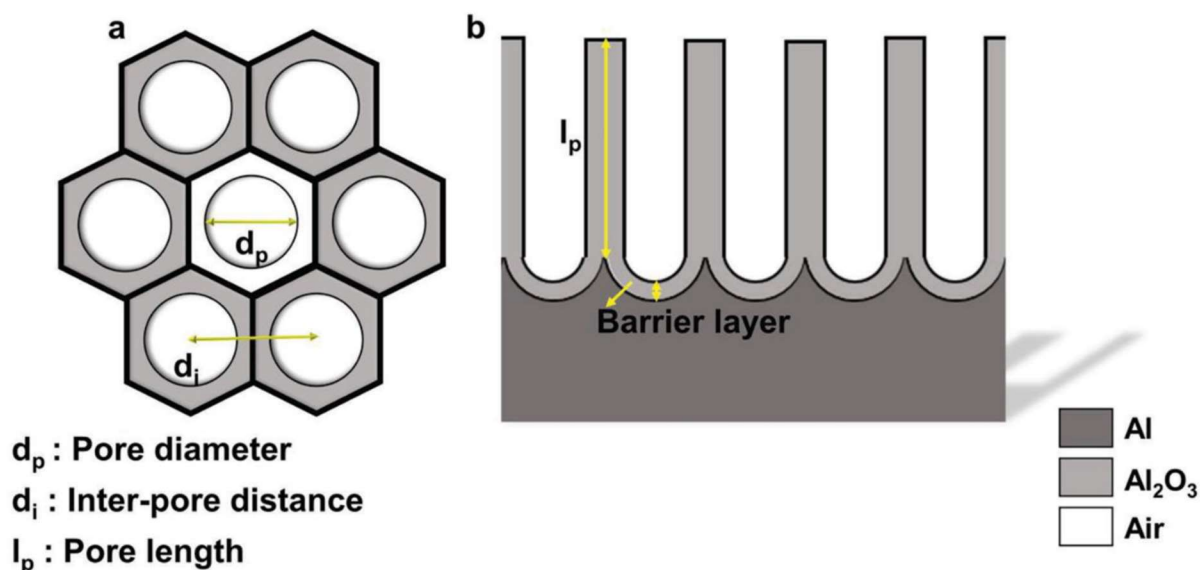


Figure 2.1. Schematic representation of nanoporous anodic alumina (NAA) structure. (a) Top-view with defined geometrical parameters; (b) cross-section with chemical composition. Reprinted with permission from [12]. Copyright 2017 Wiley.

By chemical definition, NAA is an amorphous aluminum oxide with built up water and remains of the electrolyte ions incorporated during the anodization. The distribution of the impurities resembles layered onion-like structure with the highest concentration of ionic residues at the inner walls of the pores with a gradual decrease to the outside part of the pores [32–34]. This intake is an intrinsic factor partially responsible for the variations in the thermal conductivity of NAA reported in the literature. Recently, an attempt to systematize the observed effect was reported by Vera-Londono et al. [35]. It was established that thermal conductivity depends on the presence of ionic impurities—thus the electrolyte of choice—along with water built in the structure, and the crystalline form. As temperature increases to 100°C, a drop in the thermal conductivity (~50%) is observed along with water loss. Later, however, continuous increase can be observed. Both removal of ionic impurities and transition into crystalline form result in higher thermal conductivity: $0.78 \pm 0.19 \text{ W m}^{-1} \text{ K}^{-1}$ for the sulfuric NAA heated to 100°C and reaching $4.16 \pm 0.35 \text{ W m}^{-1} \text{ K}^{-1}$ when the sample was annealed at 1300°C.

NAA is an attractive and interesting material that presents important features. One of the most prominent features of NAA is its optical responsiveness that can be tailored to act as a photonic crystal [34,36]. It exhibits a high degree of transmittance in the visible light region [37,38]. Additionally, NAA has photoluminescent properties [39]. The origin of the photoluminescent properties of NAA was examined by Cantelli et al. [40]. Recombination centers derived from oxygen defects were proposed as the origin of the emission. The outlined hypothesis pointed onto different current densities present during the anodization in different electrolytes as the contributing factor to the quantity of oxygen vacancies inside the NAA.

The material features also dielectric properties. The dielectric constant and loss are inversely proportional to the porosity of NAA and the applied alternating current frequency. The behavior of NAA is similar to other ceramic materials [41].

NAA is attractive not only due to its impressive enormous surface area combined with high chemical and thermal resistance, but due to the range of robust functionalization processes such as salinization [42], electrostatic interaction [43], and immune complexation [44] that allow versatile utility of such substrates: Sensors [45,46], templates [47], or drug delivery systems [48].

2.2.1. Electrolytic passivation of aluminum

As mentioned before, NAA is obtained by the electrochemical etching of aluminum, however the electrochemical etching of aluminum does not always result in a porous structure of alumina: Different morphology of the grown oxide can be observed depending on the chemical character of the electrolyte. Electrolyte acidity is considered the major contribution factor to the distinct growth behavior. Anodization in a neutral electrolyte (borate, oxalate, citrate etc.; pH 5–7), that does not react with aluminum oxide yields a barrier-type anodic alumina as shown in figure 2.2a [49]. However, an anodization performed in an acidic electrolyte (in which the oxide structure is slowly dissolved) results in the formation of a porous structure (figure 2.2b) [50,51]. The most common electrolytes applied to create porous alumina are phosphorous, oxalic, and sulfuric acids—all featuring unique current/voltage parameters and structure geometry [52]. The anodization profile reflects the formation stage of the structure—the creation of a barrier layer and the growth of pores. In potentiostatic conditions, the formation of a barrier-type oxide follows exponential decrease of the current over time that goes along with the growth rate decrease. This retardation of the current flow is also reflected in a significant decrease of accessible oxide thickness as compared to the porous structure (figure 2.2a). The formation of a nanoporous anodic alumina can be followed along with the current flow changes. Initial oscillations are related to the rearrangement of the structure with succeeding stabilization, when reaction reaches equilibrium. Then, quasi-stable current flow can be maintained for up to several days providing a steady growth rate (figure 2.2b). A nanoporous film can reach even several hundreds of micrometers with a thickness linearly dependent on the applied current charge [24].

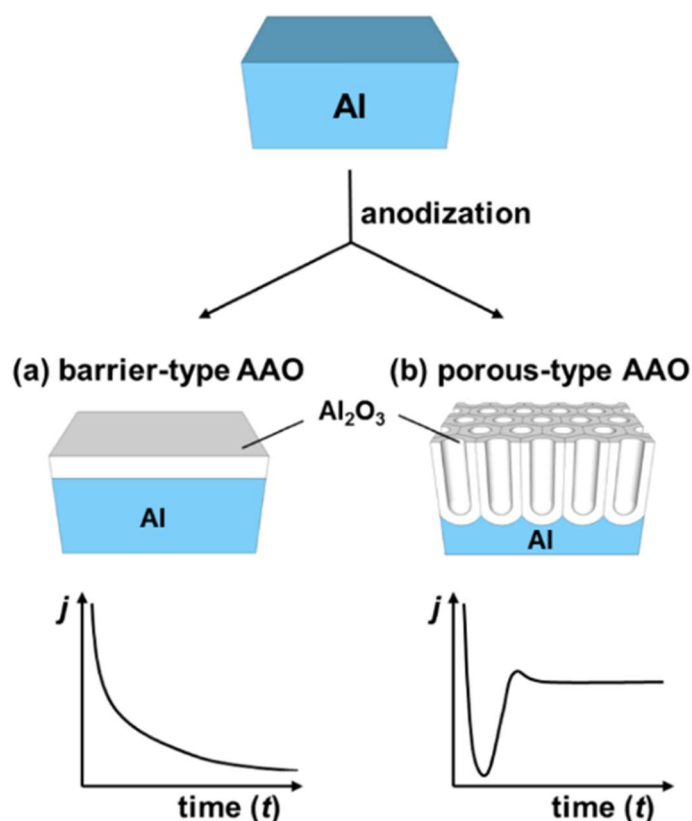


Figure 2.2. Types of anodic aluminum oxide and corresponding current-time transients.

(a) Barrier type and
(b) porous type.

Reprinted with permission from [49].
Copyright 2014 American Chemical Society.

Through the radiotracer studies, it was possible to determine the exact place in which the formation of the oxide occurs in both scenarios. During the formation of a barrier oxide, growth occurs simultaneously at two interfaces: Oxide/electrolyte and metal/oxide. When a porous type alumina is formed, growth takes place only at the metal/oxide interface [53,54]. In further parts of the review, only porous structures will be discussed due to their unique, complex morphology in the micro- and nanoscale.

2.2.2. NAA pore growth mechanism and spatial ordering

While the word 'formation' may intuitively point to the one-way character of the process, it is in fact a result of several reactions occurring collaterally [55]. Pore formation during the anodization of aluminum is generally considered as a consequence of the equilibrium between two opposing changes in the structure: (i) Growth of the aluminum oxide at the metal/oxide interface and (ii) dissolution of the aluminum oxide at the oxide/electrolyte interface [56]. Simplified representation of the changes that occur during the anodization are visualized in figure 2.3. When a constant anodic potential is applied, the entire surface of aluminum gets covered with a thin oxide barrier layer (I, figure 2.3). As the process continues, electric resistance of the setup gradually increases along with the oxide layer growth resulting in the drop of the current flow, until it reaches a minimum value (II, figure 2.3). O'Sullivan and Wood [27] suggested that at this stage the electric field concentrates on the local imperfections in the barrier layer. Different explanation, focusing on the local cracking in the barrier layer that

facilitates the electrolyte penetration, was proposed by Thompson [57,58]. Polarization of Al-O bonds that goes along with the increased electric field can further promote the dissolution of the oxide. During this stage, a rapid increase of the current density can be observed (III, figure 2.3) following a slight decrease and stabilization (IV, figure 2.3). This slight drop has been related with a decrease in the pore density at the beginning of the process attributed to merging of pores.

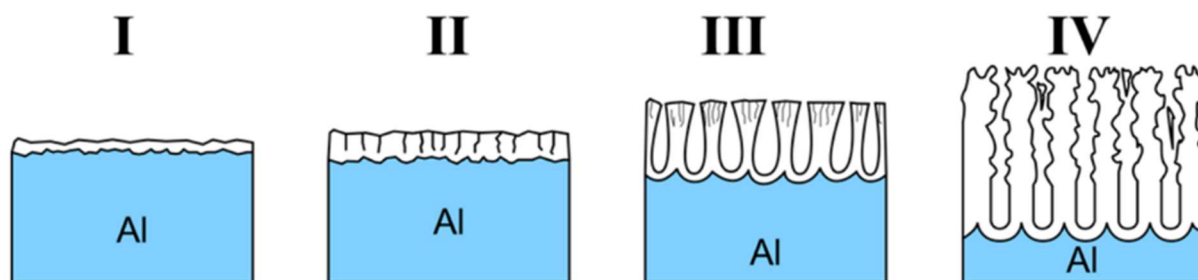


Figure 2.3. Scheme of step-by-step formation of porous oxide. (I) Formation of barrier layer, (II) formation of local cavities, (III) growth of porous structure, and (IV) schematic of nanoporous structure with initially disordered structure and following self-ordering. Reprinted (adapted) with permission from [49]. Copyright 2014 American Chemical Society.

The growth of highly organized structure from the very beginning of the process is possible only after certain preparations or pre-patterning. As shown in figure 2.3, initial porous structure is disordered. However, as the process continues, the structure below becomes ordered. To avoid the presence of disordered pores at the outer surface, the golden standard utilized during NAA fabrication is the two-step anodization process [17]. Once the structure becomes regular during the first anodization step, the oxide layer is selectively removed—surface of the aluminum plate features cavities that mirrors geometry of the organized structure. Then, when the second step of anodization is applied, the growth immediately follows this geometry. It is important to note that high regularity can be obtained only under narrow sets of anodization conditions. There are many factors that affect the course of the anodization process: Potential, current flow, ion migration, local depletion, and in certain conditions, even electrical breakdown.

The extended investigation of the anodic alumina formation had led to the conclusion that growth and self-organization of alumina are significantly affected by the internal stress occurring during the formation process. A volume expansion is one of the crucial factors that have an impact on self-ordering. It was discovered [59] that the highest ordering occurs with a moderate volume expansion. Either the significant volume expansion or the contraction is accompanied by more disordered pores. Evolution of the internal stress that occurs during pores initiation and growth leads to the increase of the compressive stress with raising alumina thickness [60]. What is more, the extent of volume expansion can be linked to the regularity of the obtained structure. A simple way to quantify the volume expansion is by comparison between the final NAA volume to the initial thickness of aluminum. The relation between the spatial ordering and the observed volume expansion is investigated in the work of Jessensky [59]. Either contraction or higher expansion would result in a lower degree of

ordering. These results were independently supported in the research of Nielsh et al. [61]. They proposed the 10% porosity rule as a requirement for the highest spatial ordering, which translates to the volume expansion of 1.23 independently of the anodization conditions. While in the most cases reported results remain in a good agreement with this implication, there are some exceptions. For example, it was possible to obtain highly ordered structures with 0.3 M selenic acid at much lower porosity of 0.8% [23].

Completely ordered NAA structures can be obtained for certain electrolytes under a narrow range of anodization conditions that are discussed in the next section.

2.2.3. Electrolyte specific geometry

While development of the technology to increase the control over the process and reach high regularity is still an important research objective, decades ago its progress was significantly restricted by the existence of the initial, disordered layer of the alumina combined with a lack of sufficient tools to force the high ordering from the very beginning of the oxide growth. To date, the most frequently cited article involving nanoporous anodic alumina—the one that elevated the moderately attractive surface functionalization approach into a sophisticated nanotechnology tool—was the discovery done by Masuda and Fukuda [17]. The exponential growth of publications in two recent decades that followed the discovery is justified by the impressive regularity achievable with this new approach [62,63]. Properties of the grown NAA depend highly on the applied potential (with the resulting current) and a specific electrolyte. An initially disordered porous structure starts to form a regular array of hexagonal cells. The size of these cells is linearly dependent on the applied potential. However, it was observed that the highly regular morphology featuring low quantity of structural defects can be achieved only in narrow sets of conditions [64,65]. Each electrolyte utilized in the formation of nanoporous anodic alumina features a set of conditions: Potential, electrolyte concentration, and temperature in which high ordering can be achieved.

It was empirically established in many independent experiments, that interpore distance—or “cell size”—of the NAA structure depends directly on the applied voltage being defined as:

$$D_{\text{int}} = k U_{\text{an}} \quad (1)$$

where U_{an} is an anodization voltage and k the constant that can be roughly estimated as $k = 2.5 \text{ nm V}^{-1}$, independently of the applied electrolyte [49,66]. However, self-ordered growth occurs only in a narrow range of anodization potential that is unique to particular ionic species. An incentive to seek for new electrolytes and self-ordering regimes is justified by the perspective to provide better covering of already accessible geometry [67].

A complete revision of the electrolytes reported in the literature that provide a high regularity of the porous structure and the corresponding range of obtainable pore distance is gathered in Table 1 and graphically represented in figure 2.4. The value of k constant was based on

calculation of all the values available in reports included in the Table 1. The presented value of $k = 2.39 \text{ nm V}^{-1}$ is close to the previously proposed simplified estimation [49,66].

The majority of research articles involves the fabrication of NAA grown in one of three acids considered “standard”: Sulfuric acid (H_2SO_4), oxalic ($\text{H}_2\text{C}_2\text{O}_4$), and phosphoric (H_3PO_4) [27,52]. They are well-known and have been utilized for decades. Sulfuric acid was the first electrolyte used to yield an anodic alumina layer—initially with the intention to improve the corrosion resistance and hardness of the aluminum components. Amongst the aforementioned, it provides a triangular lattice with the highest density, which is a desirable feature in microelectronics [68,69]. What is more, the sulfuric-NAA provides the highest versatility in terms of an available cell size. Additionally, structures formed during the hard anodization exhibit high hardness of up to 400 Hv, attractive in terms of mechanical performance [70]. Even more impressive physical properties can be achieved with the novel discovery of the etidronic-NAA. The structures made with etidronic acid are 50% harder than with the sulfuric acid hard anodization (610 Hv) and can be further strengthened with thermal annealing (769 Hv) while featuring a low porosity of ~4%. What is more, the geometry of etidronic-NAA with near-subwavelength periodicity results in a significant reflection of light in the visible region: 490–760 nm [71]. Another phosphonate compound explored as an electrolyte for aluminum anodization is phosphonoacetic acid however, it has not been thoroughly investigated so far [72]. Different instance of a structure highly attractive in terms of optical properties is oxalic acid. The oxalic-NAA is often used to prepare photonic structures [73,74]. Fabrication of photonic crystals with improved color saturation preserving the aluminum substrate, which is possible due to introduction of short, high-voltage (250 V) anodization step subsequent to the conventional sinusoidal pulse anodization, was demonstrated by Sun et al. [75]. The oxalic-NAA is also one of the most prominent examples with regards to the photoluminescence performance, exceeding that of the sulfuric- and the phosphoric-NAA and can be adjusted with fabrication conditions [76,77]. Another example of a photoluminescence-active structure can be the arsenic-NAA [78]. This recent approach is characterized with a structure featuring much thicker skeleton of pure alumina as compared to other typical electrolytes. Moreover, the arsenic-NAA exhibits unique white photoluminescence emission (515 nm) under UV irradiation (254 nm). On the other hand, the tartaric-NAA features a broad spectrum of blue luminescence (400–750 nm). Detailed analysis of the as-prepared and annealed tartaric-NAA films revealed two sources of the emission [79]. The highest intensity peak with a maximum at 460 nm originated from bulk and adsorbed OH groups, while amorphous carbon derived from the electrolyte contributed to the peak at 550 nm. Practically, the tartaric acid-NAA remains unexplored with regards to nanotechnology, but the mixture of tartaric-sulfuric acid has been implemented as an alternative replacing chromic acid anodization for European aeronautical industry in 2014 [80]. Recently, a new electrolyte has been found to yield highly ordered porous structure. A high degree of self-ordering with malic acid was discovery by Zajączkowska et al. [81]. Additionally, it was observed that the repetition of anodization—applying the same external anodization parameters—affects the current-time transient. It was suggested that a high degree of malate ion incorporated into a NAA structure could promote

attraction of these ions to the Al electrode further facilitating formation of the oxide structure—the first such observation reported in the literature so far.

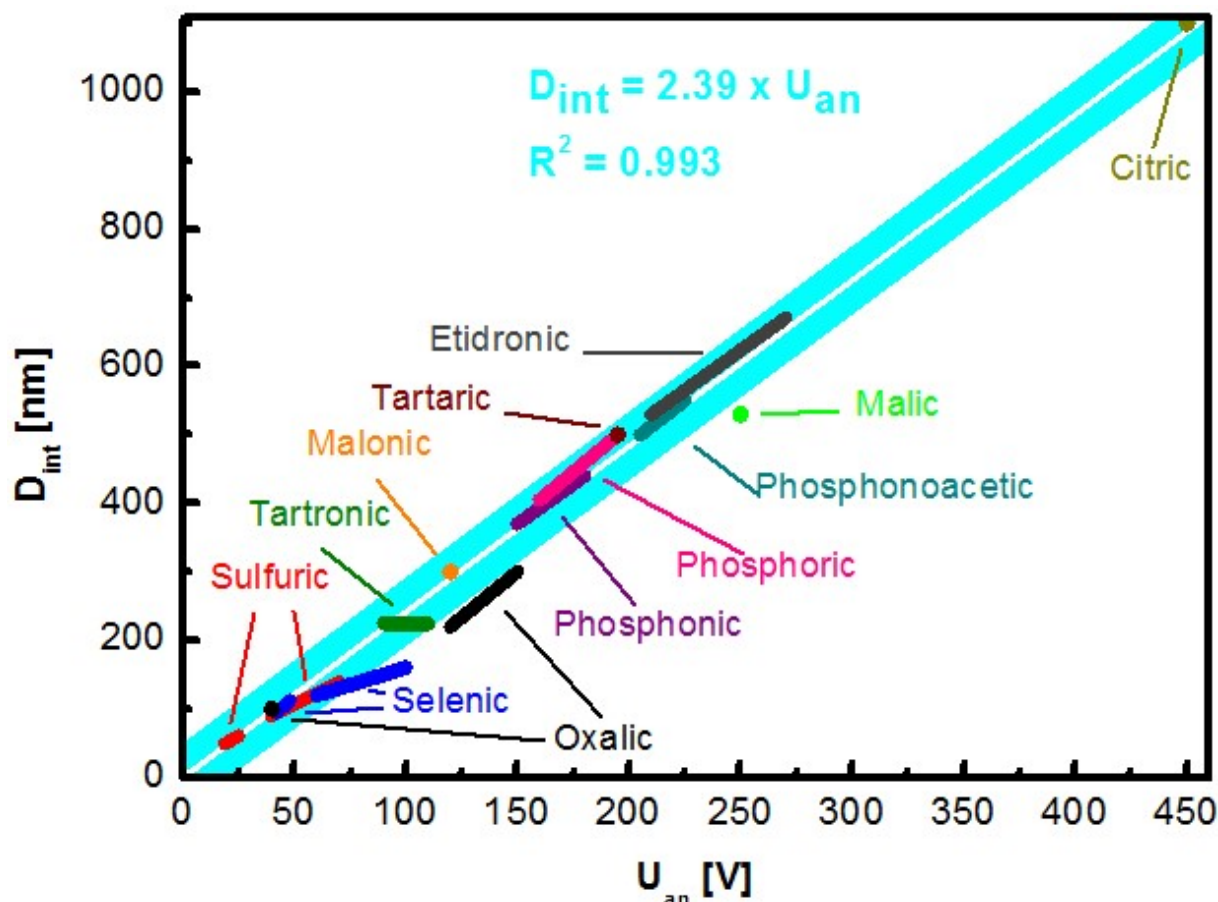


Figure 2.4. Linear relationship between anodization potential and interpore distance for self-ordered NAA formed during anodization in various electrolytes: Sulfuric, selenic, oxalic, tartronic, malonic, phosphonic, phosphoric, tartaric, phosphonoacetic, etidronic, malic, and citric acids.

Another acid that has been explored moderately recently (reported by Nishinaga et al. [23]) that can be used to yield a porous structure is selenic acid. The great potential of the selenic-NAA stems from its low porosity, colorlessness, and high transparency. Intriguingly, as compared to the NAA formed with organic electrolyte, it does not exhibit photoluminescence. It is also competitive with regards to the sulfuric-NAA due to rapid formation of the self-ordered structure of 10-nm pore diameter within 1 h. Similarly to sulfuric acid, self-ordering can be achieved for more than one potential range providing for higher fabrication versatility [23,82,83].

Table 2.1. Interpore distance reported for nanoporous anodic alumina anodized in various electrolytes.

Interpore Distance [nm]	Electrolyte	Concentration	Applied Potential [V]	Temperature [°C]	Reference
50–60	Sulfuric acid	0.3 M	19-25	5	[52]
90–140	Sulfuric acid	10 wt %	40-70	0.1	[84]
95–112	Selenic acid	0.3 M	42-48	20	[23,85]
100	Oxalic acid	0.3 M	40	5	[52]
120–160	Selenic acid	0.3 M	60-100	0	[82]
225	Tartronic acid	0.3 M	90-110	0.5	[86]
220–300	Oxalic acid	0.3 M	120-150	1–2	[24]
300	Malonic acid	5.0 M	120	0–1	[87,88]
370–440	Phosphonic acid	0.5–2.0 M	150–180	0–20	[89]
405–500	Phosphoric acid	0.3 M	160–195	5	[52]
500	Tartaric acid	2–4 wt %	195	5	[90]
530	Malic acid	0.5 M	230	5	[81]
500–550	Phosphonoacetic acid	0.1–0.9 M	205–225	10	[72]
530–670	Etidronic acid	0.3 M	210–270	0–40	[66,91]
1100	Citric acid	0.1–1 M	260–450	10–30	[92]

2.2.3.1. Impact of temperature and additives

Temperature of the electrolyte during anodization is an important factor affecting the formation of NAA. Higher temperature is a convenient measure to accelerate the alumina growth and adjust the resultant pore diameter not affecting interpore distance simultaneously [93,94]. Evaluation how—independently of the electrolyte temperature—temperature of the aluminum anode can impact the formation of NAA was performed by Chernyakova et al. [95]. For the temperature increase between 5 °C and 60 °C d_p and d_{int} remain unchanged, while structural ordering has increased. Results indicate that the rate of the NAA chemical dissolution is not temperature dependent. Furthermore, above 60°C the self-ordering drops and formed pores are 1.7 times broader. However, outcome of the anodization can be also altered using addition of various chemicals to the electrolyte.

Ethanol is a common electrolyte additive that enables to perform anodization below 0 °C reaching lower current densities. It allows to yield even smaller pores, for example 8 nm diameter pores for the sulfuric-NAA [26,96,97]. It was recently demonstrated that addition of ethanol improves the formation of NAA in sulfuric acid, suppressing its chemical dissolution and the anodization rate. What is more, the anodization was possible even with 50% ethanol content in the electrolyte [98]. Another common additive is ethylene glycol. It increases viscosity of the electrolyte decreasing the dissociation constant. Consequently, reduced electrolyte conductivity decreases current density. It is especially useful when anodizing low-purity aluminum as the increase of the current density may occur due to the localized

impurities. Additionally, the anodization in a broader range of potential is possible without burning phenomenon. Yet, above certain critical potential values, hillocks and cracks occur decreasing the quality of resulting NAA [99]. The presence of ethylene glycol in the electrolyte for aluminum anodization facilitates oxidation of the intermetallic phase. Consequently, the connection between adjacent cells is weakened and voids form at the three cell junction—the effect intensifies along with raising ethylene glycol content [100]. Furthermore, intensified oxidation was linked with the increased incorporation of elements that does not originate from the electrolyte. It was established that increased intake derives from the elements present in the AA7075 alloy. Additionally, the growth rate had decreased as compared to the anodization without ethylene glycol [101]. When different alcohols are compared, effects are more pronounced for polyhydric alcohols [102]. However, not every aspect of electrolyte additives has been revealed so far. The challenge is their impact seems to be independently affected by other modifiers such as electrolyte, current density, pH, viscosity, etc. Anodization with addition of poly(ethylene glycol) (PEG) enables to alter pore diameter of the grown structure independently of the anodization voltage [103]. Authors attribute this behavior to the increase of the electric field strength (PEG has lower dielectric coefficient than water) and restricted chemical dissolution process. It was observed that immersion of the NAA films in the acid solution with 50% addition of PEG resulted in 4 times slower dissolution as compared to solution without PEG. As a result, it was possible to modulate the pore diameter of the structure using different content of PEG, while other parameters (acid concentration, anodization voltage, and electrolyte temperature) remained constant. The impact of PEG containing electrolyte on the morphology of NAA is shown in figure 2.5.

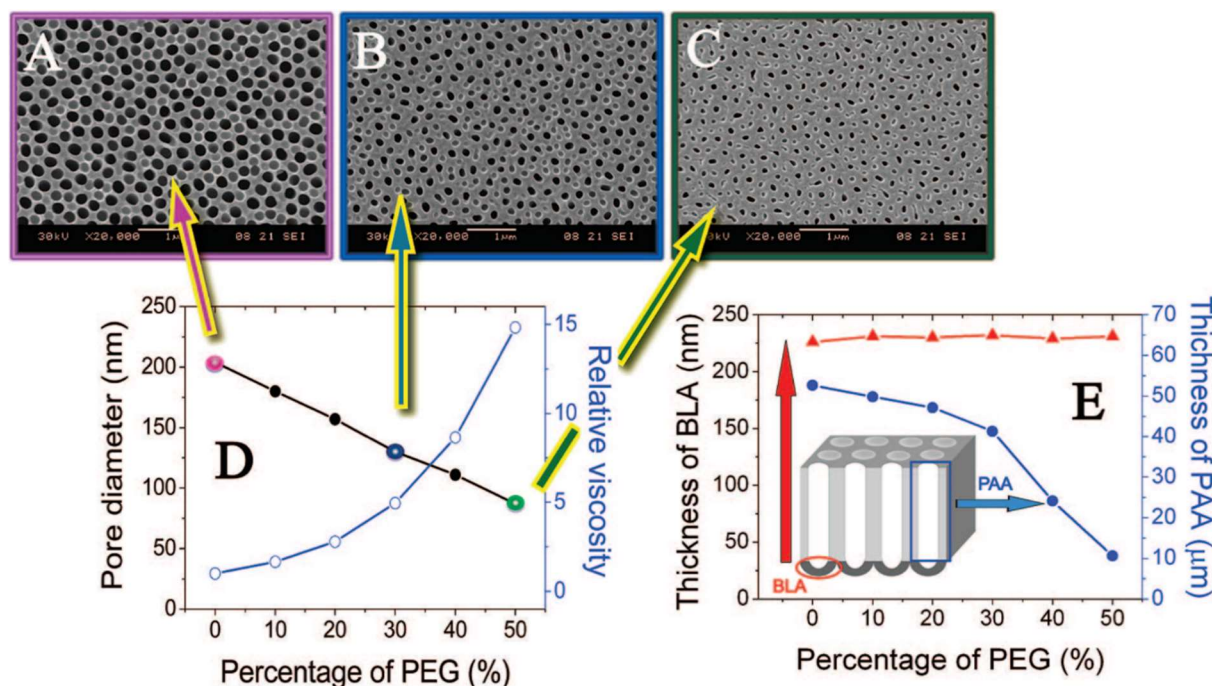


Figure 2.5. Impact of poly(ethylene glycol) (PEG) concentration on morphology of formed NAA films. Concentration of PEG in the electrolyte: (A) 0%, (B) 30%, (C) 50%, (D) influence of PEG content on the pore diameter and (E) the NAA film and barrier layer thickness in relation to PEG content in the electrolyte. Reprinted with permission from [103]. Copyright 2008 American Chemical Society.

Alternatively, an electrolyte additive may promote the incorporation of elements meant to improve properties of alumina matrix. The addition of lithium phosphate to the electrolyte successfully incorporating lithium ions into NAA during its formation is presented in [104]. The incorporation of metal ions may be potentially attractive with the intention to increase the conductivity of the material [105]. The interesting experiment involving the electrolyte composition has been presented by Christoulaki et al. [106]. Water in sulfuric and oxalic acid has been replaced with deuterated water, and in one case, the electrolyte composed of D_2SO_4 in D_2O was used. Use of deuterated water resulted in the 20% reduction of the pore diameter, improved pore ordering and increased growth rate. Observed behavior has been attributed to the decrease of the alumina formation activation energy. Furthermore, such electrolytes enabled to analyze the incorporation of hydroxyl groups during the NAA formation and effects of prolonged immersion in the solvent. Small-Angle Neutron Scattering shown no significant difference in incorporation rate between H_2O and D_2O pointing on the weak OH incorporation, while the hydration through immersion shown to be a slow process.

2.2.4. Mild and hard anodization: two growth regimes

For a long time, the default approach to the anodization of aluminum for the purpose of nanotechnology and research was the one performed under the moderate and constant potential—individually adjusted to each electrolyte—between the electrodes; under which the current flow is determined by reactions' equilibrium. Due to the constant potential and

the low current flow (that is typically below 30 mA cm^{-2}) such a process is called potentiostatic mild anodization (MA). MA conditions result in a predictable course of the process and the stable growth rate of $1\text{--}3 \text{ }\mu\text{m h}^{-1}$. However, several restraints of the process such as limited growth rate (the fabrication of self-standing membrane may require days of anodization), encouraged the exploration for a more practical, fast approach. What is more, self-ordering of NAA have narrow windows and discovery of new ordering regimes became the quest on its own.

The alternative approach commonly utilized in industry was left out of the scope in research field due to several restraints. Major characteristic of the process was a massive—as compared to the foremost—amount of the energy flow through the sample that is reflected in the widely used name: Hard anodization (HA). A basic constraint that limits access to certain benefits of the process is the amount of heat generated during formation of the alumina, related with the Joule's effect. Reaching the critical point may result in the electric breakdown that can lead to the destruction of the sample [107]. The discovery of Lee and co-workers renewed the attention to HA [24]. Principle of the discovery was based on the formation of a thin—400 nm—layer of porous alumina prior to the introduction of the high potential. This 'scaffold' prevented the breakdown enabling the uniform NAA growth. It was hypothesized that such a pre-patterning promoted the uniform pore nucleation preventing catastrophic events and defects. Growth of the oxide film with this method was also much faster. Recently, even faster growth of NAA film in a process named ultra-hard anodization Noormohammadi et al. [108]. A $58 \text{ }\mu\text{m}$ thick membrane was formed in 80 s: 30 times faster than during hard anodization and 450 times faster than with mild anodization. It was possible due to the high current density (2400 mA cm^{-2}) combined with control of the barrier layer temperature and the diffusion length to mitigate burning and the dielectric breakdown.

The new self-ordering regime that exhibits different current/voltage over time characteristics brought questions about differences in the formation mechanism. Detailed analysis of both regimes using voltametric and microscopic methods was provided by Vega et al. [109]. They point out the difference in the local ion concentration as a major factor for the observed distinction in current characteristics. During mild anodization, the ionic concentration remains stable. However, rapid growth of the structure during hard anodization leads to the local depletion that is reflected in the gradually decreasing current when a constant potential is applied—with hard anodization being controlled by the diffusion. Intriguingly, the potential at which the breakdown occurs depends on the initial sample preparation and experimental conditions [24,84,109].

The significant contribution to the field was brought by the group of Napolskii and co-workers. They provided analysis that linked the impact of voltage ramp on the morphology and thickness homogeneity. It was demonstrated that when faster 5.0 V s^{-1} ramp was applied instead of conventional 0.5 V s^{-1} , the significant reduction of morphological defects is observed [110]. While the occurrence of self-ordering regimes was well-known for spectrum of electrolytes, the question 'why' remained unaccounted. An attempt to empirically unravel

this behavior was carried out by Roslyakov et al. [111]. They performed the anodization slowly raising the potential (0.5 V s^{-1} for 30–130 V for $\text{H}_2\text{C}_2\text{O}_4$ and 50 mV s^{-1} for 15–60 V for H_2SO_4) and continued at every potential value so 105 C of charge can be utilized (corresponding to $\sim 50 \text{ }\mu\text{m}$ thick NAA) followed by the separation of alumina film into thin slices. Upon analysis of the NAA morphology, they proposed a model in which a high level of self-ordering can be achieved in two distinct regimes: The growth rate being restricted by ionic migration through the barrier layer or by diffusion inside the pore. Outside of these frames—during the “mixed” control—pore growth is disordered. Prevalence of the self-ordering depends on the applied voltage and is shown in figure 2.6. The applied potential is linked with the formation efficiency, volume expansion, and content of the electrolyte impurities for 20–130 V anodization in 0.3 M $\text{H}_2\text{C}_2\text{O}_4$ and 19–60 V 0.3 M H_2SO_4 [112]. The formation efficiency and the volume expansion were found proportional to the potential increase, while the degree of ion embedding was the highest for moderate values exceeding ones achieved with either low or high potential. Recently, detailed analysis of the electrolyte temperature effects on the alumina formation in oxalic acid at mild and hard anodization was provided [113]. Concluding the current profile, higher electrolyte temperature resulted in a shift of both kinetic and diffusion regimes to lower voltages (figure 2.6). The temperature increase from $0 \text{ }^\circ\text{C}$ to $20 \text{ }^\circ\text{C}$ raised formation speed significantly: 3.8 times for mild anodization and 2.1 times for hard anodization. However, the faster growth was accompanied by the lower formation efficiency and the number of pores grown in hexagonal coordination. The most striking case was that of thicker films (above $20 \text{ }\mu\text{m}$) for $20 \text{ }^\circ\text{C}$ 40 V anodization as the formation switched into mixed regime explicitly retarding self-ordering.

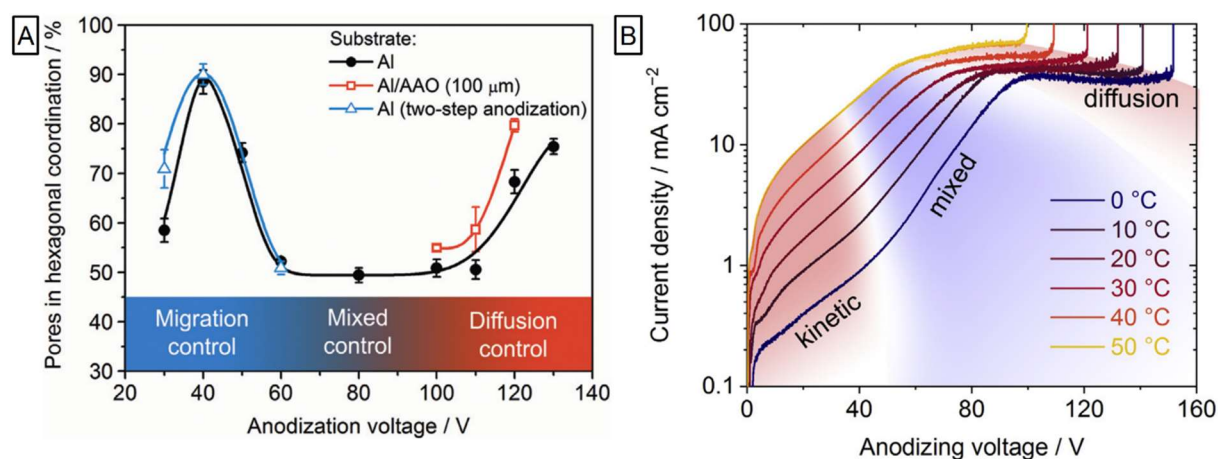


Figure 2.6. Anodization potential influence on degree of self-ordered growth and voltage/temperature dependent formation kinetics of 0.3 M $\text{H}_2\text{C}_2\text{O}_4$ anodization of aluminum. (A) Dependence of pore ordering degree during formation of alumina structure with highlighted regions of different growth kinetics. Reprinted (adapted) with permission from [111]. Copyright 2017 Elsevier. (B) Linear staircase voltammograms with highlighted growth kinetics. Reprinted (adapted) with permission from [113]. Copyright 2019 Elsevier.

2.2.5. Pore separation phenomenon

Under normal circumstances, there is no gap between adjacent pores. However, the anodization under high potential may lead to a rarely occurring phenomenon described as a cell separation. Such an incident usually appears during the anodization in sulfuric acid in the narrow range of conditions and materialize with a formation of a less dense matter at the cell boundaries [84,114]. As an outcome, structural integrity of the structure is decreased, reflected in inferior mechanical properties. To date, there is no clear experimentally supported evidence explaining the exact mechanism behind the formation of anodic alumina and this phenomenon. One of the prevalent, widely accepted explanations was the field-assisted dissolution theory first proposed by Wood et al. [27]. However, recent discoveries such as observed morphology of terminated nanotubes [115] and oxide growth locations [116] provided some insight that contradicts the long-accepted theory in some aspects. Moreover, the explanation pointing on the equilibrium between the dissolution and oxide growth as a sole mechanism of the pore initiation does not explain the presence of the anion-contaminated layer at the bottom—as formation of pores should follow the dissolution of the anion-contaminated layer, thus the lack of its presence. It can be further supported with the observation of a double-walled character of the nanoporous anodic alumina structure, where it is the inner wall that contains incorporated anions [32]. In addition, the formation of weaker triple-cell junctions was not sufficiently justified. These doubts followed the proposal of a different mechanism.

Importance of the volume expansion during the alumina growth that increases along with electrical field increase was highlighted by Yasumori et al. [84]. This factor combined with lower density of the oxide at the triple cell junction are linked with the lower expansion force in these spots (distribution of the expansion force is circular) [84]. Simulation of the stress distribution along the oxide/metal interface found existence of tensile forces focused near ridges while compressive stress elsewhere [64]. Furthermore, the NAA structure prepared in the conditions promoting cell separation behaves differently upon the chemical etching—such structure shows clear voids around cells that lost its initial hexagonal shape [117]. Interestingly, the mixture of HCl/CuCl₂ seems to work selectively solely on the three cells junction material, while etching in H₃PO₄ provides more uniform etching pattern as shown in figure 2.7 [118]. Voids at the cell boundaries seem to be characteristic for the anodization under a high electric field [119]. Additionally, size of the voids has been found to increase with higher voltage [120]. Observation about the distinct chemical composition—hydrated aluminum oxide forms like Al(OH)₃ and AlOOH—at the cell walls has been supported by Mei et al. [114]. Similar observations that demonstrate ultra-high anodization (620 V) resulting in the formation of unique structure with high fluctuations of outer diameter of the pores were reported in the work of Xinhua et al. [121]. Under certain conditions, formed anodic alumina is not homogeneously susceptible to the acid etching, pointing to a different packing density of the structure and/or slightly different composition. Such behavior of the anodic aluminum oxide has been also reported in the work of Wang et al. [122]. As shown in figure 2.7, the

initially cohesive structure turns into an array of loosely connected pores after a short etching in HCl/CuCl₂. As mentioned before, a pore separation is usually reported for the anodization in sulfuric acid-based electrolytes. However, it can also occur in different settings. Much more pronounced separation—to the extent of cells being barely connected—has been achieved through anodization in oxalic acid with different addition of ethylene glycol [100,123]. Authors explain the observed pore separation phenomenon by the extensive incorporation of $C_2O_4^{2-}$ and COO^- ions into the NAA structure promoted by the presence of ethylene glycol. Such a structure demonstrates higher susceptibility to acid etching.

The increased energy flow through the sample results in an intense generation of the oxygen bubbles derived from the water dissociation at the anode interface was proposed by Lee et al. [124]. The importance of bubbles for the formation and shape of the structure formed during the anodization has been reported in the past [117,125]. It can be supported with the observation of closed pores not accessible through the upper surface—the origin of which is not justified by the field-assisted dissolution mechanism—attributed by the authors to the presence of oxygen bubbles. This hypothesis is visualized in figure 2.7 [126]. Additionally, oxygen bubbles could force Al^{3+} and O^{2-}/OH^- ions to migrate around the bubble shaping formation of the NAA. It was proposed that the presence of these species promotes the decomposition of $Al(OH)_3$, pointing to the similarity observed during the anodization of titanium [127]. An important discovery that provides a new insight has been brought due to the work reported by group of Zhu [126,128]. For the first time it was possible to observe cavities between double walls of nanotubes, strongly supporting the oxygen bubble formation theory. The cavities distribution contradicts the mechanism of field-dissolution theory and provide new arguments in the discussion regarding mechanism of anodic formation of Ti and Al oxides. Although the adduced discovery has been observed for titania nanotubes, authors connote similarities behind the formation of both anodic oxides [116]. Moreover, the importance of oxygen bubble generation for the formation of the NAA structure has been considered previously already [129]. Certain behavior of the sample cannot be explained by the field-assisted dissolution theory, while supplemented with the recent findings, the oxygen bubble mold theory along with the plastic flow model provide more detailed explanation regarding the formation mechanism.

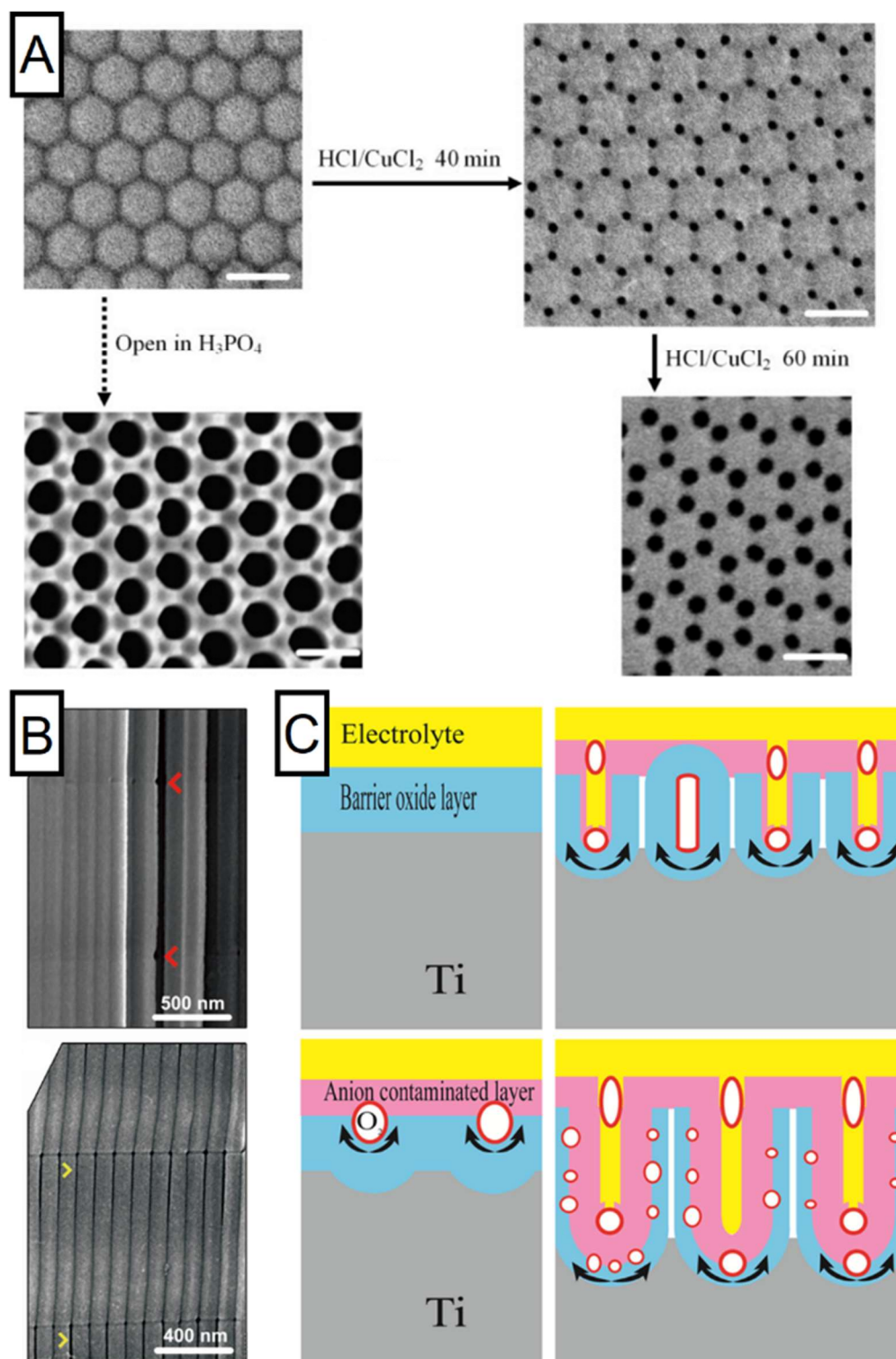


Figure 2.7. Structure periodical discrepancies and schematic explanation of its formation. (A) Selective etching with HCl/CuCl₂ and H₃PO₄ of structure with local differences in material morphology. Reprinted (adapted) with permission from [118]. Copyright 2007 Wiley. (B) SEM images of the structure before (upper panel) and after (bottom) acid etching with visible void formation. Reprinted (adapted) with permission from [122]. Copyright 2015 Elsevier. (C) Schematic representation of the cavities formation between double walls of growing titania nanotubes. Reprinted (adapted) with permission from [126]. Copyright 2019 Elsevier.

A better understanding of how nanoporous anodic alumina is formed and improved control over the process lead to many innovations. An important change that has been implemented to tame drawbacks of hard anodization regime was the concept of pulse anodization reported by Lee and co-workers [124]. The intention was to mitigate the heat generation and prevent electrical breakdown enabling to extend process duration—giving another life to the once abandoned strategy. A close observation of the NAA obtained with pulse anodization revealed that nanopore diameter is modulated along the direction of NAA growth precisely following the input voltage. While this work did not report the fabrication of nanotubes, the seminal strategy that originated, coupled with settings promoting pore separation laid foundation for the new material concept—anodic alumina nanotubes (see Section 3.2. Nanotubes).

2.2.6. Pre- and Post-anodization treatments

2.2.6.1. Pre-anodization patterning of the aluminum surface

The surface of aluminum can be also modified prior to anodization to enhance/guide the formation course. Hydrothermal treatment prior to anodization with intention to produce oxide barrier layer with complex morphology was proposed by Li et al. [130]. Usually, treatment in hot water or water-alcohol solution is applied to seal pores of the already produced alumina and create corrosion-protective layer as the pore entrance collapses. In this case, the idea was to form hydrate aluminum film prior to the anodization. The electropolished aluminum sheet was subjected to hydrothermal treatment in deionized water at 97 ± 2 °C for different time duration. Complex morphology of the obtained hydrate oxide layer was demonstrated to depend on the hydrothermal treatment time as shown in figure 2.8. What is more, such a surface was observed to promote the pore nucleation enabling to achieve the fast self-ordering during first anodization step, while the applied potential is outside of a usual self-ordering regime (e.g., 60 V, oxalic acid). This behavior is reflected in the distinct current profile at the beginning of anodization. Additionally, energy consumption during subsequent anodization can be reduced and crystallization of the alumina layer improved.

Apart from common techniques like lithography and selective etching [131], sputtering of aluminum on the surface with desired morphology may be an useful alternative to yield higher structural complexity. The structure made by aluminum sputtering on the 2 μm silica microbeads was reported by Chung et al. [132]. The obtained large-surface area substrate was proven effective for photocatalytic purposes.

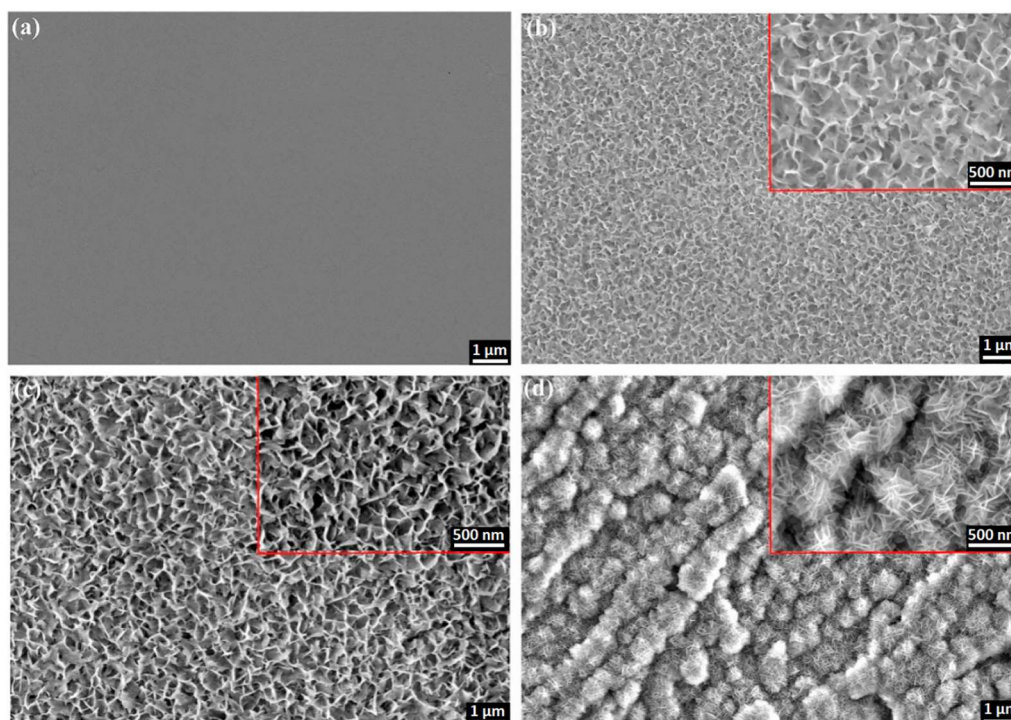


Figure 2.8. SEM images of hydrous oxide layer formed hydrothermal treatment of aluminum foils at 97 ± 2 °C for (a) 0 s, (b) 30 s, (c) 10 min, and (d) 60 min. Reprinted with permission from [130]. Copyright 2020 Elsevier.

2.2.6.2. Thermal annealing

One of the most basic method to affect properties of nanoporous anodic alumina is through thermal annealing. NAA subjected to thermal annealing maintains its mechanical stability and flexibility [133]. As temperature increases first change in the structure can be observed around 700–1200 °C, when it undergoes the rearrangement with gradual formation of γ - Al_2O_3 . As temperature increases, at 1100–1500 °C α - Al_2O_3 progressively emerges. Temperature of the crystalline shift depends also on the electrolyte of choice. For example, the transition of the oxalic-NAA from polycrystalline phase to α - Al_2O_3 occurs at 1100 °C, while the sulfuric-NAA needs to be annealed at 1230-1250°C for such a change to be observed [134–136]. Removal of ionic residues depends strongly on the applied electrolyte and tends to be gradual with rapid spikes along the rearrangement of crystalline forms [137,138]. Induced structural changes at the atomic scale are responsible for the increased transparency and hardness, yet mesoporous structure is preserved even above 1050 °C providing for the stability in high-temperature applications [139]. However, while the porous morphology is maintained, deformation of the film can occur (e.g., bending). The approach in which such deformation can be avoided was proposed by Roslyakov et al. [140]. When annealing occurs with the alumina film pressed between two layers of material, the sample maintains its initial shape. When combined with slow temperature increase (~ 1 °C) around phase transition regions, it is possible to anneal the structure at 1200°C preserving its mesoporous array forming nanoporous α - Al_2O_3 that features superior chemical stability (enhancement by two orders of magnitude).

2.3. Engineered NAA structures

2.3.1. Structures based on the modulation of the anodization current

Since a direct relationship between the anodization voltage and the diameter of NAA is a well-known fact [27,141], possibility of designing its geometry in vertical axis through dynamic, pulse-like alterations of the anodization current is expected. However, the existence of a barrier layer—a layer of the oxide that lays between a surface of the anode and the porous oxide—restricts the way in which diameter of pores can be affected during the process. The barrier layer acts as an insulator that limits the transfer of ionic species and features significant electric resistance retarding speed and range of accessible alterations in the structure through potential control [142,143]. The development and understanding of the pulse anodization mechanism pioneered by Lee et al. brought new fabrication tools to the field. An important improvement came along with the concept of applying high current pulses interlaced with low current density periods [124,144–146]. A significant aspect involved a better understanding of porosity levels as well [24]. A variant of pulse anodization yielding periodically Y branched pores is reported by Peng et al. [147]. It was possible due to a saw-tooth anodization current profile and a high current density (above 70 mA cm^{-2}). Additionally, structural features could be further altered with the duration of pulses. Applying high density current pulses to tailor optically sensitive structures bear some limitations, though. For example, the growth speed—that can be even a tenfold of that during mild anodization—is not constant in potentiostatic mode due to ionic species deficiency, contrary to mild anodization. What is more, such a process is more prone to induce cracks in the structure during growth, which is the another factor limiting their application for the optical responsivity. The major disadvantage of the mild anodization is definitely its low growth rate ($3\text{--}8 \text{ }\mu\text{m h}^{-1}$), which translates into several days long the fabrication of thick films. On the other hand, the process is much more predictable and enables more precise control during alumina growth. An advantage of NAA fabrication stems from the possibility to tailor-engineer its periodicity in the three dimensions. Sinusoidal current alterations can be utilized to fabricate photonic crystals with multispectral photonic stopbands (PSB), that in turn can be precisely tuned [148]. Infiltration of D-glucose into the pores results in a spectral shift of PSBs and the possibility of a quantitative detection based on the shift. In other work, Gaussian pulse anodization with different time gaps between the pulses has been examined [149]. The PSB optical features of the structure such as the position of the central wavelength, the width at half-maximum, and the intensity could be adjusted by altering the time gaps—with the incidence angle of photons and the porosity of the structure being relevant as well. While the previous works involved 0.3 M oxalic acid, investigation regarding properties of photonic structures made with sulfuric acid and various additives (alcohols and polyols) is provided by Lim et al. [150]. The comprehensive study revealed advantages of such approach. Potential benefits of the additives are related to the

suppression of dissolution rate during the anodization and the incorporation of impurities containing carbon, both having a significant and positive effect on the quality of forbidden light propagation within the structures. Forty percent addition of methanol provided the best results, yielding the photonic structure with the highest quality factors amongst the compared.

2.3.2. Nanotubes

The discovery of pulse anodization was a significant innovation providing for the further development of anodic alumina nanofabrication. In-depth analysis enabled to properly utilize hard anodization with its impressive growth rate and a geometry not previously accessible [151]. On the other hand, alteration of the pore diameter in length was a separate concept with its own advantages [124]. For the first time, the fabrication of nanotubes through the hard anodization with pulses was reported in 2008 [144]. The approach consisted of immersing electropolished aluminum into 0.3 M H₂SO₄ and the preparation of an initial, thin NAA layer through mild anodization at 50 V. The formation of a thin layer under low potential is important for the prevention of the electric breakdown, which occurs frequently upon immediate surge of the potential when anodizing pure aluminum. It was followed by galvanostatic pulses of 3.16 mA cm⁻² and 368 mA cm⁻² interchangeably, where high current pulses provided growth of the structure (tubes), while mild anodization pulses—apart from dissipation of heat—aimed at the production of weaker spots in the structure. These weaker spots are crucial for the selective separation in further parts of the process. The galvanostatic mode has been chosen due to the characteristics of the hard anodization with the gradual current decrease—affecting the growth rate—when constant voltage mode is applied. Such a setup enable the precise tailoring of the nanotubes length. After removal of aluminum, the structure was subjected to the chemical etching in a similar manner to the previously reported selective etching approach [118]. Then, the sample was sonicated to yield a colloid of liberated nanotubes. It is important to note that sonication itself was reported insufficient to provide the efficient liberation of nanotubes. Prior to the discovery of Woo Lee, the fabrication of anodic alumina nanotubes was more complicated and involved techniques like wet-chemical etching [152], anodization of thin layer of aluminum on silicon sheet (Al/Si) [119], hydrothermal synthesis with nanowires of a different material as a sacrificial template [153,154], atomic layer deposition [155,156], and a few more [157,158]. Moreover, these methods carried many disadvantages. Apart from a more complex protocol, reproducibility and ability to precisely tailor shape of the nanotubes was strongly limited. Nanotubes made of alumina display plenty of attractive features making them valuable candidates in fields like nanoelectronics, catalysis, or biomaterials. After fabrication, they exhibit a low surface reactivity and lack catalyst contamination. Their surface rich in hydroxyl groups facilitates functionalization through salinization. Additionally, the initial closed nature of the structure enables selective modification of outer/inner interface without complex procedures. In neutral pH DI water, nanotubes are positively charged, while in PBS, they exhibit the negative

charge. The absolute charge value is moderate providing for the decent stability and possibility of electrostatic interactions with proteins and other nanoparticles. What is more, singular elongated cell of the structure fabricated in similar conditions display significant plasticity pointing on certain level of material's flexibility [159].

Several years from the discovery carried out by Lee et al. [144], the topic of anodic alumina nanotubes has been brought back and significantly developed. The first report was a systematic study with an aim to evaluate an in vitro nanotoxicity of AANTs by Wang et al. [160]. Nanotubes of different length—ranging between 0.7 and 5.8 μm —were tested with RAW 264.7 mouse macrophage cells and MDA-MB 231-TXSA human breast cancer cells. The reported toxic window of 7.8 for AANTs was shorter than that of many other high aspect ratio materials. It was followed by detailed investigation of the fabrication process with the scope on the electrochemical aspect of the nanotubes [122]. The focus of the work was to understand the formation mechanism to optimize the process and improve its final efficiency. The fabrication protocol has been expanded with the formation of the protective/functional NAA layer—that facilitates the sample handling, and the improvement of the nanotubes separation. What is more, 10% addition of ethanol to the electrolyte during pulse anodization has been proposed to promote the Joule's heat generation associated with the increased yield of the process, obtaining even shorter nanotubes. In the next report, performance of AANTs as a 1D drug carrier has been examined [161]. The Apo2L/TRAIL model drug has been successfully loaded inside nanotubes and delivered into cancer cells inducing apoptosis. An exceptional loading capacity for the Apo2L/TRAIL protein was estimated on $104 \pm 14.4 \mu\text{g mg}^{-1}$ of AANTs supporting its promising application as a nanocarrier. The gathered findings enabled to propose AANTs in a proof-of-concept cancer therapy based on the signaling network targeting [162]. The aim was on the autophagy and endoplasmic reticulum paths of the primary human foreskin fibroblasts and the human monocytic cells. AANTs showed a promising utility in the role of a non-toxic non-degradable nanomaterial. What is more, it was possible to follow the intake mechanism of the material. The last work involved topic of in vivo toxicological and pathological studies in eight-week BALB/c immune competent mice. AANTs were introduced through an intravenous injection (IV) and a subcutaneous implantation [163]. The IV approach did not show any impact on body weight and mortality of mice during 28 days at doses between 20 and 100 mg kg^{-1} , and nanotubes were found to accumulate in liver and spleen. The highest dose, however, induced moderate hepatotoxicity. The subcutaneous introduction—on the other hand—led to an inflammatory response. It is important to note that a surface coating—for example with PEG—should improve biocompatibility of the material indicating need for further experiments.

A step forward in the fabrication of AANTs defining in detail the relation between current/voltage input and geometrical features of nanotubes was reported by Domagalski et al. [164]. Apart from defining the relation between pulse duration and the resulting nanotube length, they discovered that current density during hard anodization pulse can affect the outer diameter and the surface charge of AANTs, contributing a higher control of the process and enabling tailor-engineering of anodic alumina nanotubes. Moreover, optimization of the

technology allowed to yield even shorted nanotubes than before—424 nm in length on average. Their next work [165] involved decoration of nanotubes with maghemite superparamagnetic nanoparticles to yield magnetic nanotubes (MAANTs) combined with functionalization inside the nanotubes. The structural integrity preceding the separation was utilized to conduct the selective modification of inner walls with the padding of a protein functionalized with the fluorophore. Later, nanotubes were connected to magnetic nanoparticles through electrostatic. TEM images of native nanotubes and produced composite are shown in figure 2.9. The detection system was aimed at the recognition of enzyme molecules, demonstrated with cathepsin B and based on the enzymatic cleavage of the fluorophore-modified protein and the release to the medium. Magnetic maneuverability was used to separate nanoparticles from the main volume of the medium.

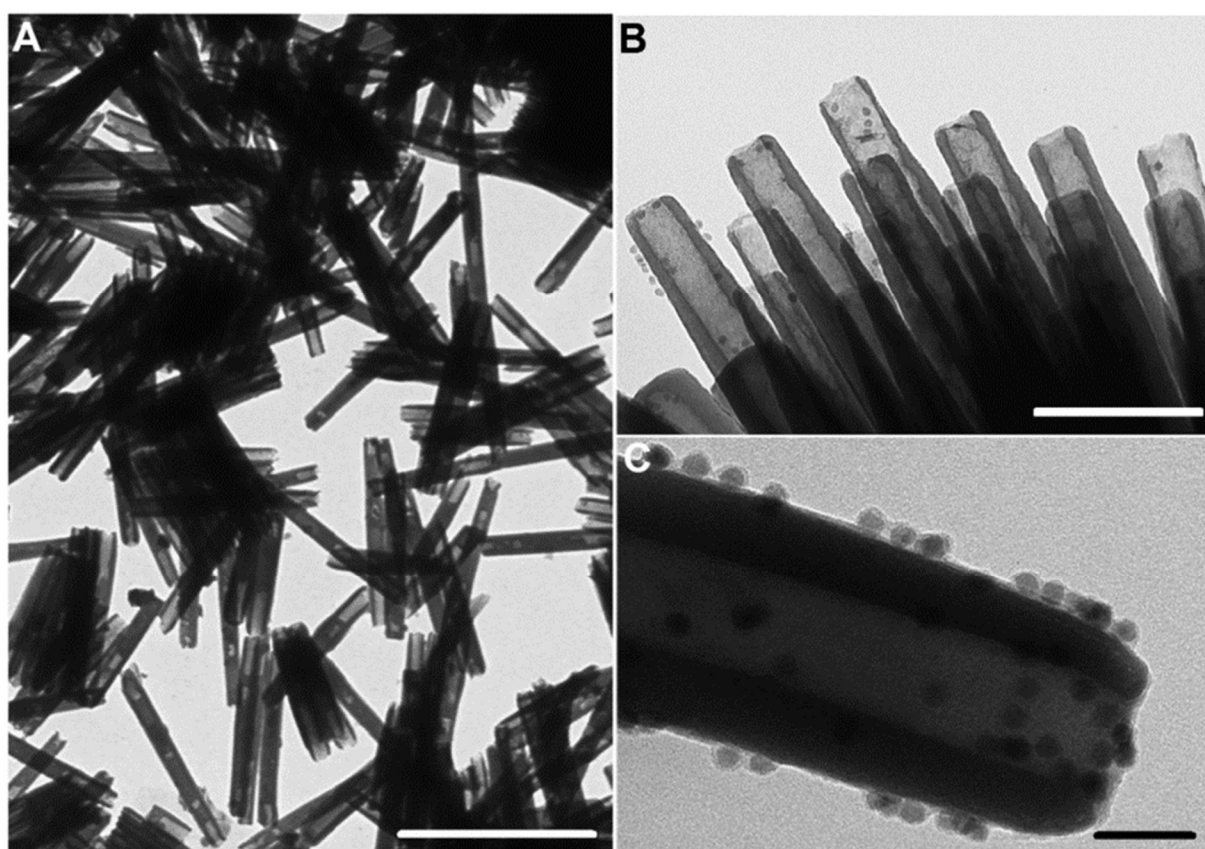


Figure 2.9. TEM images of anodic alumina nanotubes (AANTs). (A) Unmodified AANTs, (B) maghemite decorated AANTs (MAANTs), and (C) magnified capture of MAANTs; scale bars: 1 μm , 200 nm, and 50 nm respectively. Reprinted with permission from [165]. Copyright 2020 Elsevier.

2.3.3. Micro- and nanoparticles

A prevalent perception of nanoporous anodic alumina is as a 3D nanostructured material and utilized as such—with vast possibilities described before. In the field of nanofabrication, NAA is mostly used as a template due to its high surface area and periodic regularity. However, anodic alumina itself exhibits a plenty of promising properties that could make derived

nanoparticles attractive in ways not accessible for the plain NAA. Apart from the nanotubes produced with the pulse anodization (Section 3.2), there are other alternatives. An approach consisting of mechanical grinding of the alumina membrane, obtaining nano/micro-particles with the structural features of nanoporous alumina was reported by Xifre-Perez et al. [166]. These particles exhibited luminescence and were surface functionalized with antibodies. Their performance at different concentrations was demonstrated with HepG2 cells showing good biocompatibility. Microscope images of the cells incubated with alumina micro particles are shown in figure 2.10. Further studies provided more comprehensive analysis of alumina micro- and nanoparticles obtained with different methods [167]. Similar strategy to obtain alumina microparticles was employed in the work of Chen et al. [168]. However, in this case, the base material was NAA-based Bragg reflector. Particles were prepared by a mortar-grinding of the alumina film and the subsequent sonication. Obtained microparticles retained their optical properties—the same as the initial template—a promising prospect with regards to microsensors.

Another example of smart approach is the fabrication method developed by Matsuda et al. The major thought behind this idea is the preparation of aluminum in the structural shape similar to the desired outcome. One example can be alumina nanowires. At first, nanoporous alumina molds with various geometrical features (pore diameters of 15–340 nm and cell size between 30 and 500 nm) were used to form nanowires on the surface of aluminum by a applying pressure of 7 GPa, followed by the acid-dissolution of the mold to liberate the nanowires. These structures were later anodized in a similar way to the standard NAA (0.3 M H_2SO_4 at 0 °C under 12 V for 2–10 min). As result, nanowire arrays made of nanoporous anodic alumina with and without Al core were yielded [169]. A similar strategy was also conducted using aluminum microspheres. Al particles were introduced to a cylindrical holder with a porous membrane at the bottom [170]. Then, Al electrode was inserted applying appropriate pressure to ensure electrical connection between the particles. Anodization conditions (1 M HCl + 3 M H_2SO_4) were aimed at etching of the aluminum surface with deep pits rather than formation of regular nanoporous structure. At this stage, aluminum layer was selectively removed to yield etched aluminum microspheres. It is worth noting that the contact point between the spheres remained unchanged as the electrolyte could not penetrate this part. Furthermore, authors also performed standard mild anodization on these etched aluminum spheres followed by dissolution of aluminum obtaining nanoporous oxide replica of the spheres. Their next work continued this idea but introduced a two-step anodization in order to provide ordered nanoporous alumina layer on the surface of aluminum spheres (illustration of fabrication process is shown on figure 2.10) [171]. Various anodization conditions were utilized in order to yield different NAA geometry. After the etching of the aluminum core, hollow NAA spheres were obtained—presented in figure 2.10. The pits that can be observed on the surface of these structures are remnants of spots that were not anodized due to continued contact between aluminum spheres. Moreover, these spheres were later modified through electrolytic deposition of Au, forming a composite. These nanoparticles are an alternative in the field heavily dominated by mesoporous silica [172].

Decades of experiments aiming to understand the NAA formation mechanism enabled to turn the surface functionalization approach into a precise nanofabrication method. The versatility is also reflected in a broad range of reported applications that were based on nanoporous anodic alumina.

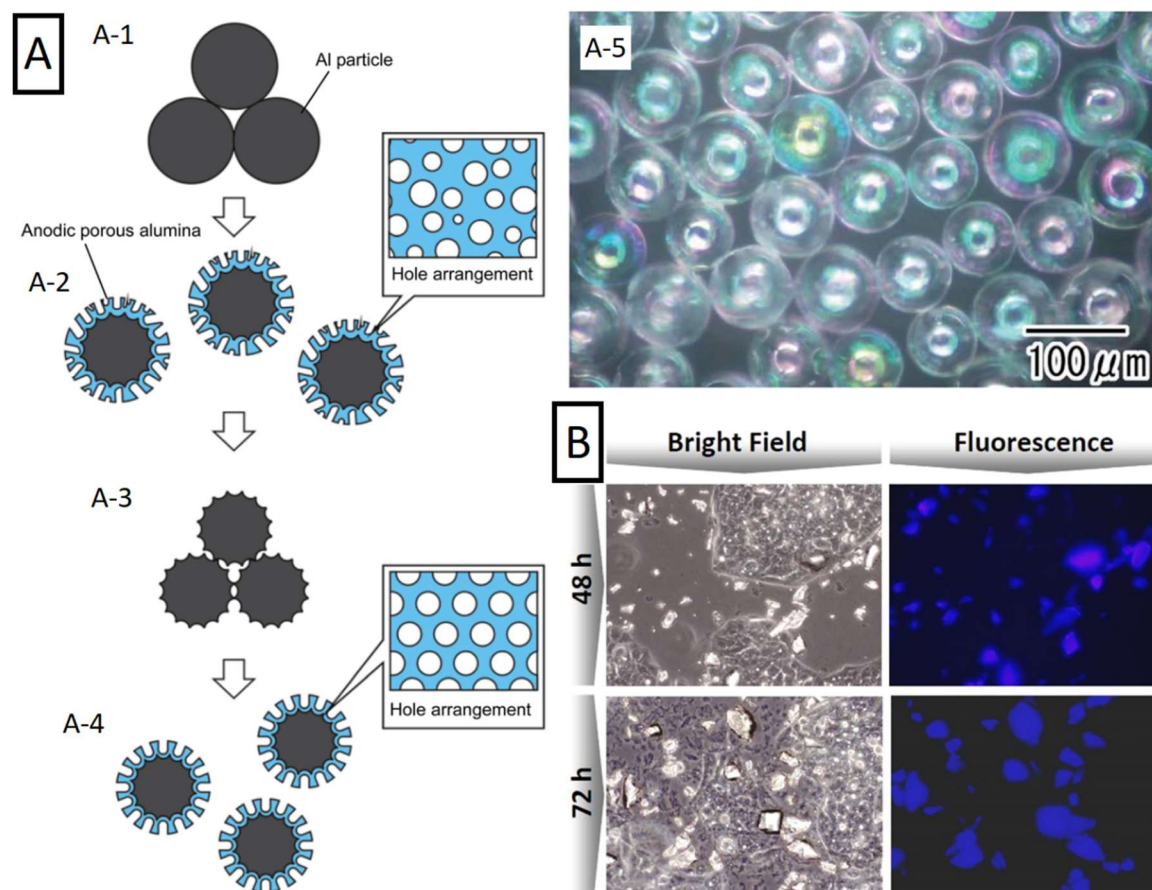


Figure 2.10. Nanoparticles based on NAA. (A) (A-1–A-4) Schematic of the multi-step formation process of nanoporous anodic spheres and (A-5) optical microscope image of hollow spheres made of porous alumina obtained by removal of aluminum residues. Reprinted (adapted) with permission from [173]. Copyright 2018 The Royal Society of Chemistry. (B) Microscope images of HepG2 cells incubated with intrinsically photoluminescent nanoporous alumina particles obtained through grinding of NAA substrate. Reprinted (adapted) with permission from [166]. Copyright 2015 American Chemical Society.

2.3.4. Funnel and inverted funnels

This alternative involves smart combination of anodization, annealing, and chemical etching allowing the production of exceptional features. Two distinct ways in which such a structure can be obtained were demonstrated by Santos et al. In the first approach, a diameter gradient was obtained applying several anodization steps [173]. After every step, the sample was subjected to the pore widening through chemical etching with 5% H_3PO_4 . That way, it was possible to obtain the structure with a gradual decrease of the pore diameter until the pore bottom. During the second experiment, it was possible to form a reversed gradient with the

diameter increase towards the pore bottom [174]. It was achieved through annealing of the sample after every anodization step with the highest annealing temperature applied to the first, external layer and applying lower annealing temperatures with each consecutive step. Then, the sample was subjected to the 5% H_3PO_4 chemical etching. The optical properties of NAA enabled to observe the formation of nanofunnels in situ in real-time by means of RfS. Similar structures were later examined by Porta-i-Batalla et al. [175] to determine the influence of the pore geometry on the drug load and its release performance. Figure 2.11 shows the morphology of reversed funnel architecture captured with ESEM (environmental scanning electron microscope) and the fabrication schematic of both normal and inverted funnels. Another example in which anodization steps are interlaced with annealing to obtain bottle shaped pore tips has been reported by Liao [176]. After two standard anodization steps, samples were annealed at 500–600 °C, reanodized, and chemically etched in phosphoric acid (with potentiostatic in situ monitoring). As result, it was possible to form NAA regions with two highly different pore diameters: 220 and 345 nm.

With a different approach to alter the pore diameter, an improvement of the process control by mitigating the tendency to form branched pores that are commonly formed upon exponential decrease of anodization potential was demonstrated [177]. The development of the process was a consequence of attempts to achieve a thinner barrier layer and allowed to tailor a step-less architecture with a gradually decreasing pore diameter. This was possible due to the combination of high electrolyte temperature and fast voltage drop—brief enough not to interrupt the anodization process. The combination of several processing procedures is important to exceed the limitation of a standard two-step anodization and yield more complex architectures.

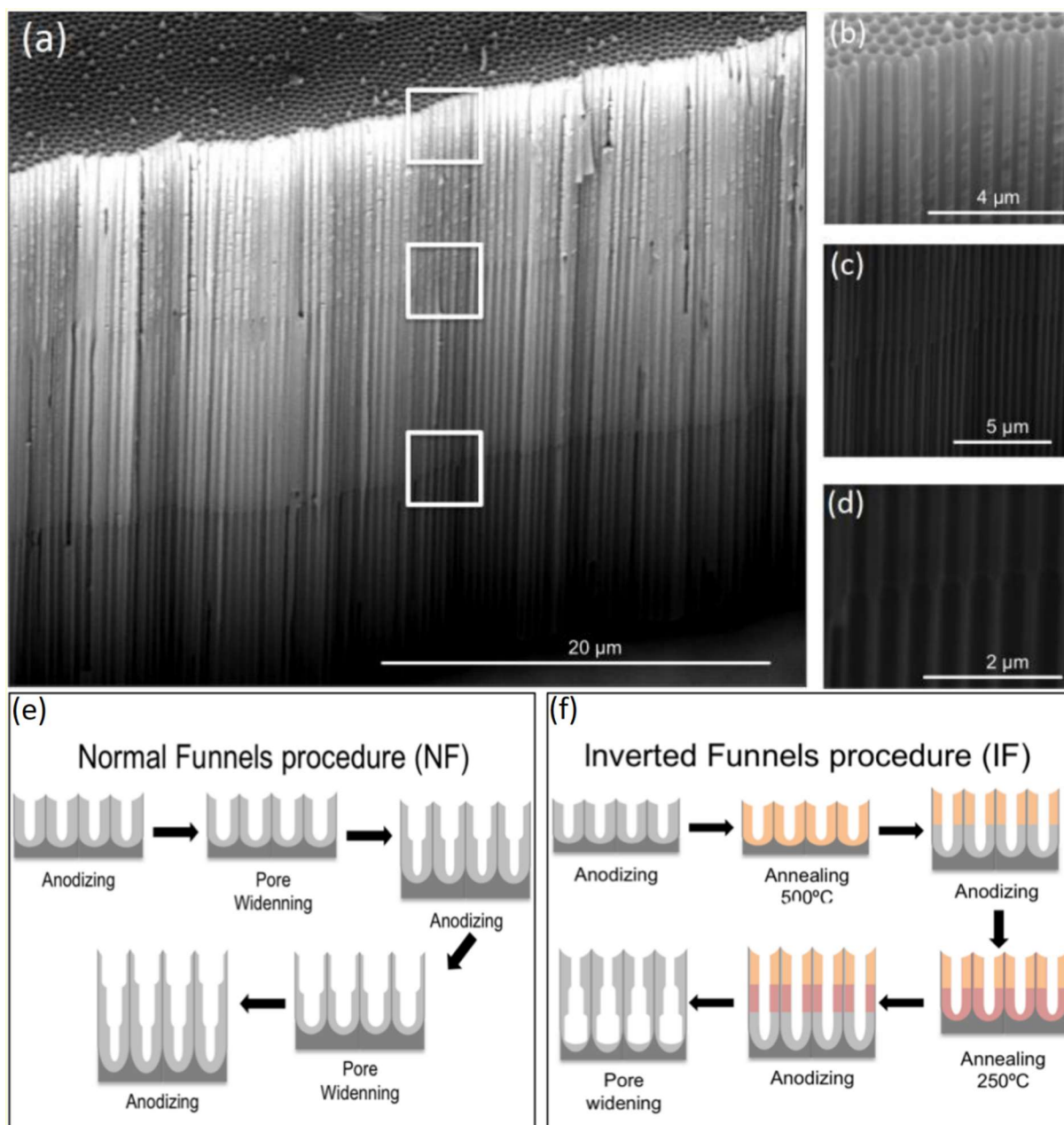


Figure 2.11. Cross-section ESEM images of inverted funnel NAA structure and fabrication schematics. (a) Entire structure, (b–d) magnified images of transitional regions, (e) fabrication procedure of funnel morphology, and (f) inverted funnels morphology. Reprinted (adapted) with permission from [175]. Copyright 2017 MDPI.

2.3.5. Hierarchical pore structures

The structure resembling funnel-like characteristics but also some hierarchical features was reported in the work of Liu and Biring [178]. The aluminum surface was pre-patterned with the nanotube array interlacing shallow and deep patterning. After the first anodization step, the second one is performed with higher anodization potential—twice the initial level—forcing interpore distance to increase twice and terminating the growth of many

nanochannels. The resulting structure consists of long-funnel like pores surrounded by short, narrow pores that ends just as the former expands.

A more pronounced hierarchical morphology can be achieved with a different approach. Usually aluminum anodization is carried out by repeating similar conditions twice—concavities left after removal of the oxide film resemble geometrical features of the oxide grown during the second step, ensuring its high regularity from the beginning. However, growing behavior is different when conditions of the second step differ. Such strategy—aimed at smaller pores grown during the second step—is presented in the work of Santos et al. and illustrated in figure 2.12 [29]. The growth of the pores is organized inside previously produced concavities. Different anodization conditions such as voltage, electrolyte, and the process temperature were examined yielding various geometries. Morphology of the structure is shown in figure 2.12. Such an approach may serve as an alternative to less accessible lithography pre-patterning, when more complex surface morphology is needed. Size of concavities did not exceed 1 μm in the report [29].

Such possibility was reported later, with the work of Jin et al. [179]. Not only the size of the initial patterning on the aluminum surface increased, but also more complex pore profile was achieved. Focusing on the anodization voltage changes, the combination of previously presented idea with periodic pulse-like anodization was utilized. As result, the structure features hierarchical morphology with pores ordered along the cavity, while the profile of the pore became serrated. The idea is further continued with the introduction of more anodization steps by Ma et al. [180]. The surface has been provided with a bowl-like array through the stable anodization in citric acid, followed by the combination of multiple mild anodization steps and the chemical etching. Architecture of such tapered pores obtained with oxalic and sulfuric acid is shown in figure 2.12. Apart from a more complex morphology, tendency of such pores to grow aligned with the radius of each cavity—perpendicularly to the outer surface—was observed. It was suggested that initial oxide film is thinner under low anodization voltage, which—due to less localized concentration of the electric field—results in nanopore nucleation, more homogeneously on the whole surface of the curvature rather than on the bottom of the curvature. Furthermore, authors compared pore density when grown on flat and bowl-like surface. Curvature of the surface enabled to yield 1.5 times higher packing density (1.68 vs. $1.15 \times 10^{15} \text{ cm}^{-1}$).

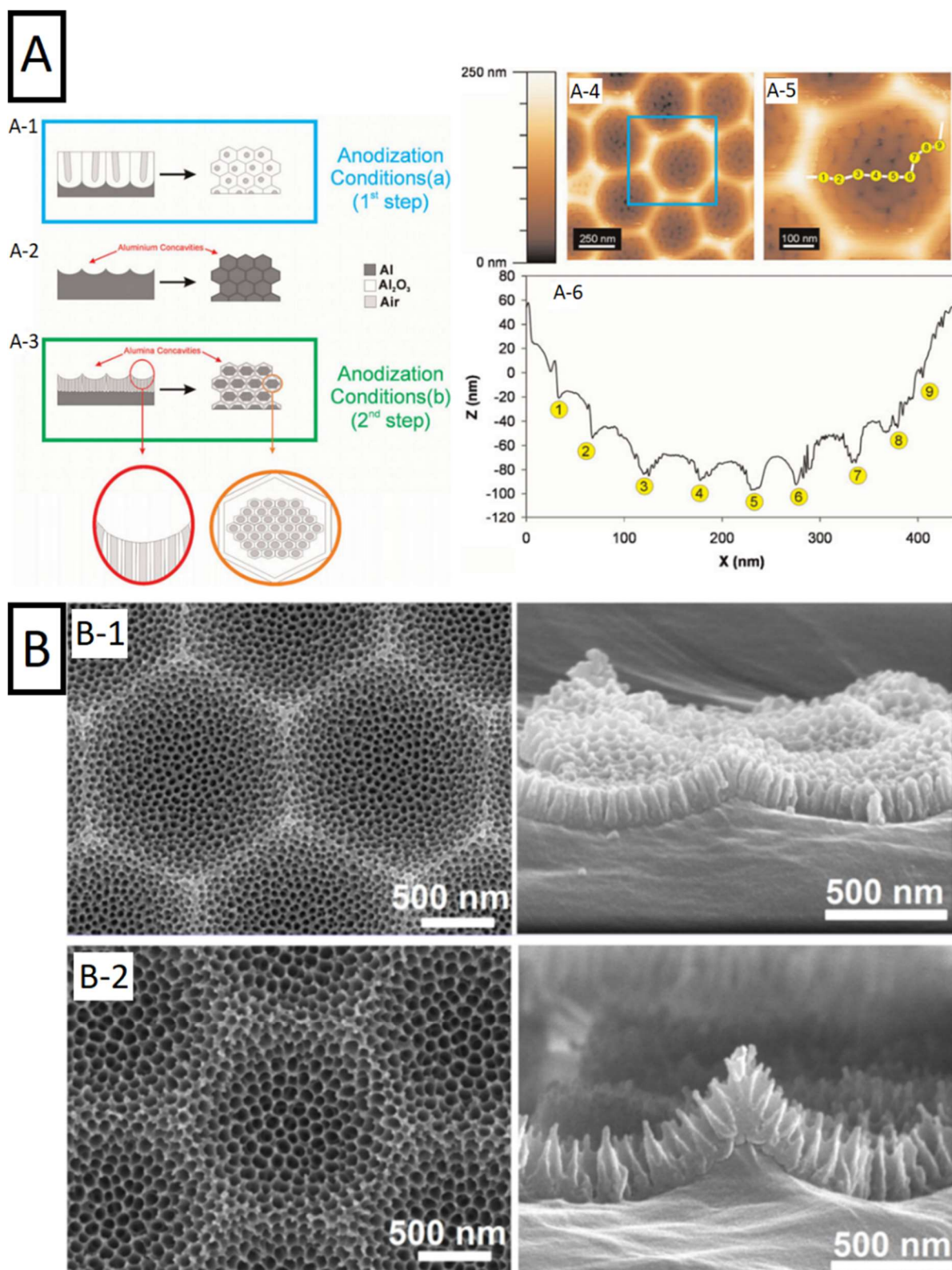


Figure 2.12. A morphology of hierarchical pore structures. (A) (A-1–A-3) Fabrication steps of hierarchical nanopore array, (A-4–A-5) AFM (atomic force microscope) top side views of hierarchical nanoporous anodic alumina, and (A-6) cross-section of the corresponding image. Reprinted (adapted) with permission from [29]. Copyright 2010 Wiley. (B) SEM images of tapered nanopores obtained by mild anodization in different electrolytes. (B-1) 0.3 M sulfuric acid, 20 s ($d_{int} = 50$ nm) and (B-2) 0.3 M oxalic acid, 40 s ($d_{int} = 95$ nm). Reprinted (adapted) with permission from [180]. Copyright 2019 Elsevier.

2.3.6. Three-Dimensional Interconnected Nanoarchitectures

A different approach to pulse anodization is presented in the work of Martin et al., in which they report the fabrication of 3D nanotubular network [181]. Contrary to the previously mentioned examples, such structures feature not only periodic modulation of the pores, but also the connection between the pores through transversal nanochannels. Geometrical features are controllable through the anodization, accessible film thickness reach dozens of microns and the array is highly regular. Process conditions were inspired by seminal discoveries of Lee et al. [124,146], introducing some differences. Pulses of potentiostatic mild anodization were interlaced with galvanostatic hard anodization at moderate current densities. An important principle during the design of the process was to preserve the longitudinal continuity of the pore arrangement. For that reason, hard anodization pulses were adjusted to yield structure with the same interpore distance. Initial attempts involved potentiostatic hard anodization pulses at 36 V—that quickly resulted in severe damage to the structure as the process continued. The long-range regularity of the structure was possible when moderate galvanostatic hard anodization pulses were applied (27.5 mA cm^{-2}). After anodization, chemical etching in phosphoric acid was performed, partially removing the oxide layer grown during hard anodization pulses and forming transversal nanochannels [181]. Different etching rates for the structure parts formed in different anodization regimes allow the distance between consecutive interconnected planes to be tailor-engineered by adjusting the pulse duration. This idea was later continued with series of works throughout the years. Thermal conductivity of these alumina networks and the possibility to tailor the conductivity through changes to the structure geometry and filler materials was reported by Abad et al. [182]. Properties were demonstrated to depend on the thickness of the membrane, the number of nanochannels, and the interchannel distance of the membrane. Metallic fillers provided the electrical conductivity in the vertical plane with the decrease of thermal conductivity as compared to the filler material itself. Later, a structure made with $\text{Co}_x\text{Ni}_{1-x}$ alloys using NAA with transversal nanochannels as a sacrificial template was reported by Ruiz-Clavijo et al. [183]. After anodization and selective etching, 3D-NAA templates were coated with a layer of chromium and gold through evaporation. These coated templates were used as working electrodes for electrochemical deposition, when the alloy was deposited. Then, the alumina template is removed revealing the 3D network of magnetic nanowires. Steps of the fabrication process and changing structure morphology is shown in figure 2.13. The report also describes how magnetic anisotropy of the network can be modified with changes to the structure geometry.

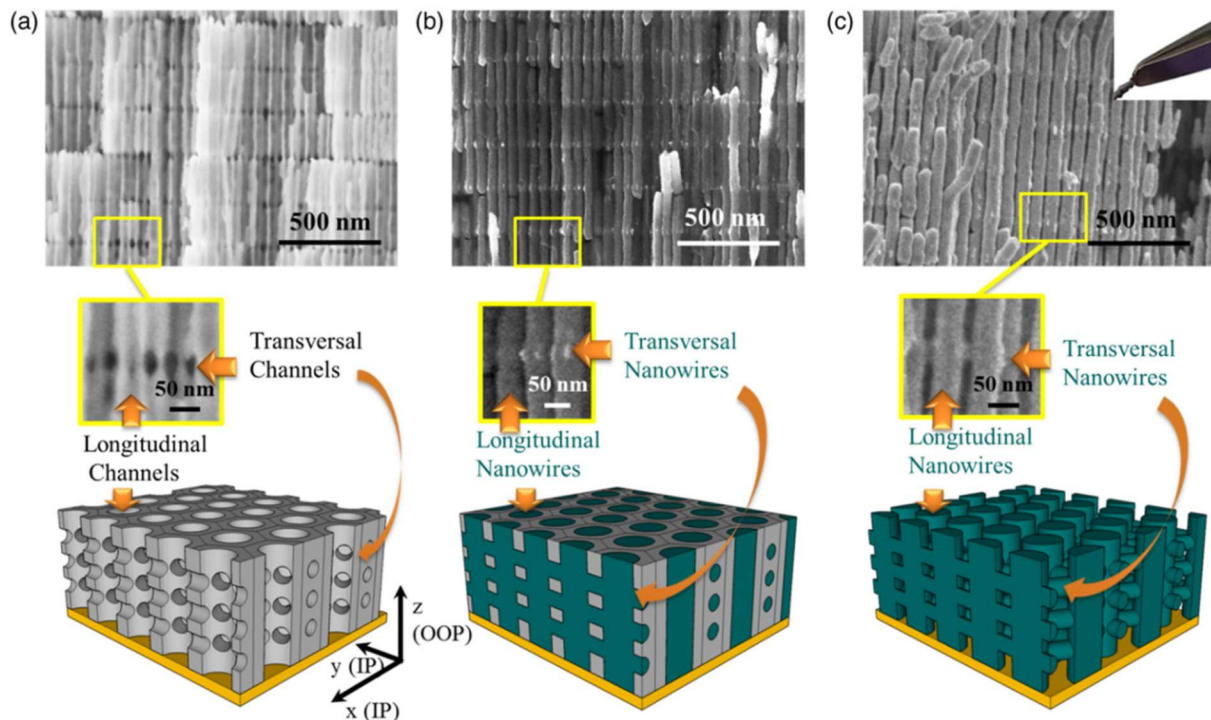


Figure 2.13. SEM images and schematics presenting template-assisted fabrication of 3D magnetic alloy network. (a) Raw alumina template, (b) structure infiltrated with magnetic alloy, and (c) 3D network of magnetic nanowires. Reprinted with permission from [183]. Copyright 2019 Wiley.

Valuable optical properties of these structure are the result of the geometry. These unique alumina networks features intrinsic reflections bands, that can be tailor-engineered in full range of visible light [184]. What is more, the structure features sensitivity to environmental changes such as material wetting. In a different example, process conditions are used to fabricate Bragg reflectors and alumina used as a sacrificial template [185]. The structure is infiltrated with polyethylene under low vacuum following by the removal of aluminum and alumina template. As a result, flexible Bragg reflectors made of nanostructured polymer are obtained.

2.4. Examples of NAA applications

There are many fields in which nanoporous anodic alumina structures demonstrated their utility. To provide overview of many functionalities discussed in Sections 4.1–4.7, they are gathered in the Table 2.2.

Table 2.2. Recently established applications of NAA-based structures.

Application	Reported Utility	Refs
Photonic structures	Reviews on photonic structures	[34,46,186]
	Principles of photonic crystals	[187–189]
	Fabry-Perót interferometer	[190]
	Gradient-index filters	[191]
	Distributed Bragg reflectors	[192]
	Optical bandpass filters	[193]
	Human protein heavy ions real-time interaction monitoring	[194]
	Tailoring of optical properties with pulse anodization	[149]
	Design of phase shift defect in effective refractive index	[195]
	Hybrid distributed DBRs and apodized GIF photonic structure	[196]
	Characterization of thermotropic ferroelectric liquid crystals confined in the NAA	[197–199]
	Glass transition of discotic liquid crystals in one-dimensional fluid	[200]
	Adjustable optical anisotropy by self-assembly of liquid crystals confined in porous structure	[201]
Sensors	NAA template-assisted fabrication of chromium substrate for SERS detection of heavy ions in aqueous solutions	[202]
	Au NPs array on NAA for SERS detection of hemoglobin	[203]
	Controlled fabrication of periodic plasmonic dimer arrays for SERS	[204]
	Graphene-NAA composite for SERS sensing	[205]
	Label-free optical sensor based on interferometric reflectance spectroscopy for TNF- α detection	[206]
	NAA-based interferometer for copper sensing	[207]
		[208]
	Rhodamine B release triggered by <i>Staphylococcus aureus</i> detection	[209]
	Determination of Pb ²⁺ with DNAzyme	[210]
	Reflectance spectroscopy based biosensor for determination of trypsin	[211]
	Salmonella sensing through DNA sequence recognition	[212]
	Reusable, molecular gated-NAA for detection of <i>Mycoplasma fermentans</i>	[97]
	Molecular gated-NAA for detection of <i>Candida albicans</i>	[213]
	Molecular gated-NAA for sensitive detection of cocaine	[26]
Adjustable sensor based on the metallic resistor suspended on NAA membrane	[214]	

Templates	Reviews of NAA template-assisted fabrication	[47,215]
	Fabrication of 2D Au nanodot arrays with tailorable geometric features for photocatalysis enhancement	[216]
	Nanostructured surface for photocatalysis	[217]
	Fabrication of Bi NWs for microelectronics	[218]
	Perovskite NWs with a tunable emission wavelength	[219]
	Electrodes for the electrochemical denitrification	[220]
	Metal-free coating for the broadband infrared absorption	[221]
	Polymer-brush structure confined in the NAA	[222]
	Segment Au-Ag nanowires for SERS detection	[223]
	Fabrication of Ni antidot arrays for spinotronic applications	[224]
	Review on NAA-derived electrochemical energy storage devices	[10]
	Co magnetic NWs	[225]
	Fe-Pd NWs for magnetic/catalytic spinoelectronics	[226]
	Ca ₂ FeIn Hensler alloy NWs for spintronics application	[227]
	Review on NAA-molded stimuli-responsive polymer structures	[228]
Membranes for filtering and separation	Tailor-engineering of narrow pore NAA membranes	[229]
	Growing covalent organic frameworks on porous substrates for molecule-sieving membranes with pores tunable from ultra- to nanofiltration	[230]
	Mechanical properties of NAA membranes	[231,232]
	Photocatalytic membrane for water disinfection	[233]
	Steric-based removal of Coliform bacteria	[234]
	Removal of Cu ²⁺ and Cd ²⁺ with pH controlled permeability	[235]
	Removal of As from aqueous media	[236]
	Switchable hydrophobicity of the membrane for selective oil/water emulsion separation	[237]
	Efficient separation of hydrocarbons	[238]
	Gas dehumidification method with selective water vapor-permeable membrane	[239]
	Selective rejection of polar molecules	[240]
	The electric eel inspired structure for energy conversion	[241]
Biological monitoring and cell culture	Reviews on NAA-based biosensors	[12,45]
	Biomimetic nanochannels for enhanced biomolecule response	[242]
	Modulation of osteo-immune response of macrophages	[243]
	Structure with three-phase interface for gas exposure as a lung airway model	[244]
	NAA-based substrate for in situ monitoring of hormonal release from human cell culture	[245]
	Osteogenic differentiation induced with NAA morphology	[246]
	Pore size-dependent growth of N2a cells	[247]
	Control of cell adhesion with functional coating of collagen and fibronectin	[248]

Drug delivery	Impact of NAA pore geometry on DOX sustained-release profile	[175]
	pH sensitive NAA platform for sustained drug release	[43]
	Bone ex vivo evaluation of drug release from NAA surface-modified aluminum wire implants	[249]
	Proof-of-concept cancer therapy with nanotube-based drug delivery system targeting autophagic and endoplasmic reticulum stress	[162]
	<i>In vivo</i> nanotubes nanotoxicity study on murine model	[163]
	Drug delivery perspectives of NAA-derived materials review	[48]
Functional layer for composites	Enhanced wear resistance through multiphase lubrication mechanism	[250]
	Tartaric-sulfuric acid NAA as “green” alternative for chromic-NAA protective layers	[80]
	NAA coating for reduction of thermal resistance and junction temperature	[251]
	Daytime passive radiative cooling layer	[252]
	Lubricant infused structure with self-healing properties and enhanced corrosion resistance	[253]
	NAA casing to reduce Ni corrosion in brine	[254]

2.4.1. Photonic structures

Optical properties of NAA are amongst the most impressive. Glass-like transparency, chemical resistance, and complex, tailorable nanomorphology makes of NAA a valuable material for optical applications. In fact, this is one of the most investigated use of nanoporous anodic alumina. Nanoporous anodic alumina can be also designed as a photonic crystal (PC)—usually through sinusoidal anodization. A detailed description of this role has been already provided in several reviews [34,46,186].

PCs are structures featuring a periodic variation of their refractive index, interlacing regions with high and low refractivity. As an effect, some wavelengths can propagate in the structure while others cannot—these are described as the photonic band gaps. It is due to multiple scattered interferences—defined by Bloch modes—that alter the flow of electromagnetic waves [187–189]. Propagation of light can be adjusted through a change in the geometry. The most common PC structures made this way are Fabry-Perót interferometers [190], gradient-index filters [191], distributed Bragg reflectors [192], and optical bandpass filters [193]. Their major utilization is as optical sensors. An exemplary application of such sensor is a real-time monitoring of the interaction between human proteins and heavy ions [194].

The precise control of the optical properties across the visible—NIR spectrum with pulse-anodized oxalic-fabricated NAA was demonstrated by Acosta et al. [149]. In addition, there are other types of structures as well. Fabrication of structures with a phase shift defect inside the sinusoidal profile of the effective refractive index was reported by Kushnir et al. [195]. Position of the resonance transmission peak could vary between 250 and 1500 nm. Recently, method combining different anodization profiles was reported by Lim et al. [196]. As result,

hybrid photonic structures composed of distributed DBRs and apodized GIFs were obtained facilitating for the design of specific photonic stopbands. The anodization profile, morphology of the structure, and resulting optical properties are shown in figure 2.14.

The structure can be provided with an additional functionality when infiltrated with material that serves as a medium different than air, for example by filling the pores with liquid crystals. Thermotropic ferroelectric liquid crystals infiltrated into 10, 15, and 20 nm NAA pores surface-modified with a polymer (the native oxalic NAA surface does not provide sufficient stability) were reported by Busch et al. [197]. The pore diameter of obtained nanohybrid materials was found to be linearly proportional with the electro-optical birefringence which affected the relaxation frequency. Group efforts done by Huber and Schönals teams with co-workers investigate the effects of liquid crystals confined in nanoporous structures—nanoporous anodic alumina and mesoporous silica. Several works of Yildirim et al. investigated a behavior of discotic ionic crystals in confined porous space. Measurements included analysis of a molecular mobility (broadband dielectric spectroscopy and specific heat spectroscopy) [198], a phase behavior, and a molecular ordering (differential scanning calorimetry and dielectric spectroscopy) [199].

In recent experiments, the focus was directed on understanding a charge transport in such systems [200]. Discotic liquid crystals were investigated with regards to molecular dynamics and phase behavior. Multiple glassy dynamics were detected thanks to detailed analysis. It was possible due to dipole functionalization. Figure 2.15 shows different types of discotic crystals motion than can occur in highly confined spaces. This finding can constitute for a next step in the future of molecular electronics. Further, self-assembly of discotic liquid crystals in NAA was presented in the work of Sentker et al. [201]. Nanoporous structures have features significantly smaller than visible light wavelengths. This provides for their potential use as a photonic metamaterial—a structure in which optical functionality is determined by its geometry rather than by the material composition itself. Introduction of liquid crystals to these confined spaces can expand possibilities of such structures to interact with light. Liquid crystals exhibit optical birefringence affected by their organization, that can be adjusted through the chemical character of the structure, its pore size and temperature. Optical properties of the porous material with liquid crystals with regards to pore diameter, pore surface functionalization, and temperature were evaluated. Modification of the optical properties through these conditions was also demonstrated. Monte-Carlo simulation of columnar discotic order in confined space of nanopores is shown in figure 2.15.

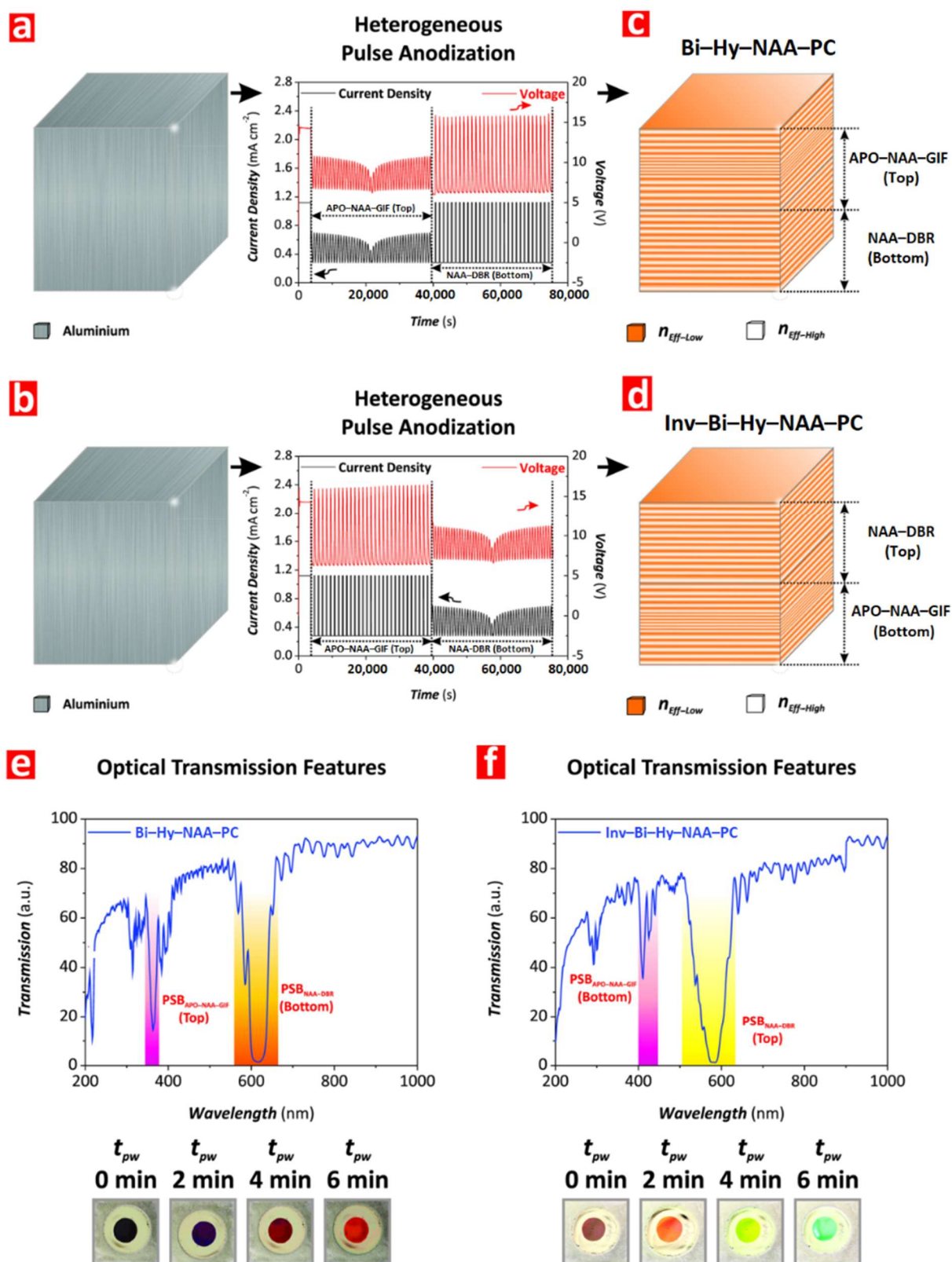


Figure 2.14. Fabrication and optical properties of hybrid photonic structures. (a,b) Anodization profiles, (c,d) resulting structures composed of two and three distinct photonic layers, and (e,f) measured transmission spectra with highlighted photonic stopbands and digital pictures demonstrating interferometric color of the PC structures depending on the pore widening time. Reprinted with permission from [196]. Copyrights 2019 Springer Nature.

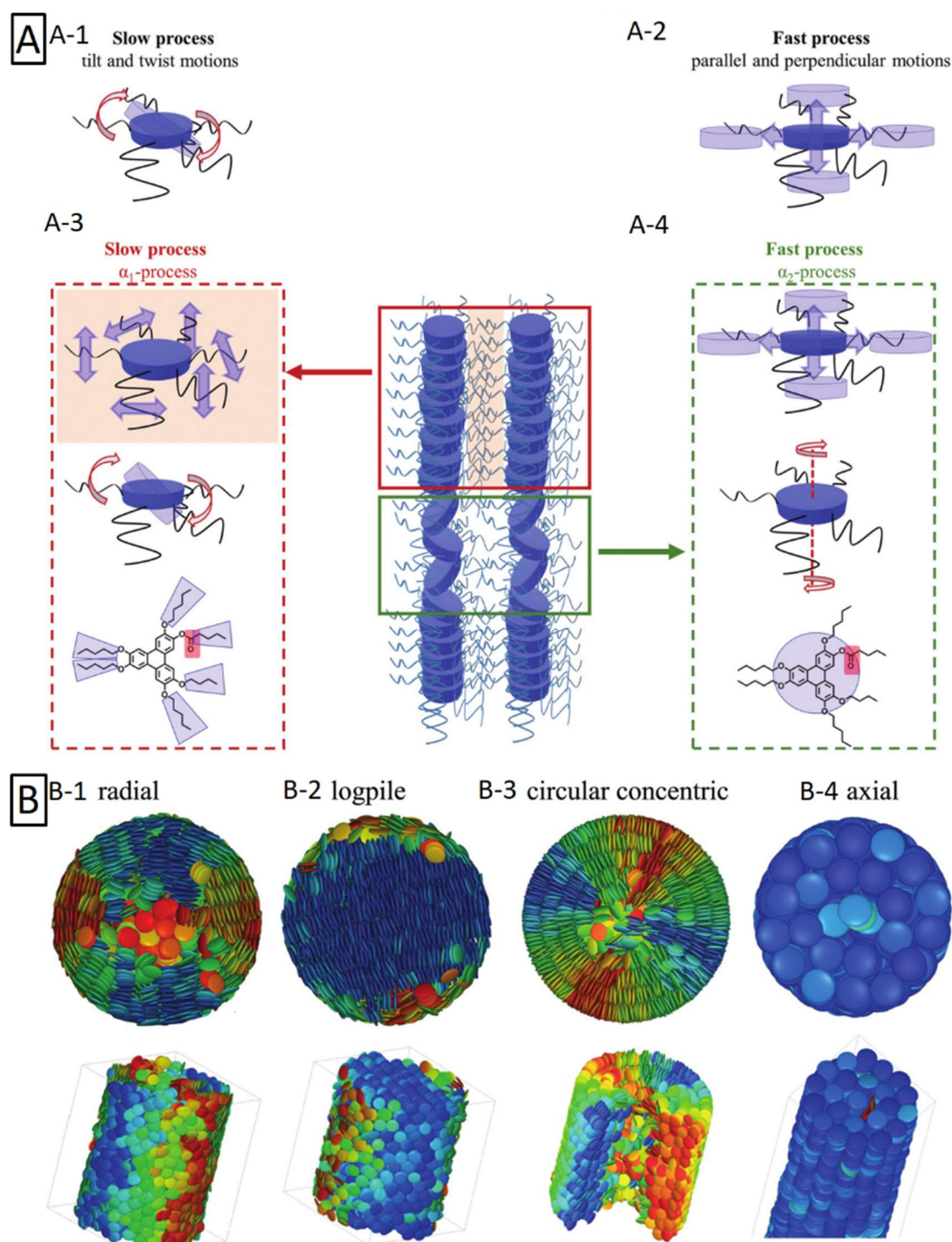


Figure 2.15. Motion and possible distribution of discotic liquid crystals in nanopore-limited space. (A) Illustration of (A-1) tilt and twist and (A-2) parallel and perpendicular motion of single discotic molecule. Cooperative molecular fluctuations and related changes to the column packing are assigned to (A-3) α_1 and (A-4) α_2 processes. Blue highlight on the structural formula represent parts assigned to glassy dynamics while red coloration represent parts of the molecule that enable to sense this glassy dynamic through Broadband Dielectric Spectroscopy. Reprinted (adapted) with permission from [200]. Copyright 2019 The Royal Society of Chemistry. (B) Monte Carlo simulation showing snapshots of columnar discotic order in cylindrical pores (B-1–B-4) in top- and side-view for different arrangement of discotic particles. Reprinted (adapted) with permission from [201]. Copyright 2019 The Royal Society of Chemistry.

2.4.2. Sensors

In recent years, the growth of publications reporting the use of NAA as a photonic structure can be observed. The value of its unique geometry has been demonstrated in many fields, for example as sensing platforms [202,203] providing a promising alternative over plasmonic nanoparticles. The idea to utilize NAA as a shadow mask to fabricate a surface covered with plasmonic dimers was presented by Schmidt et al. [204]. At first, thin (~250 nm) alumina film was subjected to removal of the barrier layer and transferred onto the surface. Different pore widening time was applied to yield various pore diameters. The substrates were placed on tilted substrates and shadow deposition was performed at different angles. Through configuration of fabrication process, it was possible to control deposition for each particle of dimer pair independently providing promising ability for tailoring plasmonic surfaces. ESEM showing exemplary dimer, variation of the calculated electric field density in relation to the laser polarization angle, and FDTD simulation of electric field distribution for angled and parallel dimers under different excitation polarization are shown in figure 2.16. Interactions with light are also utilized for practical application of NAA interferometers with purpose of copper detection [207]. In a different approach, graphene layer deposited onto the NAA surface through chemical vapor deposition serves as a platform to deposit an analyte [205]. When silver nanoparticles were introduced to the system, the platform combined both surface enhanced Raman scattering and interference amplification.

The surface of NAA can be also easily modified with several functionalization protocols such as silanization [206]. What is more, NAA's enormous surface area facilitates an efficient utilization of the material, which can be especially attractive in more sophisticated or real-time detection. Geometrical features of the NAA structure grafted with the streptavidin-biotin complex were examined by Pol et al. [208]. The setup was implemented into a flow cell system to provide real-time monitoring. In addition, an aptamer padding proved to be a valuable solution [209]. Works of Tabrizi et al. show vast versatility of such structures that are capable of the precise recognition of specific biomolecules and ions: determination of lead (II) ions [210], quantitative detection of trypsin [211], or Salmonella sensing through the recognition of specific DNA fragments [212] were reported. These systems are often based on simple principles, yet providing impressive effectivity—often employing precision and selectivity of biomolecules. Pores can be incubated with a signaling molecule and then blocked inside the structure with a stimuli-responsive capping—described as molecular gate. What is more, such substrates can be calcinated and reused. There are many examples using such concept in practice. Demonstration of such system with purpose to detect *Mycoplasma fermentans* based on the DNA recognition was reported by Pla et al. [97]. The performance of the platform was also demonstrated in the breast cancer cell media. Moreover, the recycling possibility was examined via calcination at 550°C for 5 h in order to remove the organic residues, then the substrate was successfully functionalized again. A probe enabling fast (less than 30 min) detection of *Candida albicans* was fabricated by Ribes et al. [213]. It is achieved thanks to a structure incubated with rhodamine B and the pores capped with oligonucleotide that

recognize the bacteria DNA. Upon the recognition, rhodamine is released to the media. A similar arrangement was also utilized to prepare the platform designed for precise detection of cocaine with detection limit of 5×10^{-7} M [26]. A different example that does not fall under previous categories is the Pirani sensor [214]. The sensor is composed of a resistor on the surface of the dielectric membrane. It was prepared by deposition of thin layer of tungsten and aluminum on previously prepared p-type silicon substrate. After two-step anodization in oxalic acid, the formed tungsten oxide was selectively removed ensuring perforation at the bottom of the NAA membrane. Nickel serpentine is shaped using negative photoresist and thermal evaporation. After the resistor formation, excess material at the bottom of the membrane is released through the pores. The serpentine resistor on the top of the NAA membrane serves as an electrical heating element and temperature sensor. Below the membrane, gap spacing is provided in order to provide proper thermic isolation. Elements of the sensor and SEM images displaying produced structure are shown in figure 2.16. The structure made of numerous nanopores enables lower measurable limit of pressure, due to the extent of sensing surface area and reducing the effective thermal loss. Using the membrane with porosity of 25%, it was possible to produce the device with the measurable pressure range between 0.1 mTorr to 760 Torr and was demonstrated as more sensitive than non-porous substrates.

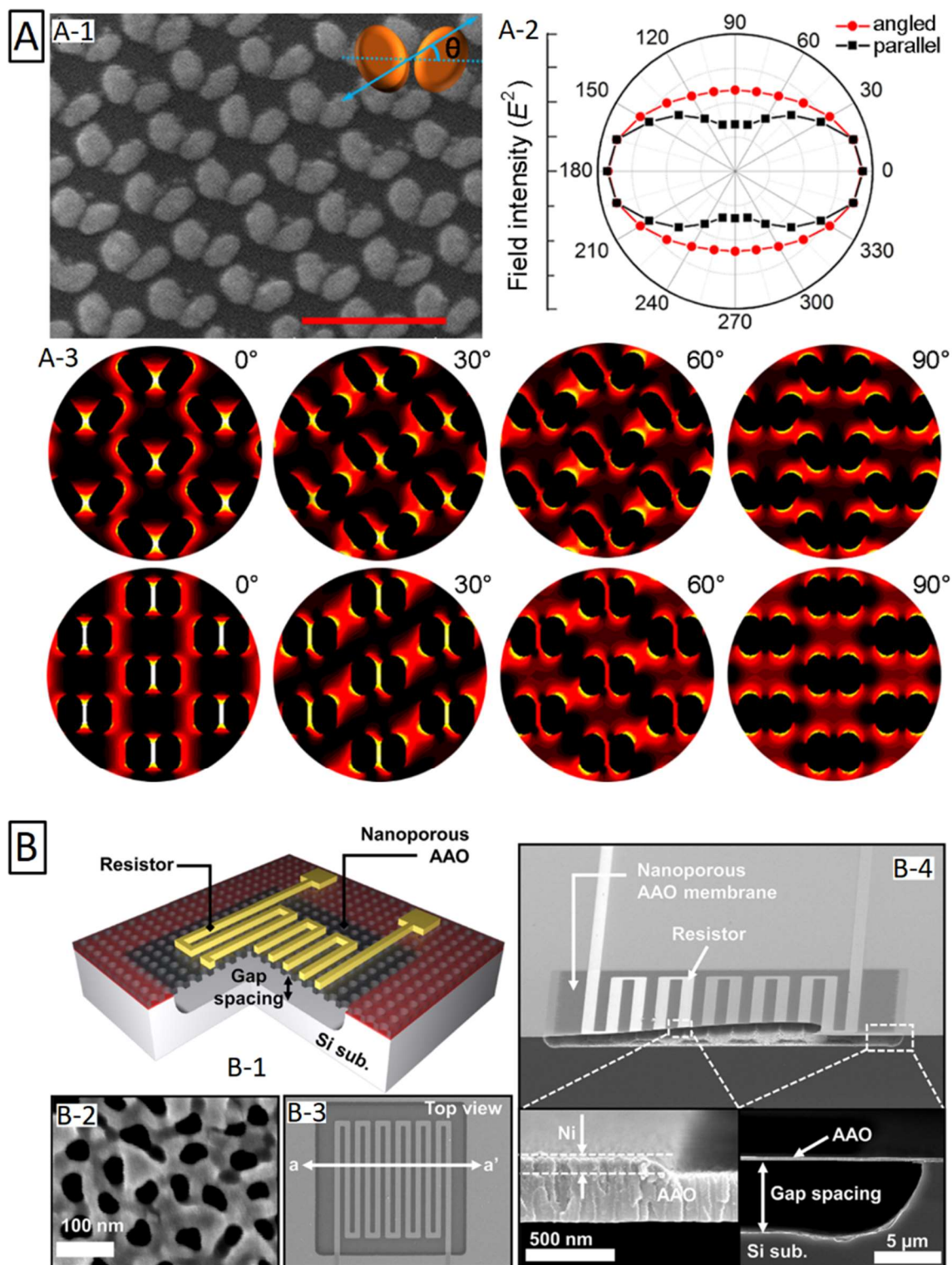


Figure 2.16. (A) Preparation of oriented nanoparticle dimers using NAA as a shadow mask. (A-1) SEM image of ellipsoidal dimers angled at 60°; (A-2) calculated electric field density with regards to dimers' angular orientation; and (A-3) FDTD simulation of electric field distribution of dimers at different conformation. Reprinted (adapted) with permission from [204]. Copyright 2017 American Chemical Society. (B) (B-1) Schematic of Pirani sensor and SEM images of (B-2) NAA membrane top view, (B-3) Pirani sensor top view, and (B-4) cross-section captures of fabricated device. Reprinted (adapted) with permission from [214]. Copyright 2016 AIP Publishing.

2.4.3. Templates

The use of NAA as a template has been explored for decades [47,215]. NAA template-based fabrication enables tailor-engineering of a periodic structure, as demonstrated by Lim et al. [216], where the fabrication of 2D Au nanodot single-lattices with different geometry is presented. There are many ways in which a material of interest can be introduced into NAA: Electrodeposition [217,218], salinization [206], inkjet printing [219], galvanic displacement [220], spraying [221], and polymerization [222]. With a precisely adjusted experimental setup, obtained structures feature an advanced morphology and can mix several functionalities or elements (figure 2.17) [223].

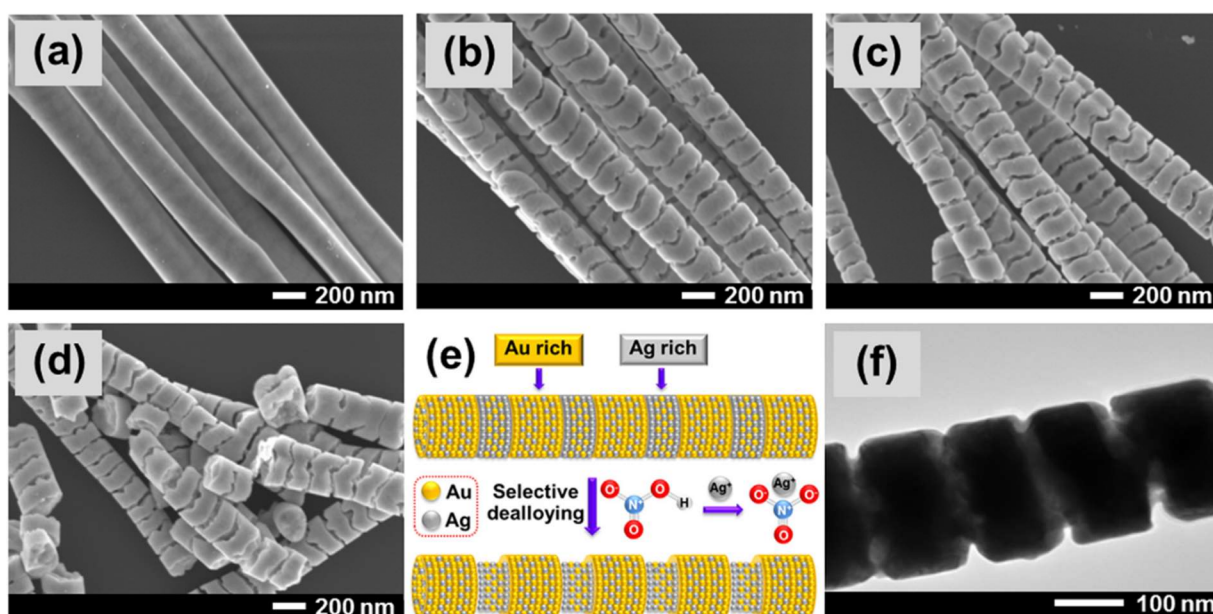


Figure 2.17. (a–d,f) SEM images of porous Au-Ag striped nanowires made through the interlaced electrodeposition supplemented with acid etching and (e) schematic of performed selective dealloying. Reprinted with permission from [223]. Copyrights 2019 Elsevier.

Recently, a material prepared with NAA membrane as a template and coated with transition metal was proposed for spintronic applications [224]. The membrane was covered by thermal evaporation technique with layer of Ni forming antidot array on the surface. Depending on the membrane geometry, different magnetic anisotropy was obtained. The shape of NAA is also favorable for the production on nano brushes in flat and spatial (3D) configurations [10,225] as well as liberated nanowires [226,227]. However, while reports demonstrate many different combinations of materials and shape, a significant fraction remains on the concept stage. As Rath and Theato wrote in their recent review: “as presented, utilizing complex NAA architectures are still in its infancy of being used as templates for stimuli-responsive polymer. Future shows great promise for advanced applications, especially when combined with multi-responsive polymers” [228].

2.4.4. Membranes for filtering and separation

Some merits of NAA structures stimulate their use in many distinct fields. Its nanostructured array of pores is highly regular. Layers up to several micrometers thick are a desirable material to produce self-standing and durable membranes [229]. The inner side of their walls can be precisely designed to serve the application requirement [230]. Such membranes can be prepared to maintain a high level of flexibility [231,232]. With growing population and raising environmental pollution, easy-to-produce, cost-effective membranes are desirable to help us face challenges of the future. For example, NAA membranes with zinc oxide nanosheets grown on the surface were reported by Stroe et al. [233]. Their performance was demonstrated to decrease *E. coli* population by 73% in UV light over 24 h. What is more, just the pore size itself enables to separate bacteria from water [234].

NAA membranes have shown their effectivity in precise chemical filtration, for example heavy ions separation: Chemical vapor deposited carbon nanotubes inside NAA enabled removal of copper (II) and cadmium (II) [235] while decoration with $\text{Fe}_3\text{O}_4/\text{SiO}_2$ bonded arsenic ions [236]. A different example is the pH-sensitive, smart membrane with switchable oil/water permeability functionalized with copolymer containing two blocks: pH-responsive poly(4-vinylpyridine) (P4VP) hydrophobic polystyrene (PS) [237]. Permeability of the membrane is controlled with pH that causes protonation/deprotonation of P4VP groups. When in a deprotonated state (pH neutral and alkaline), PS groups are exposed providing for hydrophobic properties of the surface—making membrane oil-permeable only. On the other hand, in an acidic environment, P4VP groups are protonated and thus hydrophilic. These membranes demonstrated performance over many cycles without decrease of the efficiency. NAA membranes are also useful for gas separation. Nanochannels sized 10-100 nm modified with a different density of octadecylphosphonic acid were demonstrated to affect permeability of the membranes [238]. Demonstration of how a thin layer of graphene oxide combined with NAA can function as a selective barrier that blocks most gases while preserving the high permeability to water vapors was reported by Petukhov et al. [239]. Selective separation can be also based on surface charge, for example charged cellulose nanofiber padding inside NAA pores enabled the selective separation of negatively charged molecules with a rejection rate close to 100% [240]. What is more, the morphology of NAA enables to reproduce more complex structures inspired by observation of nature. Inspiration with the electric eel skin morphology resulted in creation of material featuring a diode-like ion transport behavior [241]. The material is composed of two functional layers: Polymeric nanochannels with carboxyl groups additionally responsible for ion selectivity and NAA featuring hydroxyl groups and providing mechanical integrity of the membrane. Such structure demonstrated its performance in the energy conversion—energy generation is based on salinity gradient. Morphology of the electric eel skin that inspired the work, its functional principles, and architecture of the artificial counterpart are shown in figure 2.18 [241].

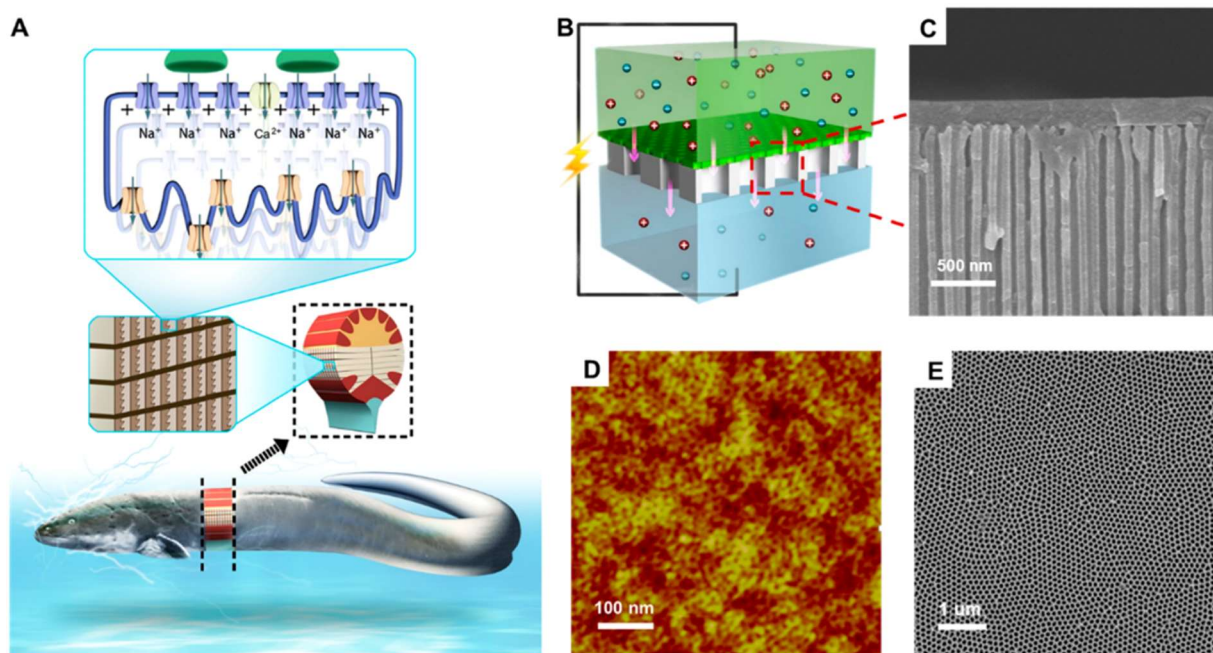


Figure 2.18. Bioinspired membrane for energy conversion. (A) Illustration demonstrating structure of electric eel skin with schematic display of ion channels, (B) schematic of bioinspired membrane for energy conversion, (C) SEM cross-section of the device, (D) AFM and (E) SEM top view of NAA membrane. Reprinted with permission from [241]. Copyright 2018 American Chemical Society.

2.4.5. Biological monitoring and cell culture

The size of NAA structures enables unique possibility to mimic and observe biological systems at the cellular level [12,45]. NAA coated with CuO and L-Cys/D-Cys with purpose to monitor response of biological molecules was demonstrated in work of Chen et al. [242]. Furthermore, the macrophage response can be modulated with differently sized pores [243]. Nanostructural features provide the adhesive cue for macrophages affecting their shape and the spread, resulting in modified inflammatory response and osteoclastic activities. They can be also used as a model to simulate certain biological behaviors. A bioinspired nanoporous membrane as a gas exposure model mimicking the airway mechanism was reported by Jiang et al. [244]. Alveolar cells on top of the membrane were in contact with the cell culture medium at the top with exposure to the gas through the pores. The setup enabled to follow the inflammatory response of alveolar cells to the gas pollution. In different approach, researchers prepared an NAA-based platform to observe the in situ hormonal release of cultured human cells [245]. These examples reflect high compatibility of NAA with biological systems. This material can be effectively used as a surface for cell cultivation/monitoring providing superior performance [246,247]. The performance of cell cultures carried out on nanoporous anodic alumina and macroporous silicon coated with collagen and fibronectin with purpose to control the adhesion of cells to the surface was compared by Formentin et al. [248]. Properties of the fibronectin coating were superior, providing the best adhesion, morphology, and proliferation of cells.

2.4.6. Drug delivery

Cost-effective, biocompatible structures of NAA along with derived materials can be tailor-engineered in all dimensions. These properties stimulate the application of nanoporous anodic alumina derived materials for drug delivery. Although several approaches has been proposed involving both structural modifications [175] and stimuli-responsive release [43], instances of practical applications are few.

One of such examples can be an implant based on the aluminum wire surface-modified through the anodization. Thin layer of NAA provided on the wire implants is examined for controlled drug delivery in vitro and ex vivo—evaluating drug release inside the bone [249]. The implant provided stable and sustained release: Sample with short pores (20 μm) reported release of 82.6% over the course of 11 days, while 45.6% of the load has been released from structures with longer pores (60 μm). Viable osteocytes in the implant surroundings detected with the bone histology demonstrating the biocompatibility of such devices.

Furthermore, nanoparticles made of NAA—the nanotubes—were investigated for such application. A drug delivery system based on AANTs for a proof-of-concept cancer therapy was investigated [162]. The system was designed to target autophagic and endoplasmic reticulum stress—nanotubes were loaded with thapsigargin (TG). Modified AANTs were initially examined with regards to their impact on the cell function, then examined with the human breast cancer cells. AANTs induced cellular response and were successfully internalized, demonstrating possibility of intracellular drug delivery. Furthermore, 3-methyladenine was used as an autophagy inhibitor that was demonstrated to improve cancer cell killing effect of TG-loaded nanotubes [162]. These nanotubes were later examined in vivo on the murine model (Balb/c mice, eight weeks) and introduced by intravenous injection and subcutaneous implantation routes [163]. The intravenous path did not display any impact on the viability while low and moderate doses were applied, with higher doses resulting in detectable accumulation in liver and spleen. More pronounced effects were observed with subcutaneous route that triggered inflammatory response.

In a recent review, drug delivery perspectives, providing an update to the state of the art of NAA and NAA-derived materials in the field were discussed by Kapruwan et al. [48].

2.4.7. Functional layer for composites

Since nanoporous anodic alumina can be grown into aluminum and its alloys, even whole components can be enhanced with an additional functionality. A coverage of aluminum surface with an NAA coating is a common practice that greatly improves the corrosion resistance and mechanical properties of the material. Apart from chemical resistance, the hard NAA layer boost surface hardness and tribological durability [80,250]. The improvement of the thermal management provided through the NAA coating may serve as another benefit. NAA layers can significantly reduce (~14%) the thermal resistance and junction temperature of the surface—which could be beneficial for packaging and casing design [251]. NAA

membranes have shown passive cooling effect that resulted in 2.6 °C below ambient temperature of the cooler when exposed to direct sunlight [252]. Complex morphology of the NAA facilitates for preparation of composites. A method to completely fill alumina nanopores of 50 μm long with mineral oil by means of vacuum impregnation was shown by Wu et al. [253]. Such a combination exhibits self-healing properties over the wear damage and surface cracks additionally providing corrosion protection over extended time periods. Morphology of the structure, behavior around the cracks, and schematic of repair behavior is shown in figure 2.19 [253]. In a different example, preparation of composite made of Ni nanopillars embedded inside the NAA structure through electrodeposition was reported by Tishkovich et al. [254]. Layers of electrodeposited Ni are commonly utilized to improve mechanical and corrosion properties of many metals. The combination with NAA was demonstrated to exhibit higher corrosion resistance in saline aqueous solution as compared to bulk Ni layer.

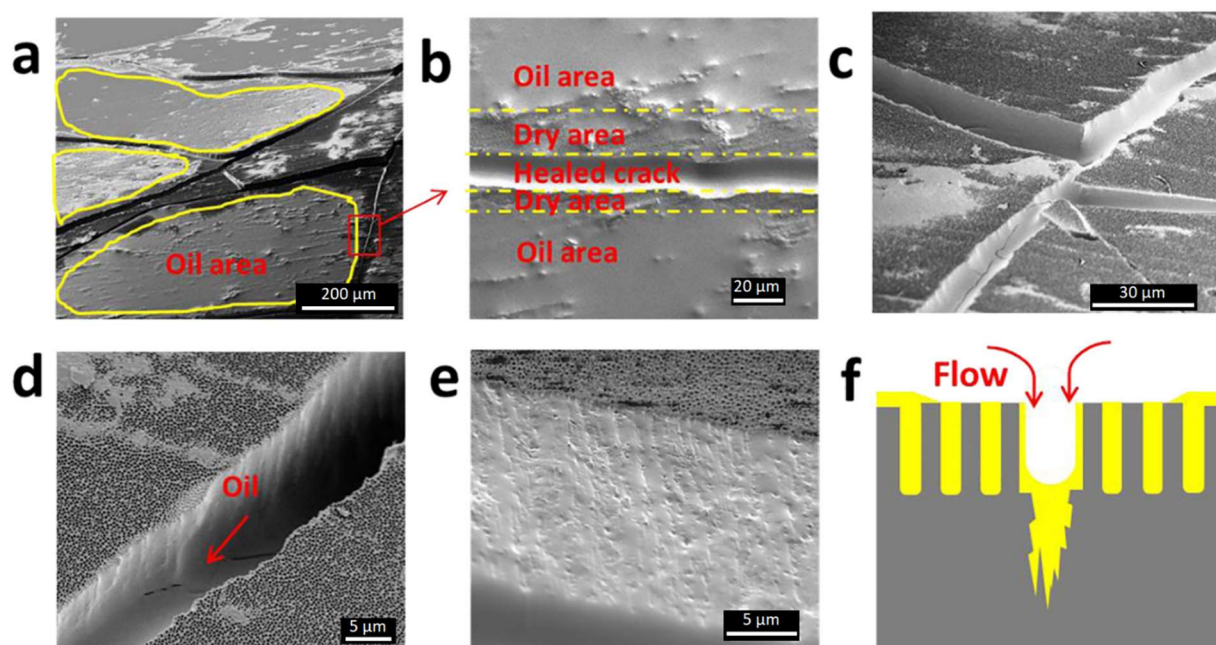


Figure 2.19. Cryo-SEM images of (a–c) generated micro-cracks, (d) surface surrounding the crack, (e) cross-section of lubricant filled crack, and (f) schematic of repair process. Reprinted with permission from [253]. Copyright 2019 Elsevier.

The aforementioned examples are not an exhaustive list covering discoveries of recent decades. Instead, the aim is to provide an update with the most recent contributions in the field and a context to account for the exponential growth of publications involving nanoporous anodic alumina. The scope involves an insight into the fabrication mechanism and design tools with intention to provide synthesis of a comprehensive knowledge about the material. Our intention is to disseminate NAA fabrication as a nanotechnology tool that—while not completely unique—definitely possess a few advantages, and that sometimes, it is imagination that restricts innovation.

2.5. Conclusions

The anodization of aluminum has changed greatly since its discovery almost 100 years ago. Decades of work done by many researchers—step by step—unveiled subtleties of the process slowly turning robust industrial method employed to cover machine parts with the protective layer, into a sophisticated and precise nanotool. Applications of NAA vary greatly, from cost-effective templates, smart surfaces to biomaterials and sensing platforms—providing vast utility. Precise control of geometrical features known today was possible due to exploration of the formation mechanism, close analysis with advanced equipment at nano- and atomic scale during different stages of formation process sometimes coincidental results and definitely, a continuous dialogue between groups of researchers. Compared to the past, today's aluminum anodization is a mature technology—facile, cost-effective, and environmentally friendly—yet another promise of a better future. We understand more and have accurate control over the material formation. NAA can be designed for specific interaction with light due to tailored morphology, choice of electrolyte can enhance photoluminescence or improve conductivity, while smart combination of simple techniques can turn amorphous oxide into chemically resistant and hard corundum, simultaneously preserving its porous morphology.

Exploration of possibilities related with NAA does not slow down. Photonic crystals itself or filled with responsive medium are still in the development and may revolutionize sensing, and microelectronics. The ability to precisely tailor nanoparticles is useful, but definitely restricted on the side of interactions with biological systems. Significant improvement has been done in taming technology to provide highly ordered surfaces even using low-grade aluminum substrates. This may enable to universalize its utility as a functional coating. Many applications have been already implemented as a proof-of-concept. It can be expected that in the future, these novelties will be introduced into already existing systems, sometimes as a fast and easy approach to enhance properties of already utilized material, but also as precisely engineered materials capable of competing and replacing more expensive alternatives.

2.6. References

- [1] E. Inshakova and O. Inshakov. World market for nanomaterials: Structure and trends. *MATEC Web Conf.* **2017**, 129, 1-5, DOI: 10.1051/mateconf/201712902013.
- [2] A. A. Taylor, E. L. Freeman, and M. J. C. van der Ploeg. Regulatory developments and their impacts to the nano-industry: A case study for nano-additives in 3D printing. *Ecotoxicol. Environ. Saf.* **2020**, 207, 111458, DOI: 10.1016/j.ecoenv.2020.111458.
- [3] H. Rauscher, K. Rasmussen, and B. Sokull-Klüttgen. Regulatory Aspects of Nanomaterials in the EU. *Chemie-Ingenieur-Technik.* **2017**, 89, 224-231, DOI: 10.1002/cite.201600076.
- [4] Garside, M. **2020**. Global nanotechnology market value 2010-2020. June 5. Available online: <https://www.statista.com/statistics/1073886/global-market-value-nanotechnology/> (accessed on 22 November 2020).
- [5] E. Van de Velde, P. Debergh, C. Rammer, P. Schliessler, B. Gehrke, P. Wassmann, M. de Heide, M. Butter, S. Wydra, O. Som and N. Weidner. **2015**. Key Enabling Technologies (KETs) Observatory. *Methodology Report*. Available online: https://ec.europa.eu/growth/tools-databases/kets-tools/sites/default/files/documents/data_use_methodology_phase_i_final_report_kets_observatory_en.pdf (accessed on 22 November 2020).
- [6] A. Michaelis. In *Electrochemical Surface Modification: Thin Films, Functionalization and Characterization*; Alkire R. C., Kolb D. M., Lipkowski J., Ross P. N., Eds; Willey-VCH, NY, USA, 2008; Chapter 1, p 1-106, DOI: 10.1002/9783527625307.ch1.
- [7] R. A. Surmenev, R. V. Chernozem, I. O. Pariy, and M. A. Surmeneva. A review on piezo- and pyroelectric responses of flexible nano- and micropatterned polymer surfaces for biomedical sensing and energy harvesting applications. *Nano Energy.* **2021**, 79, 105442, DOI: 10.1016/j.nanoen.2020.105442.
- [8] M. Shopska, D. Paneva, H. Kolev, G. Kadinov, J. Briancin, M. Fabian, Z. Cherkezova-Zheleva and I. Mitov. Characterization and catalytic activity in CO oxidation of biogenic lepidocrocite layered on anodic alumina. *Catal. Today.* **2020**, 357, 436-441, DOI: 10.1016/j.cattod.2019.07.054.
- [9] S. Kasani, K. Curtin, and N. Wu. A review of 2D and 3D plasmonic nanostructure array patterns: Fabrication, light management and sensing applications. *Nanophotonics.* **2019**, 8, 2065-2089, DOI: 10.1515/nanoph-2019-0158.
- [10] Q. Wei, Y. Fu, G. Zhang, D. Yang, G. Meng, and S. Sun. Rational design of novel nanostructured arrays based on porous AAO templates for electrochemical energy storage and conversion. *Nano Energy.* **2019**, 55, 234-259, DOI: 10.1016/j.nanoen.2018.10.070.
- [11] Q. Xu, G. Meng, and F. Han. Porous AAO template-assisted rational synthesis of large-scale 1D hybrid and hierarchically branched nanoarchitectures. *Prog. Mater. Sci.* **2018**, 95, 243-285, DOI: 10.1016/j.pmatsci.2018.02.004.
- [12] G. Rajeev, B. Prieto Simon, L. F. Marsal, and N. H. Voelcker. Advances in Nanoporous Anodic Alumina-Based Biosensors to Detect Biomarkers of Clinical Significance: A Review. *Adv. Healthc. Mater.* **2018**, 7, 1-18, DOI: 10.1002/adhm.201700904.
- [13] C. Mijangos, R. Hernández, and J. Martín. A review on the progress of polymer nanostructures with modulated morphologies and properties, using nanoporous AAO templates. *Prog. Polym. Sci.* **2016**, 54-55, 148-182, DOI: 10.1016/j.progpolymsci.2015.10.003.

- [14] L. Zaraska, K. Gawlak, M. Gurgul, D. K. Chlebda, R. P. Socha, and G. D. Sulka. Controlled synthesis of nanoporous tin oxide layers with various pore diameters and their photoelectrochemical properties. *Electrochim. Acta*. **2017**, 254, 238-245, DOI: 10.1016/j.electacta.2017.09.113.
- [15] Y. Fu and A. Mo. A Review on the Electrochemically Self-organized Titania Nanotube Arrays: Synthesis, Modifications, and Biomedical Applications. *Nanoscale Res. Lett.* **2018**, 13, 187, DOI: 10.1186/s11671-018-2597-z.
- [16] R. Herino, G. Bomchil, K. Barla, and C. Bertrand. Porosity and Pore Size Distributions of Porous Silicon Layers. *J. Electrochem. Soc.* **1987**, 134, 1994, DOI: 10.1149/1.2100805.
- [17] H. Masuda and K. Fukuda. Ordered Metal Nanohole Arrays Made by a Two-Step Replication of Honeycomb Structures of Anodic Alumina. *Science*. **1995**, 268, 1466-1468, DOI: 10.1126/science.268.5216.1466.
- [18] R. Z. Valiev, A. A. Nazarov. In *Bulk Nanostructured Materials*; Zehetbauer M. J., Y. T. Zhu, Eds; Willey-VCH: NY, USA, 2009; Chapter 2, p 21-48, DOI: 10.1002/9783527626892.ch2.
- [19] W. Lee. The anodization of aluminum for nanotechnology applications. *Jom*. **2010**, 62, 57-63, DOI: 10.1007/s11837-010-0088-5.
- [20] P. Gu, H. Miao, Z. T. Liu, X. P. Wu, and J. H. Zhao. Investigation of elastic modulus of nanoporous alumina membrane. *J. Mater. Sci.* **2004**, 39, 3369-3373, DOI: 10.1023/B:JMSE.0000026938.59949.1f.
- [21] L. Vojkuvka, A. Santos, J. Pallarès, J. Ferré-Borrull, L. F. Marsal, and J. P. Celis. On the mechanical properties of nanoporous anodized alumina by nanoindentation and sliding tests. *Surf. Coatings Technol.* **2012**, 206, 2115-2124, DOI: 10.1016/j.surfcoat.2011.09.040.
- [22] J. Dai, J. Singh, and N. Yamamoto. Nonbrittle nanopore deformation of anodic aluminum oxide membranes. *J. Am. Ceram. Soc.* **2018**, 101, 2170-2180, DOI: 10.1111/jace.15367.
- [23] O. Nishinaga, T. Kikuchi, S. Natsui, and R. O. Suzuki. Rapid fabrication of self-ordered porous alumina with 10-/sub-10-nm-scale nanostructures by selenic acid anodizing. *Sci. Rep.* **2013**, 3, 1-6, DOI: 10.1038/srep02748.
- [24] W. Lee, R. Ji, U. Gösele, and K. Nielsch. Fast fabrication of long-range ordered porous alumina membranes by hard anodization. *Nat. Mater.* **2006**, 5, 741-747, DOI: 10.1038/nmat1717.
- [25] M. Yu, W. Zhang, S. Zhang, S. Zhao, F. Ai, and X. Zhu. Morphology evolution of porous anodic alumina in mixed H₃PO₄/NH₄F electrolytes. *Surf. Coatings Technol.* **2018**, 334, 500-508, DOI: 10.1016/j.surfcoat.2017.12.012.
- [26] A. Ribes, E. Xifre-Perez, E. Aznar, F. Sancenon, T. Pardo, L. F. Marsal & R. Martinez-Manez. Molecular gated nanoporous anodic alumina for the detection of cocaine. *Sci. Rep.* **2016**, 6, 1-9, DOI: 10.1038/srep38649.
- [27] J. P. O'Sullivan and G. C. Wood. Morphology and mechanism of formation of porous anodic films on aluminum. *Proc Roy Soc Ser A Math Phys Sci.* **1970**, 317, 1731, DOI: 10.1098/rspa.1970.0129.
- [28] Y. Lin, Q. Lin, X. Liu, Y. Gao, J. He, W. Wang & Z. Fan. A Highly Controllable Electrochemical Anodization Process to Fabricate Porous Anodic Aluminum Oxide Membranes. *Nanoscale Res. Lett.* **2015**, 10, 1-8, DOI: 10.1186/s11671-015-1202-y.
- [29] A. Santos, J. Ferré-Borrull, J. Pallarès, and L. F. Marsal. Hierarchical nanoporous anodic alumina templates by asymmetric two-step anodization. *Phys. Status Solidi Appl. Mater. Sci.* **2011**, 208, 668-674, DOI: 10.1002/pssa.201026435.

- [30] L. Vojkuvka, L. F. Marsal, J. Ferré-Borrull, P. Formentin, and J. Pallarés. Self-ordered porous alumina membranes with large lattice constant fabricated by hard anodization. *Superlattices Microstruct.* **2008**, 44, 577-582, DOI: 10.1016/j.spmi.2007.10.005.
- [31] A. Poznyak, A. Pligovka, U. Turavets, and M. Norek. On-Aluminum and Barrier Anodic Oxide : Meeting Various Acids and Solutions. *Coatings.* **2020**, 10, 875, DOI: 10.3390/coatings10090875.
- [32] H. Han, S. J. Park, J. S. Jang, H. Ryu, K. J. Kim, S. Baik and W. Lee. In situ determination of the pore opening point during wet-chemical etching of the barrier layer of porous anodic aluminum oxide: Nonuniform Impurity Distribution in Anodic Oxide. *ACS Appl. Mater. Interfaces.* **2013**, 5, 3441-3448, DOI: 10.1021/am400520d.
- [33] S. J. Garcia-Vergara, H. Habazaki, P. Skeldon, and G. E. Thompson. Tracer studies relating to alloying element behaviour in porous anodic alumina formed in phosphoric acid. *Electrochim. Acta.* **2010**, 55, 3175-3184, DOI: 10.1016/j.electacta.2010.01.038.
- [34] A. Santos. Nanoporous anodic alumina photonic crystals: Fundamentals, developments and perspectives. *J. Mater. Chem. C.* **2017**, 5, 5581-5599, DOI: 10.1039/c6tc05555a.
- [35] L. Vera-Londono, A. Ruiz-Clavijo, O. Caballero-Calero, and M. Martín-González. Understanding the thermal conductivity variations in nanoporous anodic aluminum oxide. *Nanoscale Adv.* **2020**, 2, 4591-4603, DOI: 10.1039/d0na00578a.
- [36] J. Ferre-Borrull, E. Xifre-Perez, J. Pallares, and L. F. Marsal. In *Nanoporous Alumina*; Losic D., Santos A., Eds; Springer: Cham, Switzerland, 2015; Vol. 219, p 185-217, DOI: 10.1007/978-3-319-20334-8_6.
- [37] A. Santos, V. S. Balderrama, M. Alba, P. Formentin, J. Ferre-Borrull, J. Pallares & L. F. Marsal. Tunable fabry-pérot interferometer based on nanoporous anodic alumina for optical biosensing purposes. *Nanoscale Res. Lett.* **2012**, 7, 2-5, DOI: 10.1186/1556-276X-7-370.
- [38] S.-Z. Kure-Chu, K. Osaka, H. Yashiro, K. Wada, H. Segawa, and S. Inoue. Facile Fabrication of Ordered Multi-Tiered Hierarchical Porous Alumina Nanostructures with Multiple and Fractional Ratios of Pore Interval toward Multifunctional Nanomaterials. *ECS J. Solid State Sci. Technol.* **2016**, 5, 285-292, DOI: 10.1149/2.0231605jss.
- [39] Y. B. Li, M. J. Zheng, and L. Ma. High-speed growth and photoluminescence of porous anodic alumina films with controllable interpore distances over a large range. *Appl. Phys. Lett.* **2007**, 91, 8-11, DOI: 10.1063/1.2772184.
- [40] L. Cantelli, J. S. Santos, T. F. Silva, M. H. Tabacniks, A. O. Delgado-Silva, and F. Trivinho-Strixino. Unveiling the origin of photoluminescence in nanoporous anodic alumina (NAA) obtained by constant current regime. *J. Lumin.* **2019**, 207, 63-69, DOI: 10.1016/j.jlumin.2018.10.015.
- [41] M. A. Mir, M. A. Shah, and P. A. Ganai. Dielectric study of nanoporous alumina fabricated by two-step anodization technique. *Chem. Pap.* **2020**, 0123456789, DOI: 10.1007/s11696-020-01323-x.
- [42] M. Baranowska, A. J. Slota, P. J. Eravuchira, G. Macias, E. Xifre-Perez, J. Pallares, J. Ferre-Borrull and L. F. Marsal. Protein attachment to nanoporous anodic alumina for biotechnological applications: Influence of pore size, protein size and functionalization path. *Colloids Surfaces B Biointerfaces.* **2014**, 122, 375-383, DOI: 10.1016/j.colsurfb.2014.07.027.
- [43] M. Porta-i-batalla, C. Eckstein, E. Xifré-pérez, P. Formentín, and L. F. Marsal. Sustained , Controlled and Stimuli- Responsive Drug Release Systems Based on Nanoporous Anodic Alumina with Layer-by-Layer Polyelectrolyte. *Nanoscale Res. Lett.* **2016**, 11, 372, DOI: 10.1186/s11671-016-1585-4.

- [44] C. Eckstein, L. K. Acosta, L. Pol, E. Xifre-Perez, J. Pallares, J. Ferre-Borrull and L. F. Marsal. Nanoporous Anodic Alumina Surface Modification by Electrostatic, Covalent, and Immune Complexation Binding Investigated by Capillary Filling. *ACS Appl. Mater. Interfaces*. **2018**, 10, 10571-10579, DOI: 10.1021/acscami.8b00572.
- [45] M. A. Tabrizi, J. Ferre-Borrull, and L. F. Marsal. Advances in optical biosensors and sensors using nanoporous anodic alumina. *Sensors (Switzerland)*. **2020**, 20, 1-27, DOI: 10.3390/s20185068.
- [46] C. S. Law, S. Y. Lim, A. D. Abell, N. H. Voelcker, and A. Santos. Nanoporous Anodic Alumina Photonic Crystals for Optical Chemo- and Biosensing: Fundamentals, Advances, and Perspectives. *Nanomaterials*. **2018**, 8, 788, DOI: 10.3390/nano8100788.
- [47] Z. Zhou and S. S. Nonnenmann. Progress in nanoporous templates: Beyond anodic aluminum oxide and towards functional complex materials. *Materials (Basel)*. **2019**, 12, 2535, DOI: 10.3390/ma12162535.
- [48] P. Kapruwan, J. Ferré-borrull, and L. F. Marsal. Nanoporous Anodic Alumina Platforms for Drug Delivery Applications : Recent Advances and Perspective. *Advanced Materials Interfaces*. **2020**, 7, 1-17, DOI: 10.1002/admi.202001133.
- [49] W. Lee and S. J. Park. Porous anodic aluminum oxide: Anodization and templated synthesis of functional nanostructures. *Chem. Rev.* **2014**, 114, 7487-7556, DOI: 10.1021/cr500002z.
- [50] Y. Sato, H. Asoh, and S. Ono. Effects of electrolyte species and their combination on film structures and dielectric properties of crystalline anodic alumina films formed by two-step anodization. *Mater. Trans.* **2013**, 54, 1993-1999, DOI: 10.2320/matertrans.L-M2013826.
- [51] M. Yazdizadeh, A. Yelon, and D. Ménard. Characterizing and optimizing the electropolishing and pore arrangement in porous anodic aluminum oxide (AAO). *J. Porous Mater.* **2020**, 27, 995-1002, DOI: 10.1007/s10934-020-00875-3.
- [52] M. A. Mir, M. A. Shah, and P. A. Ganai. Nanoporous anodic alumina (NAA) prepared in different electrolytes with different pore sizes for humidity sensing. *J. Solid State Electrochem.* **2020**, 24, 1679-1686, DOI: 10.1007/s10008-020-04683-2.
- [53] J. A. Davies, B. Domeij, J. P. S. Pringle, and F. Brown. The Migration of Metal and Oxygen during Anodic Film Formation. *J. Electrochem. Soc.* **1965**, 112, 675, DOI: 10.1149/1.2423662.
- [54] K. Shimizu, G. E. Thompson, G. C. Wood, and Y. Xu. Direct observations of ion-implanted xenon marker layers in anodic barrier films on aluminium. *Thin Solid Films*. **1982**, 88, 255-262, DOI: 10.1016/0040-6090(82)90054-2.
- [55] F. Li, L. Zhang, and R. M. Metzger. On the Growth of Highly Ordered Pores in Anodized Aluminum Oxide. *Chem. Mater.* **1998**, 10, 2470-2480, DOI: 10.1021/cm980163a.
- [56] T. Kumeria and A. Santos. Nanoporous Anodic Alumina for Optical Biosensing. *Springer Ser. Mater. Sci.* **2015**, 219, 293-318, DOI: 10.1007/978-3-319-20334-8.
- [57] G. E. Thompson, Y. Xu, P. Skeldon, K. Shimizu, S. H. Han, and G. C. Wood. Anodic oxidation of aluminium. *Philos. Mag. B Phys. Condens. Matter.* **1987**, 55, 651-667, DOI: 10.1080/13642818708218371.
- [58] G. E. Thompson. Porous anodic alumina: fabrication, characterization and applications. *Thin Solid Films*. **1997**, 297, 192-201, DOI: 10.1016/S0040-6090(96)09440-0.
- [59] O. Jessensky, F. Müller, and U. Gösele. Self-organized formation of hexagonal pore arrays in anodic alumina. *Appl. Phys. Lett.* **1998**, 72, 1173-1175, DOI: 10.1063/1.121004.

- [60] Q. Van Overmeere and J. Proost. Stress-affected and stress-affecting instabilities during the growth of anodic oxide films. *Electrochim. Acta*. **2011**, 56, 10507-10515, DOI: 10.1016/j.electacta.2011.03.123.
- [61] K. Nielsch, J. Choi, K. Schwirn, and R. B. Wehrspohn. Self-ordering Regimes of Porous Alumina: The 10% Porosity Rule. *Nano Lett.* **2002**, 2, 1-4, DOI: 10.1021/nl025537k.
- [62] A. Santos, T. Kumeria, and D. Losic. Nanoporous anodic aluminum oxide for chemical sensing and biosensors. *TrAC - Trends Anal. Chem.* **2013**, 44, 25-38, DOI: 10.1016/j.trac.2012.11.007.
- [63] C. T. Sousa, D. C. Leitao, M. P. Proenca, J. Ventura, A. M. Pereira, and J. P. Araujo. Nanoporous alumina as templates for multifunctional applications. *Appl. Phys. Rev.* **2014**, 1, 031102, DOI: 10.1063/1.4893546.
- [64] J. E. Houser and K. R. Hebert. The role of viscous flow of oxide in the growth of self-ordered porous anodic alumina films. *Nat. Mater.* **2009**, 8, 415-420, DOI: 10.1038/nmat2423.
- [65] K. R. Hebert, S. P. Albu, I. Paramasivam, and P. Schmuki. Morphological instability leading to formation of porous anodic oxide films. *Nat. Mater.* **2012**, 11, 162-166, DOI: 10.1038/nmat3185.
- [66] T. Kikuchi, O. Nishinaga, S. Natsui, and R. O. Suzuki. Fabrication of self-ordered porous alumina via etidronic acid anodizing and structural color generation from submicrometer-scale dimple array. *Electrochim. Acta*. **2015**, 156, 235-243, DOI: 10.1016/j.electacta.2014.12.171.
- [67] R. A. Mirzoev, A. D. Davydov, S. I. Vystupov, and T. B. Kabanova. Conditions for self-ordering of porous structure of anodic aluminum oxide in weak and strong acids. *Electrochim. Acta*. **2019**, 294, 276-285, DOI: 10.1016/j.electacta.2018.10.041.
- [68] H. Masuda and F. Hasegawa. Self-Ordering of Cell Arrangement of Anodic Porous Alumina Formed in Sulfuric Acid Solution. *J. Electrochem. Soc.* **1997**, 144, L127, DOI: 10.1149/1.1837634.
- [69] G. D. Sulka and K. G. Parkoła. Anodising potential influence on well-ordered nanostructures formed by anodisation of aluminium in sulphuric acid. *Thin Solid Films*. **2006**, 515, 338-345, DOI: 10.1016/j.tsf.2005.12.094.
- [70] A. Raid, S. Pavan, V. Fridrici, C. Poilane, and P. Kapsa. Temperature effect on the kinetic alumina layer growth on 5086 aluminum substrate. *Mechanika*. **2017**, 23, 923-930, DOI: 10.5755/j01.mech.23.6.16309.
- [71] F. Arango, M. Sepúlveda, S. Aguilar-Sierra, G. Ricaurte, and F. Echeverría, Interferometric colours produced by anodised aluminium diffraction grating, *Mater. Sci. Technol. (United Kingdom)*. **2020**, 36, 1238-1244, DOI: 10.1080/02670836.2020.1765477.
- [72] A. Takenaga, T. Kikuchi, S. Natsui, and R. O. Suzuki. Self-ordered aluminum anodizing in phosphonoacetic acid and its structural coloration. *ECS Solid State Lett.* **2015**, 4, P55-P58, DOI: 10.1149/2.0021508ssl.
- [73] A. Santos, V. S. Balderrama, M. Alba, P. Formenting, J. Ferre-Borrull, J. Pallares and L. F. Marsal. Nanoporous anodic alumina barcodes: Toward smart optical biosensors. *Adv. Mater.* **2012**, 24, 1050-1054, DOI: 10.1002/adma.201104490.
- [74] G. Macias, J. Ferré-Borrull, J. Pallarès, and L. F. Marsal. 1-D nanoporous anodic alumina rugate filters by means of small current variations for real-time sensing applications. *Nanoscale Res. Lett.* **2014**, 9, 1-6, DOI: 10.1186/1556-276X-9-315.

- [75] C. Sun, S. Hao, Z. Wang, Q. Xu, Y. Wang, Q. Peng and T. Lan. Rapid fabrication of iridescent alumina films supported on an aluminium substrate by high voltage anodization. *Opt. Mater. (Amst)*. **2020**, 104, 109937, DOI: 10.1016/j.optmat.2020.109937.
- [76] A. Santos, M. Alba, M. M. Rahman, P. Formentin, J. Ferre-Borrull, J. Pallares & L. F. Marsal. Structural tuning of photoluminescence in nanoporous anodic alumina by hard anodization in oxalic and malonic acids. *Nanoscale Res. Lett.* **2012**, 7, 1-11, DOI: 10.1186/1556-276X-7-228.
- [77] P. Ramana Reddy, K. M. Ajith, and N. K. Udayashankar. Effect of electrolyte concentration on morphological and photoluminescence properties of free standing porous anodic alumina membranes formed in oxalic acid. *Mater. Sci. Semicond. Process.* **2020**, 106, 104755, DOI: 10.1016/j.mssp.2019.104755.
- [78] S. Akiya, T. Kikuchi, S. Natsui, and R. O. Suzuki. Nanostructural characterization of large-scale porous alumina fabricated via anodizing in arsenic acid solution. *Appl. Surf. Sci.* **2017**, 403, 652-661, DOI: 10.1016/j.apsusc.2017.01.243.
- [79] K. Chernyakova, R. Karpicz, S. Zavadski, O. Poklonskaya, A. Jagminas, and I. Vrublevsky. Structural and fluorescence characterization of anodic alumina/carbon composites formed in tartaric acid solution. *J. Lumin.* **2017**, 182, 233-239, DOI: 10.1016/j.jlumin.2016.10.026.
- [80] L. González-Rovira, L. González-Souto, P. J. Astola, C. Bravo-Benítez, and F. J. Botana, Assessment of the corrosion resistance of self-ordered anodic aluminum oxide (AAO) obtained in tartaric-sulfuric acid (TSA). *Surf. Coatings Technol.* **2020**, 399, 126131, DOI: 10.1016/j.surfcoat.2020.126131.
- [81] L. Zajączkowska, D. Siemiaszko, and M. Norek. Towards Self-Organized Anodization of Aluminum in Malic Acid Solutions—New Aspects of Anodization in the Organic Acid. *Materials (Basel)*. **2020**, 13, 3899, DOI: 10.3390/ma13173899.
- [82] E. O. Gordeeva, I. V. Roslyakov, and K. S. Napolskii. Aluminium anodizing in selenic acid: electrochemical behaviour, porous structure, and ordering regimes. *Electrochim. Acta.* **2019**, 307, 13-19, DOI: 10.1016/j.electacta.2019.03.098.
- [83] A. I. Sadykov, S. E. Kushnir, I. V. Roslyakov, A. E. Baranchikov, and K. S. Napolskii. Selenic acid anodizing of aluminium for preparation of 1D photonic crystals. *Electrochem. commun.* **2019**, 100, 104-107, DOI: 10.1016/j.elecom.2019.01.027.
- [84] S. Z. Chu, K. Wada, S. Inoue, M. Isogai, and A. Yasumori. Fabrication of ideally ordered nanoporous alumina films and integrated alumina nanotubule arrays by high-field anodization. *Adv. Mater.* **2005**, 17, 2115-2119, DOI: 10.1002/adma.200500401.
- [85] T. Kikuchi, O. Nishinaga, S. Natsui, and R. O. Suzuki. Self-ordering behavior of anodic porous alumina via selenic acid anodizing. *Electrochim. Acta.* **2014**, 728-735, DOI: 10.1016/j.electacta.2014.06.078.
- [86] M. Pashchanka and J. J. Schneider. Formation of Porous Anodic Alumina under Unstable Electroconvection Flow Regimes: A Case Study of Tartronic Acid Electrolyte. *J. Phys. Chem. C.* **2017**, 121, 23683-23692, DOI: 10.1021/acs.jpcc.7b06157.
- [87] S. Ono, M. Saito, and H. Asoh. Self-ordering of anodic porous alumina formed in organic acid electrolytes. *Electrochim. Acta.* **2005**, 51, 827-833, DOI: 10.1016/j.electacta.2005.05.058.
- [88] B. Sun, J. Li, X. Jin, C. Zhou, Q. Hao, and X. Gao. Self-ordered hard anodization in malonic acid and its application in tailoring alumina taper-nanopores with continuously tunable periods in the range of 290-490 nm. *Electrochim. Acta.* **2013**, 112, 327-332, DOI: 10.1016/j.electacta.2013.08.147.

- [89] S. Akiya, T. Kikuchi, S. Natsui, N. Sakaguchi, and R. O. Suzuki. Self-ordered Porous Alumina Fabricated via Phosphonic Acid Anodizing. *Electrochim. Acta.* **2016**, 190, 471-479, DOI: 10.1016/j.electacta.2015.12.162.
- [90] S. Z. Chu, K. Wada, S. Inoue, M. Isogai, Y. Katsuta, and A. Yasumori. Large-Scale Fabrication of Ordered Nanoporous Alumina Films with Arbitrary Pore Intervals by Critical-Potential Anodization. *J. Electrochem. Soc.* **2006**, 153, B384, DOI: 10.1149/1.2218822.
- [91] H. Huang, J. Qiu, M. Sun, W. Liu, X. Wei, E. Sakai and K. Ito. A hard coating with MAO/AAO double layers prepared on aluminum in etidronic acid by DC oxidation. *Surf. Coatings Technol.* **2019**, 360, 307-317, DOI: 10.1016/j.surfcoat.2019.01.021.
- [92] A. Mozalev, I. Mozaleva, M. Sakairi, and H. Takahashi. Anodic film growth on Al layers and Ta-Al metal bilayers in citric acid electrolytes. *Electrochim. Acta.* **2005**, 50, 5065-5075, DOI: 10.1016/j.electacta.2005.02.092.
- [93] L. Zaraska, W. J. Stępniewski, E. Ciepiela, and G. D. Sulka. The effect of anodizing temperature on structural features and hexagonal arrangement of nanopores in alumina synthesized by two-step anodizing in oxalic acid. *Thin Solid Films.* **2013**, 534, 155-161, DOI: 10.1016/j.tsf.2013.02.056.
- [94] W. J. Stępniewski, A. Nowak-Stępniewska, A. Presz, T. Czujko, and R. A. Varin. The effects of time and temperature on the arrangement of anodic aluminum oxide nanopores. *Mater. Charact.* **2014**, 91, 1-9, DOI: 10.1016/j.matchar.2014.01.030.
- [95] K. Chernyakova, B. Tzaneva, I. Vrublevsky, and V. Videkov. Effect of Aluminum Anode Temperature on Growth Rate and Structure of Nanoporous Anodic Alumina. *J. Electrochem. Soc.* **2020**, 167, 103506, DOI: 10.1149/1945-7111/ab9d65.
- [96] P. M. Resende and M. Martín-González. Sub-10 nm porous alumina templates to produce sub-10 nm nanowires. *Microporous Mesoporous Mater.* **2019**, 284, 198-204, DOI: 10.1016/j.micromeso.2019.04.020.
- [97] L. Pla, E. Xifre-Perez, A. Ribes, E. Aznar, D. Marcos, L. F. Marsal, R. Martinez-Manez and F. Sancenon. A Mycoplasma Genomic DNA Probe using Gated Nanoporous Anodic Alumina. *Chempluschem.* **2017**, 82, 337-341, DOI: 10.1002/cplu.201600651.
- [98] H. Asoh, M. Matsumoto, and H. Hashimoto. Effects of ethanol on the efficiency of the formation of anodic alumina in sulfuric acid. *Surf. Coatings Technol.* **2019**, 378, 124947, DOI: 10.1016/j.surfcoat.2019.124947.
- [99] M. Michalska-Domańska, W. J. Stępniewski, and L. R. Jaroszewicz. Characterization of nanopores arrangement of anodic alumina layers synthesized on low-(AA1050) and high-purity aluminum by two-step anodizing in sulfuric acid with addition of ethylene glycol at low temperature. *J. Porous Mater.* **2017**, 24, 779-786, DOI: 10.1007/s10934-016-0316-7.
- [100] M. Norek, D. Zasada, and D. Siemiaszko. Systematic study on morphology of anodic alumina produced by hard anodization in the electrolytes modified with ethylene glycol. *J. Nano Res.* **2017**, 46, 165-178, DOI: 10.4028/www.scientific.net/JNanoR.46.165.
- [101] M. Farhan and A. Anawati. Effect of additive ethylene glycol on morphology and mechanical hardness of anodic oxide film formed on AA7075. *J. Phys. Conf. Ser.* **2019**, 1191, 012033, DOI: 10.1088/1742-6596/1191/1/012033.
- [102] M. Matsumoto, H. Hashimoto, and H. Asoh. Formation Efficiency of Anodic Porous Alumina in Sulfuric Acid Containing Alcohol: Comparison of the Effects of Monohydric and Polyhydric Alcohols as Additives. *J. Electrochem. Soc.* **2020**, 167, 041504, DOI: 10.1149/1945-7111/ab741c.
- [103] W. Chen, J. S. Wu, and X. H. Xia. Porous anodic alumina with continuously manipulated pore/cell size. *ACS Nano.* **2008**, 2, 959-965, DOI: 10.1021/nn700389j.

- [104] A. M. Abd-Elnaiem and M. Rashad. Morphology of anodic aluminum oxide anodized in a mixture of phosphoric acid and lithium phosphate monobasic. *Mater. Res. Express*. **2019**, 6, 016412, DOI: 10.1088/2053-1591/aae32d.
- [105] H. Maekawa, R. Tanaka, T. Sato, Y. Fujimaki, and T. Yamamura. Size-dependent ionic conductivity observed for ordered mesoporous alumina-LiI composite. *Solid State Ionics*. **2004**, 175, 281-285, DOI: 10.1016/j.ssi.2003.12.032.
- [106] A. Christoulaki, C. Moretti, A. Chennevière, E. Dubois, and N. Jouault. Improving structural features of nanoporous alumina using deuterated electrolytes. *Microporous Mesoporous Mater.* **2020**, 303, 110201, DOI: 10.1016/j.micromeso.2020.110201.
- [107] C. Lämmel, M. Schneider, C. Heubner, W. Beckert, and A. Michaelis. Investigations of burning phenomena during the hard anodising of aluminium by local in-operando temperature measurements. *Electrochim. Acta*. **2017**, 249, 271-277, DOI: 10.1016/j.electacta.2017.07.167.
- [108] M. Noormohammadi, Z. S. Arani, A. Ramazani, M. A. Kashi, and S. Abbasimofrad. Super-fast fabrication of self-ordered nanoporous anodic alumina membranes by ultra-hard anodization. *Electrochim. Acta*. **2020**, 354, 136766, DOI: 10.1016/j.electacta.2020.136766.
- [109] V. Vega, J. Garcia, J. M. Montero-Moreno, B. Hernando, J. Bachmann, V. M. Prida and K. Nielsch. Unveiling the Hard Anodization Regime of Aluminum: Insight into Nanopores Self-Organization and Growth Mechanism. *ACS Appl. Mater. Interfaces*. **2015**, 7, 28682-28692, DOI: 10.1021/acsami.5b10712.
- [110] I. V. Roslyakov, N. S. Kuratova, D. S. Koshkodaev, D. H. Merino, A. V. Lukashin, and K. S. Napolskii. Morphology of anodic alumina films obtained by hard anodization: Influence of the rate of anodization voltage increase. *J. Surf. Investig. X-ray, Synchrotron Neutron Tech.* **2016**, 10, 191-197, DOI: 10.1134/s1027451016010298.
- [111] I. V. Roslyakov, E. O. Gordeeva, and K. S. Napolskii. Role of Electrode Reaction Kinetics in Self-Ordering of Porous Anodic Alumina. *Electrochim. Acta*. **2017**, 241, 362-369, DOI: 10.1016/j.electacta.2017.04.140.
- [112] E. O. Gordeeva, I. V. Roslyakov, A. I. Sadykov, T. A. Suchkova, D. I. Petukhov, T. B. Shatalova & K. S. Napolskii. Formation Efficiency of Porous Oxide Films in Aluminum Anodizing. *Russ. J. Electrochem.* **2018**, 54, 990-998, DOI: 10.1134/S1023193518130165.
- [113] A. P. Leontiev, I. V. Roslyakov, and K. S. Napolskii. Complex influence of temperature on oxalic acid anodizing of aluminium. *Electrochim. Acta*. **2019**, 319, 88-94, DOI: 10.1016/j.electacta.2019.06.111.
- [114] Y. F. Mei, X. L. Wu, X. F. Shao, G. S. Huang, and G. G. Siu. Formation mechanism of alumina nanotube array. *Phys. Lett. Sect. A Gen. At. Solid State Phys.* **2003**, 309, 109-113, DOI: 10.1016/S0375-9601(03)00130-0.
- [115] M. Yu, H. Cui, F. Ai, L. Jiang, J. Kong, and X. Zhu. Terminated nanotubes: Evidence against the dissolution equilibrium theory. *Electrochem. commun.* **2018**, 86, 80-84, DOI: 10.1016/j.elecom.2017.11.025.
- [116] M. Yu, Y. Chen, C. Li, S. Yan, H. Cui, X. Zhu, J. Kong. Studies of oxide growth location on anodization of Al and Ti provide evidence against the field-assisted dissolution and field-assisted ejection theories. *Electrochem. commun.* **2018**, 87, 76-80, DOI: 10.1016/j.elecom.2018.01.003.
- [117] X. Yang, X. Zhu, H. Jia, and T. Han. Oxygen evolution: The mechanism of formation of porous anodic alumina. *Monatshefte fur Chemie*. **2009**, 140, 595-600, DOI: 10.1007/s00706-008-0098-y.

- [118] S. Zhao, K. Chan, A. Yelon, and T. Veres. Novel structure of AAO film fabricated by constant current anodization. *Adv. Mater.* **2007**, 19, 3004-3007, DOI: 10.1002/adma.200701284.
- [119] L. Pu, X. Bao, J. Zou, and D. Feng. Individual alumina nanotubes. *Angew. Chemie - Int. Ed.* **2001**, 40, 1490-1493, DOI: 10.1002/1521-3773(20010417)40:8<1340::AID-ANIE1340>3.0.CO;2-%23
- [120] S. Ono. Defects in Porous Anodic Films Formed on High Purity Aluminum. *J. Electrochem. Soc.* **1991**, 138, 3705, DOI: 10.1149/1.2085484.
- [121] L. Yi, L. Zhiyuan, C. Shuoshuo, H. Xing, and H. Xinhua. Novel AAO films and hollow nanostructures fabricated by ultra-high voltage hard anodization. *Chem. Commun.* **2010**, 46, 309-311, DOI: 10.1039/b914703a.
- [122] Y. Wang, A. Santos, A. Evdokiou, and D. Losic. Rational design of ultra-short anodic alumina nanotubes by short-time pulse anodization. *Electrochim. Acta.* **2015**, 154, 379-386, DOI: 10.1016/j.electacta.2014.12.056.
- [123] M. Norek, W. J. Stępniewski, and D. Siemiaszko. Effect of ethylene glycol on morphology of anodic alumina prepared in hard anodization. *J. Electroanal. Chem.* **2016**, 762, 20-28, DOI: 10.1016/j.jelechem.2015.12.026.
- [124] W. Lee, K. Schwirn, M. Steinhart, E. Pippel, R. Scholz, and U. Gösele. Structural engineering of nanoporous anodic aluminium oxide by pulse anodization of aluminium. *Nat. Nanotechnol.* **2008**, 3, 234-239, DOI: 10.1038/nnano.2008.54.
- [125] X. Zhu, L. Liu, Y. Song, H. Jia, H. Yu, X. Xiao & X. Yang. Oxygen bubble mould effect: Serrated nanopore formation and porous alumina growth. *Monatshefte für Chemie.* **2008**, 139, 999-1003, DOI: 10.1007/s00706-008-0893-5.
- [126] M. Yu, C. Li, Y. Yang, S. Xu, K. Zhang, H. Cui and X. Zhu. Cavities between the double walls of nanotubes: Evidence of oxygen evolution beneath an anion-contaminated layer. *Electrochem. commun.* **2018**, 90, 34-38, DOI: 10.1016/j.elecom.2018.03.009.
- [127] Z. Su and W. Zhou. Formation mechanism of porous anodic aluminium and titanium oxides. *Adv. Mater.* **2008**, 20, 3663-3667, DOI: 10.1002/adma.200800845.
- [128] W. Huang, H. Xu, Z. Ying, Y. Dan, Q. Zhou, J. Zhang, X. Zhu. Split TiO₂ nanotubes – Evidence of oxygen evolution during Ti anodization. *Electrochem. commun.* **2019**, 106, 106532, DOI: 10.1016/j.elecom.2019.106532.
- [129] X. Zhu, Y. Song, D. Yu, C. Zhang, and W. Yao. A novel nanostructure fabricated by an improved two-step anodizing technology. *Electrochem. commun.* **2013**, 29, 71-74, DOI: 10.1016/j.elecom.2013.01.018.
- [130] Y. Li, N. Peng, Y. Wen, and L. Liang. Effect of hydrothermal treatment on porous anodic alumina generated by one-step anodization. *Microporous Mesoporous Mater.* **2020**, 306, 110412, DOI: 10.1016/j.micromeso.2020.110412.
- [131] M. Krupinski, M. Perzanowski, A. Maximenko, Y. Zabala, and M. Marszałek. Fabrication of flexible highly ordered porous alumina templates by combined nanosphere lithography and anodization. *Nanotechnology.* **2017**, 28, 194003, DOI: 10.1088/1361-6528/aa68ac.
- [132] C. K. Chung, K. T. Tu, C. Y. Chang, and Y. C. Peng. Fabrication of thin-film spherical anodic alumina oxide templates using a superimposed nano-micro structure. *Surf. Coatings Technol.* **2019**, 361, 170-175, DOI: 10.1016/j.surfcoat.2019.01.032.
- [133] A. Bankova, V. Videkov, B. Tzaneva, and M. Mitov. Mechanical stability of heat-treated nanoporous anodic alumina subjected to repetitive mechanical deformation. *J. Phys. Conf. Ser.* **2018**, 992, 012055, DOI: 10.1088/1742-6596/992/1/012055.

- [134] R. Ozao, H. Yoshida, Y. Ichimura, T. Inada, and M. Ochiai. Crystallization of Anodic Alumina Membranes Studied by Simultaneous Tg-Dta / Ftir. *J. Therm. Anal.* **2001**, 64, 915-922, DOI: 10.1023/A:1011566811961.
- [135] R. Ozao, M. Ochiai, H. Yoshida, Y. Ichimura, and T. Inada. Preparation of γ -alumina membranes from sulphuric electrolyte anodic alumina and its transition to α -alumina. *J. Therm. Anal. Calorim.* **2001**, 64, 923-932, DOI: 10.1023/A:1011518929708.
- [136] L. F. Marsal, L. Vojkuvka, P. Formentin, J. Pallarés, and J. Ferré-Borrull. Fabrication and optical characterization of nanoporous alumina films annealed at different temperatures. *Opt. Mater. (Amst).* **2009**, 31, 860-864, DOI: 10.1016/j.optmat.2008.09.008.
- [137] L. Fernández-Romero, J. M. Montero-Moreno, E. Pellicer, F. Peiro, A. Cornet, J. R. Morante, M. Sarret, C. Muller. Assessment of the thermal stability of anodic alumina membranes at high temperatures. *Mater. Chem. Phys.* **2008**, 111, 542-547, DOI: 10.1016/j.matchemphys.2008.05.003.
- [138] I. V. Roslyakov, I. V. Kolesnik, E. E. Levin, N. S. Katorova, P. P. Pestrikov, T. Y. Kardash, L. A. Solovyov, K. S. Napolskii. Annealing induced structural and phase transitions in anodic aluminum oxide prepared in oxalic acid electrolyte. *Surf. Coatings Technol.* **2020**, 381, 125159, DOI: 10.1016/j.surfcoat.2019.125159.
- [139] J. N. M. Aman, J. K. Wied, Q. Alhusaini, S. Muller, K. Diehl, T. Staedler, H. Schonherr, X. Jiang and J.S. auf der Gunne. Thermal Hardening and Defects in Anodic Aluminum Oxide Obtained in Oxalic Acid: Implications for the Template Synthesis of Low-Dimensional Nanostructures. *ACS Appl. Nano Mater.* **2019**, 2, 1986-1994, DOI: 10.1021/acsanm.9b00018.
- [140] I. V. Roslyakov, N. A. Shirin, M. V. Berekchiian, T. B. Shatalova, A. V. Garshev, and K. S. Napolskii. Coarse-grain alpha-alumina films with highly ordered porous structure. *Microporous Mesoporous Mater.* **2020**, 294, 109840, DOI: 10.1016/j.micromeso.2019.109840.
- [141] G. D. Sulka and K. G. Parkoła. Temperature influence on well-ordered nanopore structures grown by anodization of aluminium in sulphuric acid. *Electrochim. Acta.* **2007**, 52, 1880-1888, DOI: 10.1016/j.electacta.2006.07.053.
- [142] W. Cheng, M. Steinhart, U. Gösele, and R. B. Wehrspohn. Tree-like alumina nanopores generated in a non-steady-state anodization. *J. Mater. Chem.* **2007**, 17, 3493-3495, DOI: 10.1039/b709618f.
- [143] J. M. Montero-Moreno, M. Belenguer, M. Sarret, and C. M. Müller. Production of alumina templates suitable for electrodeposition of nanostructures using stepped techniques. *Electrochim. Acta.* **2009**, 54, 2529-2535, DOI: 10.1016/j.electacta.2008.03.067.
- [144] W. Lee, R. Scholz, and U. Gösele. A continuous process for structurally well-defined Al₂O₃ nanotubes based on pulse anodization of aluminum. *Nano Lett.* **2008**, 8, 2155-2160, DOI: 10.1021/nl080280x.
- [145] W. Lee, J. C. Kim, and U. Cösele. Spontaneous current oscillations during hard anodization of aluminum under potentiostatic conditions. *Adv. Funct. Mater.* **2010**, 20, 21-27, DOI: 10.1002/adfm.200901213.
- [146] W. Lee and J. C. Kim. Highly ordered porous alumina with tailor-made pore structures fabricated by pulse anodization. *Nanotechnology.* **2010**, 21, 485304, DOI: 10.1088/0957-4484/21/48/485304.
- [147] Q. Peng, X. Xie, Q. Xu, T. Lan, C. Sun, L. Zhang and M. Dong. The effect of the current pulse amplitude on the nanopore structures of 3D-AAO films. *Microporous Mesoporous Mater.* **2020**, 309, 110575, DOI: 10.1016/j.micromeso.2020.110575.

- [148] L. K. Acosta, F. Bertó-Roselló, E. Xifre-Perez, A. Santos, J. Ferré-Borrull, and L. F. Marsal. Stacked Nanoporous Anodic Alumina Gradient-Index Filters with Tunable Multispectral Photonic Stopbands as Sensing Platforms. *ACS Appl. Mater. Interfaces*. **2019**, 11, 3360-3371, DOI: 10.1021/acsami.8b19411.
- [149] L. K. Acosta, F. Berto-Rosello, E. Xifre-Perez, C. S. Law, A. Santos, J. Ferre-Borrull and L. F. Marsal. Tunable Nanoporous Anodic Alumina Photonic Crystals by Gaussian Pulse Anodization. *ACS Appl. Mater. Interfaces*. **2020**, 12, 19778-19787, DOI: 10.1021/acsami.9b23354.
- [150] S. Y. Lim, C. S. Law, L. Jiang, L. K. Acosta, A. Bachhuka, L. F. Marsal, A. D. Abell and A. Santos. Enhancing Forbidden Light Propagation in Nanoporous Anodic Alumina Gradient-Index Filters by Alcohol Additives. *ACS Appl. Nano Mater.* **2020**, 3, 12155-12129, DOI: 10.1021/acsanm.0c02615.
- [151] K. Schwirn, W. Lee, R. Hillebrand, M. Steinhart, K. Nielsch, and U. Gösele. Self-ordered anodic aluminum oxide formed by H₂SO₄ hard anodization. *ACS Nano*. **2008**, 2, 302-310, DOI: 10.1021/nn7001322.
- [152] Z. L. Xiao, C. Y. Han, U. Welp, H. H. Wang, W. K. Kwok, G. A. Willing, J. M. Hiller, R. E. Cook, D. J. Miller and G. W. Crabtree. Fabrication of Alumina Nanotubes and Nanowires by Etching Porous Alumina Membranes. *Nano Lett.* **2002**, 2, 1293-1297, DOI: 10.1021/nl025758q.
- [153] L. Qu, C. He, Y. Yang, Y. He, and Z. Liu. Hydrothermal synthesis of alumina nanotubes templated by anionic surfactant. *Mater. Lett.* **2005**, 59, 4034-4037, DOI: 10.1016/j.matlet.2005.07.059.
- [154] B. Tang, J. Ge, L. Zhuo, G. Wang, J. Niu, Z. Shi, Y. Dong. A facile and controllable synthesis of γ -Al₂O₃ nanostructures without a surfactant. *Eur. J. Inorg. Chem.* **2005**, 1, 4366-4369, DOI: 10.1002/ejic.200500159.
- [155] C. C. Wang, C. C. Kei, Y. W. Yu, and T. P. Perng. Organic nanowire-templated fabrication of alumina nanotubes by atomic layer deposition. *Nano Lett.* **2007**, 7, 1566-1569, DOI: 10.1021/nl070404q.
- [156] K. Lee, H. Kim, J. H. Kim, and D. Choi. Structural color and near-infrared tunability of ruthenium-coated anodic aluminum oxide by atomic layer deposition. *Scr. Mater.* **2020**, 187, 125-129, DOI: 10.1016/j.scriptamat.2020.06.007.
- [157] T. Peng, H. Yang, K. Dai, K. Nakanishi, and K. Hirao. Sol-gel template synthesis of aluminum oxide microtubules. *Adv. Eng. Mater.* **2004**, 6, 241-244, DOI: 10.1002/adem.200300573.
- [158] Y. Zhang, J. Liu, R. He, Q. Zhang, X. Zhang, and J. Zhu. Synthesis of alumina nanotubes using carbon nanotubes as templates. *Chem. Phys. Lett.* **2002**, 360, 579-584, DOI: 10.1016/S0009-2614(02)00874-6.
- [159] A. S. Esmaeily, S. Mills, and J. M. D. Coey. Exceptional room-temperature plasticity in amorphous alumina nanotubes fabricated by magnetic hard anodisation. *Nanoscale*. **2017**, 9, 5205-5211, DOI: 10.1039/c7nr00095b.
- [160] Y. Wang, G. Kaur, A. Zysk, V. Liapis, S. Hay, A. Santos, D. Losic, A. Evdokiou. Systematic invitro nanotoxicity study on anodic alumina nanotubes with engineered aspect ratio: Understanding nanotoxicity by a nanomaterial model. *Biomaterials*. **2015**, 46, 117-130, DOI: 10.1016/j.biomaterials.2014.12.008.
- [161] Y. Wang, A. Santos, G. Kaur, A. Evdokiou, and D. Losic. Structurally engineered anodic alumina nanotubes as nano-carriers for delivery of anticancer therapeutics. *Biomaterials*. **2014**, 35, 5517-5526, DOI: 10.1016/j.biomaterials.2014.03.059.

- [162] Y. Wang, G. Kaur, Y. Chen, A. Santos, D. Losic, and A. Evdokiou. Bioinert Anodic Alumina Nanotubes for Targeting of Endoplasmic Reticulum Stress and Autophagic Signaling: A Combinatorial Nanotube-Based Drug Delivery System for Enhancing Cancer Therapy. *ACS Appl. Mater. Interfaces*. **2015**, 7, 49, 27140-27151, DOI: 10.1021/acsami.5b07557.
- [163] Y. Wang, I. Zinonos, A. Zysk, V. Panagopoulos, G. Kaur, A. Santos, D. Losic and A. Evdokiou. In vivo toxicological assessment of electrochemically engineered anodic alumina nanotubes: a study of biodistribution, subcutaneous implantation and intravenous injection. *J. Mater. Chem. B*. **2017**, 5, 2511-2523, DOI: 10.1039/C7TB00222J.
- [164] J. T. Domagalski, E. Xifre-Perez, A. Santos, J. Ferré-Borrull, and L. F. Marsal, "Tailor-engineered structural and physico-chemical properties of anodic alumina nanotubes by pulse anodization: A step forward," *Microporous Mesoporous Mater.*, vol. 303, 2020, doi: 10.1016/j.micromeso.2020.110264.
- [165] J. T. Domagalski, E. Xifre-Perez, M. A. Tabrizi, J. Ferré-Borrull, and L. F. Marsal. Magnetic nanoparticle decorated anodic alumina nanotubes for fluorescent detection of cathepsin B. *J. Colloid Interface Sci*. **2021**, 584, 236-245, DOI: 10.1016/j.jcis.2020.09.109.
- [166] E. Xifre-Perez, S. Guaita-Esteruelas, M. Baranowska, J. Pallares, L. Masana, and L. F. Marsal. In Vitro Biocompatibility of Surface-Modified Porous Alumina Particles for HepG2 Tumor Cells: Toward Early Diagnosis and Targeted Treatment. *ACS Appl. Mater. Interfaces*. **2015**, 7, 18600-18608, DOI: 10.1021/acsami.5b05016.
- [167] E. Xifre-Perez, J. Ferré-Borrull, J. Pallarès, and L. F. Marsal. Micro- and nanoparticles of mesoporous anodic alumina: Morphological and physicochemical properties. *Microporous Mesoporous Mater*. **2017**, 239, 363-370, DOI: 10.1016/j.micromeso.2016.10.034.
- [168] Y. Chen, A. Santos, Y. Wang, T. Kumeria, J. Li, C. Wang and D. Losic. Biomimetic Nanoporous Anodic Alumina Distributed Bragg Reflectors in the Form of Films and Microsized Particles for Sensing Applications. *ACS Appl. Mater. Interfaces*. **2015**, 7, 19816-19824, DOI: 10.1021/acsami.5b05904.
- [169] T. Kondo, N. Kitagishi, T. Fukushima, T. Yanagishita, and H. Masuda. Fabrication of aluminum nanowires by mechanical deformation of Al using anodic porous alumina molds. *Mater. Express*. **2016**, 6, 363-366, DOI: 10.1166/mex.2016.1316.
- [170] T. Yanagishita, M. Imaizumi, T. Kondo, and H. Masuda. Formation of porous Al particles by anisotropic anodic etching. *Electrochem. commun*. **2017**, 78, 26-28, DOI: 10.1016/j.elecom.2017.03.019.
- [171] T. Yanagishita, M. Imaizumi, T. Kondo, and H. Masuda. Preparation of nanoporous alumina hollow spheres with a highly ordered hole arrangement. *RSC Adv*. **2018**, 8, 2041-4047, DOI: 10.1039/c7ra12340j.
- [172] J. G. Croissant, Y. Fatieiev, A. Almalik, and N. M. Khashab. Mesoporous Silica and Organosilica Nanoparticles: Physical Chemistry, Biosafety, Delivery Strategies, and Biomedical Applications. *Adv. Healthc. Mater*. **2018**, 7, 1-75, DOI: 10.1002/adhm.201700831.
- [173] A. Santos, P. Formentín, J. Pallarès, J. Ferré-Borrull, and L. F. Marsal. Structural engineering of nanoporous anodic alumina funnels with high aspect ratio. *J. Electroanal. Chem*. **2011**, 655, 73-78, DOI: 10.1016/j.jelechem.2011.02.005.
- [174] A. Santos, T. Kumeria, Y. Wang, and D. Losic. In situ monitored engineering of inverted nanoporous anodic alumina funnels: On the precise generation of 3D optical nanostructures. *Nanoscale*. **2014**, 6, 9991, 9999, DOI: 10.1039/c4nr01422g.
- [175] M. Porta-i-Batalla, E. Xifré-Pérez, C. Eckstein, J. Ferré-Borrull, and L. Marsal. 3D Nanoporous Anodic Alumina Structures for Sustained Drug Release. *Nanomaterials*. **2017**, 7, 227, DOI: 10.3390/nano7080227.

- [176] J. Liao. Formation of Bottle-Shaped Pores with Petaloid Shoulder within Anodic Alumina. *Surf. Eng. Appl. Electrochem.* **2018**, 54, 555-561, DOI: 10.3103/S106837551806008X.
- [177] L. Sacco, I. Florea, and C. S. Cojocar. Fabrication of porous anodic alumina (PAA) templates with straight pores and with hierarchical structures through exponential voltage decrease technique. *Surf. Coatings Technol.* **2018**, 364, 248-255, DOI: 10.1016/j.surfcoat.2019.02.086.
- [178] C. Y. Liu and S. Biring. Nanoplatfom based on ideally ordered arrays of short straight and long beer bottle-shaped nanochannels. *Microporous Mesoporous Mater.* **2019**, 287, 71-76, DOI: 10.1016/j.micromeso.2019.05.056.
- [179] S. Jin, Y. Li, Z. X. Li, X. Hu, Z. Y. Ling, X. H. He, Y. H. Shen and L. Jin. Controllable Fabrication and Microstructure Modulation of Unique AAO Structures Based on Patterned Aluminum Surface. *J. Electrochem. Soc.* **2016**, 163, H1053-H1059, DOI: 10.1149/2.0261613jes.
- [180] Y. Ma, Y. Wen, J. Li, C. Feng, Z. Zhang, T. Gou, J. Huang, J. Lu, Z. Cui and R. Sun. Fabrication of alumina with ordered tapered-nanopore nested in micro-bowl hierarchical structure by a combined anodization. *Mater. Chem. Phys.* **2020**, 239, 122023, DOI: 10.1016/j.matchemphys.2019.122023.
- [181] J. Martín, M. Martín-González, J. Francisco Fernández, and O. Caballero-Calero. Ordered three-dimensional interconnected nanoarchitectures in anodic porous alumina. *Nat. Commun.* **2014**, 5, 1-9, DOI: 10.1038/ncomms6130.
- [182] B. Abad, J. Maiz, A. Ruiz-Clavijo, O. Caballero-Calero, and M. Martin-Gonzalez. Tailoring thermal conductivity via three-dimensional porous alumina. *Sci. Rep.* **2016**, 6, 1-10, DOI: 10.1038/srep38595.
- [183] A. Ruiz-Clavijo, S. Ruiz-Gomez, O. Caballero-Calero, L. Perez, and M. Martin-Gonzalez. Tailoring Magnetic Anisotropy at Will in 3D Interconnected Nanowire Networks. *Phys. Status Solidi - Rapid Res. Lett.* **2019**, 13, 1-7, DOI: 10.1002/pssr.201900263.
- [184] A. Ruiz-Clavijo, Y. Tsurimaki, O. Caballero-Calero, G. Ni, G. Chen, S. V. Boriskina and M. Martin-Gonzalez. Engineering a Full Gamut of Structural Colors in All-Dielectric Mesoporous Network Metamaterials. *ACS Photonics.* **2018**, 5, 2120-2128, DOI: 10.1021/acsp Photonics.7b01569.
- [185] P. M. Resende, R. Sanz, O. Caballero-Calero, and M. Martín-González. Cost-Effective, Flexible, Hydrophobic, and Tunable Structural Color Polymeric Bragg Reflector Metastructures. *Adv. Opt. Mater.* **2018**, 6, 1-7, DOI: 10.1002/adom.201800408.
- [186] A. Santos, T. Kumeria, and D. Losic. Nanoporous anodic alumina: A versatile platform for optical biosensors. *Materials (Basel).* **2014**, 7, 4297-4320, DOI: 10.3390/ma7064297.
- [187] E. Yablonovitch. Inhibited Spontaneous Emission in Solid-State Physics and Electronics. *Phys. Rev. Lett.* **1987**, 58, 2059-2062, DOI: 10.1049/cp.2012.0663.
- [188] S. John. Strong localization of photons in certain disordered dielectric superlattices. *Phys. Rev. Lett.* **1987**, 58, 2486-2489, DOI: 10.1103/PhysRevLett.58.2486.
- [189] C. Lopez. Materials Aspects of Photonic Crystals. *Adv. Mater.* **2003**, 15, 1679-1704, DOI: 10.1002/adma.200300386.
- [190] L. M. M. Ferro, S. G. Lemos, M. Ferreira, and F. Trivinho-Strixino. Use of multivariate analysis on Fabry-Pérot interference spectra of nanoporous anodic alumina (NAA) for optical sensors purposes. *Sensors Actuators, B Chem.* **2017**, 248, 718-723, DOI: 10.1016/j.snb.2017.04.051.

- [191] C. S. Law, S. Y. Lim, L. Liu, A. D. Abell, L. F. Marsal, and A. Santos. Realization of high-quality optical nanoporous gradient-index filters by optimal combination of anodization conditions. *Nanoscale*. **2020**, 12, 9404-9415, DOI: 10.1039/c9nr10526c.
- [192] S. Y. Lim, C. S. Law, L. Liu, M. Markovic, A. D. Abell, and A. Santos. Integrating surface plasmon resonance and slow photon effects in nanoporous anodic alumina photonic crystals for photocatalysis. *Catal. Sci. Technol.* **2019**, 9, 3158-3176, DOI: 10.1039/c9cy00627c.
- [193] A. Santos, T. Pereira, C. S. Law, and D. Losic. Rational engineering of nanoporous anodic alumina optical bandpass filters. *Nanoscale*. **2016**, 8, 14846-14857, DOI: 10.1039/c6nr03490j.
- [194] C. S. Law, S. Y. Lim, A. D. Abell, and A. Santos. Real-Time Binding Monitoring between Human Blood Proteins and Heavy Metal Ions in Nanoporous Anodic Alumina Photonic Crystals. *Anal. Chem.* **2018**, 90, 10039-10048, DOI: 10.1021/acs.analchem.8b02732.
- [195] S. E. Kushnir, T. Y. Komarova, and K. S. Napolskii. High-quality-factor anodic alumina optical microcavities prepared by cyclic anodizing with voltage: Versus optical path length modulation. *J. Mater. Chem. C*. **2020**, 8, 3991-3995, DOI: 10.1039/c9tc07079f.
- [196] S. Y. Lim, C. S. Law, L. F. Marsal, and A. Santos. Engineering of hybrid nanoporous anodic alumina photonic crystals by heterogeneous pulse anodization. *Sci. Rep.* **2018**, 8, 1-16, DOI: 10.1038/s41598-018-27775-6.
- [197] M. Busch, A. V. Kityk, W. Piecek, T. Hofmann, D. Wallacher, S. Calus, P. Kula, M. Steinhart, M. Eich and P. Huber. A ferroelectric liquid crystal confined in cylindrical nanopores: Reversible smectic layer buckling, enhanced light rotation and extremely fast electro-optically active Goldstone excitations. *Nanoscale*. **2017**, 9, 19086-19099, DOI: 10.1039/c7nr07273b.
- [198] A. Yildirim, P. Szymoniak, K. Sentker, M. Butschies, A. Buhlmeyer, P. Huber, S. Laschat and A. Schönals. Dynamics and ionic conductivity of ionic liquid crystals forming a hexagonal columnar mesophase. *Phys. Chem. Chem. Phys.* **2018**, 20, 5626-5635, DOI: 10.1039/c7cp08186c.
- [199] A. Yildirim, K. Sentker, G. J. Smales, B. R. Pauw, P. Huber, and A. Schönals. Collective orientational order and phase behavior of a discotic liquid crystal under nanoscale confinement. *Nanoscale Adv.* **2019**, 1, 1104-1116, DOI: 10.1039/c8na00308d.
- [200] A. Yildirim, A. Buhlmeyer, S. Hayashi, J. C. Haenle, K. Sentker, C. Krause, P. Huber, S. Laschat and A. Schönals. Multiple glassy dynamics in dipole functionalized triphenylene-based discotic liquid crystals revealed by broadband dielectric spectroscopy and advanced calorimetry-assessment of the molecular origin. *Phys. Chem. Chem. Phys.* **2019**, 21, 18265-18277, DOI: 10.1039/c9cp03499d.
- [201] K. Sentker, A. Yildirim, M. Lippomann, A. W. Zantop, F. Bertram, T. Hofmann, O. H. Seeck, A. V. Kityk, M. G. Mazza, A. Schönals and P. Huber. Self-Assembly of liquid crystals in nanoporous solids for adaptive photonic metamaterials. *Nanoscale*. **2019**, 11, 23304-23317, DOI: 10.1039/c9nr07143a.
- [202] A. M. Ahmed and M. Shaban. Nanoporous chromium thin film for active detection of toxic heavy metals traces using surface-enhanced Raman spectroscopy. *Mater. Res. Express*. **2020**, 7, 015084, DOI: 10.1088/2053-1591/ab6b62.
- [203] U. Malinovskis, R. Poplausks, D. Ertis, K. Ramser, S. Tamulevicius, A. Tamuleviciene, Y. Gu and J. Prikulis. High-density plasmonic nanoparticle arrays deposited on nanoporous anodic alumina templates for optical sensor applications. *Nanomaterials*. **2019**, 9, 531, DOI: 10.3390/nano9040531.

- [204] Q. Hao, H. Huang, X. Fan, Y. Yin, J. Wang, W. Li, T. Qiu, L. Ma, P. K. Chu and O. G. Schmidt. Controlled Patterning of Plasmonic Dimers by Using an Ultrathin Nanoporous Alumina Membrane as a Shadow Mask. *ACS Appl. Mater. Interfaces*. **2017**, 9, 36199-36205, DOI: 10.1021/acsami.7b11428.
- [205] M. Aguilar-Pujol, R. Ramirez-Jimenez, E. Xifre-Perez, S. Cortijo-Campos, J. Bartolome, L. F. Marsal and A. de Andres. Supported ultra-thin alumina membranes with graphene as efficient interference enhanced raman scattering platforms for sensing. *Nanomaterials*. **2020**, 10, 1-11, DOI: 10.3390/nano10050830.
- [206] G. Rajeev, E. Xifre-Perez, B. Prieto Simon, A. J. Cowin, L. F. Marsal, and N. H. Voelcker. A label-free optical biosensor based on nanoporous anodic alumina for tumour necrosis factor-alpha detection in chronic wounds. *Sensors Actuators, B Chem*. **2018**, 257, 116-123, DOI: 10.1016/j.snb.2017.10.156.
- [207] S. Kaur, C. S. Law, N. H. Williamson, I. Kempson, A. Papat, T. Kumeria and A. Santos. Environmental Copper Sensor Based on Polyethylenimine-Functionalized Nanoporous Anodic Alumina Interferometers. *Anal. Chem*. **2019**, 91, 5011-5020, DOI: 10.1021/acs.analchem.8b04963.
- [208] L. Pol, C. Eckstein, L. K. Acosta, E. Xifré-Pérez, J. Ferré-Borrull, and L. F. Marsal. Real-time monitoring of biotinylated molecules detection dynamics in nanoporous anodic alumina for bio-sensing. *Nanomaterials*. **2019**, 9, 478, DOI: 10.3390/nano9030478.
- [209] L. Pla, S. Santiago-Felipe, M. A. Tormo-Mas, J. Peman, F. Sancenon, E. Aznar and R. Martinez-Manez. Aptamer-Capped nanoporous anodic alumina for Staphylococcus aureus detection. *Sensors Actuators, B Chem*. **2020**, 320, 128281, DOI: 10.1016/j.snb.2020.128281.
- [210] M. Amouzadeh Tabrizi, J. Ferré-Borrull, and L. F. Marsal. Highly sensitive remote biosensor for the determination of lead (II) ions by using nanoporous anodic alumina modified with DNAzyme. *Sensors Actuators, B Chem*. **2020**, 321, 128314, DOI: 10.1016/j.snb.2020.128314.
- [211] M. Amouzadeh Tabrizi, J. Ferré-Borrull, and L. F. Marsal. Remote biosensor for the determination of trypsin by using nanoporous anodic alumina as a three-dimensional nanostructured material. *Sci. Rep*. **2020**, 10, 1-10, DOI: 10.1038/s41598-020-59287-7.
- [212] M. Amouzadeh Tabrizi, J. Ferré-Borrull, and L. F. Marsal. Remote sensing of Salmonella-specific DNA fragment by using nanoporous alumina modified with the single-strand DNA probe. *Sensors Actuators, B Chem*. **2020**, 304, 127302, DOI: 10.1016/j.snb.2019.127302.
- [213] À. Ribes, E. Aznar, S. Santiago-Felipe, E. Xifre-Perez, M. A. Tormo-Mas, J. Peman, L. F. Marsal and R. Martinez-Manez. Selective and Sensitive Probe Based in Oligonucleotide-Capped Nanoporous Alumina for the Rapid Screening of Infection Produced by Candida albicans. *ACS Sensors*. **2019**, 4, 1291-1298, DOI: 10.1021/acssensors.9b00169.
- [214] G. J. Jeon, W. Y. Kim, H. Bin Shim, and H. C. Lee. Nanoporous Pirani sensor based on anodic aluminum oxide. *Appl. Phys. Lett*. **2016**, 109, 123505, DOI: 10.1063/1.4963183.
- [215] M. Hernández-Vélez. Nanowires and 1D arrays fabrication: An overview. *Thin Solid Films*. **2006**, 495, 51-63, DOI: 10.1016/j.tsf.2005.08.331.
- [216] S. Y. Lim, C. S. Law, F. Berto-Rosello, L. Liu, M. Markovic, J. Ferre-Borrull, A. D. Abell, N. H. Voelcker, L. F. Marsla and A. Santos. Tailor-engineered plasmonic single-lattices: harnessing localized surface plasmon resonances for visible-NIR light-enhanced photocatalysis. *Catal. Sci. Technol*. **2020**, 10, 3195-3211, DOI: 10.1039/c9cy02561h.
- [217] M. Hu, Z. Xing, Y. Cao, Z. Li, X. Yan, Z. Xiu, T. Zhao, S. Yang and W. Zhou. Ti³⁺ self-doped mesoporous black TiO₂/SiO₂/g-C₃N₄ sheets heterojunctions as remarkable visible-

- lightdriven photocatalysts. *Appl. Catal. B Environ.* **2018**, 226, 499-508, DOI: 10.1016/j.apcatb.2017.12.069.
- [218] A. S. Goncharova, K. S. Napolskii, O. V. Skryabina, V. S. Stolyarov, E. E. Levin, S. V. Egorov, A. A. Eliseev, Y. A. Kasumov, V. V. Ryazanov and Galina A. Tsirilina. Bismuth nanowires: Electrochemical fabrication, structural features, and transport properties. *Phys. Chem. Chem. Phys.* **2020**, 22, 14953-14964, DOI: 10.1039/d0cp01111h.
- [219] C. H. Lin, T. Y. Li, J. Zhang, Z. Y. Chiao, P. C. Wei, H. C. Fu, L. Hu, M. J. Yu, G. H. Ahmed, X. Guan et al. Designed growth and patterning of perovskite nanowires for lasing and wide color gamut phosphors with long-term stability. *Nano Energy.* **2020**, 73, 104801, DOI: 10.1016/j.nanoen.2020.104801.
- [220] A. Ganapathi, P. Swaminathan, and L. Neelakantan. Anodic Aluminum Oxide Template Assisted Synthesis of Copper Nanowires using a Galvanic Displacement Process for Electrochemical Denitrification. *ACS Appl. Nano Mater.* **2019**, 2, 5981-5988, DOI: 10.1021/acsnm.9b01409.
- [221] H. Li, L. Wu, H. Zhang, W. Dai, J. Hao, H. Wu, F. Ren and C. Liu. Self-Assembly of Carbon Black/AAO Templates on Nanoporous Si for Broadband Infrared Absorption. *ACS Appl. Mater. Interfaces.* **2020**, 12, 4081-4087, DOI: 10.1021/acsnm.9b19107.
- [222] H. Bayat, M. Raoufi, I. Zamrik, and H. Schönherr. Poly(diethylene glycol methylether methacrylate) Brush-Functionalized Anodic Alumina Nanopores: Curvature-Dependent Polymerization Kinetics and Nanopore Filling. *Langmuir.* **2020**, 36, 2663-2672, DOI: 10.1021/acs.langmuir.9b03700.
- [223] Y. Sanguansap, K. Karn-orachai, and R. Laocharoensuk. Tailor-made porous striped gold-silver nanowires for surface enhanced Raman scattering based trace detection of β -hydroxybutyric acid. *Appl. Surf. Sci.* **2020**, 500, 144049, DOI: 10.1016/j.apsusc.2019.144049.
- [224] M. Salaheldeen, M. Méndez, V. Vega, A. Fernández, and V. M. Prida. Tuning Nanohole Sizes in Ni Hexagonal Antidot Arrays: Large Perpendicular Magnetic Anisotropy for Spintronic Applications. *ACS Appl. Nano Mater.* **2019**, 2, 1866-1875, DOI: 10.1021/acsnm.8b02205.
- [225] J. Garcia, V. M. Prida, V. Vega, W. O. Rosa, R. Caballero-Flores, I. Iglesias and B. Hernando. 2D and 3D ordered arrays of Co magnetic nanowires. *J. Magn. Magn. Mater.* **2015**, 383, 88-93, DOI: 10.1016/j.jmmm.2014.10.165.
- [226] J. S. Riva, A. V. Juárez, S. E. Urreta, and L. M. Yudi. Catalytic properties of Fe-Pd ferromagnetic nanowires at liquid/liquid interfaces. *Electrochim. Acta.* **2019**, 2998, 379-288, DOI: 10.1016/j.electacta.2018.12.069.
- [227] L. Galdun, V. Vega, Z. Vargova, E. D. Barriga-Castro, C. Luna, R. Varga and V. M. Prida. Intermetallic Co₂FeIn Heusler Alloy Nanowires for Spintronics Applications. *ACS Appl. Nano Mater.* **2018**, 1, 7066-7074, DOI: 10.1021/acsnm.8b01836.
- [228] A. Rath and P. Theato. Advanced AAO Templating of Nanostructured Stimuli-Responsive Polymers: Hype or Hope?. *Adv. Funct. Mater.* **2020**, 30, 1-16, DOI: 10.1002/adfm.201902959.
- [229] A. Belwalkar, E. Grasing, W. Van Geertruyden, Z. Huang, and W. Z. Misiolek. Effect of processing parameters on pore structure and thickness of anodic aluminum oxide (AAO) tubular membranes. *J. Memb. Sci.* **2008**, 319, 192-198, DOI: 10.1016/j.memsci.2008.03.044.
- [230] X. Shi, A. Xiao, C. Zhang, and Y. Wang. Growing covalent organic frameworks on porous substrates for molecule-sieving membranes with pores tunable from ultra- to nanofiltration. *J. Memb. Sci.* **2019**, 576, 116-122, DOI: 10.1016/j.memsci.2019.01.034.

- [231] J. J. Schneider, J. Engstler, K. P. Budna, C. Teichert, and S. Franzka. Freestanding, highly flexible, large area, nanoporous alumina membranes with complete through-hole pore morphology. *Eur. J. Inorg. Chem.* **2005**, 12, 2352-2359, DOI: 10.1002/ejic.200401046.
- [232] T. Yanagishita, A. Kato, T. Kondo, and H. Masuda. Preparation of freestanding tubular alumina through-hole membranes by two-layer anodization. *Jpn. J. Appl. Phys.* **2020**, 59, 038002, DOI: 10.35848/1347-4065/ab7862.
- [233] B. Najma, A. K. Kasi, J. Khan Kasi, A. Akbar, S. M. A. Bokhari, and I. R. Stroe. ZnO/AAO photocatalytic membranes for efficient water disinfection: Synthesis, characterization and antibacterial assay. *Appl. Surf. Sci.* **2018**, 448, 104-114, DOI: 10.1016/j.apsusc.2018.04.063.
- [234] H. Aghili, B. Hashemi, M. E. Bahrololoom, and S. A. J. Jahromi. Fabrication and characterization of nanoporous anodic alumina membrane using commercial pure aluminium to remove Coliform bacteria from wastewater. *Process. Appl. Ceram.* **2019**, 13, 235-243, DOI: 10.2298/PAC1903235A.
- [235] M. Mohajeri, H. Akbarpour, and V. Karimkhani. Synthesis of highly ordered carbon nanotubes/nanoporous anodic alumina composite membrane and potential application in heavy metal ions removal from industrial wastewater. *Mater. Today Proc.* **2017**, 4, 4906-4911, DOI: 10.1016/j.matpr.2017.04.094.
- [236] A. Maghsodi, L. Adlnasab, M. Shabanian, and M. Javanbakht. Optimization of effective parameters in the synthesis of nanopore anodic aluminum oxide membrane and arsenic removal by prepared magnetic iron oxide nanoparticles in anodic aluminum oxide membrane via ultrasonic-hydrothermal method. *Ultrason. Sonochem.* **2018**, 48, 441-452, DOI: 10.1016/j.ultsonch.2018.07.003.
- [237] Y. Cai, D. Chen, N. Li, Q. Xu, H. Li, J. He and J. Lu. A smart membrane with antifouling capability and switchable oil wettability for high-efficiency oil/water emulsions separation. *J. Memb. Sci.* **2018**, 555, 69-77, DOI: 10.1016/j.memsci.2018.03.042.
- [238] I. S. Sadilov, D. I. Petukhov, and A. A. Eliseev. Enhancing gas separation efficiency by surface functionalization of nanoporous membranes. *Sep. Purif. Technol.* **2019**, 221, 74-82, DOI: 10.1016/j.seppur.2019.03.078.
- [239] D. I. Petukhov, E. A. Chernova, O. O. Kapitanova, O. V. Boytsova, R. G. Valeev. A. P. Chumakov, O. V. Konovalov and A. A. Eliseev. Thin graphene oxide membranes for gas dehumidification. *J. Memb. Sci.* **2019**, 577, 184-194, DOI: 10.1016/j.memsci.2019.01.041.
- [240] E. D. Han, C. W. Park, S. H. Lee, B. H. Kim, and Y. H. Seo. Polar molecule filtration using charged cellulose nanofiber membrane on the nanoporous alumina support for high rejection efficiency. *Cellulose.* **2020**, 27, 2685-2694, DOI: 10.1007/s10570-019-02928-6.
- [241] X. Sui, Z. Zhang, C. Li, L. Gao, Y. Zhao, L. Yang, L. Wen and L. Jiang. Engineered Nanochannel Membranes with Diode-like Behavior for Energy Conversion over a Wide pH Range. *ACS Appl. Mater. Interfaces.* **2019**, 11, 23815-23821, DOI: 10.1021/acsami.8b02578.
- [242] Q. Chen, Y. Wang, M. Zheng, H. Fang, and X. Meng. Nanostructures confined self-assembled in biomimetic nanochannels for enhancing the sensitivity of biological molecules response. *J. Mater. Sci. Mater. Electron.* **2018**, 29, 19757-19767, DOI: 10.1007/s10854-018-0101-2.
- [243] Z. Chen, S. Ni, S. Han, R. Crawford, S. Lu, F. Wei, J. Chang, C. Wu, Y. Xiao. Nanoporous microstructures mediate osteogenesis by modulating the osteo-immune response of macrophages. *Nanoscale.* **2017**, 9, 706-718, DOI: 10.1039/c6nr06421c.
- [244] L. Mi, J. Sui, Y. Wu, G. Liang, Y. Zhang, Y. Pu, Y. Tian, S. Liu and L. Jiang. Bioinspired in Vitro Lung Airway Model for Inflammatory Analysis via Hydrophobic Nanochannel

- Membrane with Joint Three-Phase Interface. *Anal. Chem.* **2019**, 91, 15804-15810, DOI: 10.1021/acs.analchem.9b04114.
- [245] A. de la Escosura-Muñiz, M. Espinoza-Castañeda, A. Chamorro-García, C. J. Rodríguez-Hernández, C. de Torres, and A. Merkoçi. In situ monitoring of PTHLH secretion in neuroblastoma cells cultured onto nanoporous membranes. *Biosens. Bioelectron.* **2018**, 107, 62-86, DOI: 10.1016/j.bios.2018.01.064.
- [246] S. Zhang, B. Ma, F. Liu, J. Duan, S. Wang, J. Qiu, D. Li, Y. Sang, C. Liu, D. Liu and H. Liu. Polylactic Acid Nanopillar Array-Driven Osteogenic Differentiation of Human Adipose-Derived Stem Cells Determined by Pillar Diameter. *Nano Lett.* **2018**, 18, 2243-2253, DOI: 10.1021/acs.nanolett.7b04747.
- [247] A. El Merhie, M. Salerno, C. Toccafondi, and S. Dante. Neuronal-like response of N2a living cells to nanoporous patterns of thin supported anodic alumina. *Colloids Surfaces B Biointerfaces.* **2019**, 178, 32-37, DOI: 10.1016/j.colsurfb.2019.02.038.
- [248] P. Formentín, Catalán, L. Pol, S. Fernández-Castillejo, R. Solà, and L. F. Marsal. Collagen and fibronectin surface modification of nanoporous anodic alumina and macroporous silicon for endothelial cell cultures. *J. Biol. Eng.* **2018**, 12, 1-9, DOI: 10.1186/s13036-018-0111-x.
- [249] S. Rahman, G. J. Atkins, D. M. Findlay, and D. Losic, "Nanoengineered drug releasing aluminium wire implants: A model study for localized bone therapy," *J. Mater. Chem. B*, vol. 3, no. 16, pp. 3288–3296, 2015, doi: 10.1039/c5tb00150a.
- [250] M. Sarraf, B. Nasiri-Tabrizi, A. Dabbagh, W. J. Basirun, and N. L. Sukiman. Optimized nanoporous alumina coating on AA3003-H14 aluminum alloy with enhanced tribo-corrosion performance in palm oil. *Ceram. Int.* **2020**, 46, 7306-7323, DOI: 10.1016/j.ceramint.2019.11.227.
- [251] M. Sundararajan, S. Subramani, M. Devarajan, and M. Jaafar. Synthesis and analysis of anodic aluminum oxide-nanopore structure on Al substrates for efficient thermal management in electronic packaging. *J. Mater. Sci. Mater. Electron.* **2020**, 31, 9641-9649, DOI: 10.1007/s10854-020-03507-3.
- [252] Y. Fu, J. Yang, Y. S. Su, W. Du, and Y. G. Ma. Daytime passive radiative cooler using porous alumina. *Sol. Energy Mater. Sol. Cells.* **2019**, 191, 50-54, DOI: 10.1016/j.solmat.2018.10.027.
- [253] D. Wu, D. Zhang, Y. Ye, L. Ma, B. Minhas, B. Liu, H. A. Terry, J. M. C. Mol and X. Li. Durable lubricant-infused anodic aluminum oxide surfaces with high-aspect-ratio nanochannels. *Chem. Eng. J.* **2019**, 368, 138-147, DOI: 10.1016/j.cej.2019.02.163.
- [254] D. I. Tishkevich, A. I. Vorobjova, D. I. Shimanovich, D. A. Vinnik, T. I. Zubar, A. I. Kozlovskiy, M. V. Zdorovets, D. V. Yakimchuk, S. V. Trukhanov and A. V. Trukhanov. Formation and corrosion properties of Ni-based composite material in the anodic alumina porous matrix. *J. Alloys Compd.* **2019**, 804, 139-146, DOI: 10.1016/j.jallcom.2019.07.001.

Chapter 3. AA Nanotubes Fabrication System and Characterization methods

3.1. Introduction

This chapter consist of a detailed description of the experimental set-up, the preparation process and techniques utilized in the fabrication of anodic alumina nanotubes.

First, arrangement of the “home-made” anodization setup will be explained. The anodization setup was designed in the Nephos group in a series of consecutive upgrades, that enabled to increase efficiency and the precision of the fabrication process [1]. Moreover, role of every component will be discussed. The combination of materials, devices and the software provide for a of cost-effective setup that enable to tailor-engineer various nanostructures such as membranes, optically responsive substrates, or nanoparticles.

Secondly, overview of the fabrication conditions (i.e. current/voltage, temperature, electrolyte) and their impact will be presented. Reasoning behind such assortment of the parameters is explained and discussed. Furthermore, description of the base material and its preparation until yielding the final product is provided.

3.2. Fabrication Setup

The electrochemical setup utilized in the fabrication of anodic alumina nanotubes and nanoporous anodic alumina – as demonstrated on figure 3.1 – can be divided into 3 major components:

- i) Computer
- ii) Power supply
- iii) Electrochemical cell

The computer communicates with the source equipped with two multimeters responsible for precise monitoring of the process. The output from the source is controlled via dedicated software (LabView, see Section 3.3) installed on the computer. Moreover, the computer receives feedback information as well – data provided by multimeters is recorded as a text file. Lifetime monitoring of the process is crucial as the current/voltage-time transient reflects behavior of the sample – exact stage of the growth, while total current charge consumed can be used to estimate thickness of the film. Potential applied at the electrodes enables the flow of the current between the electrodes, resulting in chemical changes on the anode made of aluminum. Initiated growth of the oxide results in a rapid surge of the anode resistivity that limits possible current flow – reflected by the current drop. Images that show the construction of the cell utilized in these experiments are provided in Section 3.2. Basically, it is a container filled with an electrolyte equipped with a stirrer, that provides for uniform electric conductivity and electrical connection between two electrodes.

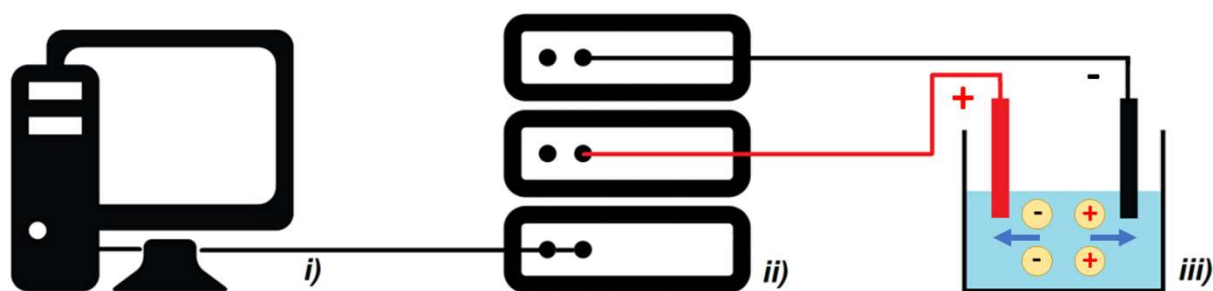


Figure 3.1. Schematic illustration of the anodization setup. i) Computer equipped with the software and directly connected with ii) the source and multimeters that pass electrical current through iii) the electrochemical cell.

Depending on various parameters (i.e. voltage, current, electrolyte, temperature) this setup can be utilized to obtain various structures. Constant current flow is convenient to prepare structures like membranes [2], while its variation enables to fabricate nanotubes [3] or structures capable of intrinsic interaction with light – highly valued photonic structures [4].

3.2.1. Electrochemical cell

The electrochemical cell is a part of the setup at which growth of the oxide nanostructure takes place physically. There are two major components of this device: the cell and the cooling system. An electrochemical cell used in aluminum anodization is made of few major elements:

- i) Anode (aluminum foil)
- ii) Cathode (platinum wire)
- iii) Electrolyte reservoir

Aforementioned parts are a must for to perform the anodization. However, development of the experimental cell resulted in a construction of more complex device, that enables more precise control of the parameters and promotes reproducibility. Components and the mounted setup used during experiments for this PhD thesis is shown on figure 3.2. Parts used to build the setup are as follows:

- | | | |
|------------------------------|-----------------------------|---------------------|
| 1) Upper part | 2) Base | 3) Cooling system |
| 1.1. Plastic case | 2.1. Plastic case | 3.1. Cooler |
| 1.2. Electric motor | 2.2. Rubber O-ring | 3.2. Cooling pad |
| 1.3. Rotor | 2.3. Aluminum wafer (anode) | 3.3. Cooling coil |
| 1.4. Platinum wire (cathode) | 2.4. Cooper plate | 3.4. Tubes |
| 1.5. Thermometer | 2.5. Screws | 3.5. Isolation foam |

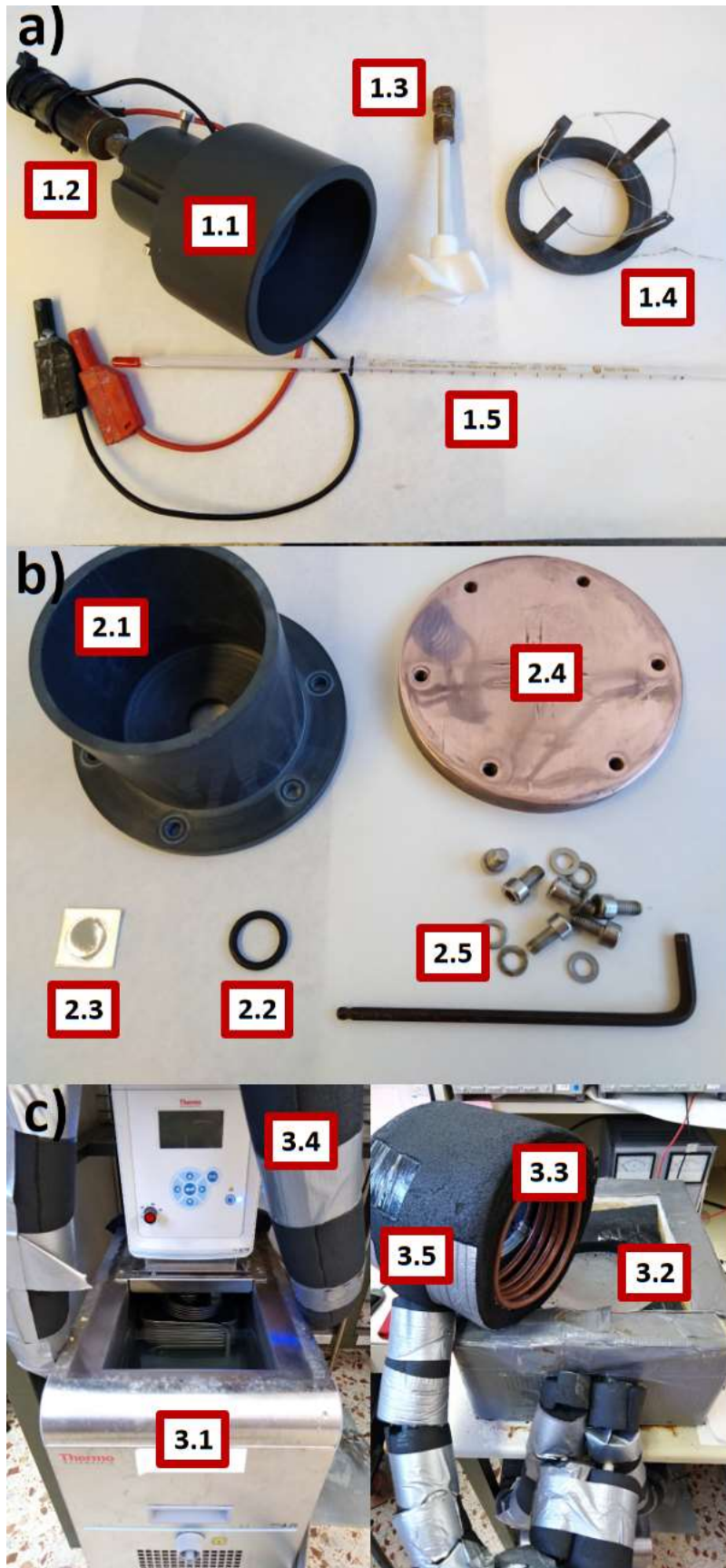


Figure 3.2. Photography of the electrochemical cell used to fabricate AAN, separated into individual components.
a) Upper part of the electrochemical cell.
b) Bottom part (base) of the electrochemical cell.
c) Cooling system used during experiments.

Body of the upper part consist of a molded plastic case to enable a few functional attachments. Drilled holes enable to mount a thermometer and a cathode. For this particular setup, platinum wire is attached to the separate plastic scaffold that fits to the inside of the upper part. The corrosion-resistant motor is attached to the body with two screws and can be removed for cleaning purpose (although fabricated to withstand exposure to acid solutions, longer exposition may incur formation of rust that glues motor to the case). Use of a Teflon stirrer is beneficial with regards to homogenous distribution of an electrolyte temperature, and to prevent any inconsistencies that could occur at the anode/electrolyte interface due to local ion depletion. Furthermore, the material enables long-lasting application due to chemical inertness.

The upper part is slightly broader than the bottom one, enabling to introduce it on the top of the bottom plastic part preventing movements of any element during anodization. Cooper plate serve as a thermally/electrically conductive base that is in a direct contact with a cooling surface and contains a plug for one connection from the source – anode. The plate is connected with an aluminum wafer that serves as an anode. Introduction of a rubber O-ring and plastic body of the cell enables to seal the bottom preventing any leakage from the cell – thus, there is no direct electrical contact between the cooper plate and the platinum cathode. It is possible due to force applied between the plastic case and the cooper plate with six screws.

While a cooling system is not mandatory in all circumstances, it significantly elevates the precision of the process, additionally enabling to conduct highly exothermic processes or adjust anodization current density through an electrolyte temperature. Some processes generate enormous amount of heat that – if not dispersed – could drastically affect geometry leading to structural defects and inhomogeneous growth rate. On the other hand, low temperatures (even below 0°C given for appropriate electrolyte composition) are beneficial to yield small pore diameters [5]. Design of the cooler was aimed at providing the best performance during the anodization. For that reason, cooling liquid (which temperature can be precisely controlled) is distributed with tubes isolated with the foam. While a basic version of the cooler was provided only with a cooling surface, this equipment has been provided with additional cooling coil that accelerates reaching temperature and its stability afterwards. Temperature variation affects the current flow and thus, regularity of the formed pores. The electrochemical cell has been designed with several principles: robustness, temperature stability, reproducibility, and accuracy. Figure 3.3 shows components of the electrochemical cell mounted together, prepared to start the anodization. In case of longer (i.e. possible temperature variations overnight) or exothermic processes cooling coil is applied as well.

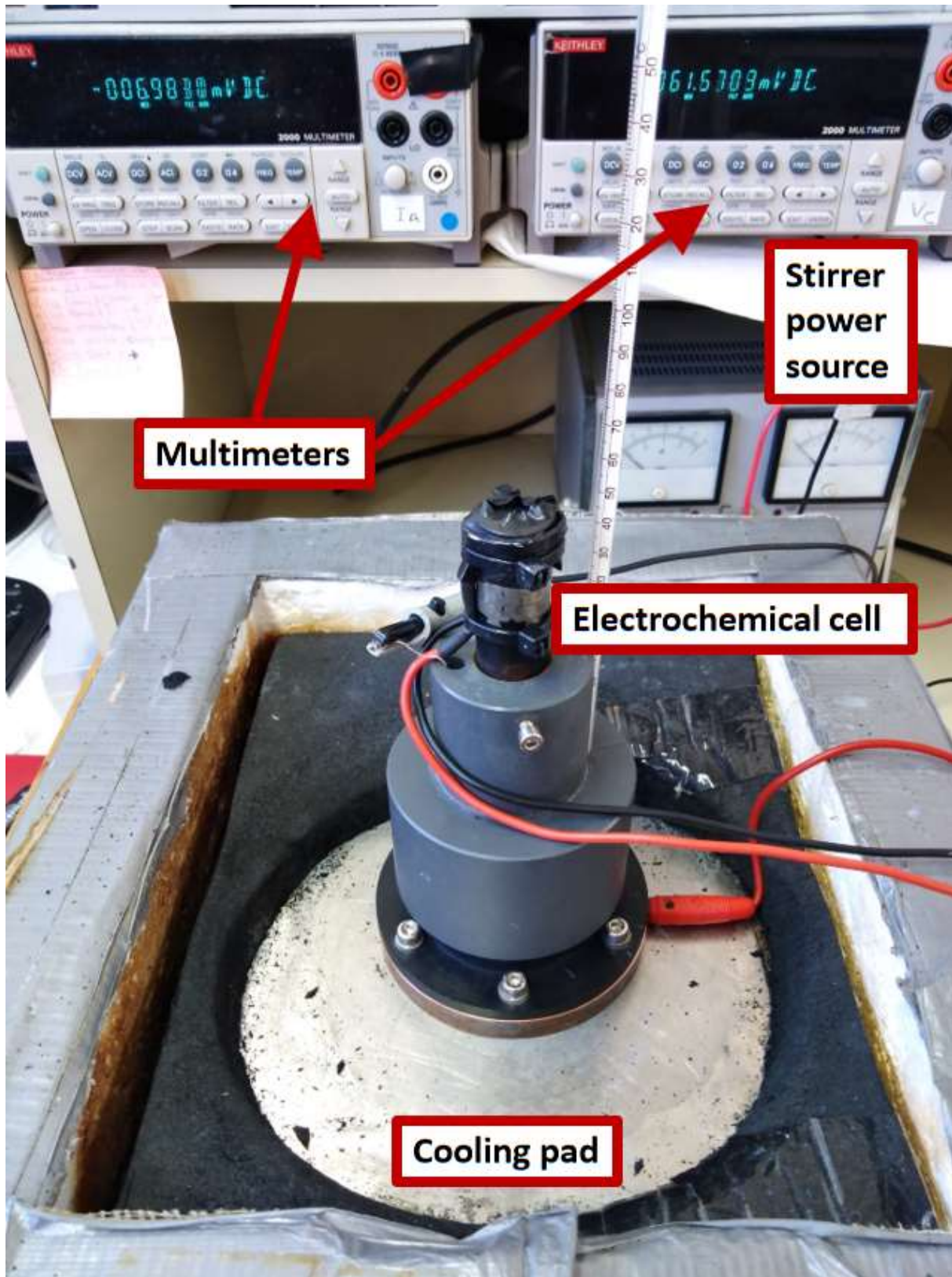


Figure 3.3. Photography of the electrochemical cell with all the components mounted – prepared to start the anodization.

3.2.2. Source for growth control

Precise control over the current/voltage output is crucial for the outcome of anodization. Furthermore, since an anodization profile provides valuable information about the status of the process, life monitoring is a necessity when reproducibility and accuracy are considered. The work of Montero-Rama et al. is a good demonstration of its utility [6]. Changes occurring in a sample can be estimated that way – in this case to partially open the barrier layer with the additional anodization step. Figure 3.4 shows the source (SM 300-5; DC power supply 0-300 V, 0-5 A 1500 W) and two multimeters (Agilent 34401A) used as a voltmeter and ammeter, that were used during fabrication of anodic alumina nanotubes. The source is controlled through the LabView program located on the computer – further explained in Section 3.5.

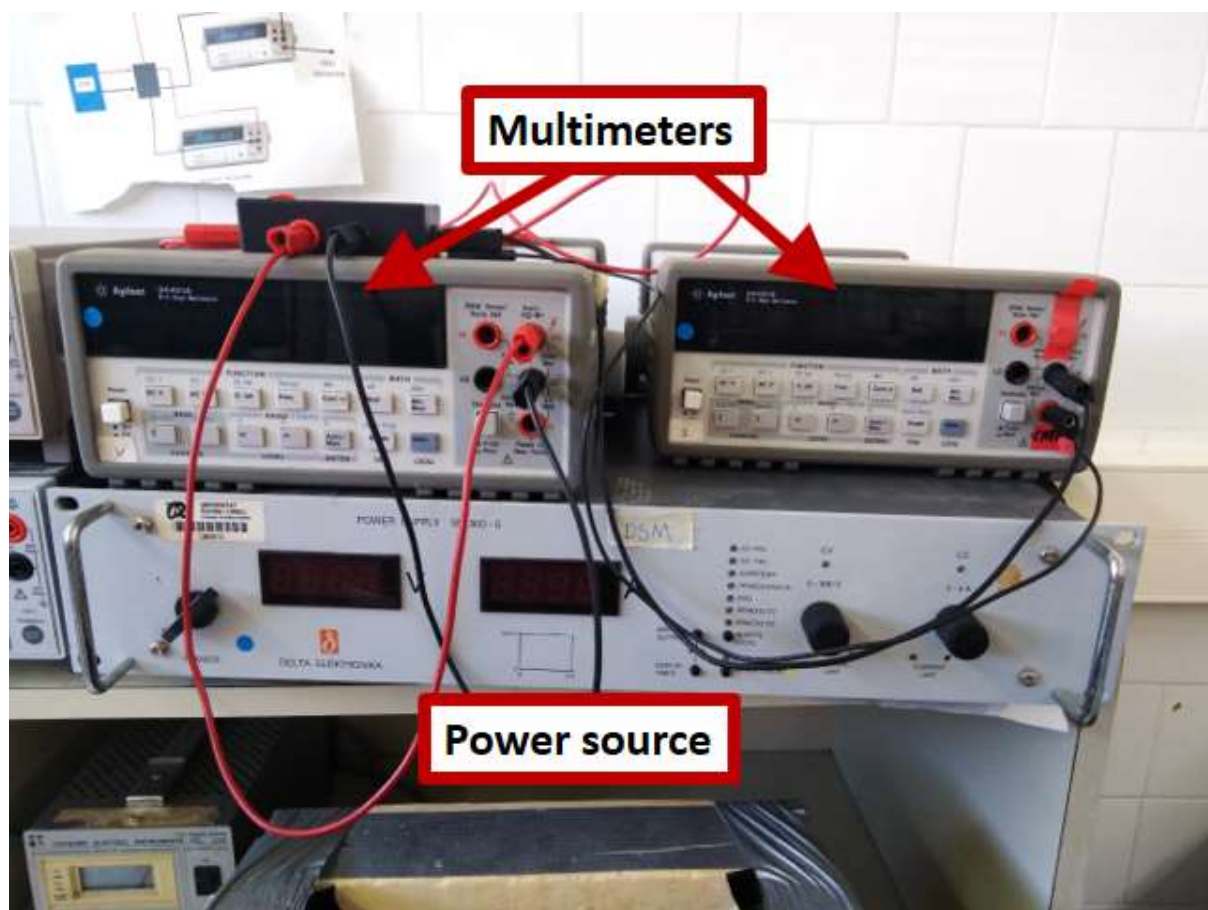


Figure 3.4. Photography of the power source and connected multimeters that serves as a power supply for the anodization setup.

For the electrochemical setup to be fully functional, devices need to be connected in a certain way. Connections that were made between devices are presented on the circuit diagram on figure 3.5. Detailed information about the software used to control the electrochemical setup is provided in Section 3.4.

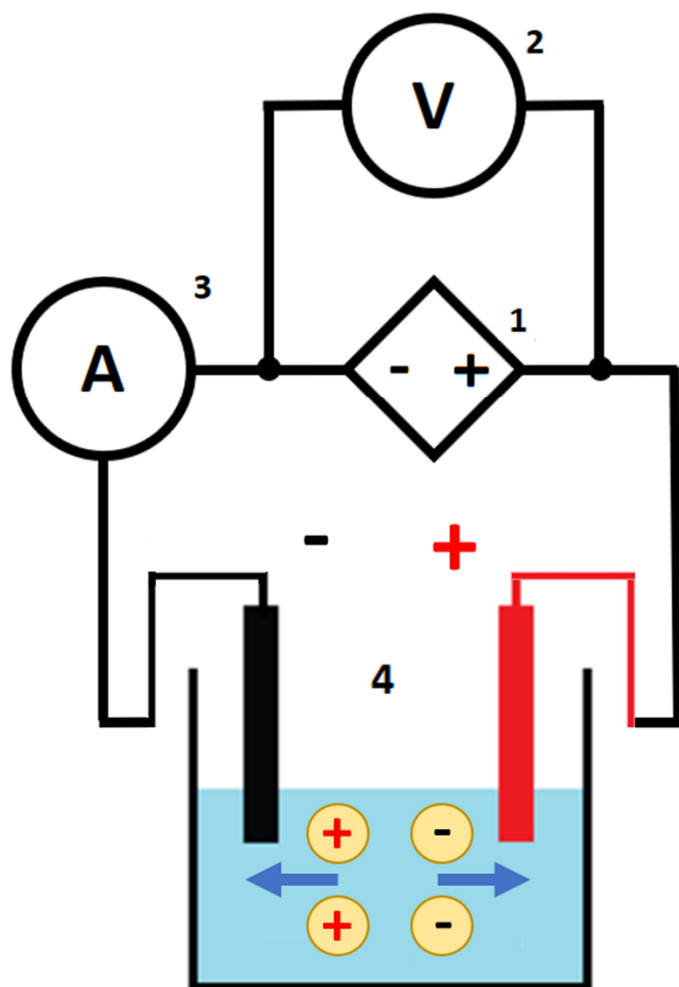


Figure 3.5. Circuit diagram of the anodization setup.
1) Power supply.
2) Voltmeter.
3) Ammeter.
4) Electrochemical cell.

3.2.2.1. Voltage control

Voltage control is the most common anodization mode utilized to fabricate nanoporous anodic alumina films. Stable temperature and constant potential enable producing long membranes with uniform pore diameter throughout the process, which is defined as potentiostatic mild anodization. During the AAN fabrication, voltage control serves two different objectives.

First, fabrication of the starting layer is a standard mild anodization process. During the first anodization step, voltage is set on a specific value corresponding to the self-ordering regime. It is a well-established dependence, that under specific potential values – unique for each electrolyte – regularity of the growing structure is the highest [7]. As can be seen on figure 3.6, after initial variation related to reaching reaction equilibrium potential remains constant during whole duration of the process. For purpose of this work 0.3 M H_2SO_4 electrolyte is used under 25 V, which corresponds to a cell size of 63 nm.

Specificity of the hard anodization with pulses is different, however. For that reason, process is mainly controlled through the current control – further explained in Section 3.3.2 – and the source provides potential required to deliver output induced by the software. For a major part

of the process, voltage oscillates between 40 and 70 V for low and high current pulse respectively. As the process continues, after long stable plateau increase of the voltage amplitude can be observed. While potential values during mild anodization pulse continue to decrease, high current anodization pulse is accompanied by a significant increase with each consecutive pulse. Usually, the process is interrupted when first symptoms of the voltage increase occurs – to provide reproducibility. Figure 3.6 shows the anodization profile reaching the burning point, where pulses reach the set limit of 100 V. Once the threshold has been reached, source cannot deliver required current – which can be observed by incomplete shape of current pulses at the end of the process. Intention of such maximum voltage limit is to prevent damage of the sample.

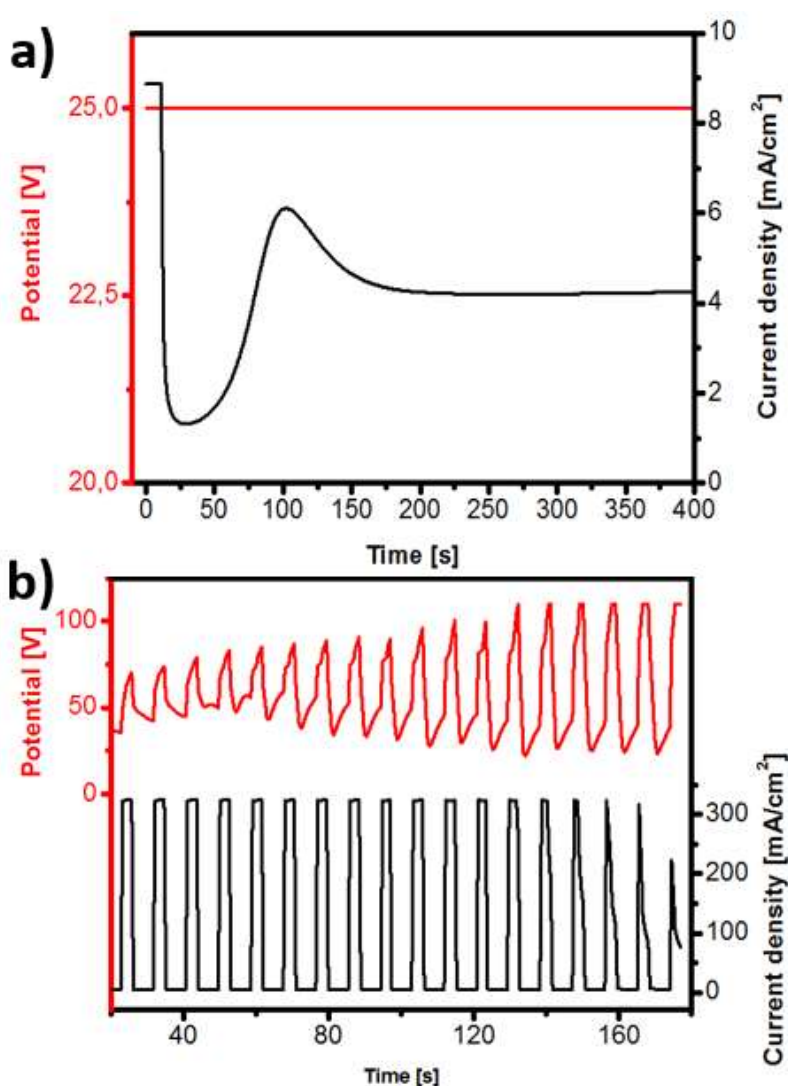


Figure 3.6. Current/voltage time transients of AAN fabrication process. a) Initial stage of potentiostatic mild anodization. b) Galvanostatic pulse anodization process reaching the set voltage limit.

3.2.2.2. Current control

Mechanism and growth behavior are different for hard anodization. Therefore, distinct set of conditions are needed to provide necessary accuracy. It has been experimentally demonstrated, that during potentiostatic anodization when high current densities are applied, current – thus growth speed – decreases over time making it nonlinear [8]. In depth analysis enabled conclusion that such conditions and corresponding rapid growth may lead to a local ion depletion. With longer pores, diffusion through the pores becomes limitation reflected in decrease of anodization current density. For that reason the process developed by the Lee et al. is conducted in galvanostatic conditions – allowing for more precise control of the nanotubes length [9]. Figure 3.7 shows magnified view on individual pulses while the process reaches quasi-stable plateau. With current control, the source provides potential value required to deliver the set current value, which resembles shape of a sail – with potential increase as a hard anodization pulse continues.

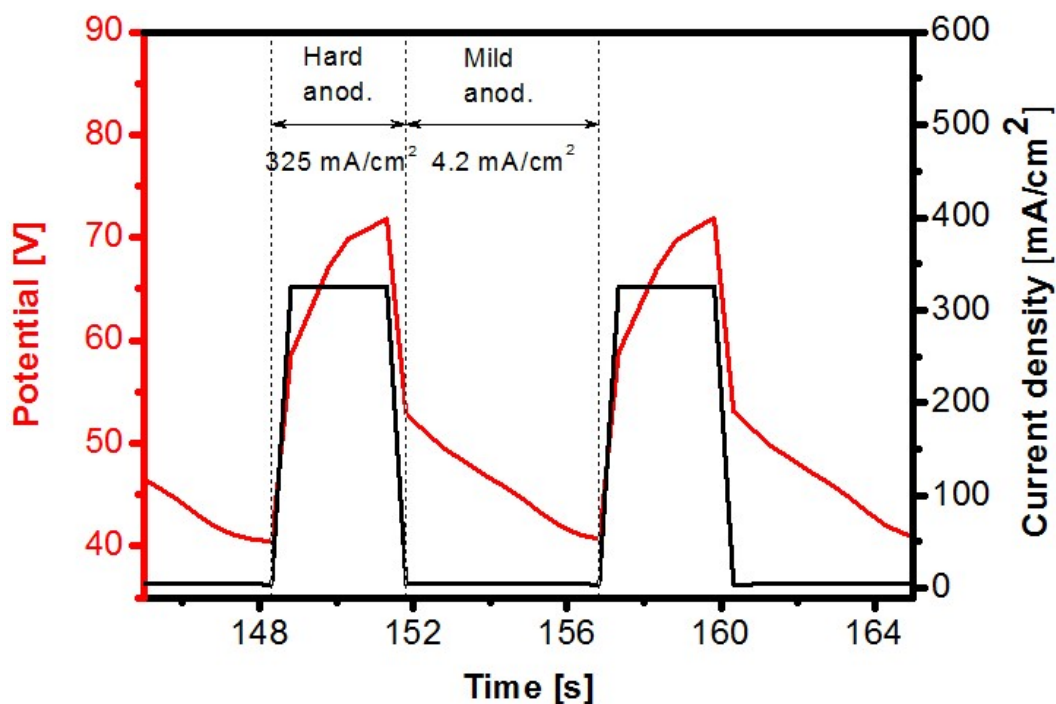


Figure 3.7. Current/voltage time transient of the galvanostatic pulse anodization, magnified view on individual current pulses.

3.2.3. Control Program

The source and thus, the outcome of the process is controlled by the software installed on the computer. For this purpose, application based on the LabVIEW environment has been utilized. Series of home-made programs enable to create complex potential and current profiles and define specific anodization parameters such as anodization time or total current charge. The program provides monitoring function as well. Figure 3.8 shows the program interface made to control the pulse anodization process. This particular program enables to define source output current and time duration for distinct parts of the process described as “pulses”, that interlace each other in cycles – amount of which can be defined as well. During the course of anodization, real source output of current and voltage are displayed in function of time enabling live monitoring of the process.

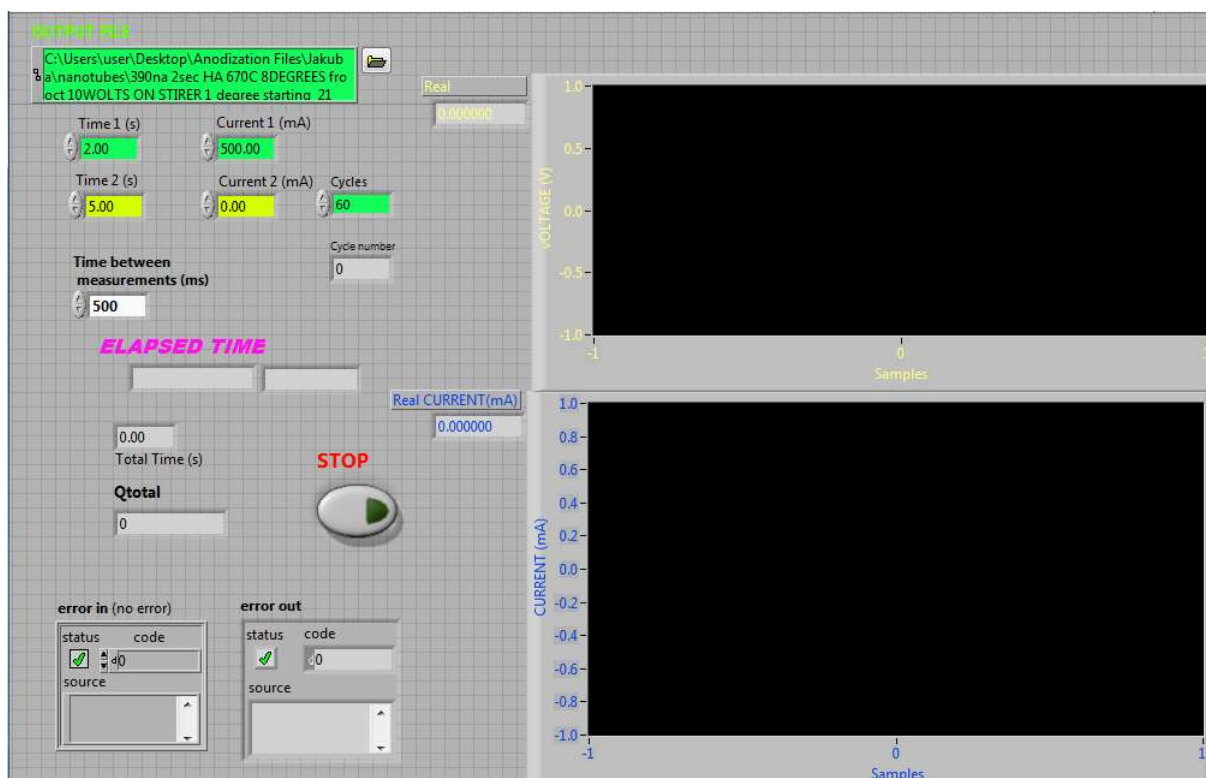


Figure 3.8. Screenshot of the anodization control program interface made in the LabView environment.

The computer with the software is connected with the source and multimeters through the high speed GPIB-USB controller (National Instruments).

3.3. Electrolytes

Electrolyte used during both anodization steps is a 0.3 M H₂SO₄ with 10% of EtOH aqueous solution. There are many reasons to introduce ethanol to the electrolyte. First of all, it enables

handling electrolyte at temperatures below the water freezing point, for example as in reported by Asoh et al. anodization carried out in -20°C that served as a mean to effectively reduce anodization current (and the growth speed as a consequence) [10]. Lower temperatures are also convenient to mitigate effects of the enormous heat generation during certain anodization processes – for example with phosphoric acid that occurs at high potential values. According to study carried out by Qin et al., addition of ethanol can affect the pore ordering and the growth rate during anodization, but not the pore diameter and interpore distance [11]. What is more, presence of ethanol affects the growth rate. With ethanol content increase to up to 10%, growth speed was reported to increase 5 times. Further increase resulted in lower growth speed and 50% content resulted in the slower growth than without ethanol – reflected in the observed current density. For the purpose of this PhD thesis, major motivation for using the same electrolyte in both steps was a simplicity. Furthermore, using electrolyte at temperatures below the water freezing point was convenient from the perspective of time needed to reach temperature of the anodization ($9-10^{\circ}\text{C}$ for the first step and 1°C for the pulse anodization), when other components of the electrochemical cells were at the ambient temperature. No study was performed to compare properties of nanotubes prepared with a starting layer made with and without ethanol. However, comparison of previous experimental studies indicates, that addition of ethanol is not mandatory during formation of the starting layer as nanotubes can be obtained in both cases [12], [13].

On the other hand, presence of ethanol is crucial during the pulse anodization to obtain anodic alumina nanotubes. Only when sufficient degree of pore separation occurs, nanotubes can be selectively etched and liberated through sonication. Usually, it occurs during high current anodization in sulfuric acid and is reflected by the formation of less dense structure at the cell boundaries. Such structure is less mechanically stable and more susceptible to acid etching [14]. The phenomenon has been attributed to mechanical stress that occurs when adjacent pores expand along with the generation of oxygen bubbles at the pore bottom during the growth. Study conducted by Wang et al. compares outcome of pulse anodization carried out with electrolyte containing 0-25% EtOH with regards to anodic alumina nanotubes formation [12]. During the pulse anodization in galvanostatic mode, specific voltage recovery can be observed. It was noticed, that in case of shorter pulses such recovery is not fully developed – as result the structure cannot be separated into nanotubes. Furthermore, such voltage recovery retardation is also dependent on the content of ethanol in the electrolyte. Authors suggest that this effect is related with the heat generation at the pore bottom and the oxygen generation promoted with the presence of ethanol that comes along with it. Quantity between 5 and 10% turned out to be the most effective – full voltage recovery pattern could be observed even for shorter pulses. However, when electrolyte with 20% ethanol was used, electric breakdown had occurred after several seconds restricting such electrolyte composition from any practical application with regards to AAN production. These findings were crucial to establish initial conditions for the nanotube's fabrication conducted in PhD project.

3.4. Preparation of Aluminum wafers

Aluminum foils used in this work were provided by Goodfellow Cambridge Ltd. All characteristics provided by the supplier has been gathered in Table 3.1.

Table 3.1. Technical characteristics of aluminum foil utilized for experiments in this PhD thesis

Feature	Information
Supplier	Goodfellow Cambridge Ltd
Product code	AL000650 (431-346-90)
Purity	99.999%
Impurities (ppm)	Cu 0.3
	Fe 0.3
	Mg 1.2
	Si 0.8
Size	300 x 300 x 0.5 mm
Temper	As rolled

At first, foil sheets were cut with paper cutter into 2 x 1.5 cm pieces that served as individual samples. The foil was supported on a flat surface with a paper to prevent any bending and surface scratches at this stage. Then, aluminum pieces were subjected to several preparation steps aimed at higher quality of the final material. Commercially available aluminum foils/wafers, while seemingly flat – contain many irregularities in microscale. This initial roughness affects regularity of the structure grown later during the anodization. With purpose to reduce this surface roughness, the electropolishing step is applied. At first, aluminum films are subjected to sonication in DI water and ethanol for 10 minutes each to remove impurities that can be present on the surface of aluminum. The preparation for electropolishing resembles succeeding anodization steps. Aluminum wafers are introduced to the electrochemical cell later filled with cold HClO_4 : EtOH (1:4) (v/v). The solution is stored in -20°C which facilitates its use: the process generates significant amount of heat that can decrease effectivity of the process or burn the sample. 20 V potential is applied for the total duration of 6-10 minutes and duration of stirring was changed every minute to prevent formation of uneven surface due to liquid flow. Every time the rotation direction is changed, current flowing through the sample change slightly, which can be observed on the electropolishing current time transient on figure 3.9. Such processing provides much smoother surface and enables to avoid uneven surface in macroscale, which is caused by continuous electrolyte flow in one direction. Visual outcome of electropolishing is demonstrated on figure 3.9.

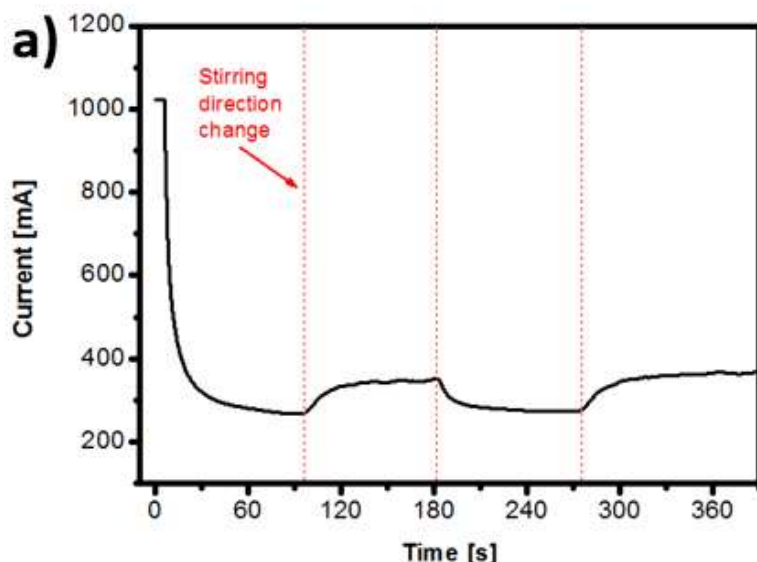
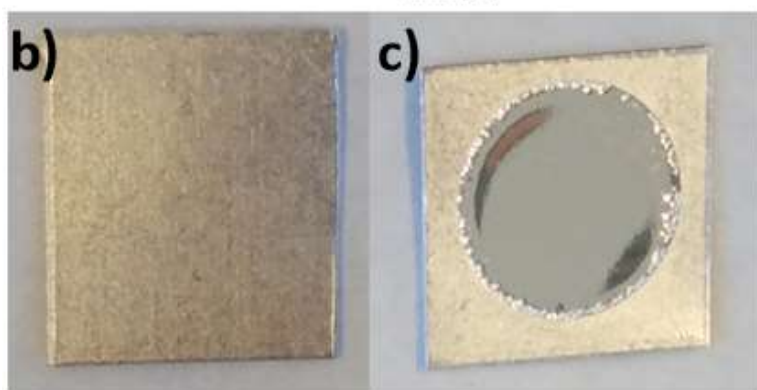


Figure 3.9. Course of the electropolishing process and its outcome.

a) Current time transient of the electropolishing process.

b) Commercially available aluminum foil without further processing.

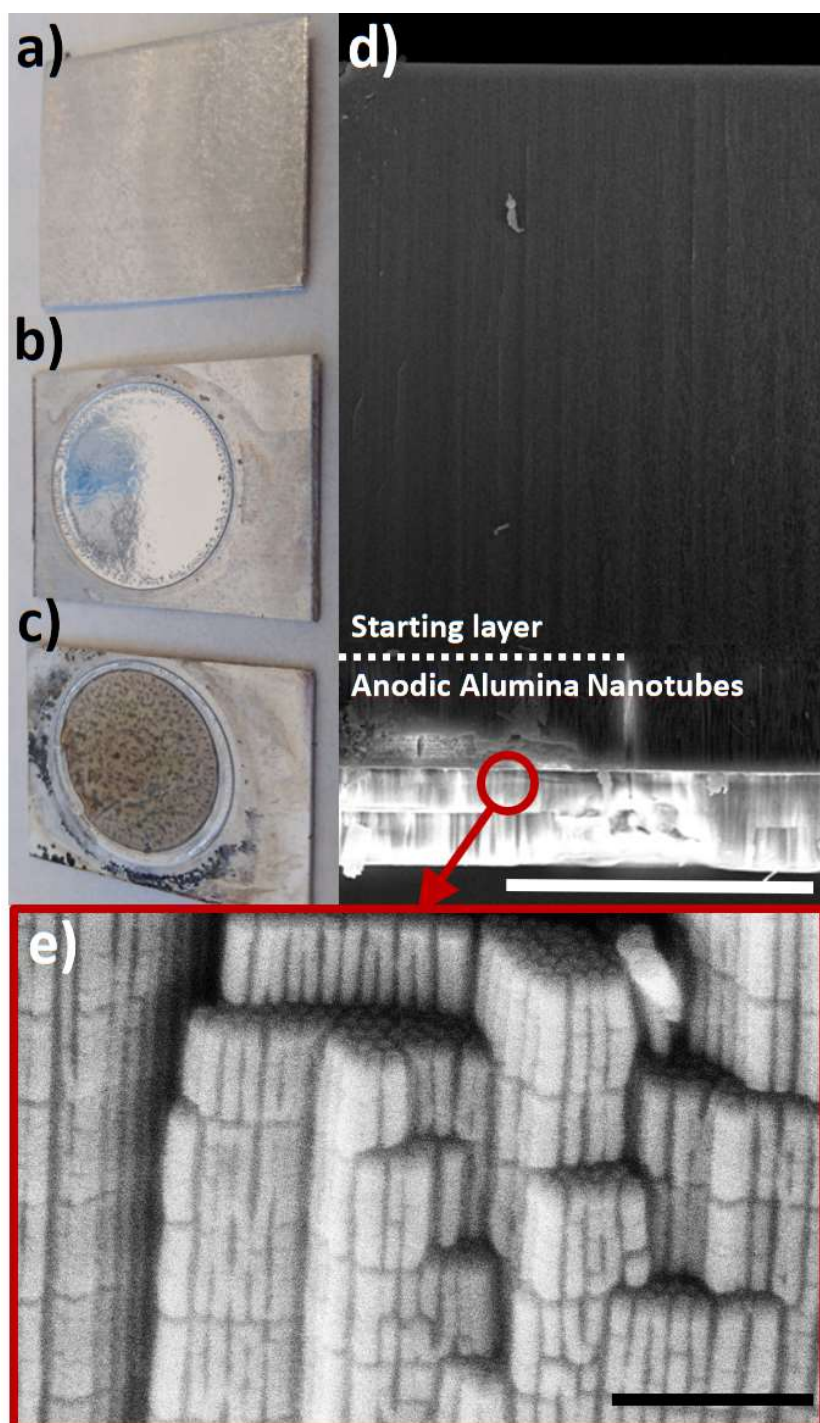
c) Aluminum foil after 6 minutes of electropolishing.



While not employed during this work, for applications in which long-range ordering regularity is crucial (i.e. sensors), annealing of the aluminum foil prior to electropolishing can be considered. Grain boundaries of aluminum present in the raw sample become domain boundaries in the formed NAA structure. Exposure to higher temperatures enables to homogenize the crystalline phase and increase the grain size. Chi et al. reports grain size of the NAA being twice the size when aluminum foil was annealed at 500°C for 1 h [15].

3.5. Fabrication Parameters

Fabrication of nanotubes involves several fabrication steps: preparation of the aluminum wafer, the mild anodization step, pulse anodization and post-processing. First, aluminum wafers are subjected to electropolishing (see Section 3.6). When the aluminum surface is prepared for anodization, mild anodization step in 0.3 M H₂SO₄ with 10% EtOH at 25 V and 8-10°C is performed for 20 hours. Purpose of this step is to produce the initial layer of the oxide of approx. 100 μm or more. It was observed by Wang et al., that in order to effectively liberate nanotubes, pulse anodization should be performed on a sample with a starting layer of the oxide [12]. First, preparation of starting layer is a common procedure before high current anodization in order to prevent electric breakdown. Moreover, thickness of this layer directly affects outer wall morphology of the structure grown during the pulse anodization. This difference is also reflected in the shape of the hard anodization profile – voltage amplitude during high current part is higher for thicker starting layer. It turns out, that with thin starting layer (33 μm) nanotubes could be produced applying 10 s pulse but liberation of nanotubes could not be observed for pulses of 2 s – effectively restricting fabrication of short nanotubes. For that reason, mild anodization step was adjusted to yield initial layer of approx. 110 μm. figure 3.10 shows how sample's appearance changes with consecutive anodization steps. Initial, protective layer of is highly transparent and colorless. It changes after pulse anodization: sample becomes opaquer and darker. Furthermore, scent of sulfur can be sensed from the sample after pulse anodization.



These two layers of the oxide film can be easily distinguished while observing sample under ESEM as demonstrated on figure 3.10. Structure grown during mild anodization is more regular and tightly packed – which can be concluded when compared to nanotube layer with visible bright spots. The sample morphology resembles already nanotubes, that are stacked together layer by layer (figure 3.10).

3.6. From AAN substrate to nanotubes

Appearance of the structure just after anodization processes and schematic definition of the nanotube geometry is shown on figure 3.11. To obtain liberated nanotubes in form of aqueous suspension, a few more processing steps are needed.

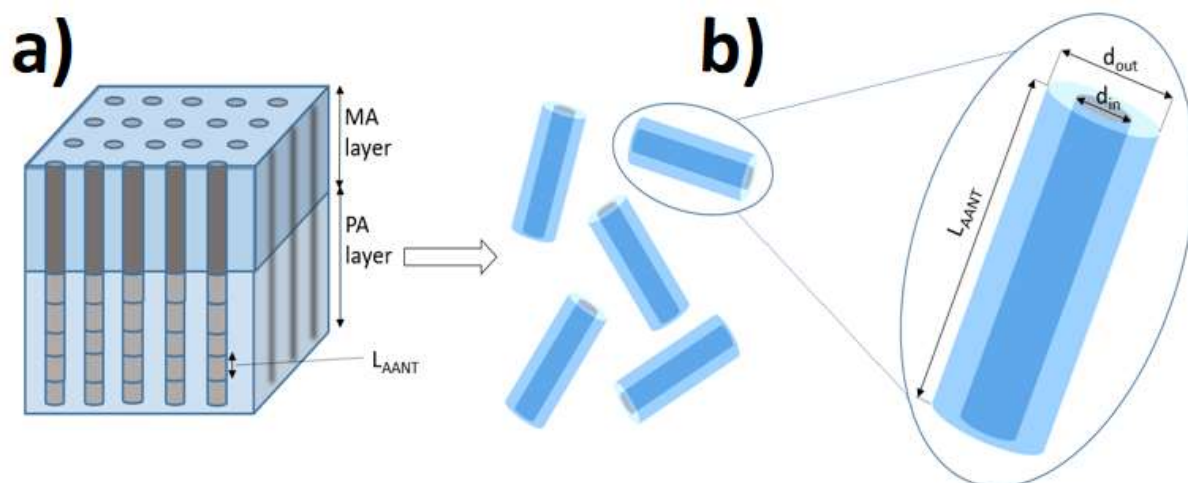


Figure 3.11. Schematics of AAN sample, from template to nanoparticles. a) Morphology of AAN film prior to separation into nanotubes b) Definition of geometrical features of the liberated nanotube.

First, remaining aluminum is removed by the selective etching using $\text{CuCl}_2 \times \text{HCl}$ solution. Sample is introduced into the bottom part of the electrochemical cell, this time with the oxide layer touching the copper plate – this enable to selectively remove aluminum only from below of the AAN substrate. While the film can be directly introduced to the acid solution, more acid is consumed, and cleaning of the sample is more difficult. Example of sample after such selective etching is shown on figure 3.12. In order to further weaken the junctions between cells (work of Wang et al. describes how the acid selectively removes the space in-between of the pores, while leaving the major part of the structure unaffected [12]), additional exposure to the acid for 30 minutes is performed. Then, film is dried and weighted – difference in weight before and after liberation of nanotubes is used to calculate concentration of the suspension. As shown on figure 3.12, AAN film is introduced to the thin glass bottle followed by introduction of 1-2 mL of deionized water. Then, the sample is sonicated using BANDELIN SONOREX ultrasonic bath (figure 3.12). The most optimal conditions for sonication are cold sonication (5-10°C) for 10-30 minutes. While sonication in ambient temperature for 30 minutes will not affect the morphology, water in the bath gets warmer overtime – which can lead to a complete degradation of the nanotube structural features. What is more, separation of tubes is more effective in low temperatures. Successful liberation of nanotubes can be concluded from opaqueness of the liquid – see figure 3.12.

After sonication, suspension of nanotubes is centrifuged at low velocity (4 k RCF, 15 minutes) using Thermo SCIENTIFIC ESPRESSO centrifuge (figure 3.12). Higher rotation speed results in difficult to separate clusters of nanotubes, while lower does not provide expected effectivity.

After centrifugation, nanotubes are resuspended in 0.1 M PBS $pH = 7.4$. This prevents aggregation of nanotubes greatly improving their stability – no visible changes to the nanotube morphology is observed even after several months of storage in ambient conditions – figure 3.13 shows TEM images nanotubes immediately following sonication and after 9 months of storage in the PBS solution.

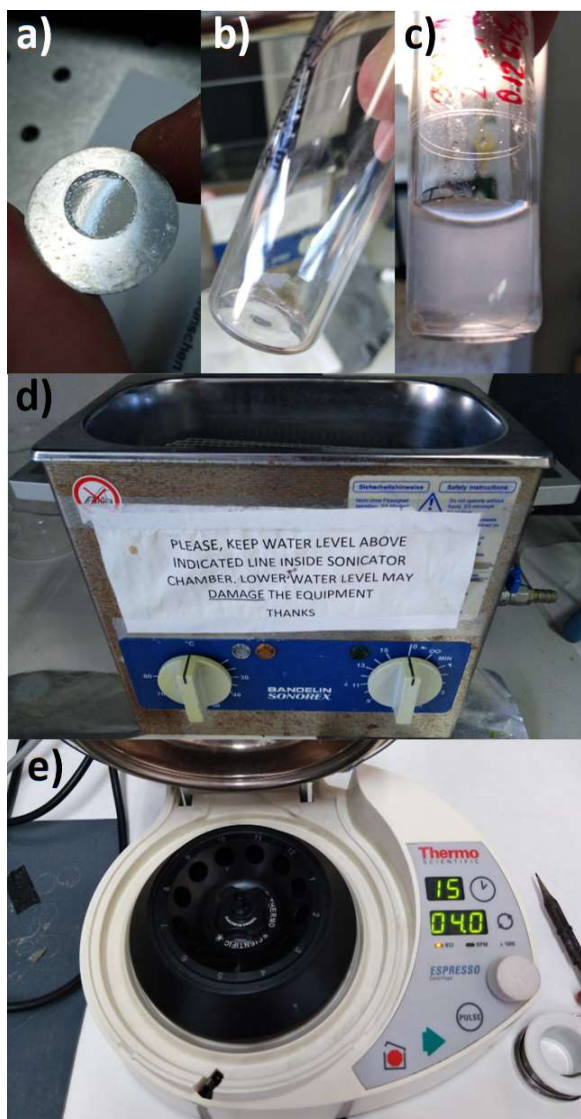
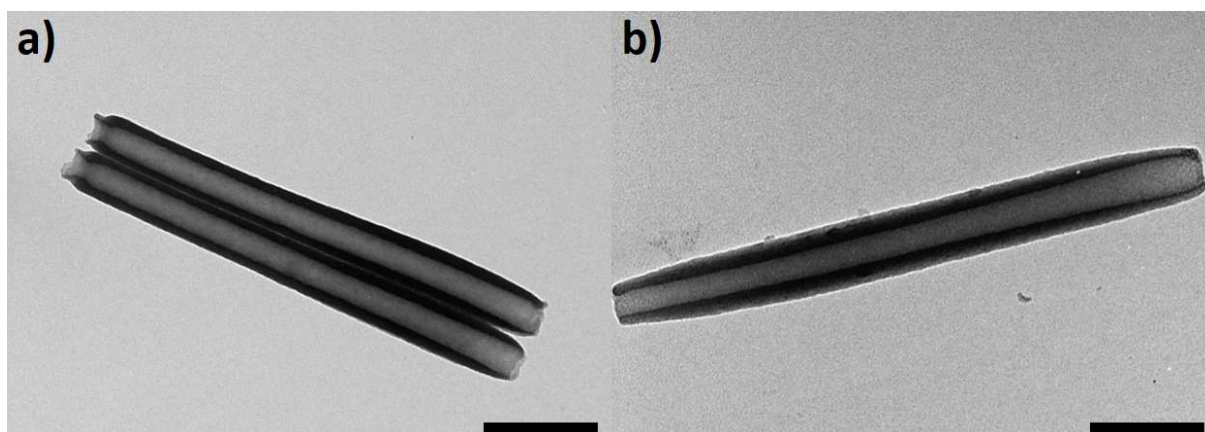


Figure 3.12 (left). Course of the AANTs preparation process and required equipment.

- a) Sample with selectively removed aluminum and visible alumina film in the middle.
- b) Flakes of the AAN film introduced to the glass vial – prior to sonication.
- c) Visible outcome of sonication: opaque suspension of AANTs.
- d) Ultrasonic bath used during liberation of AANTs.
- e) centrifuge used for precipitation of AANTs suspensions.

Figure 3.13 (below). TEM images of nanotubes suspended in 0.1 M PBS $pH = 7.4$.

- a) Nanotubes immediately after liberation from the substrate, scale bar: 200 nm.
- b) Nanotubes after 9 months of storage in a glass vial at ambient temperature and exposure to daylight, scale bar: 200 nm.



3.7. Characterization Techniques

This work involves fabrication, engineering and functionalization of nanomaterials. In order to analyze and follow changes occurring in the sample, detailed insight is required. While the size is of great benefit with regards to potential applications of nanomaterials – for the first time features as small as individual components of living organisms can be tailored – it is also a significant limitation concerning their analysis and development.

It is especially the case for microscopy techniques. In the majority of instances, light-based techniques have resolution limited by diffraction of light. The maximum resolution of standard optical microscope can be approximately a half of the light wavelength – which corresponds to around 200 nm. Although recently, new, disruptive possibilities have been discovered (rewarded with the Nobel prize in 2001 and 2014 [16], [17]), they are not yet commonly implemented, and features different restrictions of what can be measured. For that reason, the most common techniques employed to measure nanomaterials are based on electron interactions with a sample – de Broglie wavelength for electron is much shorter than for a photon, offering much higher precision of such microscopes. Additionally, specificity of interactions enables to unravel even more information as compared to photon-based techniques.

However, the use of electromagnetic radiation continues to be important mean to explore properties of the matter. Several diffractive and spectroscopic techniques are used in this work – involving radiation from a broad range of spectrum – and enable to understand the sample chemical composition, crystalline structure, and luminescence properties. Following section will elaborate on techniques used in this thesis.

3.7.1. Electron Microscopy

Electron microscopy is based on a similar principle as optical microscopy: a source of illumination passes through an optical aperture that shapes the beam. After interaction with a sample, particles are gathered by a detector. However, in order to reach higher resolution, accelerated electrons are used instead of photons. This enables much higher resolution. Instead of glass lenses used in standard microscope, electron microscope contain system of electrostatic lenses that can modulate the beam through manipulation of the electrostatic field [18].

After the electron beam touches the sample, it expands along with the penetration depth with a pear-shaped distribution of the electrons due to strong elastic scattering effects – as shown in figure 3.14 [19], [20]. Penetration depth is proportional to the electron energy and inversely proportional to the atomic mass of the material and can reach as deep as several micrometers below the surface. Due to the interaction of the electrons with matter's atoms and depending on the distance from the surface, several signals are emitted – these can be gathered by a detector. Excitation on the uppermost layer involving several layers of atoms (4-8 Å) and results in ejection of specimens without any energy loss: emission of the Auger electrons. They

are emitted due to relaxation to a lower energy state of ionized atoms. Auger electrons provide information about surface atomic composition. They require high vacuum – for that reason they are not usually measured in standard SEM techniques. In layer stretching to several nanometers, emission of secondary electrons (SE) takes place. They also originate from the sample's atoms – their emission is caused by inelastic interactions with the electron beam. They are useful to measure the topography of the sample. In deeper layers – up to dozens of nanometers – backscattered electrons (BSE) signal is generated. It originates from elastic collisions with electrons from the sample's atoms that change trajectory of electrons. The higher atomic mass of the atom is, the stronger the scattering effect is – which can be observed as brighter signal from such elements. This enables to differentiate the sample by the atomic number and phase differences. SE and BSE are the most commonly utilized source of signal in scanning electron microscopy. The electron beam reaching further (up to few micrometers) provides another useful signal: the emission of X-ray radiation. The electrons can decelerate in the Coulombic field of the sample's atoms, the occurring energy loss can be emitted as a photon. Energy of the X-ray photon is specific to the element of the origin, which enables using the technique to conduct quantitative elemental analysis of the sample [18].

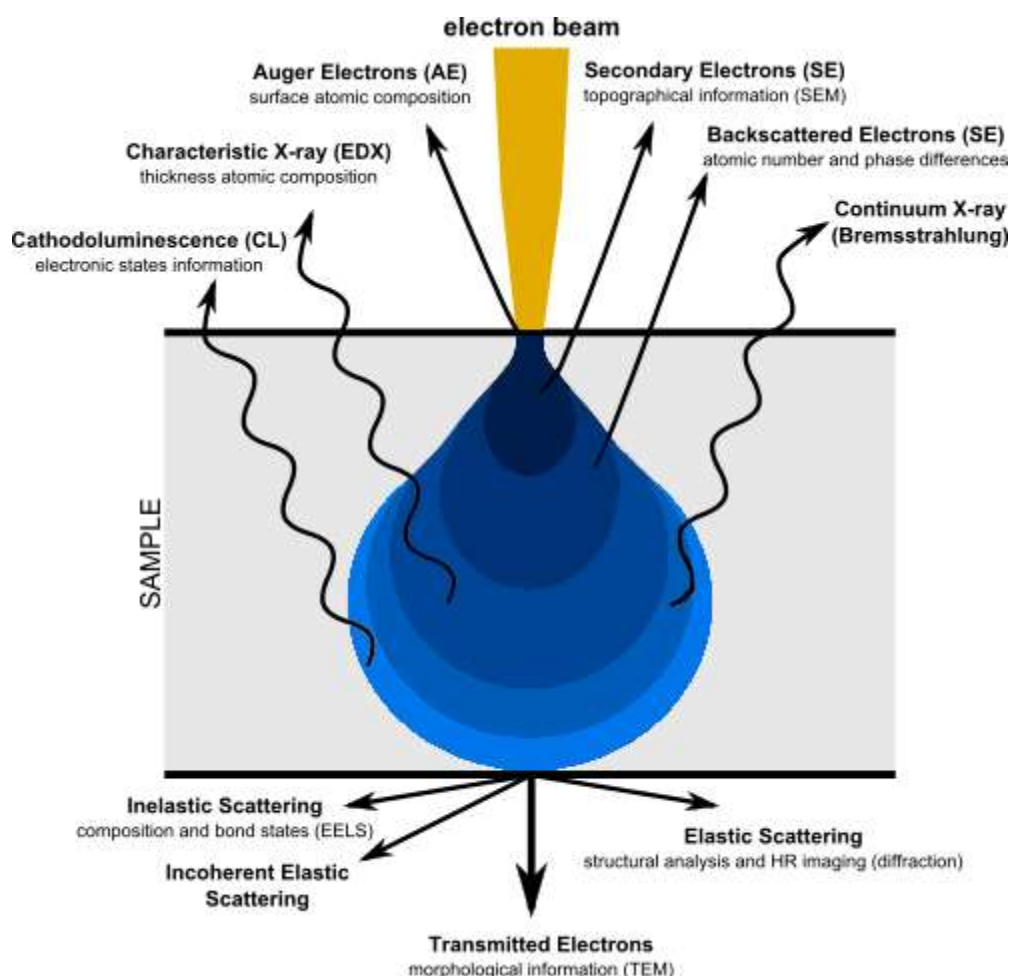


Figure 3.14. Pear model of interaction between an electron beam and a sample [19].

3.7.1.1. Environmental Scanning Electron Microscopy

ESEM is a convenient technique that provides overview of a sample, in a broad range of magnification – a valuable feature that enables to analyze the specimen in bulk (contrary to TEM and its sample thickness requirement) Apart from morphology analysis, it features a function to analyze elemental composition as well.

‘Scanning’ stands for the way the image is being produced. The surface of the sample is scanned with a properly adjusted electron beam. As the electrons interact with atoms from a sample, various signals are produced. These signals requires different detectors: the most common mode involving secondary electrons involves Everhart-Thornley detector, it is also capable of capturing signal from back-scattered electrons.

‘Environmental’ stands for the expanded functionality of a scanning electron microscope, allowing to measure samples with less strict preparation procedure. While apparatus responsible for the formation and adjustments of the electron beam is the same as in standard SEM, other elements are substantially different. The beam is generated in vacuum conditions, but the specimen chamber of ESEM features high-pressure gas environment separated from the electron optics column. In-between, chamber with low gas pressure is located to prevent leakage of gas directly to the vacuum chamber. The particles of gas are responsible for scattering of electrons and results in weakening of the beam. However, at a proper distance from the sample – that depends on gas pressure and the beam acceleration voltage – retains useful amount of electrons for imaging purposes. Development of environmental SEMs was crucial to increase availability of the technique: since this discovery on, it was possible to measure samples containing water or without metal sputtering – enabling to measure samples in their natural form [18].

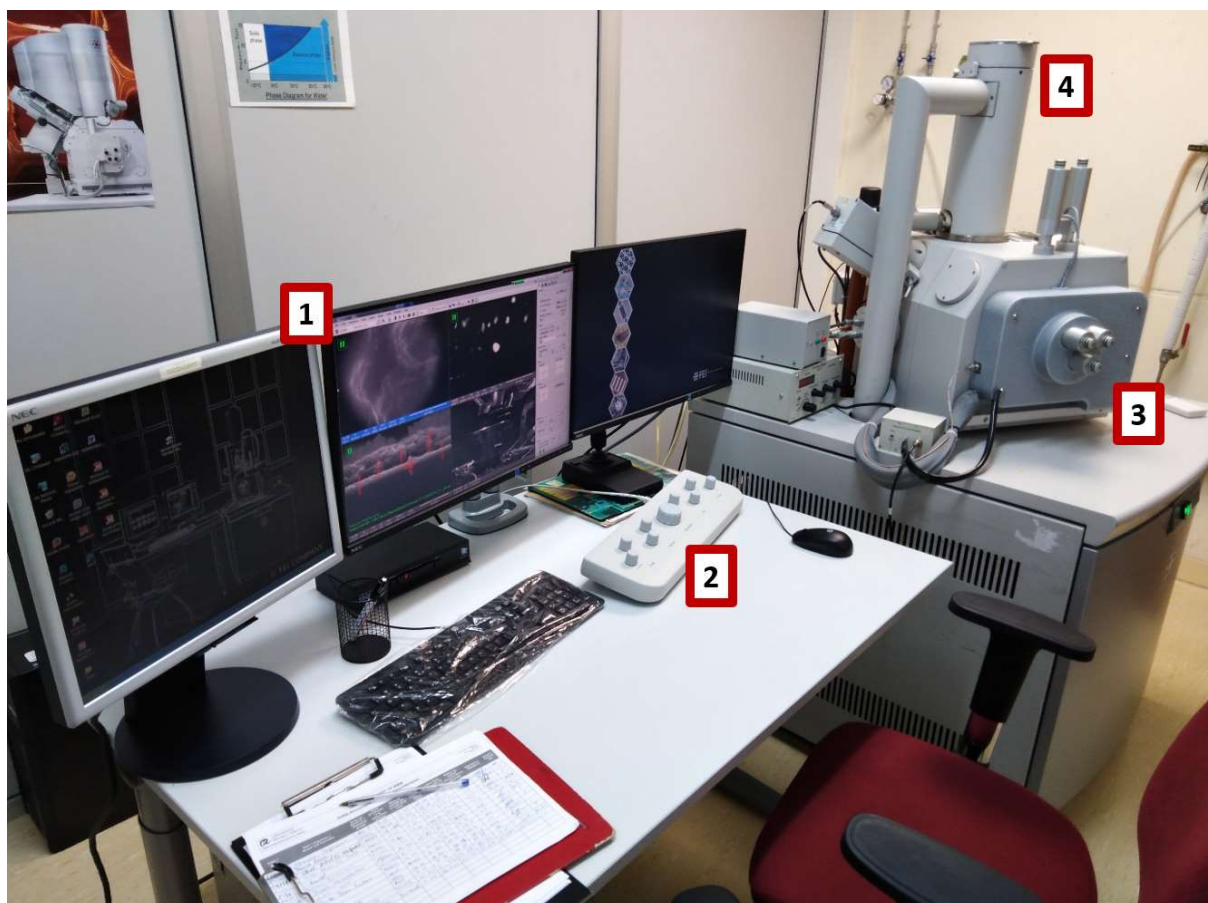


Figure 3.15. FEI Quanta 600 ESEM utilized in this work. (1) Monitors and PC used to communicate and operate the microscope, (2) Control panel of the ESEM, (3) Specimen chamber and (4) Electron column.

ESEM used in this work shown in figure 3.15 was FEI Quanta 600 using Everhart-Thornley and backscattered electron detectors, acceleration voltage between 20-30 kV and high vacuum conditions. Furthermore, energy dispersive X-ray (EDX) function with EDS Thermo Noran Vantage Detector was used for elemental analysis. To increase the conductivity of the sample – for higher resolution of morphology measurements – NAA samples were sputtered with 5 nm thick layer of gold. For EDX measurements, nanotubes were deposited on the aluminum substrate.

3.7.1.2. Transmission Electron Microscopy

Transmission electron microscopy takes a different approach. In this instance, electron beam is transmitted through the sample. For the sample to be measured, it needs to be relatively transparent to the electron beam: prepared substrate needs to be much thinner (usually 100 nm or less), while applied acceleration voltage is higher (50-400 kV).

Furthermore, since travel distance of the electron beam through the sample is short, spreading of the beam is minimal as compared to SEM. TEM enables reaching higher resolutions than SEM and this type of microscope operates similarly to conventional optical

one: bright image of a specimen can be projected on a phosphor screen or special camera [18]. TEM analysis was the most important, with regards to providing quick oversight into exact structure of the obtained nanotubes. Moreover, the technique enables to analyze morphology of nanotubes with minute detail – not accessible with other methods at the disposal.

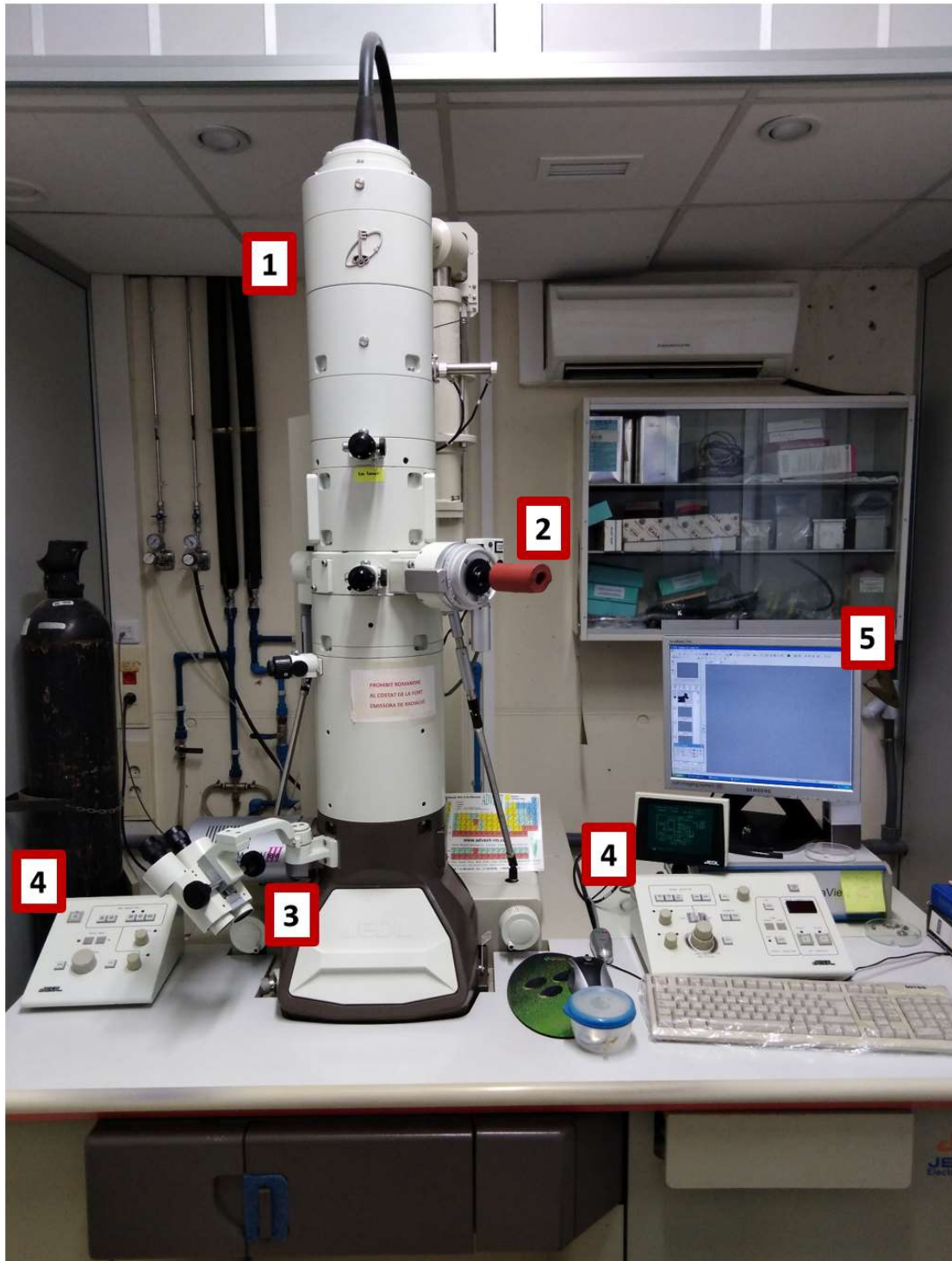


Figure 3.16. JEOL model 1011 TEM utilized in this work. (1) Electron gun and column (2) Specimen holder, (3) Fluorescent screen and camera, (4) Control panels and (5) PC communicating with the TEM.

TEM used in this work is JEOL model 1011 equipped with a digital camera shown in figure 3.16. Acceleration voltage applied to measure nanotubes was always 80 kV, while acquisition time varied between 100 and 1000 ms. Samples were deposited on Cu grids.

3.7.2. Confocal microscopy

Optical microscope is a device, that enables observation of small objects using visible light through the system of lenses used to manipulate the light path. Light can either illuminate a sample from below – if the specimen is transparent – or lit a sample from above. Confocal microscopy is a variant of optical microscopy with improved optical resolution and contrast. The improvement was possible due to the introduction of a spatial pinhole and point illumination. The pinhole blocks out-of-focus-signal – combined with illumination only close to the focal plane, higher precision is achievable. Magnification provided by the confocal microscope makes it an attractive tool to analyze biological samples and other objects with distinguishable features in microscale (limit related to diffraction of light restricts resolution to around 200 nm) [16].

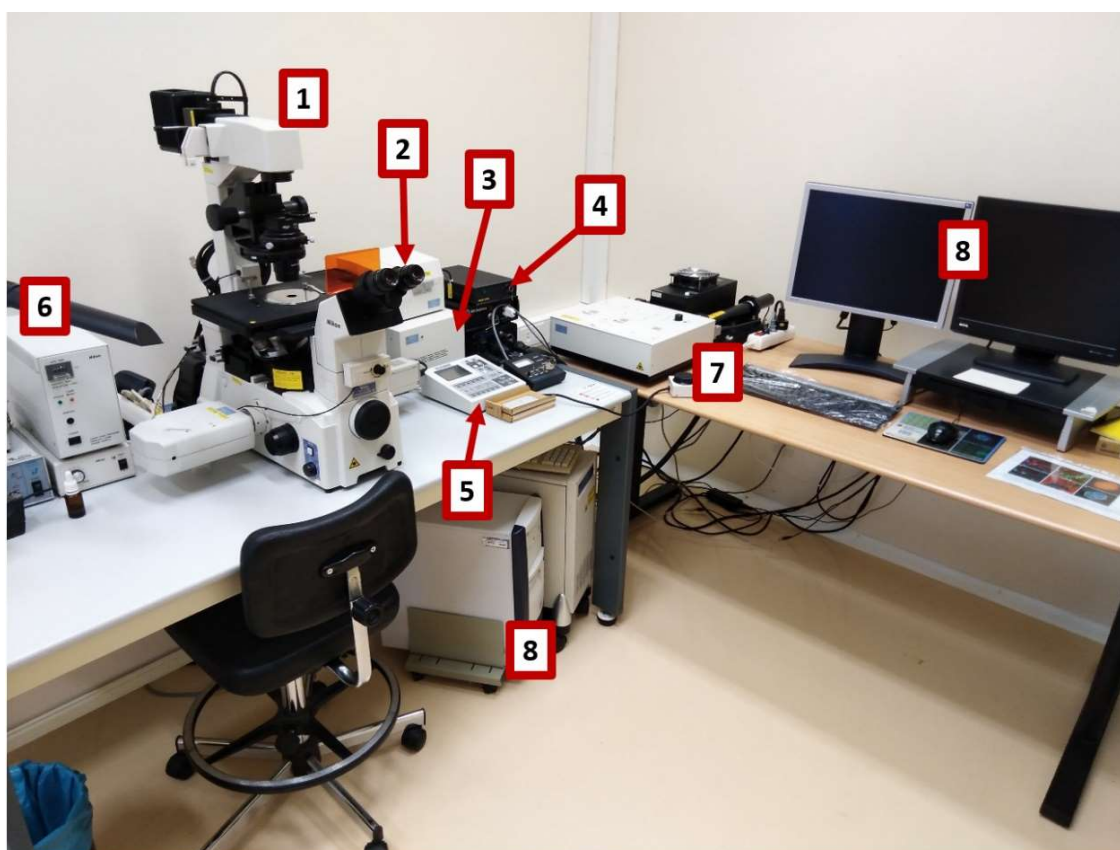


Figure 3.17. Nikon Eclipse TE2000-E confocal microscope utilized in this work. (1) Inverted microscope Eclipse TE2000-E, (2) Detector unit, (3) Acusto-optical modulators controller, (4) Power supplies for lasers, (5) T-RCP remote control pad, (6) Power supply for the high pressure mercury lamp, (7) Laser light sources (Violet diode laser MOD 404 nm, Argon-Ion laser 457/476/488/514 nm and Green He-Ne Laser 543 nm) and (8) PC connected with the microscope.

Confocal microscope used in this work is Nikon Eclipse TE2000-E inverted microscope equipped with a C1 laser confocal system (EZ-C1 software, Nikon) shown in figure 3.17 488 nm argon laser was used as the excitation source when functionalization with fluorophore was observed – and collected at 515 ± 15 nm using bandpass emission filter. All images were captured with a 5 MP CCD, 100x objective and excitation time of 500 ms.

3.7.3. Dynamic Light Scattering and ζ -potential

DLS is a convenient measurement method to perform a quick and cost-effective analysis of a suspension. It is also convenient to analyze biological sample: size of proteins, micelles or monitor aggregation of proteins over time. Dynamic light scattering is a method based on analysis of the particles motion in a suspension based on the way monochromatic light beam is scattered. Small particles in the suspension undergo constant chaotic motion defined as Brownian motion [21]. The laser light is scattered in all directions as it travels through the sample. The scattering is not constant and its intensity fluctuates. Fluctuation dynamic depends on the speed of particles located in a suspension and can be used to calculate their size based on the Einstein-Stokes model. In principle, the motion speed is size-dependent and smaller particles moves faster. The method enables to obtain hydrodynamic diameter of particles in range from below 1 nm up to several microns.

DLS enables also to measure ζ -potential – the value of the electrical charge of particles in liquid – when equipped with a proper cuvette. It is a result of calculations originating from theoretical models and based on the mobility of particles in response to the electric field. Charged particles will travel towards an electrode of the opposite charge. The rate of migration is used to calculate ζ -potential. Z-potential value is an important information about stability of suspensions – suspensions featuring values higher than ± 30 mV are considered stable [21].



Figure 3.18. ZetaSizer Nano utilized in this work. a) Folded capillary cell for ζ -potential and DLS measurements. b) ZetaSizer Nano.

DLS used in this work is a ZetaSizer Nano shown in figure 3.18. Folded capillary cell DTS1070 enabling to measure both, hydrodynamic diameter and ζ -potential was used. Measurement temperature in all cases was 25°C and stabilization time prior to measurement 60 s.

3.7.4. Fourier Transform Infrared Spectroscopy

IR light absorbed by the molecule influences its energy – oscillational and rotational. However, absorption can occur only if the energy of light is equal to the energy difference between its two oscillational levels. It means that only specific wavelengths can be absorbed by the molecule. This translates into specific ranges of light frequencies that interact with particular molecular formations. The sample is irradiated with IR light from the whole spectrum. The measurement can be conducted in either absorbance or transmittance mode. The detector analyses which frequencies are transmitted/reflected as they were not absorbed by the specimen. Obtained interferogram is later calculated using Fourier transformation to produce the spectrum. FT-IR is a robust method that enables quick analysis of chemical composition of the sample – allowing to determine specific chemical bonds [22].

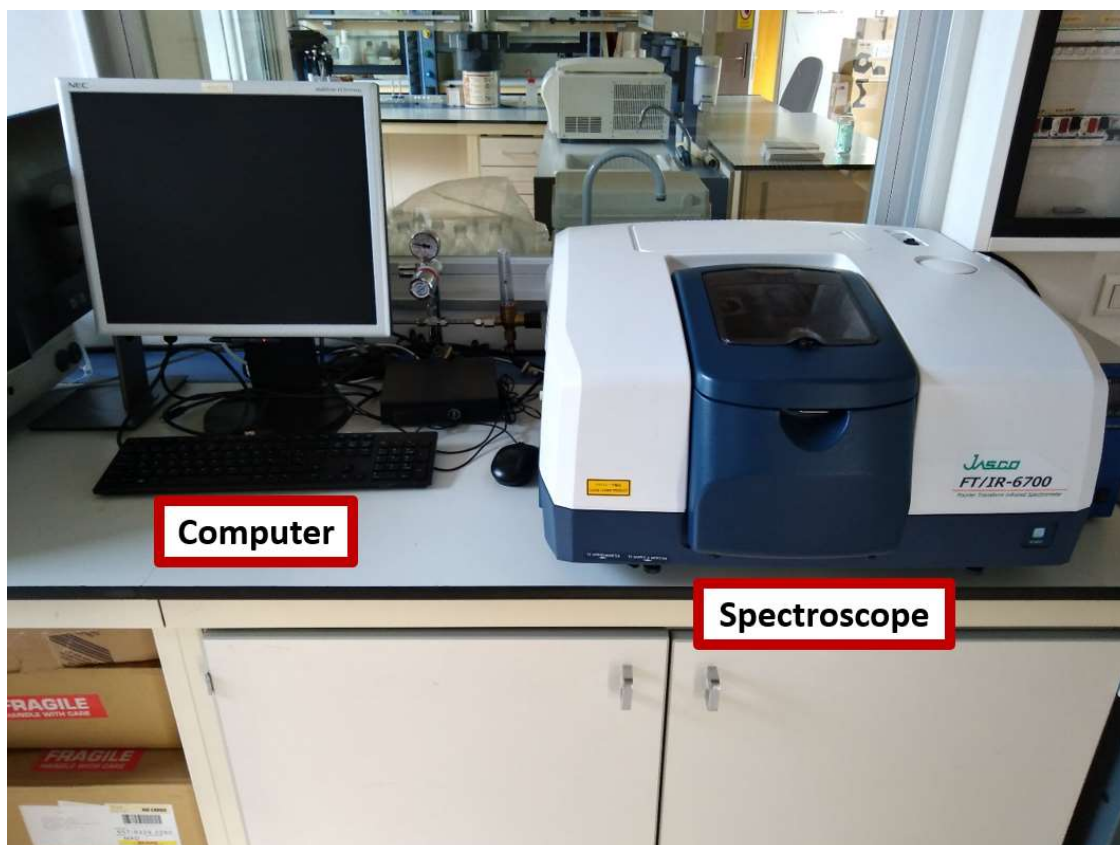


Figure 3.19. Fourier Jasco FT/IR-600 Plus utilized in this work.

FTIR used in this work shown in figure 3.19 was Fourier Jasco FT/IR-600 Plus with ATR S attachment. Resolution of the measurement was 0.96 cm^{-1} , accumulation 32 and applied incident angle 45° .

3.7.5. Spectrophotometry

It is a method used to analyze whether the sample exhibit luminescence. The specimen is illuminated with high intensity light of specified frequency. If the light corresponds to excitation wavelength of the molecule, it gets absorbed. Initially, molecule reaches higher energy level. Then, due to relaxation molecule goes back into the ground state – photon corresponding to the energy difference is emitted. Fluorescent emission is always red-shifted as compared to the excitation wavelength as some part of the absorbed energy gets dissipated through non-radiative transition. These emitted photons can be collected by the detector providing information about luminescence of the specimen. The method is highly valuable in biological, analytical chemistry, but is more versatile [23].



Figure 3.19. QuantaMaster 400 Photon Technology International spectrophotometer utilized in this work. (1) Sample compartment, (2) DeltaRAM X™ random access monochromator, (3) Emission monochromator and grating, (4) Detector, (5) Power sources.

Spectrophotometer used in this work was Photon Technology International spectrophotometer with Xe lamp shown in figure 3.19. Measurements were performed at ambient conditions, excitation wavelength was 450 nm, while emission spectrum was gathered between 460 and 600 nm with 1 nm resolution.

3.7.6. X-ray Diffraction

X-ray diffraction (XRD) is an important analytic technique in chemistry and crystallography. It is utilized to determine atomic and molecular structure of a crystal. The method is especially convenient to quickly analyze unknown crystalline materials. X-rays are generated through the exposition of the filament to the accelerated electron beam – with sufficient energy of the beam specific X-ray spectrum is produced. The spectrum is characteristic to the material of the filament. Later, it is filtered in order to obtain monochromatic X-rays used in diffraction measurements. Angle and intensity of these diffracted beams can be translated into a three-dimensional portrait of electron distribution within the crystal. The sample and detector are rotated when the specimen is exposed to the X-rays, and intensity of reflected X-rays is recorded. It is later converted to the spectrum. This information enables to determine the

position of the atoms inside the crystal. Also, chemical bonds and crystallographic disorder can be measured [24].

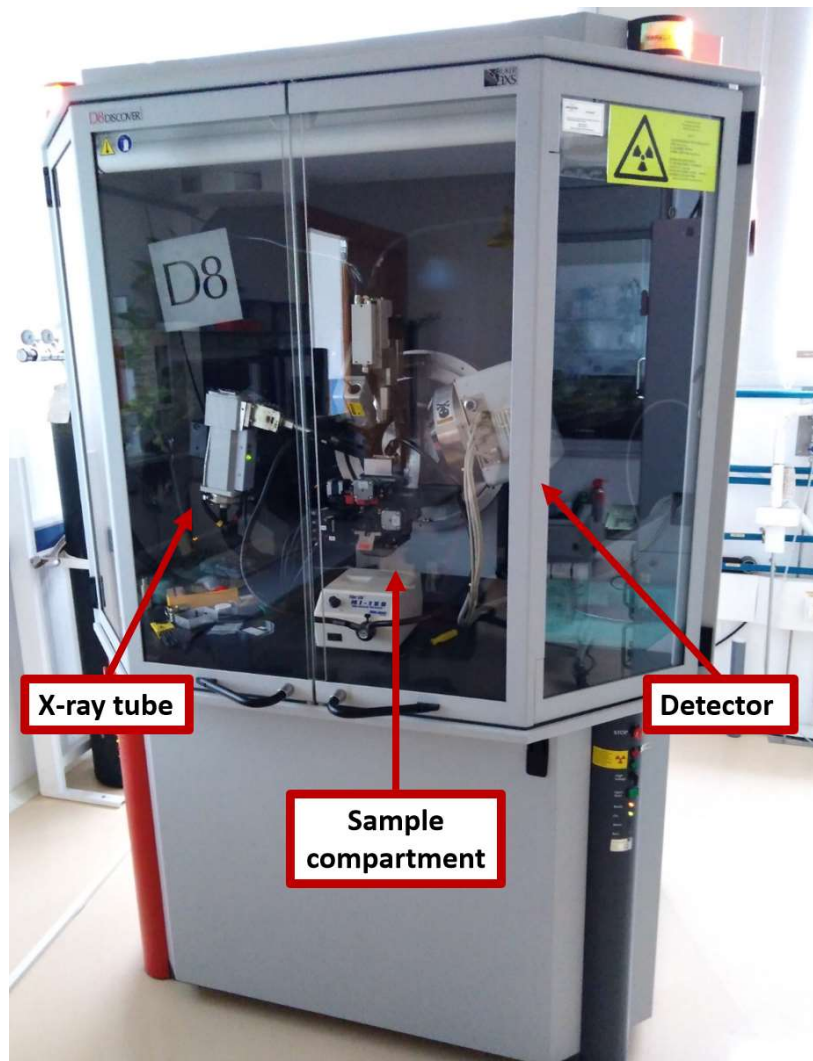


Figure 3.20. Siemens D5000 diffractometer (XRD) utilized in this work.

XRD used in this work was Siemens D5000 diffractometer shown in figure 3.20. The radiation ($Cu_{K\alpha}$) was emitted from copper X-ray tube operated at 40 kV and 30 mA (1.54 \AA).

3.8. Conclusions

This chapter provided description of the electrochemical setup, laboratory equipment and experimental techniques used in the fabrication of anodic alumina nanotubes.

First, we have described elements of the electrochemical setup, role of every component and reasoning behind such the arrangement. Presented setup was developed over many years and a few elements – while not all necessarily obligatory – enabled the precision, that created new possibilities along with the improvements. The fabrication of anodic alumina nanotubes is a great example of vast utility provided by the setup that continues to expand. After all, the discussed material is only one of many alternatives accessible through the anodization of aluminum.

Further, preparation of the substrates, laboratory techniques required to yield the final product and overview of the material morphology were presented. Although the fabrication starts with anodization of aluminum, more steps are required to obtain the suspension of nanotubes – and provide their stability. Since the discovery of AAN fabrication is just over a decade old, it is relatively young method that continuously develops. Currently, it is possible to tailor-engineer its geometrical features and certain physical properties. Moreover, a few functionalization approaches have been examined in the past. However, introduction of functionalities that could enable practical applications is still at its initial stage – with an attempt to contribute to such, presented in this thesis.

At last, an introduction to the measurement techniques utilized during the work was provided. Description consisted of theoretical background that helps to understand mechanism of interaction between the system and the sample.

3.9. References

- [1] Santos, A. *Structural Engineering of Nanoporous Anodic Alumina and Applications: Structural Engineering of Nanoporous Anodic Alumina and Applications*, 1rd ed; LAP LAMBERT Academic Publishing, Saarbrücken, Germany, 2011.
- [2] A. Belwalkar, E. Grasing, W. Van Geertruyden, Z. Huang, and W. Z. Misiolek. Effect of processing parameters on pore structure and thickness of anodic aluminum oxide (AAO) tubular membranes. *J. Memb. Sci.* **2008** 319, 1-2, doi: 10.1016/j.memsci.2008.03.044.
- [3] W. Lee, K. Schwirn, M. Steinhart, E. Pippel, R. Scholz, and U. Gösele. Structural engineering of nanoporous anodic aluminium oxide by pulse anodization of aluminium. *Nat. Nanotechnol.* **2008**, 3, 234-239, doi: 10.1038/nnano.2008.54.
- [4] A. Santos. Nanoporous anodic alumina photonic crystals: Fundamentals, developments and perspectives. *J. Mater. Chem. C* **2017**, 5, 5581-5599, doi: 10.1039/c6tc05555a.
- [5] G. D. Sulka and K. G. Parkoła. Temperature influence on well-ordered nanopore structures grown by anodization of aluminium in sulphuric acid. *Electrochim. Acta* **2007**, 52, 1880-1888, doi: 10.1016/j.electacta.2006.07.053.
- [6] M. P. Montero-Rama, A. Viterisi, C. Eckstein, J. Ferré-Borrull, and L. F. Marsal. In-situ removal of thick barrier layer in nanoporous anodic alumina by constant current Re-anodization. *Surf. Coatings Technol.* **2019**, 380, p125039, doi: 10.1016/j.surfcoat.2019.125039.
- [7] W. Lee and S. J. Park. Porous anodic aluminum oxide: Anodization and templated synthesis of functional nanostructures. *Chem. Rev.* **2014**, 114, 7487-7556, doi: 10.1021/cr500002z.
- [8] V. Vega, J. Garcia, J. M. Montero-Moreno, B. Hernando, J. Bachmann, V. M. Prida and K. Nielsch. Unveiling the Hard Anodization Regime of Aluminum: Insight into Nanopores Self-Organization and Growth Mechanism. *ACS Appl. Mater. Interfaces* **2015**, 7, 28682-28692, doi: 10.1021/acsami.5b10712.
- [9] W. Lee, R. Scholz, and U. Gösele. A continuous process for structurally well-defined Al₂O₃ nanotubes based on pulse anodization of aluminum. *Nano Lett.* **2008**, 8, 2155-2160, doi: 10.1021/nl080280x.
- [10] J. Wu, Y. Li, Z. Li, S. Li, L. Shen, X. Hu and Z. Ling. Ultra-slow growth rate: Accurate control of the thickness of porous anodic aluminum oxide films. *Electrochem. commun.* **2019**, 109, 6-10, doi: 10.1016/j.elecom.2019.106602.
- [11] X. Qin, J. Zhang, X. Meng, L. Wang, C. Deng, G. Ding, H. Zeng and X. Xu. Effect of ethanol on the fabrication of porous anodic alumina in sulfuric acid. *Surf. Coatings Technol.* **2014**, 254, 398-401, doi: 10.1016/j.surfcoat.2014.06.050.
- [12] Y. Wang, A. Santos, A. Evdokiou, and D. Losic. Rational design of ultra-short anodic alumina nanotubes by short-time pulse anodization. *Electrochim. Acta* **2015**, 154, 379-386, doi: 10.1016/j.electacta.2014.12.056.
- [13] J. T. Domagalski, E. Xifre-Perez, A. Santos, J. Ferré-Borrull, and L. F. Marsal. Tailor-engineered structural and physico-chemical properties of anodic alumina nanotubes by pulse anodization: A step forward. *Microporous Mesoporous Mater.* **2020**, 303, 110264, doi: 10.1016/j.micromeso.2020.110264.
- [14] S. Zhao, K. Chan, A. Yelon, and T. Veres. Novel structure of AAO film fabricated by constant current anodization. *Adv. Mater.* **2007**, 19, 3004-3007, doi: 10.1002/adma.200701284.

- [15] C. S. Chi, J. H. Lee, I. Kim, and H. J. Oh. Effects of microstructure of aluminum substrate on ordered nanopore arrays in anodic alumina. *J. Mater. Sci. Technol.* **2015**, 31, 751-758, doi: 10.1016/j.jmst.2014.09.019.
- [16] V. Westphal, S. O. Rizzoli, M. A. Lauterbach, D. Kamin, and S. W. Hell. Far-field optical nanoscopy. *Opt. InfoBase Conf. Pap.* **2009**, 2, 1153-1159, doi: 10.1364/ntm.2009.nma1.
- [17] S. W. Hell, S. J. Sahl, M. Bates, X. Zhuang, R. Heintzmann, M. J. Booth, J. Bewersdorf, G. Shtengel, H. Hess and P. Tinnefeld. The 2015 super-resolution microscopy roadmap. *J. Phys. D. Appl. Phys.* **2015**, 48, 443001, doi: 10.1088/0022-3727/48/44/443001.
- [18] F. J. García De Abajo. Optical excitations in electron microscopy. *Rev. Mod. Phys.* **2010**, 82, 209-275, doi: 10.1103/RevModPhys.82.209.
- [19] Scanning electron microscopy (SEM), what is it for? August 24. 2020. Available online: <https://www.atriainnovation.com/en/scanning-electron-microscopy-uses/> (accessed on 15 January 2021).
- [20] R. F. Egerton, P. Li, and M. Malac. Radiation damage in the TEM and SEM. *Micron* **2004**, 35, 399--409, DOI: 10.1016/j.micron.2004.02.003.
- [21] S. Bhattacharjee. DLS and zeta potential - What they are and what they are not? *J. Control. Release* **2016**, 235, 337-351, DOI: 10.1016/j.jconrel.2016.06.017.
- [22] S. Wartewig and R. H. H. Neubert. Pharmaceutical applications of Mid-IR and Raman spectroscopy. *Adv. Drug Deliv. Rev.* **2005**, 57, 1144-1170, DOI: 10.1016/j.addr.2005.01.022.
- [23] S. Eaton-Magaña and C. M. Breeding. An introduction to photoluminescence spectroscopy for diamond and its applications in gemology. *Gems & Gemology* **2016**, 52, 130-145, doi: 10.5741/GEMS.52.1.2.
- [24] Birkholz, M. *Thin Film Analysis by X-Ray Scattering*, 1rd ed; Willey-VCH, Weinheim, Germany, 2006.

Chapter 4. Tailor-engineered structural and physico-chemical properties of anodic alumina nanotubes by pulse anodization: A step forward.

Abstract

A study on advanced structural engineering of anodic alumina nanotubes (AANTs) manufactured by pulse anodization is presented. In-depth analysis of the pulse anodization was carried out, distinctive sections of the anodization were defined. Evolution of the profiles has been quantified and described with regards to different current density applied and pulse duration during hard anodization. A smart combination of different anodization conditions enables precise control over the nanotubes' geometric features and physiochemical properties. Nanotubes are produced with varying pulse period, current density level and various post-anodization treatments (different sonication time, temperature and thermal annealing of anodic alumina film before fragmentation) under galvanostatic mode in sulfuric acid electrolyte modified with 10% (v/v) ethanol. The average length of nanotubes is tailor-engineered from 424 ± 92 to 1010 ± 118 nm, with an average inner diameter that ranges from 37 and 48 nm. It is also demonstrated that the level of current density input during pulse hard anodization has a direct effect on the ζ -potential of nanotubes, which can be tuned between 25 and 8.5 mV. Additionally, it is possible to produce nanotubes with a negative ζ -potential of -6.3 mV upon post-annealing treatment. Separation of nanotubes from the original template is improved by sonication at low temperature, providing a new means of increasing the production yield of these nanostructures. Furthermore, nanotubes are found to increasingly degrade with the bath temperature during separation. To better understand the impact of the fabrication parameters over the physical and chemical properties of nanotubes is a key step to design and tailor-engineer these model 1D nanostructures for specific applications. AANTs provide many attractive features that could find broad applicability in disciplines such as catalysis, drug delivery, nanofabrication and sensing.

4.1. Introduction

Anodization is an electrochemically driven process widely used in industry to passivate and modify the properties of metals (e.g. color, wear resistance, wettability) by growing a layer of insoluble anodic oxide. The metal of interest (anode) – typically aluminum alloys and other valve metals such as magnesium, zinc or titanium – is immersed into an acid electrolyte and electrochemically oxidized (anodized) under controlled conditions [1]. Application of current density (galvanostatic mode) or potential (potentiostatic mode) input signal drives the growth of anodic oxide layers in which two competing processes occur: i) current-driven growth of the metal oxide at the interface metal/oxide and ii) chemical dissolution of the oxide at the

oxide/electrolyte interface [2], [3]. Under appropriate anodization conditions, the aluminum oxide layer can be produced with straight cylindrical pores from top to bottom, which grow perpendicularly to the underlying metal [4], [5]. The most widespread method to fabricate highly-ordered aluminum oxide for research applications is the two-step anodization, which is typically performed under potentiostatic conditions [6]. This seminal discovery boosted intensive research in this area with an exponential raise of publications on anodic alumina (AA) with mesoporous structure [7], [8]. The two-step anodization process is performed under the so-called mild anodization (MA) conditions – relatively low input voltage and moderate electrolyte temperatures – which provides the highest ordering in mesoporous structure after initial stabilization of pore growth.

There are sets of conditions of aluminum anodization causing self-ordered growth of anodic alumina being commonly described in the literature as “standard” due to long history of application and their prevalence in the field : sulfuric acid at 25 V, oxalic acid at 40 V and phosphoric acid at 195 V. These honeycomb-like mesoporous structures are created with interpore distances of 63, 100 and 500 nm respectively [2], [6], [9]. But as more novel structures are get discovered extend of structure geometry expands enabling aluminum anodization process to fit even better for specific application. As example, selenic acid (H_2SeO_4) AA provide promising properties with possibility to create highly ordered narrow pores of 10 nm diameter previously achievable only with sulfuric acid, which along with high transparency and lack of material photoluminescence provide for high potential of such structures [10]. Additionally, selenic acid anodization can yield self-ordering process covering interpore distance between 120 and 160 nm (at 60 – 100 V) which was not accessible before [11]. Another less common variant of anodization is one performed in phosphonic acid (H_3PO_3). Its recent discovery cover new range of interpore distance available with aluminum anodization – from 370 to 440 nm at voltage range between 150 to 180 V [12]. These new findings with regards to anodization regimes – even if providing only narrow window when self-arrangement occurs – cumulatively provide for better accessibility of the technique for specific application. When anodization is performed under conditions that are outside the self-ordering regimes, the spatial ordering ratio of pores in anodic alumina decreases dramatically. After initial pore nucleation, stable growth of the AA film is achieved during anodization due to dynamic equilibrium between the formation and dissolution of the oxide [13]. However, two-step anodization requires remarkably long fabrication times (>24 h). Further to that, AA’s geometric features under mild anodization conditions are constrained within a limited range of dimensions (i.e. pore diameter, interpore distance). These intrinsic limitation encouraged researchers to find alternative anodization conditions that overcome these technical constraints [14]–[16].

While so-called hard anodization (HA) is a process known for many decades [17], for long time it was left aside in scientific research. Major constraint of HA is the amount of heat generated at the pore bottom associated with Joule effect which can lead to dramatic electric breakdown (or burning) and result in destruction of the anodic alumina film [18]. Attention to such anodization approach has been brought back with pioneering work of Lee and co-workers as

they reported creation of highly ordered aluminum oxide fabricated with anodization in oxalic acid under hard anodization conditions. This allowed to create oxide films at significantly faster rates than standard anodization protocol established back then, while keeping high level of regularity [19]. Novelty of their idea relied on creation of thin layer of oxide by means of mild anodization prior to applying higher current densities, which prevented immediate electric breakdown. Hard anodization is typically performed at much higher current densities ($>30 \text{ mA/cm}^2$) and low electrolyte temperatures. Major difference between standard anodization and HA, however, is aluminum oxide formation mechanism. During mild anodization, current density during potentiostatic anodization is determined by electric field-driven migration of ions across the oxide layer providing creation of pores prevalently at hexagonal coordination (90%). When potential increases forcing faster growth of the oxide structure, occurrence of hexagonal coordination drops up to 50% under mixed control regime. Nevertheless, further increase of the potential leads to even faster growth with depletion of specific ions at the pore bottom. As result, current density is now limited by diffusion of ionic species involved in formation of the AA, mechanism described as diffusion control characteristic for hard anodization regime. Under diffusion control process, prevalence of hexagonal arrangement reaches high values of above 80% again [20], [21]. The growth rate of anodic alumina under hard anodization regime is increased $\sim 92.5\text{--}98.7\%$ as compared to that of mild anodization ($1\text{--}3 \text{ }\mu\text{m/h}$), reaching between 40 to $80 \text{ }\mu\text{m h}^{-1}$. Hard anodization also enables the fabrication of mesoporous structures with small pore diameters, while expanding the interpore distances to longer and previously unexplored ranges, between 70 and 450 nm [14], [19]. In contrast with the two-step mild anodization process, hard anodization enables fast fabrication of highly ordered mesoporous structures in one single anodization step, with processing times $\sim 1 \text{ h}$ [22]. 2 years later, Lee and co-workers reported modification to hard anodization that could help reduce issues related to high heat generation which was inevitable during longer HA process. New process was called pulse anodization (PA) – intercalation of pulses at high and low current density or voltage – as an optimal means to minimize the generation of heat during hard anodization and suppress electric breakdown [23]. Close observations of the AA structure produced under pulse anodization revealed nanopore diameter modulations along the oxide growth direction, which were found to precisely follow the input voltage. This finding provided a broad range of opportunities to tailor-engineer anodic alumina structures with highly sophisticated morphologies. Amongst other, diameter-modulated nanowire arrays [24], biomimetic films [25] and range of photonic crystal structures [26] such as rugate filters [27] and photonic coating for optical sensing [28] are some of AA-based nanostructures fabricated *via* pulse-like anodization process.

Efforts to optimize pulse anodization lead to higher control over the geometric features of AA structures with mesoporous modulations in depth, and to the discovery of the formation of voids along the cell boundaries during hard anodization. Pulse anodization weakens the junction strength of the nanopore cells, cracking the structure of anodic alumina along its cell boundaries. This key finding enabled pulse anodization as a new nanofabrication approach to generate 1D alumina-based nanotubes – anodic alumina nanotubes (AANTs) – with highly

controlled dimensions by splitting the periodically modulated structure of anodic alumina [29], [30]. Fabrication of AANTs consists of two anodization steps: i) a first step at constant mild anodization conditions to generate a starting layer of anodic alumina and ii) a pulse anodization step to modulate the nanopore diameter in depth. The starting anodic alumina layer provides mechanical integrity to the oxide film, a shuttle to achieve pore arrangement prior to pulse anodization, and prevents the film from plastic deformation and breakdown due to Joule heat generated during hard anodization. AANTs are produced by stepwise pulse anodization under current density control, in which each pulse combines a hard anodization step at high current density and a mild anodization step at low current density. The former step is responsible for the formation and engineering of AANTs, while the latter step of the pulse makes it possible to efficiently dissipate the excess of heat generated during the hard anodization step and prevent the oxide film from catastrophic burning. Another characteristic of anodization under high potential is rarely occurring phenomenon described as cell separation. Formation of such structure usually occurs during anodization with sulfuric acid at high potentials [31], [32]. Usually undesired due to formation of mechanically weaker structure, properly adjusted allows for selective partition of such structure and liberation of nanoparticles [30]. So far there is no direct experimental proof pointing on the origin of these weaker spots. However, modulation of the outer walls of nanopores during pulse anodization relies strongly on the thickness of the starting anodic aluminum oxide layer. No significant outer wall modulation is observed for thicknesses of anodic alumina starting layers $<65 \mu\text{m}$. However, structural engineering of the outer nanopore walls becomes apparent at a starting layer thickness above $100 \mu\text{m}$ [33]. Such sites are mechanically more fragile than non-hydrated alumina, providing crevices to breakdown the structure of anodic alumina into nanotubes. While heat generation is usually an undesired factor in standard hard anodization [18], this phenomenon can be readily exploited to engineer weak cleavages at specific positions along the structure of anodic alumina and tailor-engineer the geometric features of nanotubes. Due to their inert chemical nature, AANTs have been devised as model nanocontainers for potential deployment in drug delivery and biomaterials applications. As-produced nanotubes with positive surface charge ($\sim 15 \text{ mV}$) exhibit negative charge (-11 mV) when mixed with 10% FCS. Such nanotubes were proven to exhibit a superior non-cytotoxicity than other high aspect ratio nanomaterials, being able to load drugs within their structure and deliver efficiently their therapeutic cargoes inside cells [34], [35]. The surface chemistry of nanotubes can be further modified by silanization, providing new opportunities to tune functional groups on the surface of this 1D model nanomaterial [36]. Despite advances in AANTs technology, there is still need for further fundamental and applied research in pulse anodization to achieve versatile and precise control over the structural and physiochemical properties of these unique nanostructures. Herein, we develop an advanced pulse anodization approach to tailor-engineer the structural and physiochemical properties of anodic alumina nanotubes (figure 4.1). In-depth analysis of the pulse anodization was carried out, distinctive sections of the anodization were defined. Evolution of the profiles has been quantified and described with regards to different current density applied and pulse duration during hard anodization. A

smart combination of anodization conditions and post-fabrication treatments is demonstrated to provide improved control over the nanotubes' dimensions and physiochemical properties. This approach makes it possible to alter and fine-tune the structural and physico-chemical properties of nanotubes such as length, inner diameter, wall thickness, ζ -potential and crystallinity. This study lays the ground for future applications of this novel nanomaterial in disciplines such as catalysis, drug delivery, nanofabrication and sensing.

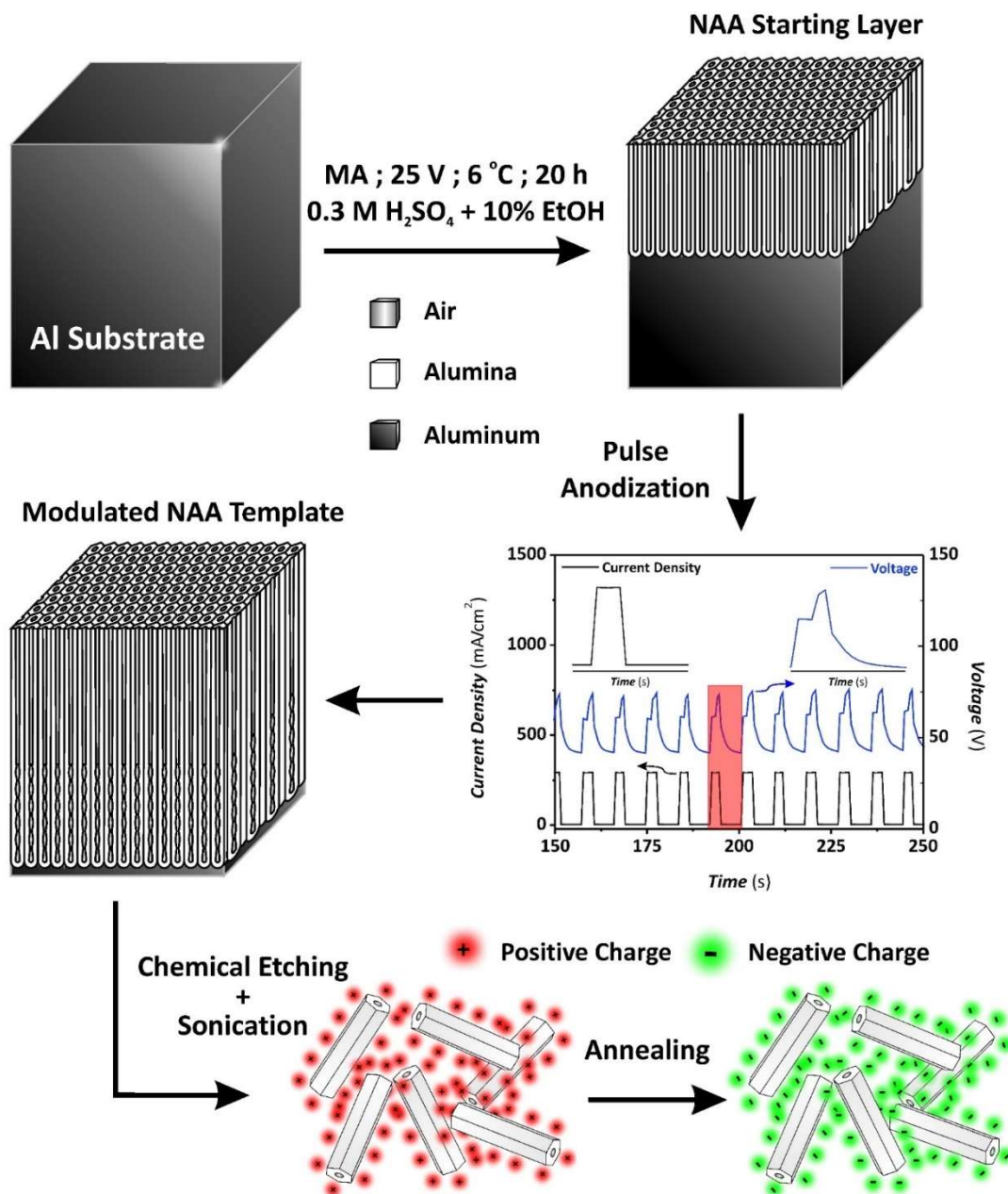


Figure 4.1. Conceptual scheme describing the fabrication of AANTs by pulse anodization : MA of aluminum in sulfuric acid electrolyte followed by pulse anodization to grow a anodic alumina structure with modulated nanopore diameter (NB: representative current density–voltage profile of a modulated AA template produced with HA current density – $J_{\text{HA}} = 290 \text{ mA/cm}^2$, MA current density – $J_{\text{MA}} = 4.5 \text{ mA/cm}^2$, time at J_{HA} – $t_{\text{HA}} = 3.5 \text{ s}$, and time at J_{MA} – $t_{\text{MA}} = 5 \text{ s}$). After chemical etching and sonication nanotubes are liberated. Surface charge of AANTs can be tuned from positively to negatively charged by annealing treatment.

4.2. Experimental

4.2.1. Materials

Aluminum (Al) disc of thickness 0.5 mm and purity 99.999 % were supplied by Goodfellow Cambridge Ltd. Sulfuric acid (H_2SO_4) and ethanol ($\text{C}_2\text{H}_5\text{OH}$) were purchased from Scharlau. Cooper (II) chloride (CuCl_2), hydrochloric acid (HCl) and perchloric acid (HClO_4) were purchased from Sigma-Aldrich. Chemicals were used as received, without further purification steps. PURELAB® Option-Q (18.2 M Ω cm) was used for preparing all the solutions used in this study.

4.2.2. AANTs fabrication

Al discs 2 cm in diameter were sequentially sonicated in ethanol and ultrapure water for 10 min each. Prior to anodization, Al discs were electropolished in a mixture of HClO_4 and ethanol 1:4 (v/v) at 20 V and 5°C for 7 min. Then, the first anodization step was performed in an aqueous 0.3 M H_2SO_4 electrolyte modified with 10% ethanol at 25 V and 6°C for 20 h to generate a starting anodic alumina layer of ~ 100 μm . Next, the anodization process was switched to galvanostatic pulse anodization, using the same acid electrolyte but at 1°C under vigorous stirring. Pulse anodization consisted of sequential pulses between mild anodization and hard anodization conditions, in which the current density (J) input was periodically switched between high and low values for a given time in a stepwise fashion. Each pulse was formed by a mild anodization step at 4.5 mA/cm² for 5 s and hard anodization section at 290–390 mA/cm² with duration between 2.0 and 3.5 s. Time analysis of individual pulse with all experimental points marked for different duration of the pulse are provided in supplementary data – figure 4.S.1. The effective anodization area was 1.54 cm², and J was calculated by dividing the input current by the anodization area. After anodization, the remaining Al substrate was removed by wet chemical etching in a mixture of 0.2 M CuCl_2 and 6.1 M HCl followed by further immersion of the structured anodic alumina film into the same etchant solution for 1 h.

4.2.3. Structural and physiochemical characterization of AANTs

The geometric features and morphology of structured anodic alumina films and liberated nanotubes were analyzed by transmission electron microscopy (JEOL model 1011) and environmental scanning electron microscopy (ESEM, FEI Quanta 600). Structured films were attached to ESEM mounts with a sticky conductive carbon tape, while free-standing nanotubes were deposited by drop casting of suspension onto aluminum substrates. Structured films and nanotubes were coated with a ~ 5 nm thin layer of gold prior to ESEM

imaging. The size distribution of nanotubes was calculated by analysis of TEM images in ImageJ, using approximately 100 individual reading points for each parameter (i.e. nanotube's length, and inner and outer nanotube diameter). ζ -potential and size distribution profiles of anodic alumina nanotubes were analyzed by a ZetaSizer Nano, using suspension of nanotubes with a concentration of 2.5 mg/mL measured immediately after sonication. A xs analytical balance with 0.01 mg readability (KERN ABT 120-5DNM) was used during all experiments for sample weighting. Sonication was performed using a sonicating bath Bandelin Sonorex RK 102H.

4.2.4. Annealing and crystallographic characterization of AA and AANTs

After chemical etching and prior to liberation through sonication, structured anodic alumina films were divided into pieces and introduced into a ceramic oven (ELECTRIC LABORATORY KILN Series LKN 75) for annealing treatment at 850, 1050 and 1200°C for 2 h. After thermal treatment, standard sonication procedure was employed. Crystallographic phases of nanotubes were analyzed by XRD measurements in a Siemens D5000 diffractometer. The source $Cu_{K\alpha}$ radiation was cooper X-ray tube operated at 40 kV and 30 mA (1.54 Å). Elemental composition of AANTs produced at distinct annealing temperatures was analyzed by EDS Detector Thermo Noran Vantage that was mounted to aforementioned ESEM microscope.

4.3. Results

4.3.1. Structure of AA template and AANTs produced by pulse anodization

Figure 4.2a shows a schematic description of the structure of the original anodic alumina template featuring the starting MA layer with straight nanopores and the pulsed layer (PA) with nanopore modulations in depth. A combination of selective chemical etching and sonication makes it possible to break down the structure of the AA template into AANTs. The AA structure breaks at the crevices generated at specific positions within its structure during the PA process. These crevices define the geometric features of the resulting AANTs. The geometric features defining the structure of AANTs are the nanotube length (L_{AANT}), and the nanotube inner and outer diameter (d_{in} and d_{out}). Figures 4.2b–d compile a set of representative SEM images of structured anodic alumina films after this anodization process. Figure 4.2b shows a top view SEM image (inset) of the AA template revealing self-organized cylindrical nanopores that follow a honeycomb-like hexagonal arrangement, with average nanopore diameter and interpore distance of 37.6 ± 2.9 nm and 64.8 ± 4.4 nm, respectively. The thicknesses of the MA and PA layers can be clearly discerned in the general cross-sectional SEM image of the AA template. The thickness of the MA layer under the conditions of study (i.e. MA at 25 V using 0.3 M H_2SO_4 electrolyte modified with 10% ethanol at 6°C for 20 h) was 100.9 ± 1.7 μm , while the thickness of the PA layer generated by 70 MA-HA pulses at 325 and 4.5 mA/cm² with durations of 2.5 and 5 s was 41.3 ± 2.0 μm . The interface between the MA and PA layers can be clearly discerned by the formation of stacked layers of AA featuring nanopore modulations (figure 4.2c). Under these anodization conditions, stepwise MA-HA current density pulses can be precisely translated into modulations of nanopore diameter, which in turn generate crevices along the structure of the AA template and lead to the liberation of free-standing AANTs upon selective chemical etching and sonication (figure 4.2d).

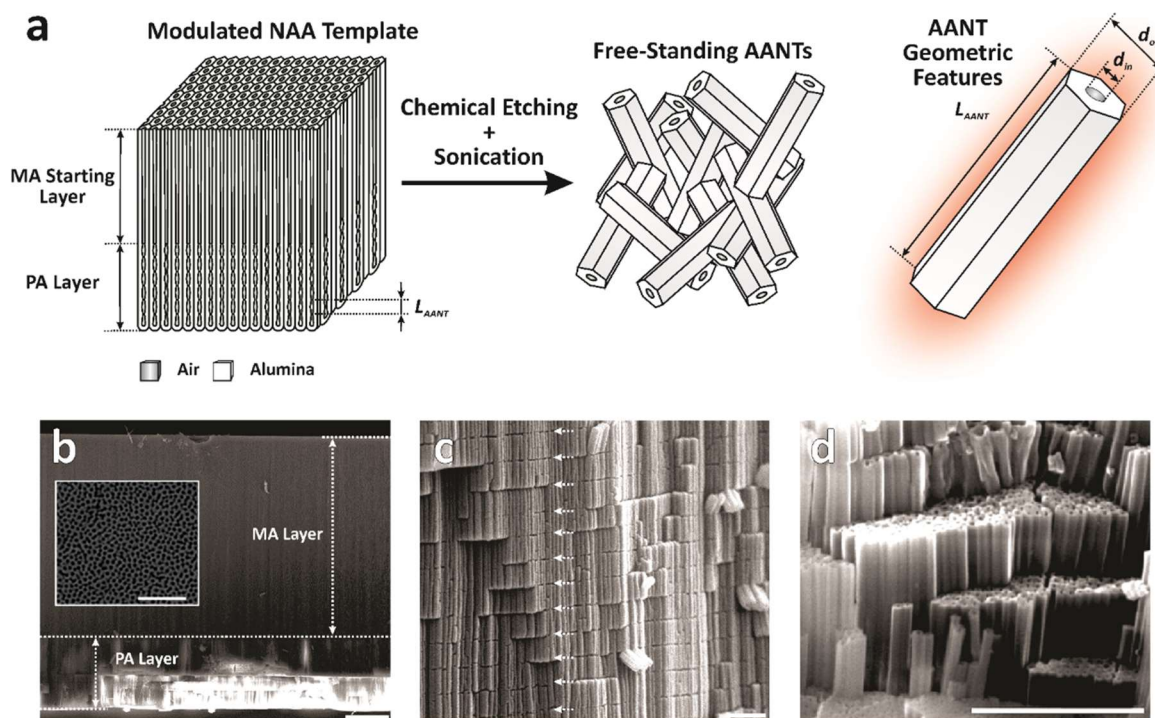


Figure 4.2. Definition of geometric features and SEM characterization of modulated AA template and AANTs (NB: representative SEM images of a modulated AA template produced with HA current density $-J_{HA} = 325 \text{ mA/cm}^2$, MA current density $-J_{MA} = 4.5 \text{ mA/cm}^2$, time at $J_{HA} - t_{HA} = 2.5 \text{ s}$, and time at $J_{MA} - t_{MA} = 5 \text{ s}$). (a) Illustrated scheme of a AA template after pulse anodization (PA) and definition of geometric features of AANTs, with nanotube length (L_{AANT}), and the nanotube inner and outer diameter (d_{in} and d_{out}). (b) General cross-sectional view SEM image of a AA film with dotted line indicating the interface between the MA starting layer and the PA layer (scale bar: $20 \mu\text{m}$) and inset showing a top view SEM image of self-organized nanopores (scale bar: 500 nm). (c) Magnified cross-sectional view SEM image showing details of nanopore modulations and structural crevices in the PA layer (scale bar: $2 \mu\text{m}$). (d) Magnified cross-sectional view SEM image showing non-liberated AANTs within the PA layer (scale bar: $2 \mu\text{m}$).

4.3.2. Evolution of current density/voltage during pulse anodization

Under voltage-control mild anodization regime, nanopore growth is driven by the strength of the applied electric field and the diffusion-controlled migration of ions and electrolytic species across the oxide barrier layer. Conversely, under voltage-control hard anodization regime, nanopore growth is determined by the diffusion path of ionic species along the continuously growing nanopores. Thus, after an initial rapid increase of current density upon application of high voltage, the current density output decreases exponentially with time. This phenomenon has been attributed to the rapid growth rate and the length-dependent nature of nanopore growth under potentiostatic hard anodization conditions [14], [19]. Therefore, under voltage control conditions, the growth rate of nanopores in AA produced by MA-HA pulse anodization

relies on the nanopore length, making it difficult to achieve precise controllability over the nanotubes' length. However, this technical drawback can be overcome by performing MA-HA pulse anodization under current density control since under such conditions the growth rate of nanopores is constant, as established by Faraday's law [30]. Under current density-control conditions, the input current density is the main anodization parameter driving the formation of crevices along the structure of AA during the pulse anodization process. MA-HA current density pulses (input) are translated into voltage pulses (output), which are an indicator of the electrochemical phenomena occurring at the oxide barrier layer during the pulse anodization process. The shape of the output pulse figure 4.3a anodization voltage profile can be divided into two main sections (i): i) an initial section of gradual increase of voltage pulse offset and amplitude (Section I); and ii) a quasi-stable state section with voltage pulse offset and amplitude (Section II) that lasts until electric breakdown occurs, which is denoted by a drastic increase of voltage amplitude. As figure 4.3b reveals, stepwise MA-HA current density pulses are translated into asymmetric sawtooth-like voltage pulses that resemble the characteristic charge–discharge cycle of an electronic capacitor. Voltage pulses can be defined by the voltage amplitude (V_{amp}) and offset (V_{offset}). Efficient formation of AANTs by PA relies strongly on the controlled generation of Joule's heat at the nanopore's bottom. Although there is no in-situ experimental method to quantify the amount of Joule's heat generated during this process, the time at which the critical temperature (T_C) is achieved at the nanopore's bottom is reached (t_{TC}) can be established with precision by analysing the anodization profile (figure 4.3a). Formation of AANTs is denoted by the stabilization of the voltage amplitude and offset upon application of stepwise MA-HA current density pulses.

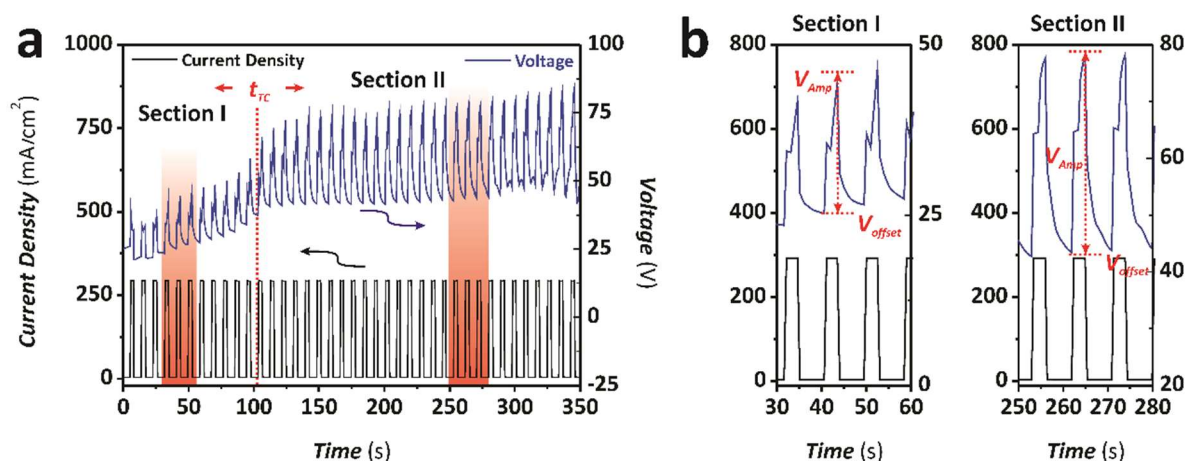


Figure 4.3. Analysis of PA profile obtained during the fabrication of AANTs under current density-control conditions (NB: representative profile for HA current density – $J_{HA} = 290 \text{ mA/cm}^2$, MA current density – $J_{MA} = 4.5 \text{ mA/cm}^2$, time at $J_{HA} - t_{HA} = 3.5 \text{ s}$, and time at $J_{MA} - t_{MA} = 5 \text{ s}$). (a) PA profile showing the initial increment in voltage amplitude (V_{amp}) and offset (V_{offset}) (Section I) and stabilization of the PA process after reaching the critical temperature at t_{TC} (Section II). (b) Magnified view of current density and voltage pulses (red rectangles in (a)) in the PA profile before (Section I) and after (Section II) reaching the critical temperature at t_{TC} .

4.3.3. Effect of hard anodization current density on the physical and chemical properties of AANTs

The current density input is a key anodization parameter in driving the generation of AANTs by MA-HA pulse anodization. To investigate the effect of this parameter on the geometric features of AANTs, AA templates with a 100 μm thick MA starting layer were pulse-anodized with varying HA current density ($J_{HA} = 290, 325$ and 390 mA/cm^2). The rest of anodization parameters (i.e. MA current density – J_{MA} , time at J_{MA} – t_{MA} , and time at J_{HA} – t_{HA}) were kept constant at 4.5 mA/cm^2 , 5 s and 3.5 s, respectively. Figures 4.4a–c show representative current density–voltage PA anodization profiles at varying HA current density (i.e. $J_{HA} = 290, 325$ and 390 mA/cm^2). At first glance, it is apparent that the higher J_{HA} the shorter t_{TC} is, with $t_{TC} \sim 93.5, 51.0$ and 25.5 s (i.e. 11, 6 and 3 pulses) for $J_{HA} = 290, 325$ and 390 mA/cm^2 . From this result, it is inferred that higher HA current densities are more favorable for the generation of AANTs since the critical temperature is reached at shorter t_{TC} . Analysis of the output voltage pulses characterizing this process reveal that the rise of voltage amplitude during Section I is much more pronounced as J_{HA} is increased. The increment of V_{amp} during Section I for pulse-anodized AA templates produced with $J_{HA} = 290, 325$ and 390 mA/cm^2 was $0.935 \pm 0.001, 2.785 \pm 0.611$ and $12.051 \pm 0.157 \text{ V/pulse}$, respectively. However, V_{amp} is stabilized after the critical temperature is reached, as indicated by the small variation of this parameter with the number of pulses during Section II. The increment of V_{amp} during Section II was $0.208 \pm 0.030, -0.036 \pm 0.009$ and $-0.085 \pm 0.007 \text{ V/pulse}$ for $J_{HA} = 290, 325$ and 390 mA/cm^2 , respectively. These results indicate that V_{amp} increases slightly with the number of pulses at $J_{HA} = 290 \text{ mA/cm}^2$, and remains almost constant at $J_{HA} = 325$ and 390 mA/cm^2 (i.e. negative but almost negligible change in V_{amp}). Analysis of V_{offset} (figure 4.S.2 – Supplementary data) reveals that this electrochemical parameter follows qualitatively comparable trend to that shown by V_{amp} , with marked increment prior to t_{TC} and stabilizing after reaching the critical temperature at the nanopore's bottom. The increment of V_{offset} within Section I for PA AA templates produced with $J_{HA} = 290, 325$ and 390 mA/cm^2 was $1.092 \pm 0.143, 4.195 \pm 1.111$ and $0.913 \pm 0.370 \text{ V/pulse}$, with maximum and minimum V_{offset} values of 21–33, 20–44 and 22–26 V, respectively. The increment of V_{offset} during Section II is less marked, with rates of $0.268 \pm 0.032, 0.017 \pm 0.010$ and $0.099 \pm 0.006 \text{ V/pulse}$ for PA AA templates produced with $J_{HA} = 290, 325$ and 390 mA/cm^2 , respectively. The maximum and minimum V_{offset} values within this stage of the anodization process were 37–48, 41–42 and 37–41 V, respectively.

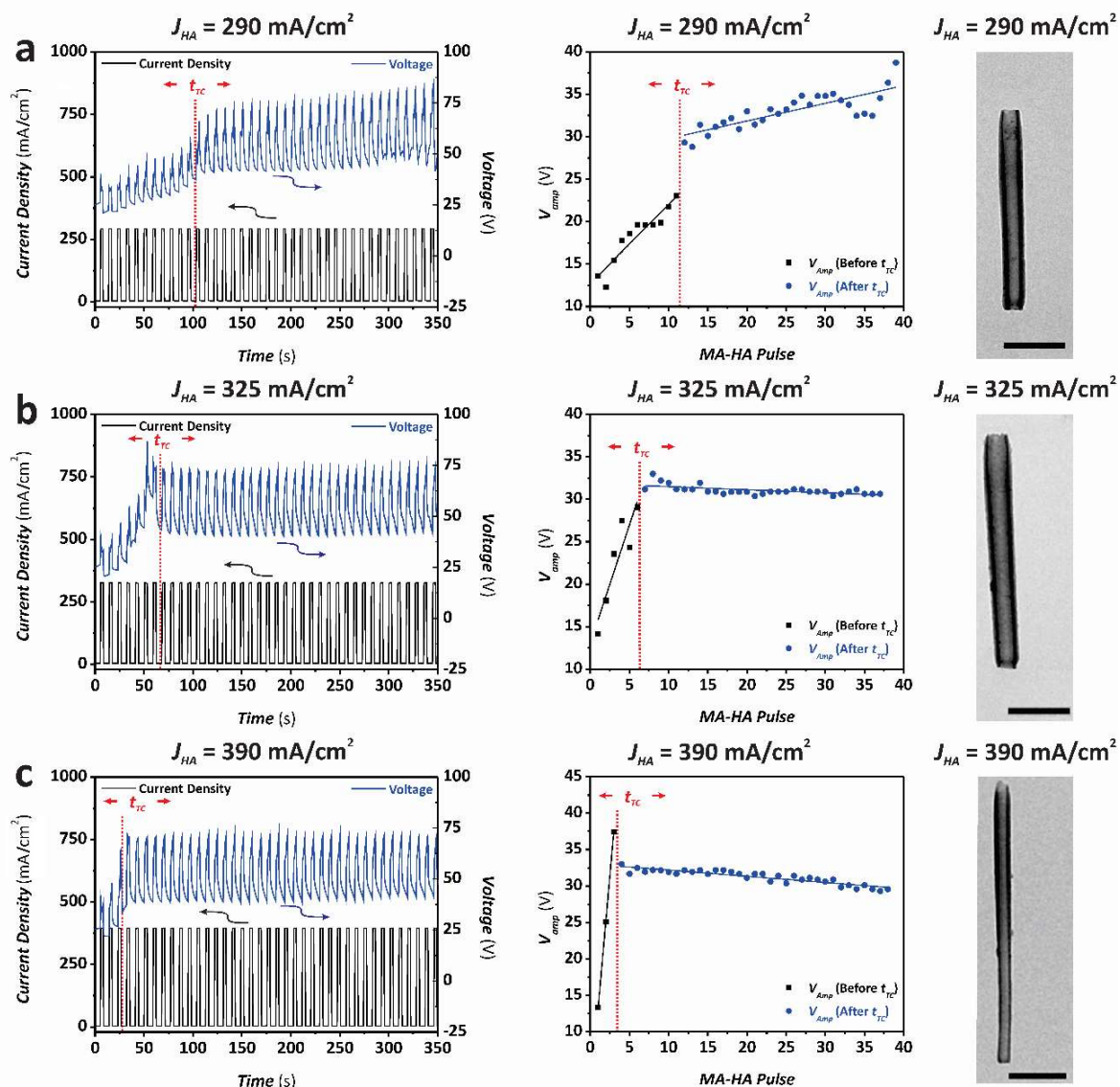


Figure 4.4. Analysis of PA profile (voltage amplitude – V_{amp} and offset – V_{offset}) obtained during the fabrication of AANTs under current density-control conditions at different HA current density inputs ($J_{HA} = 290, 325$ and 390 mA/cm^2) (NB: representative profiles for MA current density – $J_{MA} = 4.5 \text{ mA/cm}^2$, time at $J_{HA} - t_{HA} = 3.5 \text{ s}$, and time at $J_{MA} - t_{MA} = 5 \text{ s}$). (a) Full PA current density/voltage profile showing the initial increment in V_{amp} and V_{offset} and stabilization of the PA process after reaching the critical temperature at t_{TC} (dotted red line) for $J_{HA} = 290 \text{ mA/cm}^2$ (left), dependence of V_{amp} with the number of MA-HA pulses before and after reaching the critical temperature at t_{TC} (center), and TEM image of a representative AANT (scale bar: 200 nm). (b) Full PA current density/voltage profile showing the initial increment in V_{amp} and V_{offset} and stabilization of the PA process after reaching the critical temperature at t_{TC} (dotted red line) for $J_{HA} = 325 \text{ mA/cm}^2$ (left), dependence of V_{amp} with the number of MA-HA pulses before and after reaching the critical temperature at t_{TC} (center), and TEM image of a representative AANT (scale bar: 200 nm). (c) Full PA current density/voltage profile showing the initial increment in V_{amp} and V_{offset} and stabilization of the PA process after reaching the critical temperature at t_{TC} (dotted red line) for $J_{HA} = 390 \text{ mA/cm}^2$ (left), dependence of V_{amp} with the number of MA-HA pulses before and after reaching the critical temperature at t_{TC} (center), and TEM image of a representative AANT (scale bar: 200 nm).

TEM images of free-standing AANTs generated from modulated AA templates produced with $J_{HA} = 290, 325$ and 390 mA/cm^2 after selective chemical etching and sonication reveal that AANTs increase their length (L_{AANT}) with J_{HA} (figures 4.4a–c). Graphs shown in figures 4.5a and b illustrate the dependence of AANTs' geometric features (L_{AANT} , d_{in} and d_{out}) with J_{HA} for $J_{HA} = 290, 325$ and 390 mA/cm^2 . Figure 4.5a reveals a linear correlation between L_{AANT} and J_{HA} , with the former structural feature increasing at a rate of $2.9 \pm 0.5 \text{ nm}/(\text{mA/cm}^2)$ with the latter anodization parameter. AANTs produced with $J_{HA} = 290, 325$ and 390 mA/cm^2 feature an average total length of $720 \pm 96, 847 \pm 79$ and $1008 \pm 118 \text{ nm}$, respectively (distribution histograms shown in figure 4.5.3 – Supplementary data). We also estimated thickness to charge density ratio (α) during hard anodization pulses. For $J_{HA} = 290, 325$ and 390 mA/cm^2 , charge value is $83, 93$ and $111 \text{ mA/cm}\cdot\text{s}$. In all cases, ratio value remains on similar level of $1.40 \text{ C}/\mu\text{m}\cdot\text{cm}^2$, which is lower than for typical values for mild anodization sulfuric acid at 25 V ($1.70\text{-}1.90 \text{ C}/\mu\text{m}\cdot\text{cm}^2$) [37]. Analysis of the interplay between J_{HA} and d_{out} and d_{in} is shown in figure 4.5b, revealing a linear dependence between these geometric features and the HA current density input. AANTs produced with $J_{HA} = 290, 325$ and 390 mA/cm^2 feature an average d_{out} of $98.2 \pm 11.4, 81.3 \pm 12$ and $65.5 \pm 10.1 \text{ nm}$, respectively, with a decreasing linear rate of $-0.32 \pm 0.05 \text{ nm}/(\text{mA/cm}^2)$. The inner diameter of AANTs fabricated with $J_{HA} = 290, 325$ and 390 mA/cm^2 has value of $47.9 \pm 7.4, 42.1 \pm 4.9$ and $36.8 \pm 5.7 \text{ nm}$, respectively. d_{in} was found to decrease at a linear rate of $-0.11 \pm 0.02 \text{ nm}/(\text{mA/cm}^2)$ with J_{HA} under the conditions of study. To the best of our knowledge, there is no study assessing the impact of the hard anodization current density on the nanotubes' inner and outer diameter. Similar trend, however, has been observed for anodic alumina produced during continuous hard anodization [13], [38]. These studies found that the cell size decreases with the current density input. One of the hypothesis regarding creation of these weaker spots is that high current density may result in the formation of less dense forms of alumina, which will also contribute to the nanotube diameter contraction due to partial dissolution of more susceptible alumina upon the acid etching treatment applied during liberation [39]. Control over the geometric features of AANTs is critical to engineer the properties of these 1D nanostructures for specific applications. However, AANTs' physico-chemical properties are also a key factor in determining the applicability of this model nanomaterial in disciplines such as drug delivery and nanotoxicity. Motivated by these results, we analyzed the effect of J_{HA} on the ζ -potential of AANTs produced by pulse anodization.

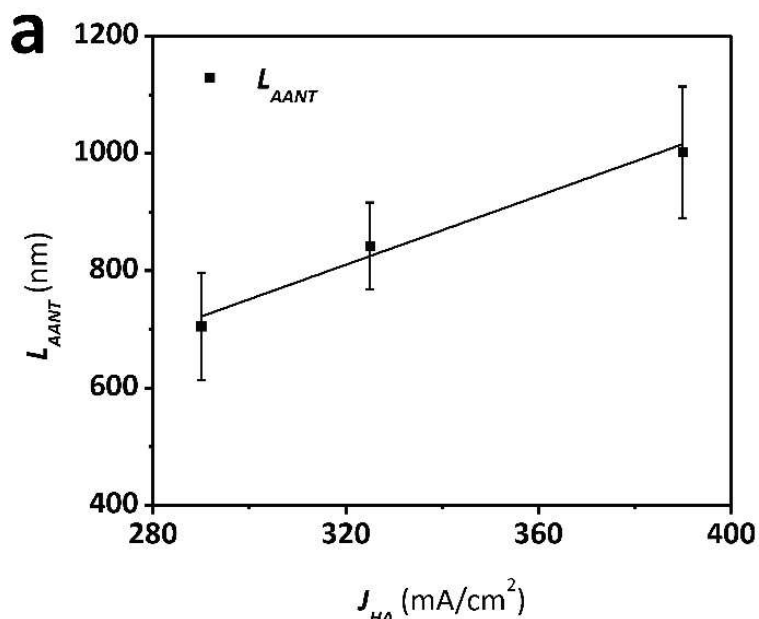
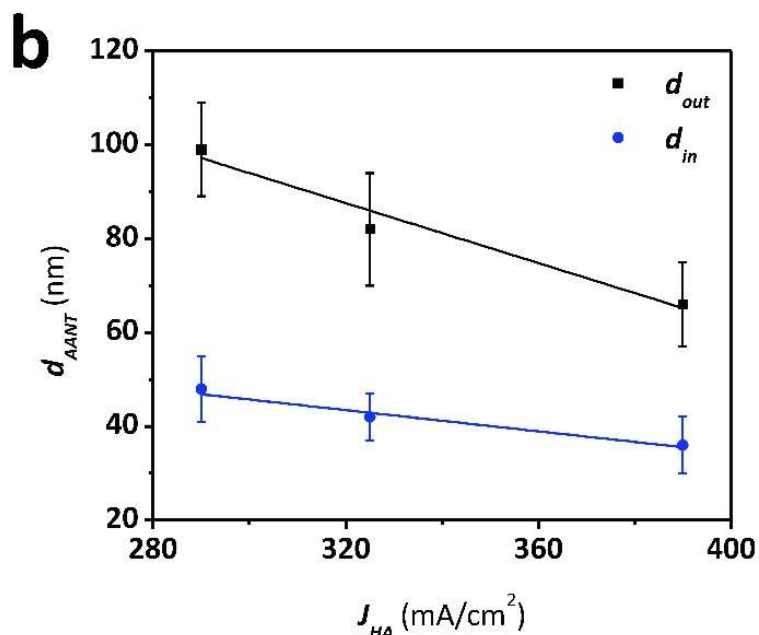
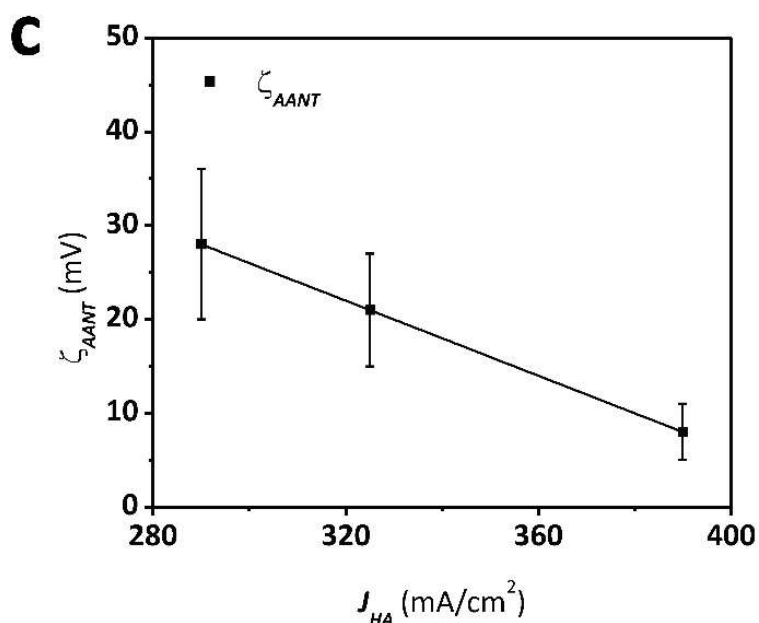


Figure 4.5. Analysis of effect of HA current density (J_{HA}) on the geometric and physico-chemical properties of AANTs produced by PA.

(a) Linear dependence between the total length of AANTs (L_{AANT}) and J_{HA} , in which the later structural feature increases at a rate of $2.9 \pm 0.5 \text{ nm}/(\text{mA}/\text{cm}^2)$ with the former anodization parameter.



(b) Linear dependence between the outer and inner diameter of AANTs (d_{out} and d_{in}) and J_{HA} , in which the later geometric features decrease at rates of -0.32 ± 0.05 and $-0.11 \pm 0.02 \text{ nm}/(\text{mA}/\text{cm}^2)$ with the former anodization parameter, respectively.



(c) Linear dependence between the ζ -potential of AANTs (ζ_{AANT}) and J_{HA} , in which the later physico-chemical property decreases at a rate of $-0.20 \pm 0.01 \text{ mV}/(\text{mA}/\text{cm}^2)$ with the former anodization parameter.

Figure 4.5c indicates that the ζ -potential of AANTs decreases linearly with J_{HA} at a rate of -0.20 ± 0.01 mV/(mA/cm²) with J_{HA} , where AANTs fabricated with $J_{HA} = 290, 325$ and 390 mA/cm² have a $\zeta_{AANT} = 25.1 \pm 6.8, 19.3 \pm 4.7$ and 8.6 ± 2.3 mV, respectively. Chemistry of AANTs walls is twofold. While outer surface is rich in hydroxyl group, inside walls contain incorporated sulfate anions [23], [40]. During the anodization process, ions from the acid electrolyte are incorporated into the structure of the growing alumina, which features an onion-like distribution of incorporated anions that is higher at the inner layers of the nanopores (i.e. alumina exposed to acid electrolyte) [41]. While in this study we do not evaluate effects of ion incorporation density on resulting zeta potential, it was previously pointed out that sulfate ions are expected to impact behavior of the particles as compared to commercially available alumina nanoparticles [36].

4.3.4. Effect of hard anodization pulse duration on the physical and chemical properties of AANTs

The duration of the hard anodization pulse (t_{HA}) is another key anodization parameter in controlling the structural and physico-chemical properties of AANTs produced by pulse anodization [30]. However, to the best of our knowledge, no study has performed an in-depth analysis on the impact of this anodization parameter over the physio-chemical properties of AANTs. To assess the impact of this parameter on the geometric features of AANTs, AA templates with a MA starting layer of 100 μ m thickness were pulse-anodized at varying hard anodization pulse duration ($t_{HA} = 2.0, 2.5$ and 3.5 s). The rest of anodization parameters (i.e. MA current density – J_{MA} , HA current density – J_{HA} , and time at J_{MA} – t_{MA}) were kept constant at 4.5 mA/cm², 325 mA/cm² and 5 s, respectively. Figures 4.6a–c show representative current density–voltage PA anodization profiles at varying HA duration (i.e. $t_{HA} = 2.0, 2.5$ and 3.5 s). From these graphs, it is apparent that the longer t_{HA} the shorter t_{TC} is, with $t_{TC} = 235, 98.5$ and 43.5 s (i.e. 33, 14 and 6 pulses) for $t_{HA} = 2.0, 2.5$ and 3.5 s. This analysis reveals that longer HA durations enable a more optimal generation of AANTs since the critical temperature is reached at shorter t_{TC} . Analysis of the output voltage pulses characterizing this process reveal that the rise of V_{amp} during Section I is more marked as t_{HA} is increased. The increment of V_{amp} during Section I for pulse-anodized AA templates produced with $t_{HA} = 2.0, 2.5$ and 3.5 s was 0.089 ± 0.001 , and 0.745 ± 0.115 and 2.785 ± 0.611 V/pulse, respectively. However, it is worthwhile noting that a 1.462 ± 0.063 V/pulse sharp increment in V_{amp} is observed at $t_{HA} = 2.0$ s after ~ 25 pulses (50 s).

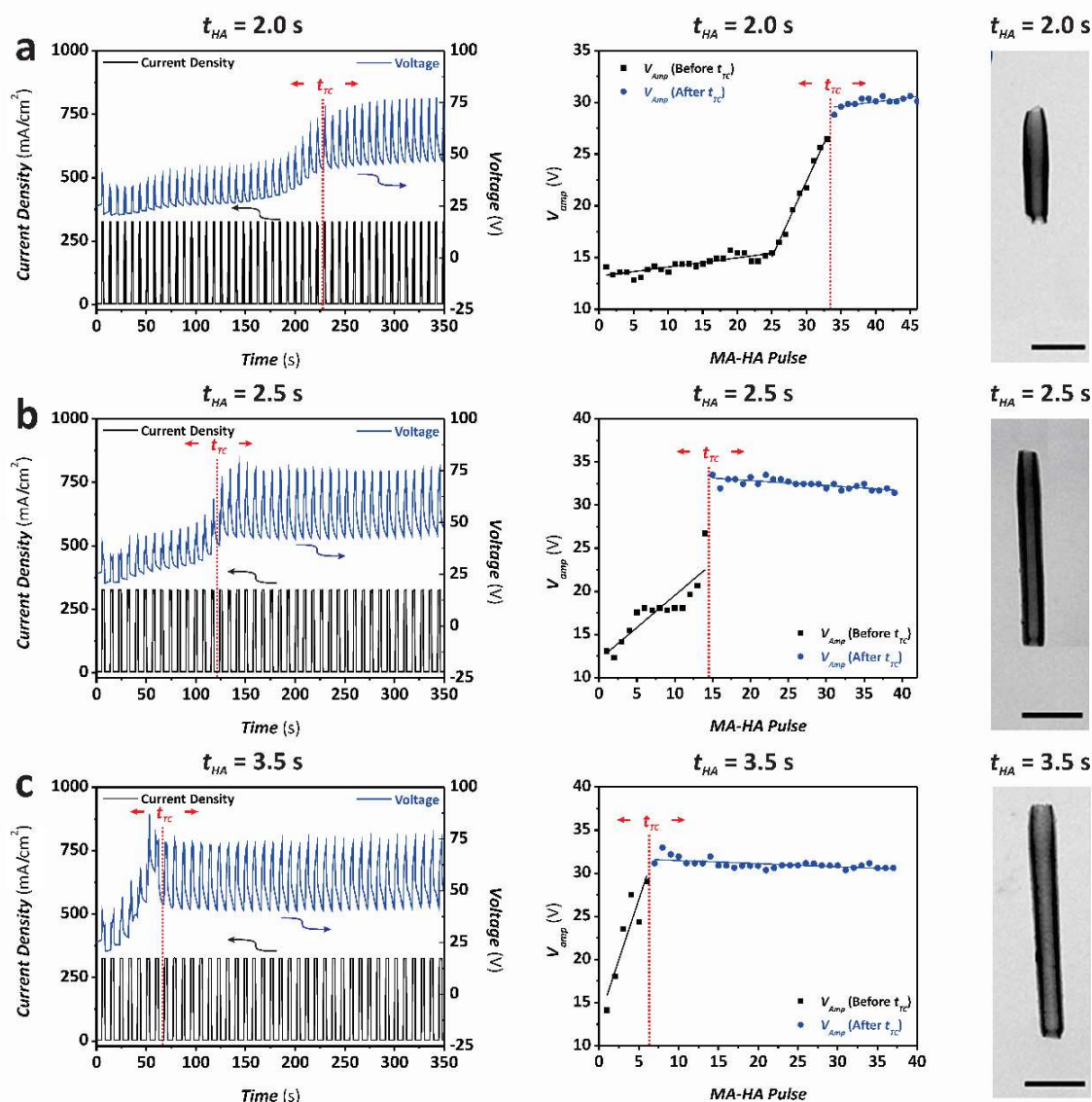


Figure 4.6. Analysis of PA profile (voltage amplitude – V_{amp} and offset – V_{offset}) obtained during the fabrication of AANTs under current density-control conditions at different HA durations ($t_{HA} = 2.0, 2.5$ and 3.5 s) (NB: representative profiles for MA current density – $J_{MA} = 4.5$ mA/cm², HA current density – $J_{HA} = 325$ mA/cm², and time at J_{MA} – $t_{MA} = 5$ s). (a) Full PA current density/voltage profile showing the initial increment in V_{amp} and V_{offset} and stabilization of the PA process after reaching the critical temperature at t_{TC} (dotted red line) for $t_{HA} = 2.0$ s (left), dependence of V_{amp} with the number of MA-HA pulses before and after reaching the critical temperature at t_{TC} (center), and TEM image of a representative AANT (scale bar: 200 nm). (b) Full PA current density/voltage profile showing the initial increment in V_{amp} and V_{offset} and stabilization of the PA process after reaching the critical temperature at t_{TC} (dotted red line) for $t_{HA} = 2.5$ s (left), dependence of V_{amp} with the number of MA-HA pulses before and after reaching the critical temperature at t_{TC} (center), and TEM image of a representative AANT (scale bar: 200 nm). (c) Full PA current density/voltage profile showing the initial increment in V_{amp} and V_{offset} and stabilization of the PA process after reaching the critical temperature at t_{TC} (dotted red line) for $t_{HA} = 3.5$ s (left), dependence of V_{amp} with the number of MA-HA pulses before and after reaching the critical temperature at t_{TC} (center), and TEM image of a representative AANT (scale bar: 200 nm).

Once the critical temperature is reached, V_{amp} stabilizes and the generation of AANTs becomes efficient. This stage is denoted by small variation of this parameter with the number of pulses during Section II. The increment of V_{amp} during Section II for $t_{HA} = 2.0, 2.5$ and 3.5 s was $0.085 \pm 0.027, -0.058 \pm 0.011$ and -0.036 ± 0.009 V/pulse, respectively. These results reveal that V_{amp} increases slightly with the number of pulses at $t_{HA} = 2.0$ s, and decreases slightly at $t_{HA} = 2.5$ and 3.5 . V_{offset} (figure 4.S.4 – Supplementary data) follows a qualitatively comparable trend to that observed for V_{amp} , with marked increment prior to t_{TC} and stabilizing after reaching the critical temperature at the nanopore's bottom. The increment of V_{offset} within Section I for PA AA templates produced with $t_{HA} = 2.0, 2.5$ and 3.5 s was $0.622 \pm 0.053, 0.857 \pm 0.101$ and 4.195 ± 1.111 V/pulse, with maximum and minimum V_{offset} values of 25–35, 25–44 and 25–27 V, respectively. The increment of V_{offset} during Section II is less marked and decreases with increasing t_{HA} , with rates of $0.215 \pm 0.019, 0.085 \pm 0.019$ and 0.017 ± 0.010 V/pulse for PA AA templates produced with $t_{HA} = 2.0, 2.5$ and 3.5 s, respectively. The maximum and minimum V_{offset} values within this stage of the anodization process were 37–49, 41–42 and 37–41 V, respectively. Figures 4.6a–c show TEM images of free-standing AANTs fabricated with $t_{HA} = 2.0, 2.5$ and 3.5 s after selective chemical etching and sonication. At first glance, it is evident that the longer t_{HA} the longer AANTs are. The dependence of AANTs' geometric features (L_{AANT} , d_{in} and d_{out}) with t_{HA} for $t_{HA} = 2.0, 2.5$ and 3.5 s is shown in figures 4.7a and b. Figure 4.7a reveals a linear correlation between L_{AANT} and t_{HA} , in which the former structural feature increases at a rate of 268 ± 3 nm/s with the latter anodization parameter. AANTs produced with $t_{HA} = 2.0, 2.5$ and 3.5 s feature an average total length of $424 \pm 46, 562 \pm 47$ and 830 ± 53 nm, respectively (distribution histograms shown in figure 4.S.5 – Supplementary data). Figure 4.7b shows analysis of the relationship between t_{HA} and d_{out} and d_{in} . This graph indicates that t_{HA} has small impact on the dimensions of these geometric features in AANTs from 2.0 to 3.5 s. For instance, while d_{out} undergoes a slight linear increment with t_{HA} (i.e. 0.562 ± 0.056 nm/s), d_{in} decreases at a rate of -0.451 ± 0.440 nm/s from $t_{HA} = 2.0$ to 3.5 s. AANTs produced with $t_{HA} = 2.0, 2.5$ and 3.5 s feature an average d_{out} of $80.1 \pm 5.2, 82.8 \pm 8.0$ and 81.3 ± 6.0 nm, and an average d_{in} of $42.7 \pm 4.7, 42.1 \pm 3.8$ and 42.2 ± 2.4 nm, respectively. Assessment of the effect of the hard anodization duration on the nanotubes' geometric features indicates that, in contrast to J_{HA} , t_{HA} is a suitable anodization parameter to produce AANTs with tunable total length and controlled inner and outer diameter. In other words, t_{HA} makes it possible to fabricate AANTs with distinct length and same inner and outer diameter.

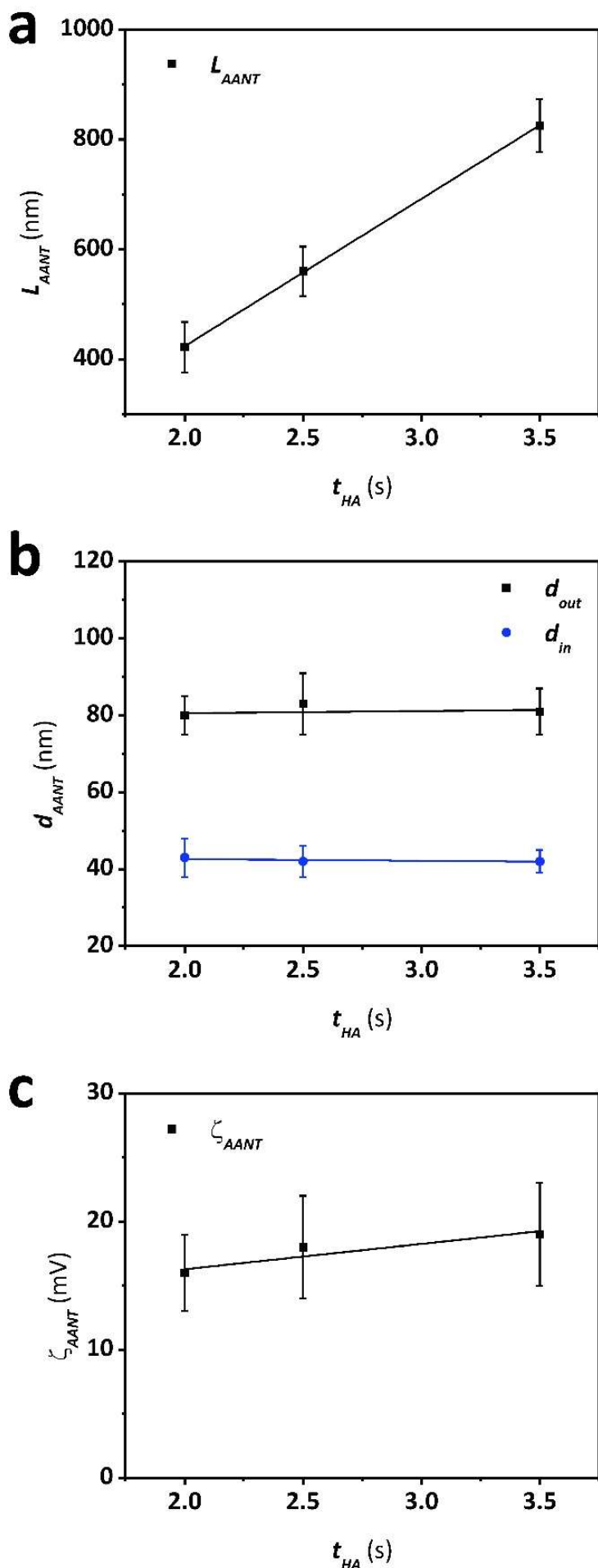


Figure 4.7. Analysis of effect of HA duration (t_{HA}) on the geometric and physico-chemical properties of AANTs produced by pulse anodization.

(a) Linear dependence between the total length of AANTs (L_{AANT}) and t_{HA} , in which the later structural feature increases at a rate of 268 ± 3 nm/s with the former anodization parameter.

(b) Linear dependence between the outer and inner diameter of AANTs (d_{out} and d_{in}) and t_{HA} , in which the later geometric features vary at rates of 0.562 ± 0.056 and -0.451 ± 0.440 nm/s with the former anodization parameter, respectively.

(c) Linear dependence between the ζ -potential of AANTs (ζ_{AANT}) and t_{HA} , in which the later physico-chemical property increases at a rate of 1.98 ± 0.71 mV/s with the former anodization parameter.

Therefore, t_{HA} provides excellent accuracy to tailor-engineer the length of AANTs without modifying the inner and outer diameter of AANTs. The duration of the hard anodization pulse is also found to moderately impact ζ -potential of AANTs. Figure 4.7c shows that ζ_{AANT} increases at a rate of 1.98 ± 0.71 mV/s with t_{HA} from 2.0 to 3.5 s. It is worthwhile noting that the total surface area is higher for shorter nanotubes. So, the influence of the AANTs' inner surface on the average ζ -potential it is expected to be higher in shorter nanotubes. Another factor affecting ζ_{AANT} is the heterogeneous distribution of electrolyte anions following an onion-like structure between the outer and inner layers of AANTs, which also affects the average ζ -potential of these nanostructures.

4.3.5. Post-treatment modification of AANTs produced by pulse anodization

Pulse anodization provides an effective approach to tune the geometric and physico-chemical features of AANTs. This nanofabrication approach was devised as a cost-effective means for mass-production of AANTs. However, liberation of AANTs from the original pulsed AA template remains challenging, requiring precise-tuning of the post-treatment conditions so nanotubes can be efficiently liberated [42]. This aspect is of paramount importance if we are to enable AANT technology for applications requiring high production yields, such as catalysis and drug delivery. Motivated by this challenge, we studied the effect of different post-treatment processes to selectively weak the structure of pulsed AA templates and facilitate the liberation of AANTs, including sonication, thermal treatment, and chemical etching.

4.3.5.1. Effect of sonication parameters on dispersity and separation of AANTs

Sonication time

Fabrication of AANTs by pulse anodization is a top-down process in which the anodic alumina structure is typically grinded down by sonication. Weaker spots and crevices along the pulsed AA structure promote the selective breaking of the structure at designed spots, leading to the liberation of nanotubes with controlled geometric features. However, imperfections in the structure of the AA template result in incomplete or partial fragmentation and liberation of nanotubes, minimizing the production yield. A sonication treatment of 1 h performed at room temperature conditions leads to presence of AANTs aggregates and bundles. Figure 4.8a shows a schematic showing the impact of the sonication time on AANTs. TEM images of AANTs shown in figure 4.8b reveal a significant change in surface morphology when the sonication time is increased from 1 to 2 h. The surface of AANTs after sonication time >1 h is covered with dust-like nanoparticles, which are thought to be generated from the alumina matrix during the sonication process. Alumina nanoparticles are electrostatically attached onto the surface of AANTs.

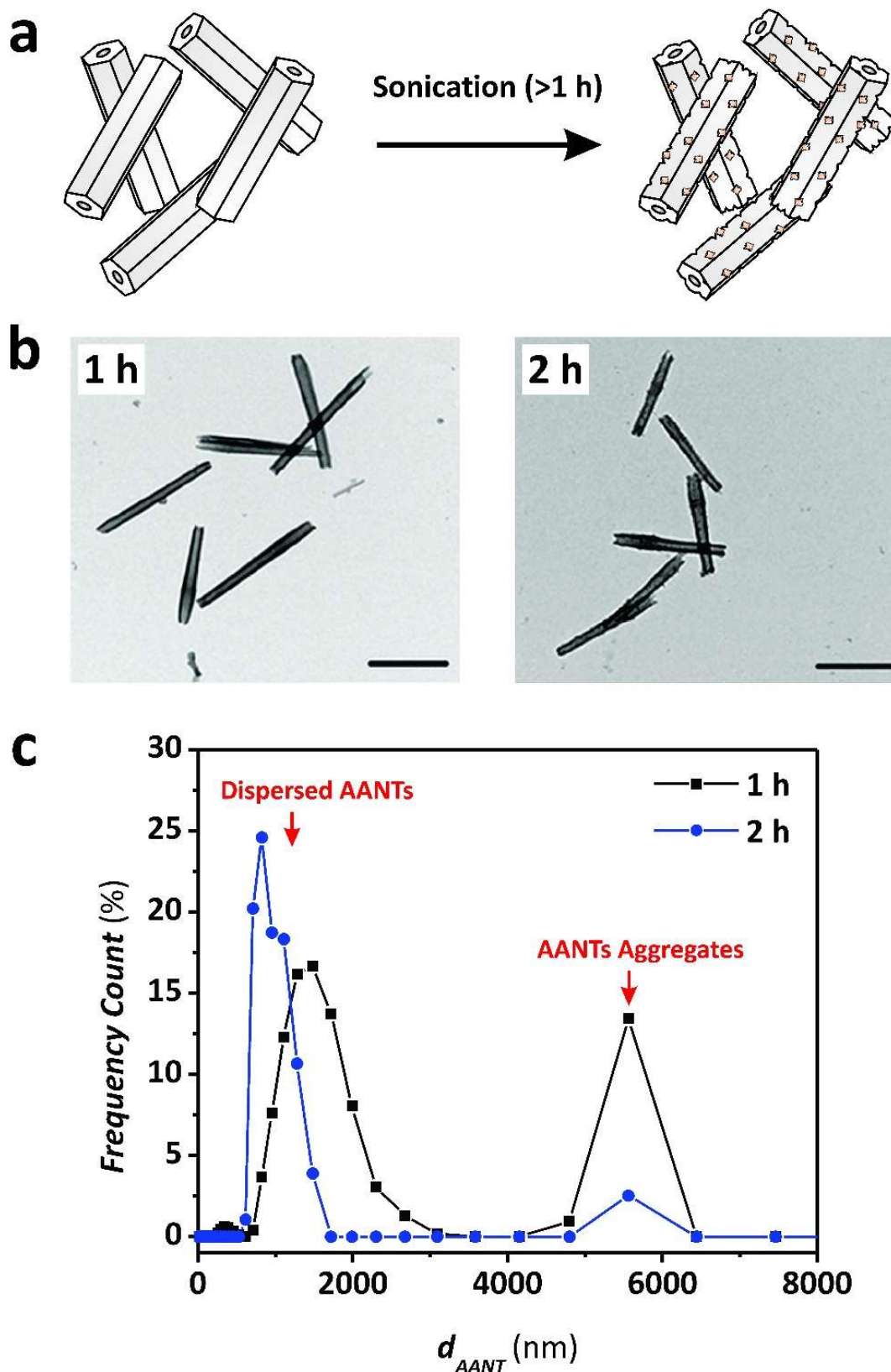


Figure 4.8. Effect of sonication time on the dispersity and morphology of AANTs fabricated by pulse anodization (NB: AANTs fabricated with $J_{MA} = 4.5 \text{ mA/cm}^2$, $J_{MA} = 325 \text{ mA/cm}^2$, $t_{MA} = 5 \text{ s}$ and $t_{HA} = 3.5 \text{ s}$). (a) Schematic illustrating the impact of sonication (1 and 2 h) on the morphology of AANTs. (b) TEM images of AANTs after 1 h (left) and 2 h (right) of sonication (scale bars: 500 nm). (c) DLS size distribution of AANTs after 1 and 2 h of sonication.

Analysis of AANTs' size distribution by DLS shows two distinct peaks associated with the separated fraction and aggregates of AANTs upon 1 and 2 h of sonication treatment (figure 4.8c). After 1 h of sonication treatment, the DLS profile shows a relatively more intense size peak located at ~ 1400 nm, which corresponds to liberated AANTs. The peak associated with the fraction of unseparated structures is also relatively intense, with an average diameter of ~ 6 μm . This result indicates that the liberation of nanotubes from the anodic alumina structure is not so effective after 1 h of sonication treatment. However, upon longer sonication time the peak representing the fraction of liberated nanotubes becomes narrower and shifted towards smaller sizes (~ 820 nm average), indicating that the liberation of nanotubes is much more efficient under such conditions. Furthermore, the size peak from aggregates is significantly reduced. These results indicate that, although longer sonication treatment enhances the liberation of AANTs and minimizes the aggregate fraction, this treatment leads to a partial degradation of the nanotubes' structure.

Sonication temperature

The impact of the temperature of the sonication bath on the dispersion and morphology of nanotubes was investigated by performing sonication of nanotubes for 1 h at three different temperatures: 15, 30 and 65°C. Note that the temperature below ambient conditions was maintained using ice to cool down the sonication bath under constant temperature monitoring. Figure 4.9a shows a schematic description of morphological changes in AANTs liberated at different sonication temperatures. From these results it is apparent that increased sonication temperature affects the morphology of AANTs. No visible changes in morphology are observed in nanotubes liberated under sonication at 15°C (figure 4.9b). Although the structure of AANTs keeps its original morphology, sonication at 30°C results in formation of a coating layer. When the sonication bath temperature is increased to 65°C, the degradation of the structure of nanotubes is apparent, with the formation of partially dissolved and unzipped nanotubes forming aggregates without defined shape. DLS size distribution analysis shown in figure 4.9c reveals two major size peaks corresponding to liberated nanotubes and aggregates. While the location of these size peaks remains within similar ranges (~ 1000 nm for liberated AANTs and ~ 6 μm for aggregates), their intensity ratio (or relative intensities) varies significantly with the sonication temperature. An increase in sonication temperature leads to the gradual increment and decrement of the size peak associated with the aggregates and liberated nanotubes, respectively.

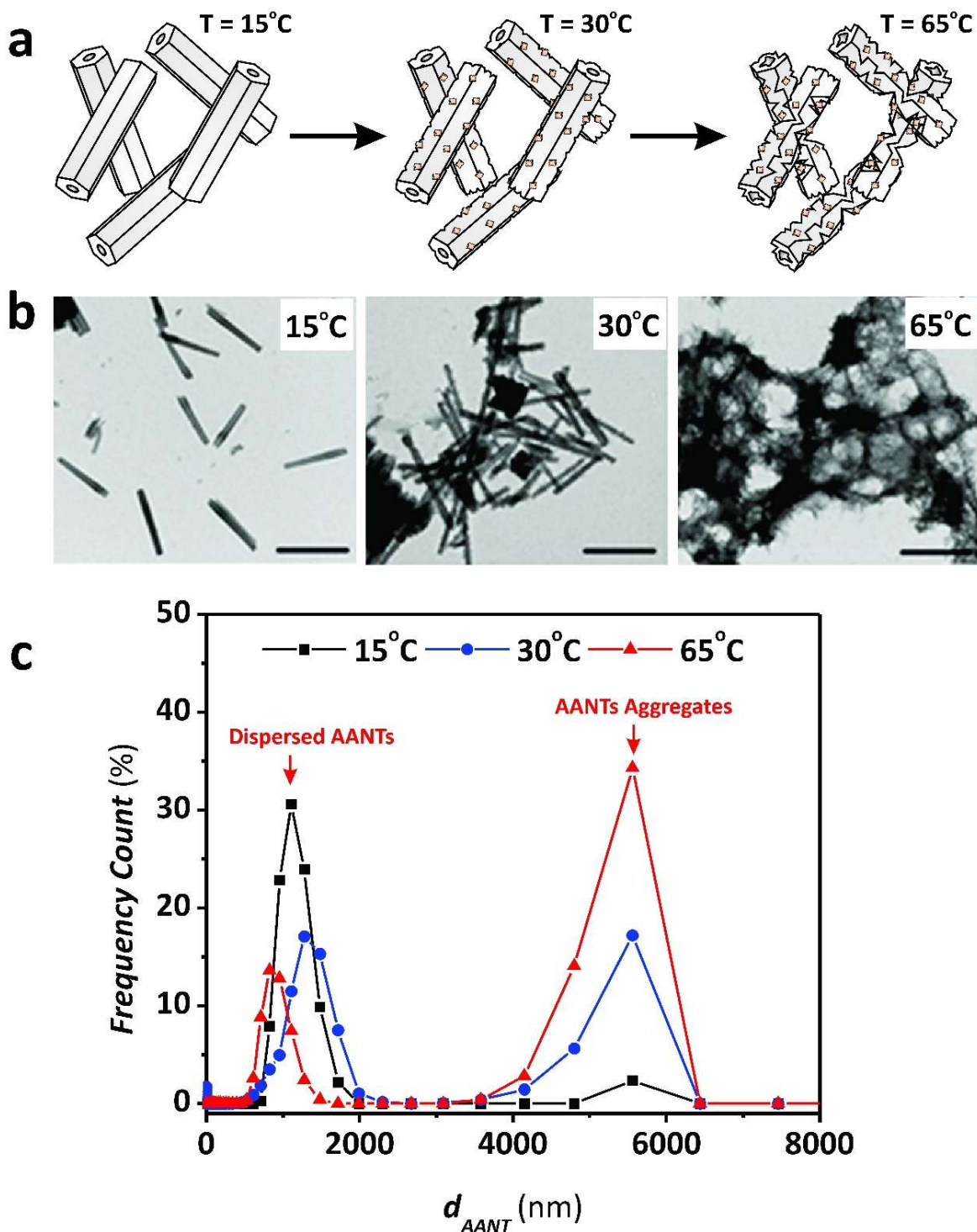


Figure 4.9. Effect of bath temperature on the dispersity and morphology of AANTs fabricated by pulse anodization (NB: AANTs fabricated with $J_{\text{MA}} = 4.5\ \text{mA}/\text{cm}^2$, $J_{\text{MA}} = 325\ \text{mA}/\text{cm}^2$, $t_{\text{MA}} = 5\ \text{s}$ and $t_{\text{HA}} = 3.5\ \text{s}$). (a) Schematic illustrating the impact of the bath temperature (15, 30 and 65°C) on the morphology of AANTs. (b) TEM images of AANTs at 15°C (left), 30°C (center) and 65°C (right) bath temperature (scale bars: $1\ \mu\text{m}$). (c) DLS size distribution of AANTs after liberation in 15, 30 and 65°C bath temperature.

Several factors are thought to promote the formation of nanotubes aggregates under these conditions. Different sonication bath temperature results in increasing number of nanotube–nanotube interactions. Brownian motion of AANTs is faster at higher temperature, resulting in more frequent interactions between nanotubes, which may weaken the mechanical strength of AANTs. Also, viscosity of water at 65°C is 2.7 times lower than of water at 15°C. Higher viscosity can increase shear forces between individual nanotubes, promoting a more efficient separation. Other factors such as cavitation could also have an impact on the AANTs' structure at different sonication temperatures [43], [44]. Additionally, a combination of temperature and sonication could promote the formation of hydrated forms of alumina, which in turn would weaken the structure of AANTs [45]. To summarize, sonication at lower temperature provides the best separation yield within the conditions of study, preventing AANTs from undesired degradation.

4.3.5.2. Effect of annealing temperature on the crystallinity and physio-chemical properties of AANTs

Aluminum oxide (Al_2O_3) can feature amorphous and several crystalline phases. The composition of the crystalline phase of anodic alumina depends on the fabrication process and its processing conditions. Phase transition of initially amorphous AA can be induced with annealing. Formation of crystallites occurs with annealing above 700°C when gamma alumina emerge. Then, at temperature above 1100°C another crystalline form, alpha alumina appear initially as a small fraction. Further increasing temperature, ratio of gamma to alpha crystalline forms decrease and above 1200°C only alpha alumina form can be detected. Alpha alumina exhibit far higher resistance to acid and chemical etching, compared to other crystalline and amorphous forms [46]. Thermal and chemical resistance along with other physical properties makes anodic alumina attractive material platform amongst other ceramic-base materials [47]. In order to analyze impact of the annealing temperature on the phase composition of AANTs, a set of pulsed AA structures were exposed to thermal treatment at different temperatures: 850, 1050 and 1200°C. Annealed pulsed AA templates and liberated AANTs were analyzed by XRD, TEM, DLS, SEM (figure 4.10). As-produced AANTs have a smooth surface. However, small morphological changes can already be observed in AANTs after annealing at 850°C. These AANTs show small pits homogeneously distributed across their surface and much darker walls, denoting a much dense form of alumina upon 850°C thermal treatment (figure 4.10a). These changes might be associated with decomposition of electrolyte anions and water loss from the Al_2O_3 structure, and starting transition of its crystallographic phase into gamma Al_2O_3 . EDS analysis (figure 4.S.6 – Supplementary data) reveals that the elemental concentration of sulfur in AANTs decreases by a 77% (from 12.2% to 2.8%) upon thermal annealing at 850°C. This analysis also indicates a slight decrement in oxygen content – from 45.22% to 41.9% – and a noticeable increment in the relative content of aluminum from 42.6% to 55.3%. As annealing temperature increases, morphological

changes in AANTs become more apparent. AANTs show higher granulation on their surface after thermal annealing at 1050°C. This may be associated with further removal of sulfur from their structure, the content of which decreases to 0.82% due to oxidation and gradual release of SO₂ gas. Gas release might induce morphological changes in the structure of AANTs [48]. Deformation of the AANTs' walls also becomes substantial under these conditions. Much apparent morphological changes can be observed in nanotubes annealed at 1200°C. While nanotubes still exhibit elongated shape, the initial nanotubular structure is completely lost. No walls or hollow space inside the nanotubes can be observed, suggesting complete collapse of the structure and the formation of fiber-like aluminum oxide nanoparticles. Additionally, EDS analysis indicates that sulfur has been completely removed from the AANTs' structure. XRD analysis of AANTs reveal no crystalline phases for as-produced AANTs. Subtle changes in diffractogram patterns can be observed at 850°C (figure 4.10b) with presence of peaks at 39.43° (2 2 2), 45.85° (4 0 0) and 66.85° (4 4 0) that are attributed to gamma Al₂O₃. Presence of crystalline phase is more pronounced with sample annealed at 1050°C, with gamma Al₂O₃ alumina phase denoted by major reflection peaks at 39.43° (2 2 2), 45.85° (4 0 0) and 66.85° (4 4 0) and slightly visible peaks at 32.85° (2 2 0), 36.85° (3 1 1) and 61.25° (5 1 1) in the XRD diffractogram (JCPDS cards nos. 00-056-0457). Crystallographic phase transition can induce morphological alterations in the structure of AANTs. As the annealing temperature is raised to 1200°C, a considerable change in the XRD spectrum is observed. Peaks of gamma Al₂O₃ are not visible anymore, instead, sharp peaks of alpha-Al₂O₃ can be observed. Peaks are present at 25.60° (0 1 2), 35.15° (1 0 4), 37.80° (1 1 0), 43.36° (1 1 3), 52.55° (0 2 4), 57.50° (1 1 6), 66.50° (2 1 4) and 68.25° (3 0 0) (JCPDS cards nos. 00-046-1212) and represent only alpha-Al₂O₃. The annealing temperature is also found to impact the surface charge of liberated AANTs. Figure 4.10c shows the effect of this post-treatment parameter on the ζ-potential of AANTs. Reference non-annealed AANTs have a ζ-potential of ~19 mV. As the annealing temperature increases, ζ_{AANT} decreases to 10 and 5 mV at annealing temperatures of 850 and 1050°C, respectively. This surface charge decrement may be attributed to the decrease in sulfur content and hydroxide groups (i.e. water loss) in the structure of AANTs [48]. Further annealing at 1200°C makes ζ_{AANT} negative (-7 mV). Under such conditions, sulfur is completely removed from the structure of AANTs, changing the charge of these 1D nanostructures dramatically [48], [49].

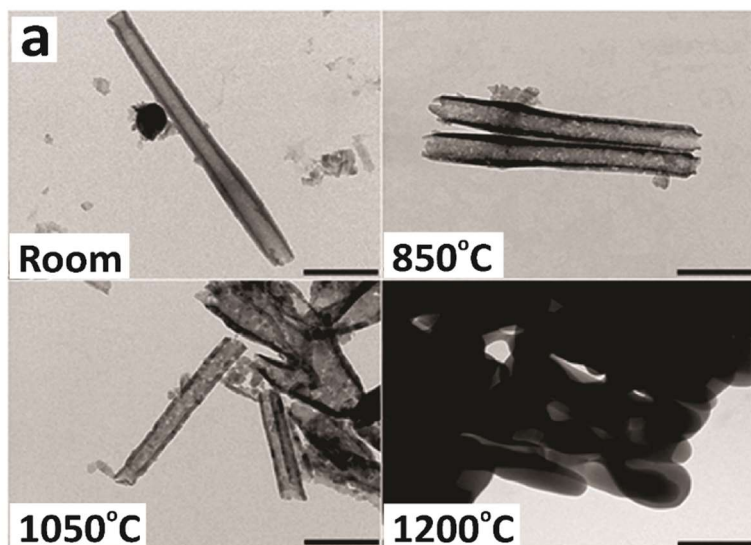
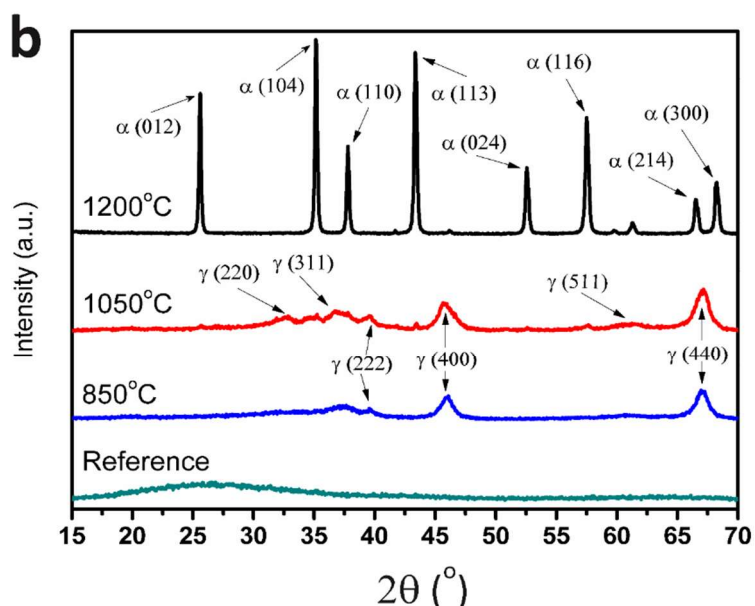
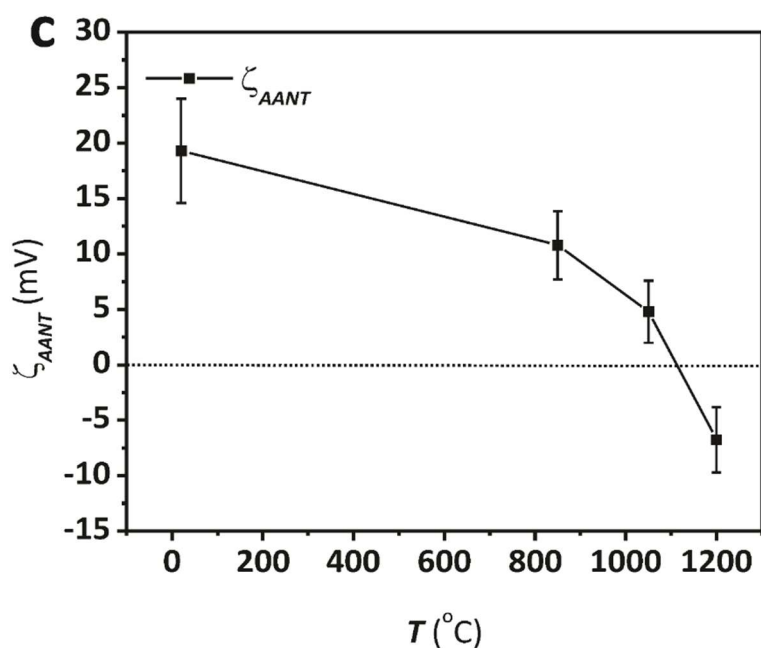


Figure 4.10. Effect of annealing temperature on morphology, crystallographic phase and physico-chemical properties of AANTs produced by pulse anodization (NB: AANTs fabricated with $J_{MA} = 4.5 \text{ mA/cm}^2$, $J_{MA} = 325 \text{ mA/cm}^2$, $t_{MA} = 5 \text{ s}$ and $t_{HA} = 3.5 \text{ s}$). (a) TEM images of AANTs at room, 850, 1050 and 1200°C (scale bars: 200 nm).



(b) XRD spectra of AANTs at room, 850, 1050 and 1200°C.



(c) Change in ζ-potential of AANTs (ζ_{AANT}) with annealing temperature (T).

4.4. Conclusions

In summary, this is a systematic study on the influence of different anodization conditions and post-fabrication treatments on the physical and chemical properties of anodic alumina nanotubes fabricated by current density–control pulse anodization. Our results indicate that the current density input can be readily used as a fabrication parameter to tailor-engineer the AANTs' features such as the inner and outer diameters, the total length and the surface charge. We have demonstrated that higher current density values during hard anodization pulses promote lower surface charge and more narrow shape of nanotubes. A linear dependence between the hard anodization pulse duration and nanotubes average length demonstrates that the hard anodization pulse duration a precise parameter to tailor the nanotubes' length without changing the inner and outer diameters. A systematic optimization of the pulse anodization process has allowed us to fabricate the shortest nanotubes reported so far, with average length of 422 ± 46 nm. Additionally, different sonication parameters were examined to optimize the liberation of AANTs. However, the structure of AANTs is found to be compromised at long sonication times (>1 h) and high sonication bath temperatures (>40°C). The combination of low sonication bath (15°C) with moderate sonication time (1 h) is found to be the most optimal approach to increase the production yield of AANTs while maintaining the structural integrity of these nanostructures. Our study also demonstrates that a post-fabrication annealing treatment can be used to alter the crystalline phase composition and ζ -potential of nanotubes. However, high annealing temperatures (>850°C) lead to a gradual structural degradation of AANTs due to decomposition of sulfur and water loss. This study provides new insights to better understand the impact of the fabrication parameters over the physical and chemical properties of AANTs produced by pulse anodization. This step forward in AANTs technology could provide new and exciting opportunities to design and tailor-engineer these model 1D nanostructures for specific applications, including catalysis, drug delivery, nanofabrication and sensing.

4.5. Supplementary data

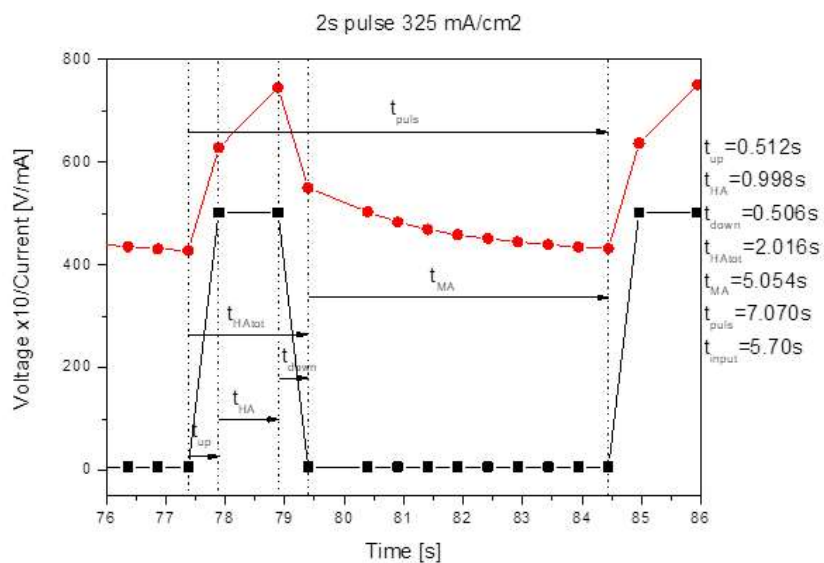
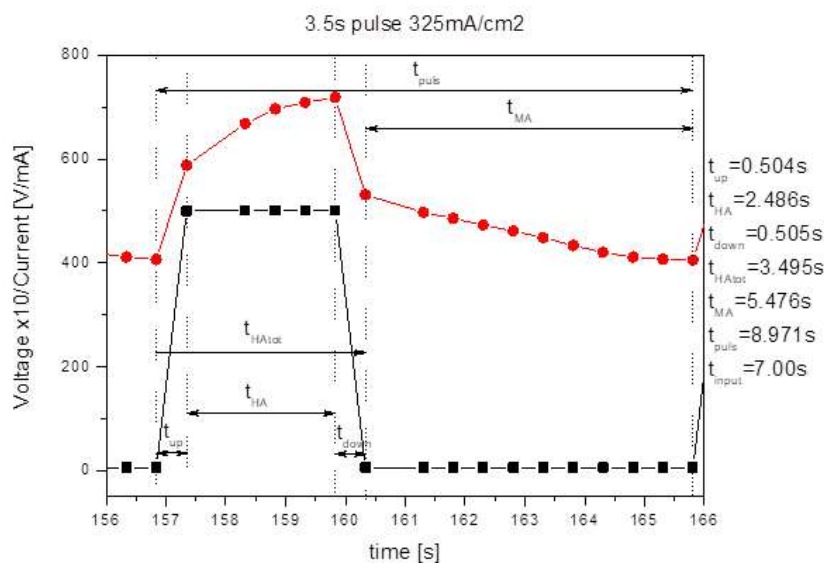
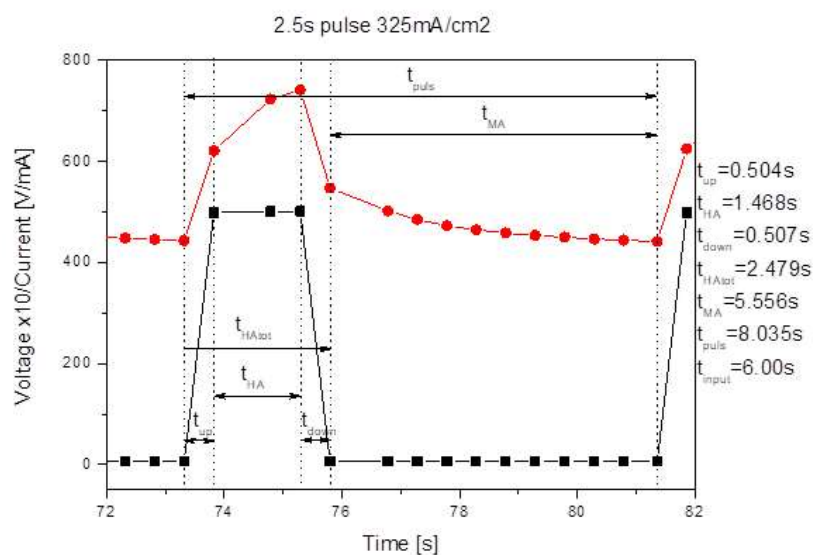


Figure 4.S.1. Magnified view on current/voltage profile of the pulse of different duration with time duration of each part of the pulse and with all experimental points marked.



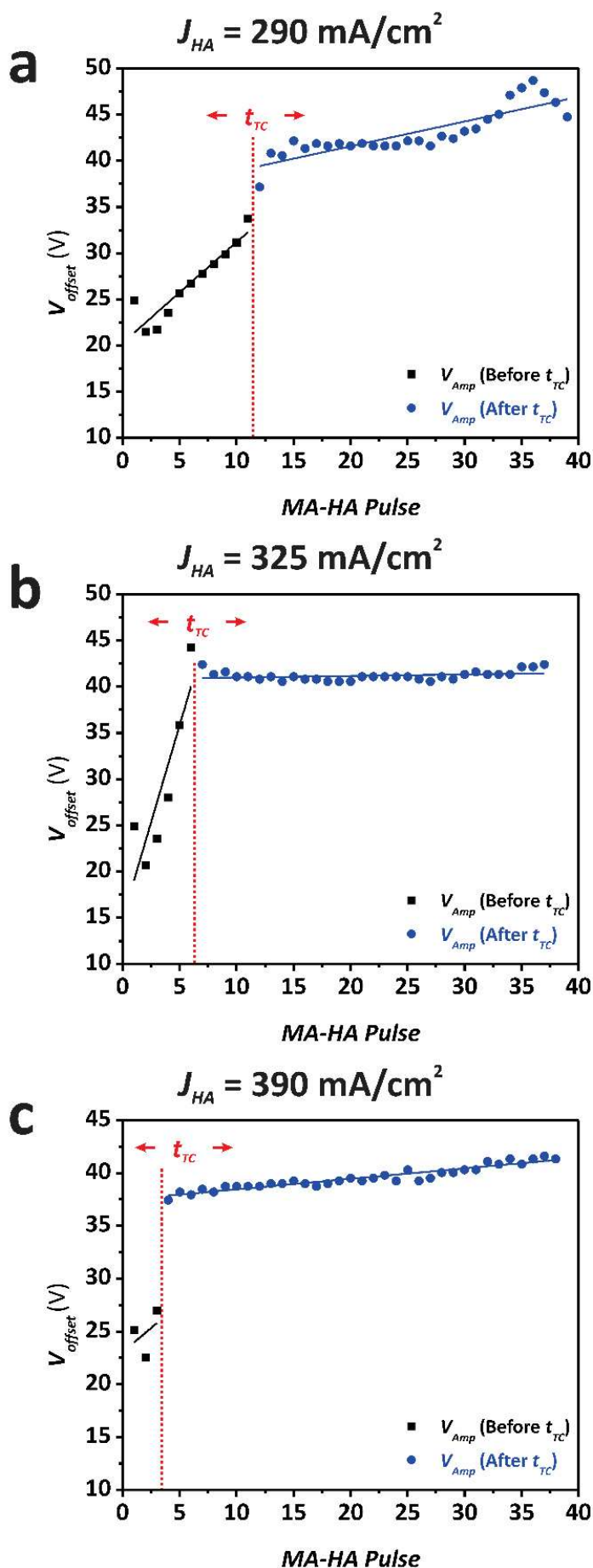


Figure 4.S.2. Evolution of V_{amp} over time for pulse anodization carried out at different current densities, (a) 290 mA/cm², (b) 325 mA/cm², (c) 390 mA/cm². Red line indicate reaching quasi-stable plateau when voltage amplitude remains stable.

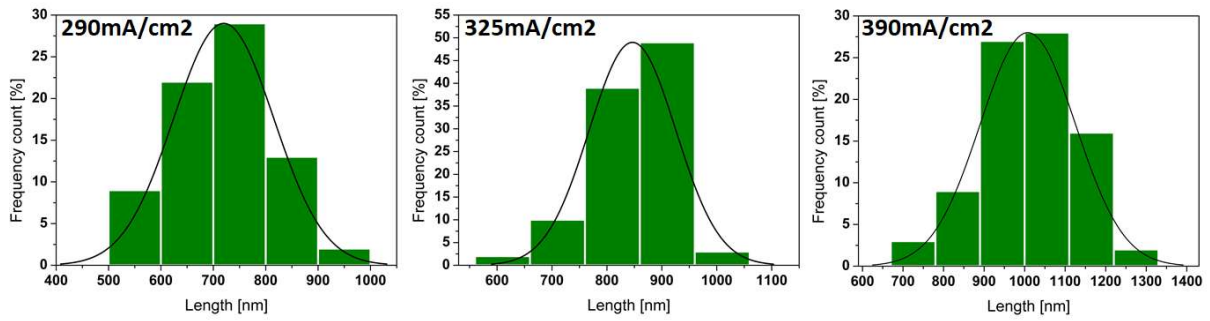


Figure. 4.S.3. Size distribution histogram for AANTs fabricated at different current densities.

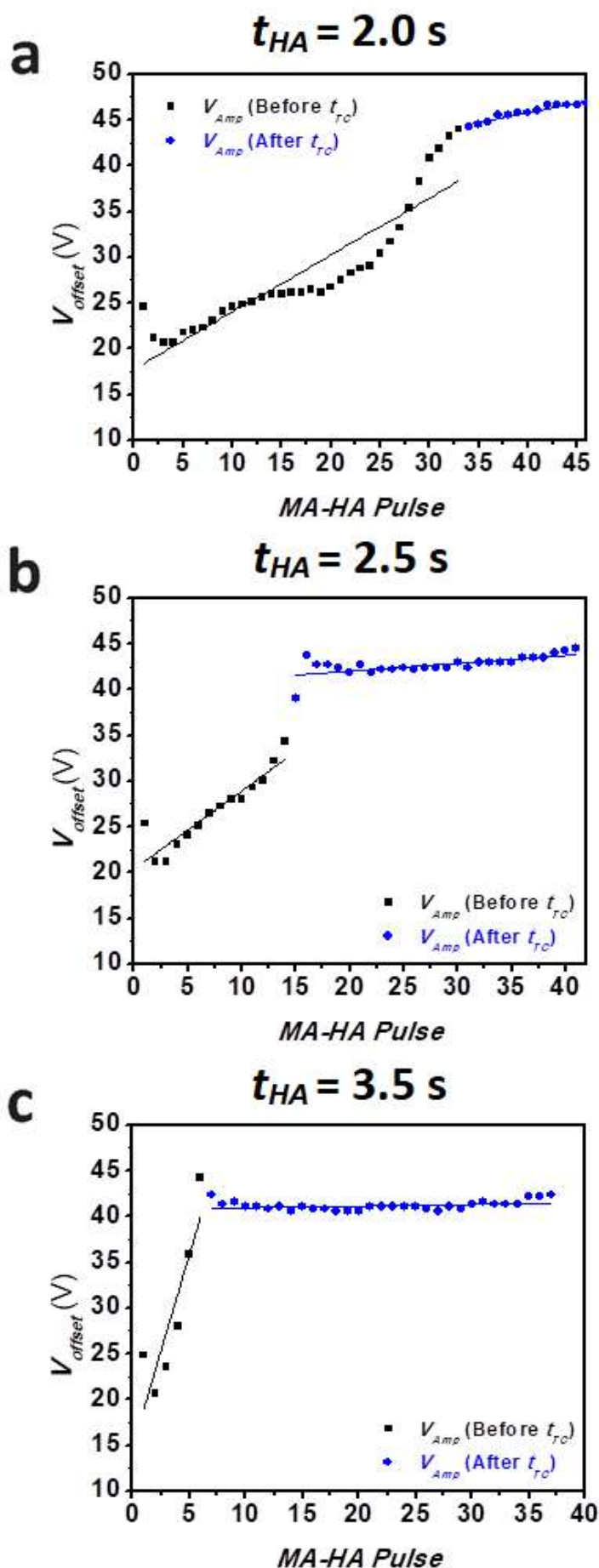


Figure 4.S.4. Evolution of V_{amp} over time for pulse anodization carried out with different duration of HA pulses: (a) 2.0 s, (b) 2.5 s, (c) 3.5 s.

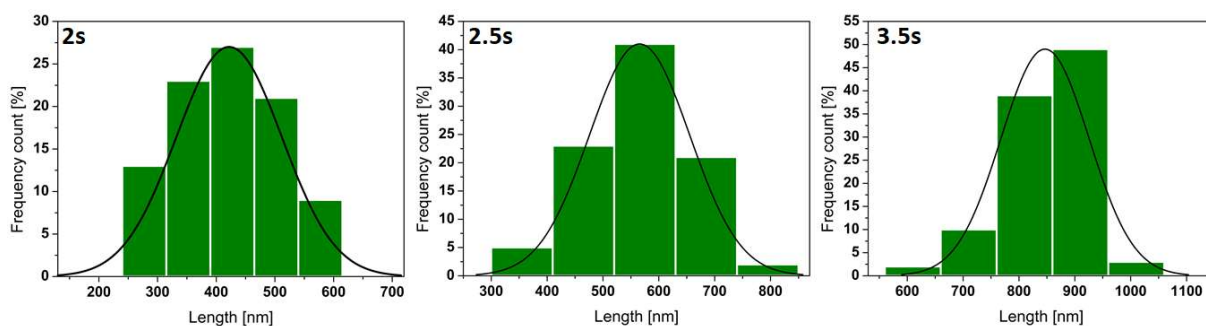


Figure. 4.S.5. Size distribution histogram for AANTs fabricated with different pulse duration.

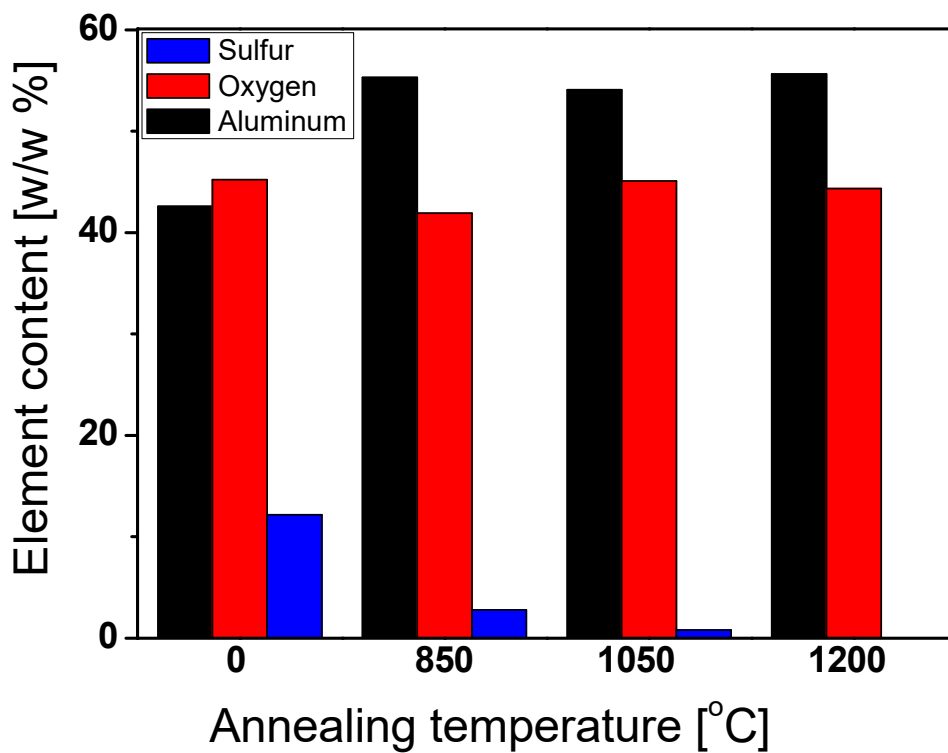


Figure. 4.S.6. Element composition of unmodified AANTs and after thermal annealing at temperatures from 850 to 1200°C.

4.6. References

- [1] A. K. Vijh, Sparkling Voltages and Side Reactions During an Anodization of Valve Metals in Terms of Electron Tunneling. *Corrosion Science* **1971**, 11, 411-417, doi: 10.1016/S0010-938X(71)80125-7.
- [2] F. Li, L. Zhang, R. M. Metzger. On the Growth of Highly Ordered Pores in Anodized Aluminum Oxide. *Chem. Mater.* **1998**, 10, 2470-2480, doi: 10.1021/cm980163a.
- [3] W. Lee, S. J. Park. Porous anodic aluminum oxide: Anodization and templated synthesis of functional nanostructures. *Chem. Rev.* **2014**, 114, 7487-7556, doi: 10.1021/cr500002z.
- [4] A. Santos, L. Vojkuvka, M. Alba, V.S. Balderrama, J. Ferre-Borrull, J. Pallares, L.F. Marsal. Understanding and morphology control of pore modulations in nanoporous anodic alumina by discontinuous anodization. *Phys. Status. Solidi A* **2012**, 209, 2045-2048, doi: 10.1002/pssa.201228150.
- [5] A. Santos, J. Ferre-Borrull, J. Pallares, L.F. Marsal. Hierarchical nanoporous anodic alumina templates by asymmetric two-step anodization. *Phys. Status. Solidi A* **2011**, 208, 668-674, doi: 10.1002/pssa.201026435.
- [6] H. Masuda. Self-Ordering of Cell Arrangement of Anodic Porous Alumina Formed in Sulfuric Acid Solution. *J. Electrochem. Soc.* **1997**, 144, L127, doi: 10.1149/1.1837634.
- [7] A. Santos, T. Kumeria, D. Losic. Nanoporous Anodic Aluminum Oxide for Chemical Sensing and Biosensors. *Trends Anal. Chem.* **2013**, 44, 25-38, doi: 10.1016/j.trac.2012.11.007.
- [8] C. T. Sousa, D. C. Leitao, M. P. Proenca, J. Ventura, A. M. Pereira, J. P. Araujo. Nanoporous alumina as templates for multifunctional applications, *Appl. Phys. Rev.* **2014**, 1, 031102, doi: 10.1063/1.4893546.
- [9] K. Nielsch, J. Choi, K. Schwirn, R. B. Wehrspohn. Self-ordering Regimes of Porous Alumina: The 10% Porosity Rule. *Nano Lett.* **2002**, 2, 677-680, doi: 10.1021/nl025537k.
- [10] Y. V. Nazarkina, S. A. Gavrilov, A. A. Polohin, D. Gromov, Y. P. Shaman. Application of porous alumina formed in selenic acid solution for nanostructures investigation via Raman spectroscopy. *Int. Conf. Micro- Nano- Electronics* **2016**, 10224, 102240J, doi: 10.1117/12/2267148.
- [11] E. O. Gordeeva, I. V. Roslyakov, K. S. Napolskii. Aluminium anodizing in selenic acid: electrochemical behaviour, porous structure, and ordering regimes. *Electrochim. Acta* **2019**, 307, 13-19, doi: 10.1016/j.electacta.2019.03.098.
- [12] S. Akiya, T. Kikuchi, S. Natsui, N. Sakaguchi, R. O. Suzuki. Self-ordered Porous Alumina Fabricated via Phosphonic Acid Anodizing. *Electrochim. Acta* **2016**, 190, 471-479, doi: 10.1016/j.electacta.2015.12.162.
- [13] L. Yi, L. Zhiyuan, H. Xing, L. Yisen, C. Yi. Investigation of intrinsic mechanisms of aluminium anodization processes by analyzing the current density. *RSC Adv.* **2012**, 2, 5164-5171, doi: 10.1039/C2RA01050J.
- [14] K. Schwirn, W. Lee, R. Hillebrand, M. Steinhart, K. Nielsch, U. Gösele. Self-Ordered Anodic Aluminum Oxide Formed by H₂SO₄ Hard anodization. *ACS Nano* **2008**, 2, 302-310, doi: 10.1021/nn7001322.
- [15] L. Zaraska, G. D. Sulka, M. Jaskula. Anodic alumina membranes with defined pore diameters and thicknesses obtained by adjusting the anodizing duration and pore opening/widening time. *J. Solid State Electrochem.* **2011**, 15, 2427-2436, doi: 10.1007/s10008-011-1471-z.

- [16] A. Santos, P. Formentin, J. Pallares, J. Ferre-Borrull, L. F. Marsal. Structural engineering of nanoporous anodic alumina funnels with high aspect ratio. *J. Electroanal. Chem.* **2011**, 655, 73-78, doi: 10.1016/j.elechem.2011.02.005.
- [17] P. Csokan. Some Observations on the Growth Mechanism of Hard Anodic Oxide Coatings on Aluminium. *Trans. IMF* **1964**, 41, 51-56, doi: 10.1080/00202967.1964.11869884.
- [18] C. Lammel, M. Schneider, C. Heubner, W. Beckert, A. Michaelis. Investigations of burning phenomena during the hard anodising of aluminium by local in-operando temperature measurements. *Electrochim Acta* **2017**, 249, 271-277, doi: 10.1016/j.electacta.2017.07.167.
- [19] W. Lee, R. Ji, U. Gösele, K. Nielsch. Fast fabrication of long-range ordered porous alumina membranes by hard anodization. *Nat. Materials* **2006**, 5, 741-747, doi: 10.1038/nmat1717.
- [20] I. V. Roslyakov, E. O. Gordeeva, K. S. Napolskii. Role of Electrode Reaction Kinetics in Self-Ordering of Porous Anodic Alumina. *Electrochim. Acta* **2017**, 241, 362-369, doi: 10.1016/j.electacta.2017.04.140.
- [21] V. Vega, J. Garcia, J. M. Montero-Moreno, B. Hernando, J. Bachmann, V. M. Prida, K. Nielsch. Unveiling the Hard Anodization Regime of Aluminum: Insight into Nanopores Self-Organization and Growth Mechanism. *ACS Appl. Mater. Interfaces* **2015**, 7, 28682-28692, doi: 10.1021/acsami.5b10712.
- [22] Y. C. Ha, D. Y. Jeong. Fast Fabrication of a High-aspect-ratio, Self-ordered Nanoporous Alumina Membrane by Using High-field Anodization. *J. Korean Phys. Soc.* **2010**, 57, 1661-1666, doi: 10.3938/jkps.57.1661.
- [23] W. Lee, K. Schwirn, M. Steinhart, E. Pippel, R. Scholz, U. Gösele. Structural engineering of nanoporous anodic aluminium oxide by pulse anodization of aluminium. *Nat. Nanotechnol.* **2008**, 3, 234-239, doi: 10.1038/nnano.2008.54.
- [24] G. D. Sulka, A. Brzozka, L. Liu. Fabrication of diameter-modulated and ultrathin porous nanowires in anodic aluminum oxide templates. *Electrochim. Acta* **2011**, 56, 4972-4979, doi: 10.1016/j.electacta.2011.03.126.
- [25] Y. Chen, A. Santos, Y. Wang, T. Kumeria, J. Li, Ch. Wang, D. Losic. Biomimetic Nanoporous Anodic Alumina Distributed Bragg Reflectors in the Form of Films and Microsized Particles for Sensing Applications. *ACS Appl. Mater. Interfaces* **2015**, 7, 19816-19824, doi: 10.1021/acsami.5b05904.
- [26] J. Ferre-Borrull, J. Pallares, G. Macias, L. F. Marsal. Nanostructural engineering of nanoporous anodic alumina for biosensing applications. *Materials* **2014**, 7, 5225-5253, doi: 10.3390/ma7075225.
- [27] A. Santos, J. H. Yoo, C. V. Rohatgi, T. Kumeria, Y. Wang, D. Losic. Realisation and advanced engineering of true optical rugate filters based on nanoporous anodic alumina by sinusoidal pulse anodisation. *Nanoscale* **2016**, 1360-1373, doi: 10.1039/C5NR05462A.
- [28] Y. Chen, A. Santos, Y. Wang, T. Kumeria, C. Wang, J. Li. Interferometric nanoporous anodic alumina photonic coatings for optical sensing. *Nanoscale* **2015**, 7, 7770-7779, doi: 10.1039/C5NR00369E.
- [29] Y. F. Mei, X. L. Wu, X. F. Shao, G. G. Siu, X. M. Bao. Formation of an array of isolated alumina nanotubes. *Europhys. Lett.* **2003**, 62, 595, doi: 10.1209/epl/i2003-00392-7.
- [30] W. Lee, R. Scholz, U. Gösele. A Continuous Process for Structurally Well-Defined Al₂O₃ Nanotubes Based on Pulse Anodization of Aluminum. *Nano Lett.* **2008**, 8, 2155-2160, doi: 10.1021/nl080280x.

- [31] Y. F. Mei, X. L. Wu, X. F. Shao, G. S. Huang, G. G. Siu. Formation mechanism of alumina nanotube array. *Phys. Lett. Sect. A Gen. At. Solid State Phys.* **2003**, 309, 109-113, doi: 10.1016/S0375-9601(03)00130-0.
- [32] S. Z. Chu, K. Wada, S. Inoue, M. Isogai, A. Yasumori. Fabrication of ideally ordered nanoporous alumina films and integrated alumina nanotubule arrays by high-field anodization. *Adv. Mater.* **2005**, 17, 2115-2119, doi: 10.1002/adma.200500401.
- [33] Y. Wang, A. Santos, A. Evdokiou, D. Losic. Rational design of ultra-short anodic alumina nanotubes by short-time pulse anodization. *Electrochim. Acta* **2015**, 154, 379-386, doi: 10.1016/j.electacta.2014.12.056.
- [34] Y. Wang, G. Kaur, Y. Chen, A. Santos, D. Losic, A. Evdokiou. Bioinert Anodic Alumina Nanotubes for Targeting of Endoplasmic Reticulum Stress and Autophagic Signaling: A Combinatorial Nanotube-Based Drug Delivery System for Enhancing Cancer Therapy. *ACS Appl. Mater. Interfaces* **2015**, 7, 27140-27151, doi: 10.1021/acsami.5b07557.
- [35] Y. Wang, G. Kaur, A. Zysk, V. Liapis, S. Hay, A. Santos, D. Losic, A. Evdokiou. Systematic invitro nanotoxicity study on anodic alumina nanotubes with engineered aspect ratio: Understanding nanotoxicity by a nanomaterial model. *Biomaterials* **2015**, 46, 117-130, doi: 10.1016/j.biomaterials.2014.12.008.
- [36] Y. Wang, A. Santos, G. Kaur, A. Evdokiou, D. Losic. Structurally engineered anodic alumina nanotubes as nano-carriers for delivery of anticancer therapeutics. *Biomaterials* **2014**, 35, 5517-5526, doi: 10.1016/j.biomaterials.2014.03.059.
- [37] I. V. Roslyakov, D. S. Koshkodaev, A. A. Eliseev, D. Hermida-Merino, V. K. Ivanov, A. V. Petukhov, K. S. Napolskii. Growth of Porous Anodic Alumina on Low-Index Surfaces of Al Single Crystals. *J. Phys. Chem. C* **2017**, 121, 27511-27520, doi: 10.1021/acs.jpcc.7b09998.
- [38] C. Cheng, A. H. W. Ngan. Fast fabrication of self-ordered anodic porous alumina on oriented aluminum grains by high acid concentration and high temperature anodization. *Nanotechnology* **2013**, 24, 215602, doi: 10.1088/0957-4484/24/21/215602.
- [39] S. Zhao, K. Chan, A. Yelon, T. Veres. Novel structure of AAO film fabricated by constant current anodization. *Adv. Mater.* **2007**, 19, 3004-3007, doi: 10.1002/adma.200701284.
- [40] A. A. Tsyganenko, P. P. Mardilovich. Structure of alumina surfaces. *J. Chem. Soc. - Faraday Trans.* **1996**, 92, 4843-4852, doi: 10.1039/FT9969204843.
- [41] G. C. Wood. A Model for the Incorporation of Electrolyte Species into Anodic Alumina. *J. Electrochem. Soc.* **2006**, 143, 74, doi: 10.1149/1.1836389.
- [42] A. Santos, M. J. Deen, L. F. Marsal. Low-cost fabrication technologies for nanostructures: State-of-the-art and potential. *Nanotechnology* **2015**, 26, 042001, doi: 10.1088/0957-4484/26/4/042001.
- [43] F. Ali, L. Reinert, J.-M. Leveque, L. Duclaux, F. Muller, S. Saeed, S. S. Shah. Effect of sonication conditions: Solvent, time, temperature and reactor type on the preparation of micron sized vermiculite particles. *Ultrason. Sonochem.* **2014**, 21, 1002-1009, doi: 10.1016/j.ultsonch.2013.10.010.
- [44] L. Dumeé, K. Sears, J. Schütz, N. Finn, M. Duke, S. Gray. Influence of the Sonication Temperature on the Debundling Kinetics of Carbon Nanotubes in Propan-2-ol. *Nanomaterials* **2013**, 3, 70-85, doi: 10.3390/nano3010070.
- [45] W. Vedder, D. A. Vermilyea. Aluminum + water reaction. *Trans. Faraday Soc.* **1969**, 65, 561-584, doi: 10.1039/TF9696500561.

- [46] L. F. Marsal, L. Vojkuvka, P. Formentin, J. Pallares, J. Ferre-Borrull. Fabrication and optical characterization of nanoporous alumina films annealed at different temperatures. *Opt. Mater.* **2009**, 31, 860-864, doi: 10.1016/j.optmat.2008.09.008.
- [47] T. Shirai, H. Watanabe, M. Fuji and M. Takahashi. Structural Properties and Surface Characteristics on Aluminum Oxide Powders. *Materials Science* **2009**, 9, 23-31, doi: n/a.
- [48] R. Ozao, M. Ochiai, H. Yoshida, Y. Ichimura, T. Inada. Preparation of γ -alumina membranes from sulphuric electrolyte anodic alumina and its transition to α -alumina. *J. Therm. Anal. Calorim.* **2001**, 64, 923-932, doi: 10.1023/A:101158929708.
- [49] M. R. Das, J. M. Borah, W. Kunz, B. W. Ninham, S. Mahiuddin. Ion specificity of the zeta potential of α -alumina, and of the adsorption of p-hydroxybenzoate at the α -alumina-water interface. *J. Colloid Interface Sci.* **2010**, 344, 482-491, doi: 10.1016/j.jcis.2009.12.048.

Chapter 5. Magnetic nanoparticle decorated anodic alumina nanotubes for fluorescent detection of cathepsin B.

Abstract

In this work, we present the process to provide anodic alumina nanotubes with magnetic responsivity based on magnetic nanoparticles. We demonstrate the possibility to cause the motion of these composite nanotubes under magnetic field, providing them with guided mobility. The obtained magnetic anodic alumina nanotubes are completely characterized and their potential to undergo selective and effective functionalization, and stimuli-responsive load release is demonstrated. For this purpose, protease-triggered release of fluorescent molecules loaded inside the magnetic anodic alumina nanotubes (MAANTs) by selective functionalization is performed. The inner walls of the MAANTs were selectively covered with protein padding of albumin-fluorescein isothiocyanate conjugate (FITC-BSA) through means of silanization. Protein functionalization was designed to undergo proteolytic hydrolysis in presence of cathepsin B- protease highly expressed during growth and initial stages of tumor metastasis – in order to cleave peptide bond of albumin and release fluorescent fragments of the protein. Proteolytic reaction with the enzyme is performed under acidic conditions. Presented arrangement is an exemplary combination of functionalities – which are vast – and of value for applications like drug delivery and biosensing applications.

5.1. Introduction

Development of new materials and constant progress of technology enable to produce more advanced and highly specified systems based on nanoparticles. Due to scale, nanostructures can interact with biological systems in ways not possible before, they exhibit unique interaction with electromagnetic radiation and have intrinsic properties originated from unprecedented surface area to volume ratio. Quantum dots, nanospheres, nanorods, nanostars, nanotubes and many more, composed from different chemicals and in a range of sizes have been developed [1]–[5]. Amongst the most popular – with almost 200,000 results with Elsevier search engine – high aspect ratio hollow inside elongated structures called nanotubes, carbon nanotubes being (CNTs) the most prevalent example [6].

Means to functionalize nanotubes and their potential applications are vast [7]–[11]. An important aspect of nanosized particles behavior is their motion – both passive and active – especially for the interaction with biological systems where precision and selectivity is crucial [12]–[14]. Passive solutions can conveniently exploit properties of the environment, although they lack rapid and precisely aimed movement. Attachment of magnetic nanoparticles to

bigger nanostructures – either covalently or electrostatically – is common practice to provide these nanostructures with magnetic properties [15]. For example, nanotubes with enhanced maneuverability can serve as nanoadsorbent for selective removal of heavy metal ions and organic molecules as they enable impurities removal by simply using a magnet [16], [17]. Magnetic responsivity of carbon nanotubes decorated with magnetic nanoparticles enabled to form epoxy laminate preserving forced orientation of nanotubes, providing superior mechanical properties and reduced thermal expansion of the composite [18]. Nanotubes modified with magnetic nanoparticles serve as electromagnetic attenuation material in electronic components [19]. What is more, bigger nanoparticles coated with small magnetic nanoparticles can display three dimensional magnetism – newly emerging approach to nanomagnetism. For bioimaging, magnetic and fluorescent carbon nanotubes have been demonstrated to work effectively as imaging agents for the observation on living mice [3]. Physical effects featuring geometry, topology and chirality provide their potential use in memory and sensing [20]. In future, it may be possible to create nanoparticle motors/robots with precise movement control [21]. In general, systems based on nanoparticles have potential to bring novelty in many fields. Apart from broadly known materials with long history, new materials are being developed as well.

Porous anodic alumina (PAA) is a material generated through environmentally friendly and facile process of electrochemical aluminum etching in acid electrolyte. With tailored parameters of the anodization process, highly ordered hexagonal array of perpendicularly aligned pores of aluminum oxide can be formed on the surface of aluminum anode [22]–[25]. In addition, under specific anodization conditions, the pore diameter can be modulated in depth or combine different pore diameters in the same structure [26]–[28]. Moreover, process carried out under high current density may yield structure with weaker connection between adjacent pores – sometimes featuring voids at three cell junction or loose array of pores [29]. This “cell separation phenomenon”, combined with pulse pattern of high-low current input leads to formation of highly regular modulated structure that – after specific treatment – can be split into well-defined nanoparticles called anodic alumina nanotubes (AANTs) [30], [31]. As prepared nanotubes have no catalyst contamination and low surface reactivity. Their surface is rich in hydroxyl group, an important factor that determines the surface charge of the nanotubes and enables to provide covalent/electrostatic modification. Zeta potential of AANTs in acidic PBS is positive, becomes neutral at pH 4.3 and remains negative in higher pH [32]. Specificity of the synthesis allows easy regulation of the resulting nanotube length with a slight adjustment of the process parameters. These features make AANTs attractive candidates as model nanostructures for toxicity studies. Their interaction with cells has been analyzed by Wang and colleagues. It has been demonstrated, that alumina nanotubes exhibit superior biocompatibility – during 3 days exposition to 700 nm average length nanotubes cell viability of RAW 264.7 and MDA-MB231-TXSA cell lines was consistently above 90%. This behavior is, however, length dependent as increasing nanotoxicity has been reported for longer nanotubes (>2.5 μm) [32], [33]. Another advantage lays in the nature of the fabrication process that allows the selective functionalization of the inner surface of the

nanotube independently of the outer surface. Additional procedures for selective surface modification or purification/shielding steps are not needed enabling precise design of the multifunctional nanoparticle system. The first study reporting such possibility was carried out solely by incubation of the PAA in drug solution, prior to the separation of the structure [33]. In this paper, we present the development of magnetic anodic alumina nanotubes, their design and functionalization for enzyme-triggered release of the nanotubes' load. To our knowledge, this is the first work to report anodic alumina nanotubes provided with magnetic responsivity. A complete characterization of the MAANTs is presented. Besides, the MAANTs are designed and optimized for enzyme-triggered release of fluorescent protein fragment. Protein padding of albumin fluorescein isothiocyanate conjugate was created solely inside the nanotubes exploiting top-down fabrication approach and initial integrity of the porous structure. Functionalization steps were followed with microscopic and spectroscopic analysis of the sample. Performance of these magnetic nanotubes is demonstrated using cathepsin B – protease highly expressed during cancer growth and early stages of metastasis. The developed MAANTs have a high maneuverability in response to magnetic fields. This very interesting property along with the high degree of structure's regularity makes MAANTs valuable nanostructures in many fields like drug delivery, detection and precise separation.

5.2. Materials and methods

5.2.1. Materials

Aluminum (Al) discs of thickness 0.5 mm and purity 99.999 % were supplied by Goodfellow Cambridge Ltd. Sulfuric acid (H_2SO_4 , 95.0-98.0 % ACS reagent), ethanol absolute ($\text{C}_2\text{H}_5\text{OH}$, 99.9 % ACS reagent) and hydrogen peroxide (H_2O_2 , 30 %, stabilized) were purchased from Scharlau. Copper (II) chloride dihydrate (CuCl_2 , ≥ 99.0 % ACS reagent), hydrochloric acid (HCl, 37% ACS reagent), perchloric acid (HClO_4 , 70.0-72.0 % ACS reagent) and glutaraldehyde 25 wt. % in H_2O (GA) were purchased from Sigma-Aldrich. (3-aminopropyl)triethoxysilane (3-APTES, 99 %) was purchased from Aldrich. Albumin-fluorescein isothiocyanate conjugate from bovine (FITC-BSA), phosphate buffered saline (PBS, BioPerformance, pH 7.4) and cathepsin B from bovine spleen lyophilized powder, ≥ 10 units/mg protein were bought from Sigma. Aforementioned chemicals were used as received. Iron oxide nanoparticles (II, III) 10 nm avg part. size (TEM) carboxylic acid (citrate) functionalized 5 mg/mL in H_2O dispersion were supplied by Aldrich and followed purification protocol of resuspension cycles and finally suspended in 0.01 M PBS pH = 7.4. Deionized (DI) H_2O PURELAB® Option-Q (18.2 M Ω cm) was used for preparing all the solutions used in this study.

5.2.2. Characterization methods

Electron microscope images and elemental composition of the materials were measured with environmental scanning electron microscopy (ESEM, FEI Quanta 600) using Everhart-Thornley detector (ETD) and backscattered electron (BSE) detectors and energy dispersive X-ray (EDX) function, number of iterations for EDX measurement was 4. Structured films were coated with a ~ 5 nm thin layer of gold prior to ESEM imaging. Before EDX analysis, a suspension of nanotubes was deposited on copper tape and dried. Structure was characterized with Fourier-Transform Infrared Spectroscopy with ATR attachment (Fourier Jasco FT/IR-600 Plus with ATR S) to verify successful covalent conjugation with protein, with a measurement resolution of 0.96 cm^{-1} , accumulation of 32 with applied incident angle of 45° . ζ -potential and dynamic light scattering (DLS) were measured with a ZetaSizer Nano, using 0.6 mg/mL suspension of nanotubes and 12.5 $\mu\text{g/mL}$ maghemite colloid at 25°C . All samples were cold-sonicated for 10 s prior to measurement. Each result of ζ -potential was an average of 3 individual measures that consisted of at least 12 runs each, while hydrodynamic diameter measurement consisted of 12 runs processed by Malvern® software. AANTs and MAANTs geometric features and morphology were captured with transmission electron microscopy (TEM, JEOL model 1011). Size distribution of the AANTs was prepared based on 300 individual measurements for each nanotubes dimension from TEM images analyzed with ImageJ software. Proteolytic hydrolysis of the albumin and resulting release of the fluorescent component caused by cathepsin B has been followed by measuring fluorescence emission intensity with spectrophotometer (Photon

Technology International Inc, Birmingham, NJ) with Xe lamp light source. All measurements were performed at room temperature with excitation wavelength of 450 nm, emission spectrum was measured between 340 and 600 nm with a resolution of 1 nm. Finally, fluorescence images were acquired using a Nikon Eclipse TE2000-E inverted microscope mounted with a C1 laser confocal system (EZ-C1 software, Nikon). Excitation source applied was 488 nm argon laser and the emission was collected at 515 ± 15 nm using a bandpass emission filter (green channel). All confocal images were captured using a 5 MP CCD, objective x100 and excitation time of 500 ms. A xs analytical balance with 0.01 mg readability (KERN ABT 120-5DNM) was used during all experiments for sample weighting. Sonication was performed using a sonicating bath Bandelin Sonorex RK 102H.

5.3. Magnetic anodic alumina nanotubes (MAANTs)

5.3.1. Preparation of magnetic anodic alumina nanotubes

Aluminum discs were sequentially sonicated in ethanol and ultrapure water for 10 min each. Prior to anodization, Al discs were electropolished in a mixture of HClO_4 and ethanol 1:4 (v/v) under 20 V at 5°C during 7 min. Then, the first anodization step was performed in an aqueous 0.3 M H_2SO_4 electrolyte modified with 10% ethanol at 25 V and 8°C for 20 h to generate a starting nanoporous anodic alumina layer of $\sim 110 \mu\text{m}$. Next, the anodization process was switched to galvanostatic pulse anodization, using the same acid electrolyte but at 1°C under vigorous stirring. Pulse anodization consisted of sequential pulses between mild anodization and hard anodization regimes, in which the current density (J) input was periodically switched between low and high values for a given time in a stepwise fashion. Each pulse was formed by a mild anodization step at 4.5 mA/cm^2 for 5 s and hard anodization step at 390 mA/cm^2 for 3.5 s. The formation of nanostructured PAA and the course of pulse anodization are visualized in figure 5.1A. The obtained structured PAA film was chemically etched to remove aluminum support and weaken the structure to provide good separation into nanoparticles. Impact on the morphology of PAA film during acid etching has been reported previously – cell boundaries in horizontal and vertical axes has been significantly exposed [31].

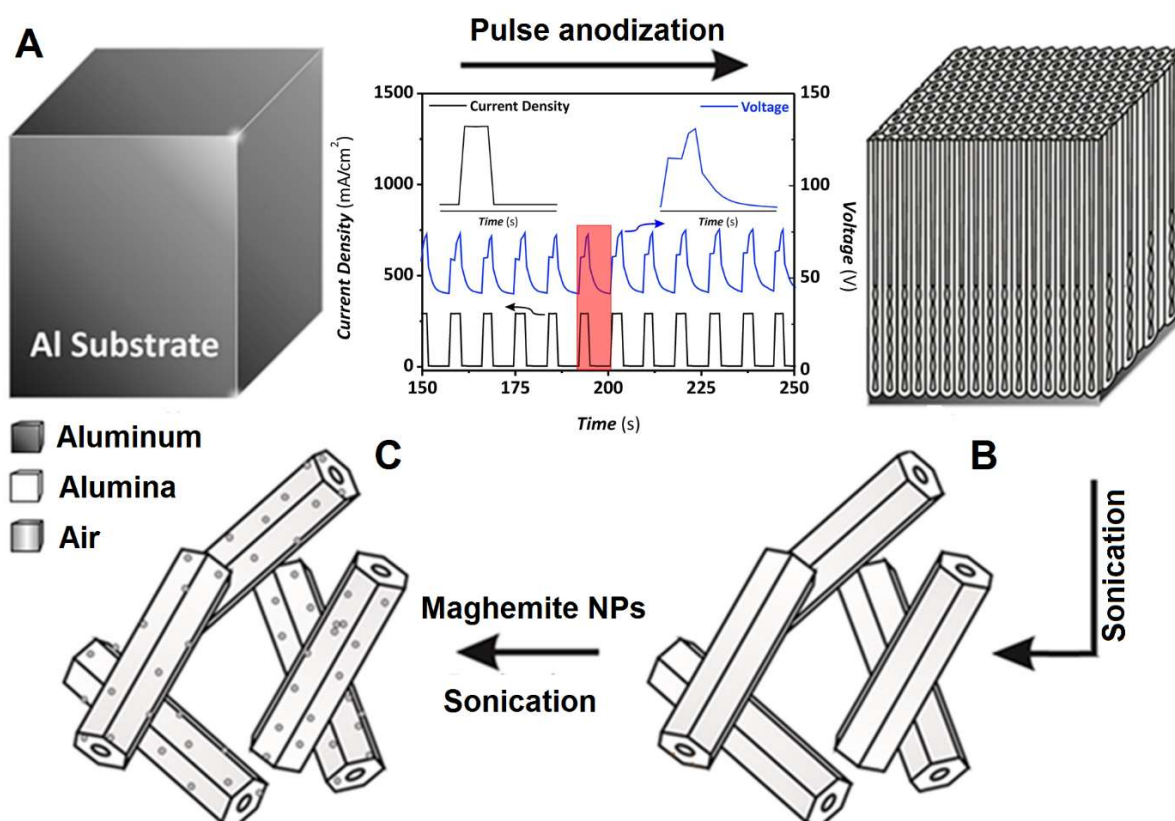


Figure 5.1. Fabrication of magnetic alumina nanotubes. (A) pulse anodization of aluminum resulting in formation of a periodical porous structure; (B) liberation of nanotubes and (C) interaction of the nanotubes with maghemite nanoparticles.

Ice bath sonication for 20 minutes was performed on etched PAA film immersed in DI water pH = 7.0 to yield highly regular nanotubes (fig. 5.1B). It has been observed that sonication in PBS produces a visible degradation after 20 minutes, similarly to the degradation attributed to an increment of temperature observed in previous works [44]. For this reason sonication in PBS is carried out only in 10 s periods. Nanotubes and maghemite nanoparticles are centrifuged and dispersed in 0.01 M PBS pH = 7.4, 5 % hydrochloric acid solution was utilized to reach expected pH. PBS pH = 7.4 provides better stability of the suspension than DI H₂O, reduces aggregation effects over time and is utilized for long storage of as-prepared AANTs. Since surface of alumina nanotubes is charged in aqueous suspensions, it is possible to initiate electrostatic interaction with particles exhibiting opposite surface charge. Initial experiments allowed to estimate the ratio of nanoparticles to nanotubes at which saturation occurs (unbounded maghemite nanoparticles detected by DLS). This facile approach enabled to provide nanotubes with magnetically induced motion. The positively charged nanotubes were mixed with excess of carboxylic acid functionalized maghemite nanoparticles, stirred overnight and centrifuged several times to remove unbounded maghemite nanoparticles, obtaining MAANTs (fig. 5.1C).

5.3.2. Characterization of magnetic anodic alumina nanotubes (MAANTs)

Cross-section of the structured PAA film formed with pulsed chemical anodization is presented in fig. 5.2A. The structure displays the characteristic pore diameter modulation caused by current pulse oscillations. After sonication and functionalization with magnetic nanoparticles, the resulting MAANTs were deposited on copper tape and observed under ESEM (fig. 5.2B). The magnetic nanoparticles are difficult to observe using standard ETD detector due to their small size (10 nm). Their presence becomes more apparent when back-scattering detector is applied (fig. 5.2C). Since backscattering effect is stronger with elements of higher atomic number, areas with different chemical composition can be clearly distinguished.

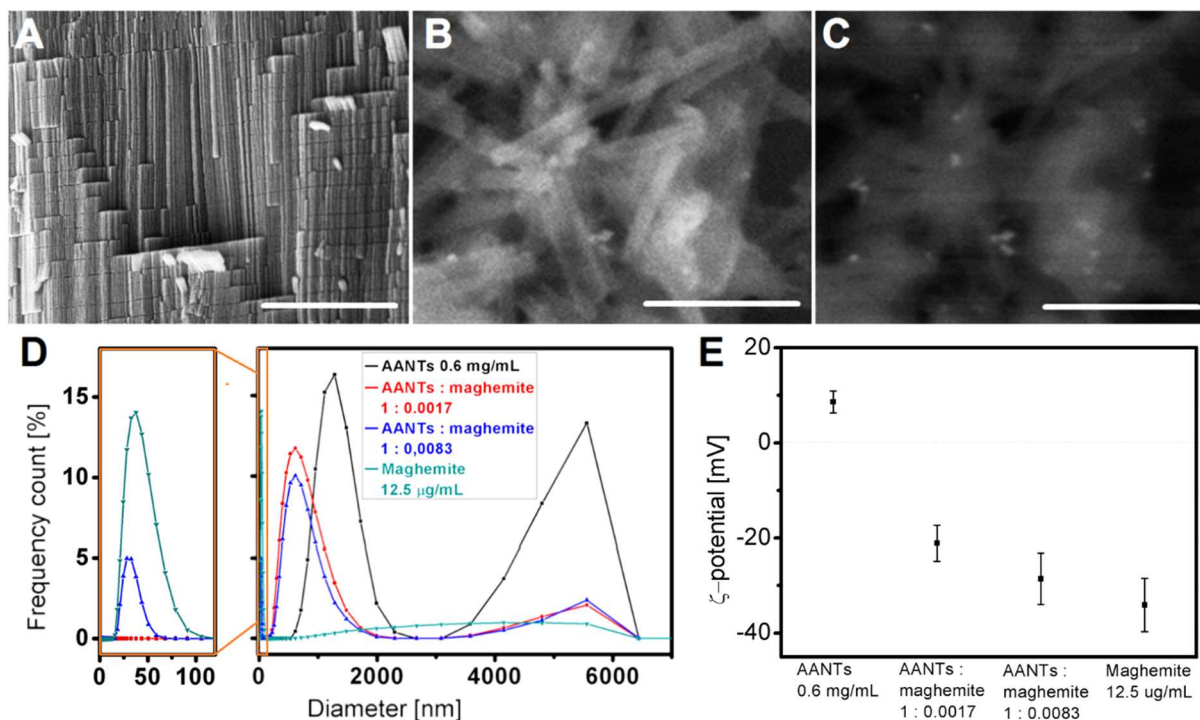


Figure 5.2. (A) ESEM cross-section of structured PAA; (B) ESEM image of MAANTs and (C) BS ESEM image of MAANTs; (D) DLS size distribution of AANTs, maghemite nanoparticles and AANTs mixed with maghemite in 0.01 M PBS pH = 3.6 and (E) ζ -potential measurements of AANTs and AANTs mixed with different ratios of maghemite nanoparticles in 0.01 M PBS pH = 3.6. Scale bars: 5 μ m, 1 μ m and 1 μ m respectively.

AANTs are composed of amorphous alumina. The surface of this material features a high density of oxygen groups. As a result of protonation in H₂O, these groups are responsible for positively charged surface in a broad range of pH. When mixed with negatively charged maghemite NPs – self-assembly driven by electrostatic force occurs. On the other hand, AANTs in PBS are negatively charged for pH 5-8, reaching isoelectric point at pH = 4.3. Below this value, AANTs are positively charged [33]. To evaluate effects of interaction between nanotubes and maghemite nanoparticles and estimate concentration of maghemite colloids needed for effective interaction with nanotubes, unmodified nanotubes were combined with several different concentrations of magnetic nanoparticles: 1, 2, 5, 10, 25, 50 and 100 μ m/mL in 0.01 M PBS pH = 3.6. Nanoparticle colloids and nanotube suspension were mixed and stirred overnight. DLS measurements as well as the collection of samples for TEM were preceded by 10 s of cold sonication. For the lowest concentration, the presence of maghemite nanoparticles was barely visible. However, for the highest concentration, coating of the maghemite nanoparticles is formed. Two different concentrations – before and after saturation – were selected: 10 and 50 μ g/mL. Their hydrodynamic diameter and ζ -potential were measured, including those of as-prepared AANTs and maghemite nanoparticles for comparison (fig. 5.2D-E). Accuracy of DLS size measurement is the highest for spherical nanoparticles. For that reason, determination of size of high-aspect ratio materials like nanotubes yields level of uncertainty. These results, however, can still be informative with

regards to behavior of colloid dispersion and tendency to form clusters [35]. Size distribution of unmodified AANTs display two major peaks: one at 1290 nm representing singular nanotubes along with small clusters and another at 5560 nm representing bigger agglomerates. It is clear, that addition of maghemite nanoparticles results in a shift towards smaller size indicating increase of repulsive forces and higher stability of the suspension [36]. We expect that presence of carboxylic groups on magnetic nanoparticles provide for more pronounced electrostatic character. Apart from higher prevalence of smaller particles, signal representing bigger agglomerates decreased significantly. What is more, the addition of a higher quantity of magnetic nanoparticles (8.3 μg for 1 mg of AANTs) leads to saturation – excess of maghemite nanoparticles represented by peak at 38 nm.

These observations are supported by ζ -potential measurements shown in fig. 5.2E. At given conditions, unmodified suspension of 0.6 mg/mL nanotubes display positive potential value of 8.6 ± 2.3 mV, while 12.5 $\mu\text{g}/\text{mL}$ maghemite nanoparticles have negative ζ -potential of -34.1 ± 5.61 mV. The charge difference between positively charged nanotubes and negatively charged maghemite (reflected in measured ζ -potential) enabled to achieve self-assembly with no presence of surfactants [37]. When nanotubes and nanoparticles are mixed at different weight ratios of 1:0.0017 and 1:0.0083, measured ζ -potential is -21.1 ± 3.82 mV and -28.6 ± 5.42 mV respectively. It is expected that this increase of absolute charge is reflected in the DLS size distribution, since repulsive forces reduce nanotubes' tendency to aggregate.

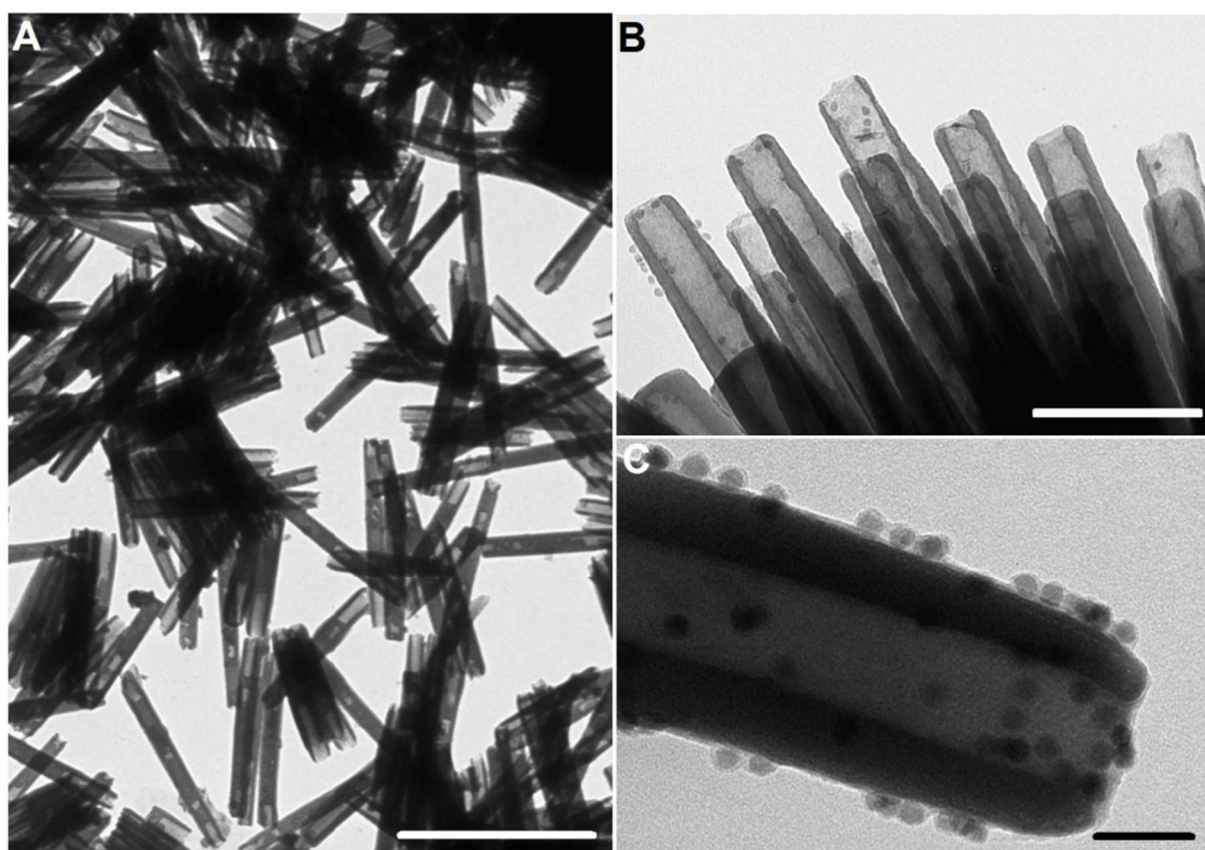


Figure. 5.3. (A) TEM overview on unmodified AANTs; (B) TEM image of MAANTs and (C) magnified view of individual MAANT; Scale bars: 1 μm , 200 nm and 50 nm respectively.

The individual nanotubes can be easily distinguished. Liberated AANTs are shown in fig. 5.3A. These nanotubes are later combined with excess of maghemite nanoparticles. Basing on TEM images, calculated average length of created structures was 1008 ± 118 nm. Additionally, average outer diameter of the tube was 65.5 ± 10.1 nm while average inner diameter is 36.8 ± 5.7 nm. Fig. 5.3B-C reveals successful attachment of superparamagnetic nanoparticles that can be observed as small spheres on the surface of these nanotubes (average diameter of maghemite nanoparticles is 10 nm). These nanotubes are magnetic field-responsive and their motion can be easily observed.

5.4. Stimuli-responsive release of MAANTs load for drug delivery and biosensing applications

Our work aims to lay foundation towards employing this novel material in more advanced multifunctional systems. These biologically inert nanotubes can be designed to serve in many fields like drug delivery, biosensing and catalysis [38]–[40]. In this section, we describe in detail how nanotubes with magnetically induced mobility can be successfully used as reservoirs with stimuli-responsive release of their load. Concretely, the triggered release of fluorescent protein fragments due to the interaction of the protein layer with proteolytic enzyme cathepsin B is proved. Description of the synthesis is followed by explanation of the experimental setup in which magnetic mobility and enzymatic responsivity is demonstrated.

5.4.1. Magnetic AANTs(FITC-BSA) fabrication and characterization

For this experiment, a selective functionalization of the inner wall of the nanotubes has been performed. For this purpose, the MAANTs formation steps presented in fig. 5.1 have been combined with the functionalization procedure. To provide protein cladding exclusively on the inner part of the nanotubes, silanization process is performed before dividing PAA structure into nanotubes as outer walls of the structure are inaccessible at this stage. Chemical changes that occurred during functionalization with protein are presented in fig. 5.4. The PAA substrate with ordered and structured pores (fig. 5.4A) was immersed in 0.3 M H_2O_2 at 70°C for 1 h in order to activate hydroxyl groups on the surface of the aluminum oxide (fig 5.4B). Then, sample was cleaned and dried in oven for 3 hours at 110°C . Afterwards, introduction of silane groups was performed through immersion of sample in 3:1 mixture of ethanol and H_2O v/v with 1% of APTES. Solution is heated to 45°C . The addition of water initiates the reaction (fig. 5.4C). After reacting for 2 h, the sample is washed and dried in oven at 110°C overnight. After reaction with APTES, the remaining Al substrate was removed by wet chemical etching in a mixture of 0.2 M CuCl_2 and 6.1 M HCl followed by further immersion of the structured nanoporous anodic alumina film into the same etchant solution for 1 h. The structured PAA film is then dried and weighted – difference in mass of the template before and after liberation

of the nanotubes was used to calculate initial concentration of the suspension. Suspension was later diluted to reach final concentration. Nanotubes template was immersed in DI H₂O and sonicated for 15 minutes in ice bath (~5°C) to liberate the nanotubes (fig. 5.4D). Incorporation of crosslink and albumin is performed after sonication in order to avoid potential damage to the protein. Glutaraldehyde (GA) is added to the suspension with final concentration of 2.5 % and shaken for an hour (fig. 5.4E). Attachment of crosslink is followed by addition of albumin-fluorescein isothiocyanate conjugate (5 %) and subjected to overnight stirring (fig. 5.4F). Sample is centrifuged several times to remove excess reagent. Several cycles of centrifuging and redispersion in water were applied.

After thorough washing, water was changed for PBS pH = 4.1 needed for enzymatic reaction and electrostatic interaction. Change of pH was necessary for enzymatic cleavage experiment. Both AANTs and albumin become positively charged in acidic pH (positive charge is further increased when FITC-BSA is attached). Yet, activity of cathepsin B decreases with increasing acidity. Reported pH of 4.1 was the highest at which electrostatic interaction between AANTs(FITC-BSA) and maghemite nanoparticles could occur. Finally, AANTs(FITC-BSA) become magnetic by mixing 0.6 mg/mL AANTs(FITC-BSA) suspension with 12.5 µg/mL maghemite nanoparticles colloid and shaken intensively overnight. Suspension was repeatedly cleaned to remove excess of magnetic nanoparticles (fig. 5.4G). Hydrodynamic diameter and ζ-potential measurements were carried out on the same day as MAANTs(FITC-BSA) preparation.

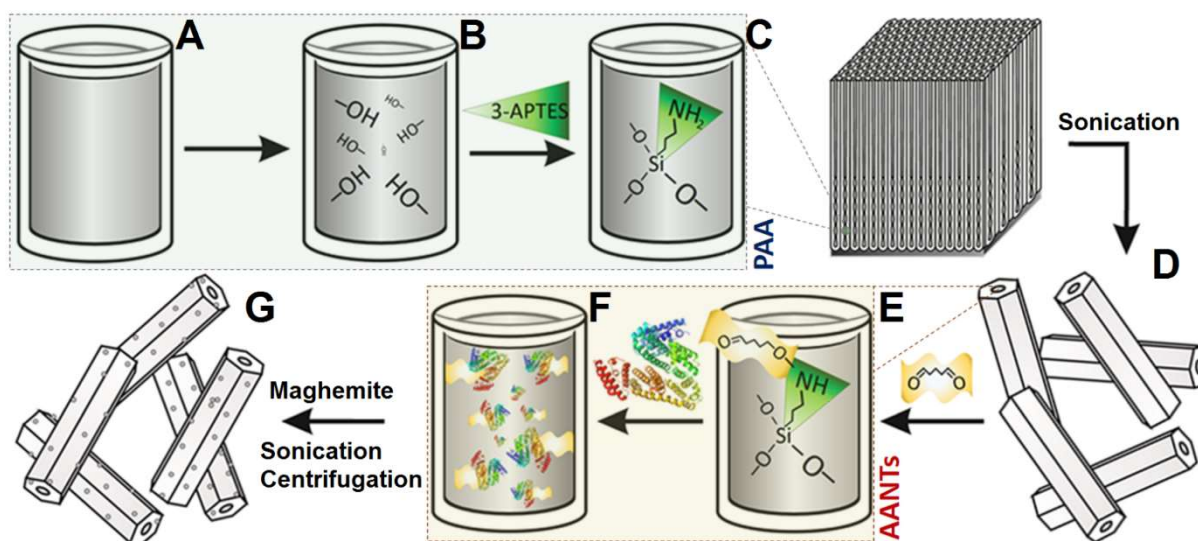


Figure 5.4. Schematics of MAANTs(FITC-BSA) fabrication and enzymatic triggered release: (A) PAA structured film with unmodified pores; (B) activation of hydroxide groups; (C) attachment of APTES; (D) liberation of nanotubes through sonication; (E) addition of GA crosslink; (F) functionalization with protein and (G) electrostatic decoration of AANTs with maghemite nanoparticles.

Verification of successful formation of chemical bonds during the functionalization of the MAANTs was carried out with FTIR. First measurement was performed prior to silanization on as prepared PAA. After silanization and attachment of the albumin, PAA(FITC-BSA) was

measured to compare occurring changes. Results of analysis shown in figure 5.5A are consistent with previous reports [41], [42]. Modification was confirmed by appearance of peaks of Si-Al-O at 1105.98 cm^{-1} , -NH bending at 1643.05 cm^{-1} , C=O stretching at 1729.83 cm^{-1} , CH_3 stretching at 2850.27 cm^{-1} and CH_3 stretching at 2917.77 cm^{-1} indicating successful creation of silane bond and attachment of the albumin.

Functionalization of nanotubes and self-assembly of maghemite-AANTs composite were observed at different stages with measurements of ζ -potential (figure 5.5B). Unmodified nanotubes in acidic PBS (pH = 4.1) exhibit positive ζ -potential of $2.08 \pm 0.69\text{ mV}$. When inner wall of the tube is modified with albumin, ζ -potential value increases and reaches $4.01 \pm 0.77\text{ mV}$. We expect this increment of charge being related to the appearance of positively charged protein [43]. After intense mixing and a few washing steps, obtained composite shows negative ζ -potential of $-4.77 \pm 0.74\text{ mV}$.

Elemental composition of MAANTs(FITC-BSA) is shown in figure 5.5C. In principle, nanoporous anodic alumina consists of aluminum and oxygen, with traces of the electrolyte present in the structure, the amount of which depends on the process conditions [44]. Our recent study provides some insight into elemental composition of PAA fabricated under hard anodization pulses [45]: considerable increase of sulfur content is observed compared to alumina obtained under more commonly anodization conditions [46]. Apart from significant share of sulfur in the structure, phosphorus from PBS buffer can be observed along with carbon and trace quantity of iron, that are expected to indicate presence of protein and iron oxide nanoparticles respectively.

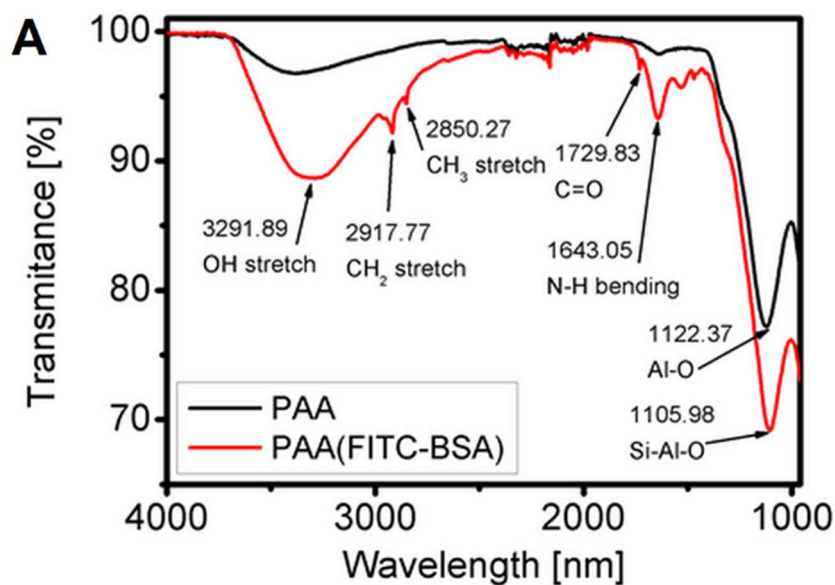
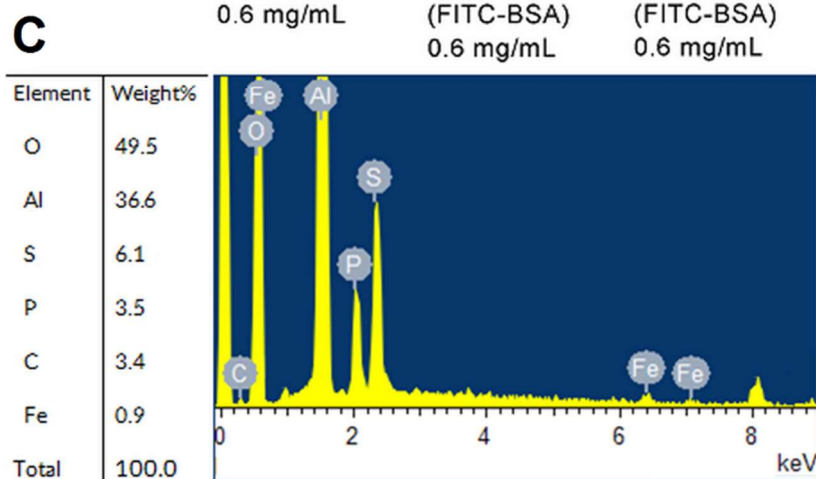
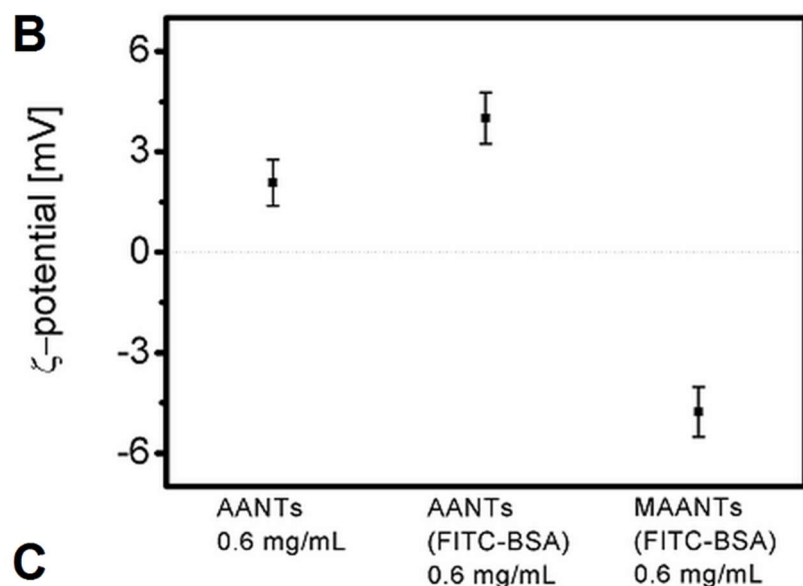


Figure 5.5. Characterization of PAA template and nanotube colloid. (A) FTIR-ATR characterization of PAA; (B) ζ -potential measurements of nanotubes after consecutive functionalization steps (0.01 M PBS pH=4.1) and (C) elemental distribution of MAANTs(FITC-BSA).



5.4.2. Interaction of MAANTs(FITC-BSA) with cathepsin B

Proteases are class of enzymes that catalyses proteolysis – breakdown of proteins into polypeptides and amino acids through peptide bond cleavage. While exopeptidases cut single amino acids of the terminal peptide bond – endopeptidases such as cathepsin B – flank specific scissible peptide bond. Cleavage site is based on the recognition of the specific amino acid sequence in the protein by enzyme’s subsite (figure 5.6). In general, cathepsins are not very specific enzymes. S2 site is the only defined pocket and along with S1 and S1’ comprise major recognition sites of cathepsins. They exhibit pronounced preference for small hydrophobic amino acid residues in the P2 position (Leu, Val, Ile). Exception for cathepsin B is also acceptance of Arg in P2 position [47]. Analyzing sequences of bovine serum albumin derived peptides, it has been revealed that cleavage occurs between following residues: Arg⁸¹-Glu⁸², Val²²³-Glu⁴²⁴ and Gly⁴³⁰-Lys⁴³¹. Cathepsin B cleaves BSA into several relatively large fragments [48]. Interaction between enzyme and FITC-BSA leads to release of these FITC-labeled protein residues into the solution.

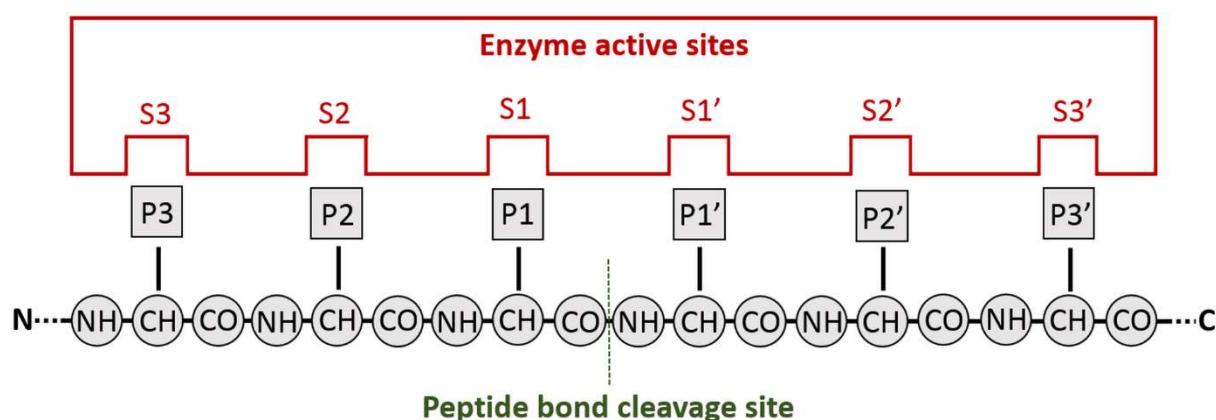


Figure 5.6. Proteolytic interaction between protease and polypeptide using Schechter and Berger nomenclature for substrate-protease interactions. Active site of a protease contain several subsites. Subsites are marked in both directions from the catalytic site (green line). Sites S1-S3/S1'-S2' of the enzyme corresponds to P1-P3/P1'-P3' locations of amino acid residues in the peptide substrate. Cleavage takes place between P1 and P1' residues.

All MAANTs(FITC-BSA) experiments were performed 48 h after FITC-BSA incubation (24 h after maghemite nanoparticles attachment). To prevent damage to the chromophore, samples were stored in cool place without light. Cathepsin B at concentration of 8.3 ng/mL (220 nM) has been introduced into 0.6 mg/mL MAANTs(FITC-BSA) suspension. Injection was followed by intense stirring. Then, precipitation of nanotubes was accelerated with a magnet. To measure fluorescence, particles were separated from the main volume of the liquid to prevent contribution of protein fragments inside MAANTs(FITC-BSA).

Magnet and sample were hold in racks preserving their location during the experiment. Sample was kept above the magnet for 15 minutes, and then analyte solution was measured with spectrophotometer, reintroduced to the suspension and shaken again. These steps were

repeated at time intervals of 15, 30, 60, 90 minutes and 2, 4 hours. Schematic arrangement of the experiment setup is shown in figure 5.7A-C. To promote homogenous distribution of the fluorescent protein fragments in measured sample, it was shaken intensively every time prior to precipitation using magnet. Movements of the magnetic suspensions can be observed with naked eye. Such maneuverability in response to the magnetic field together along with the high regularity of the structure makes them a valuable material in many fields like drug delivery, detection and precise separation procedures.

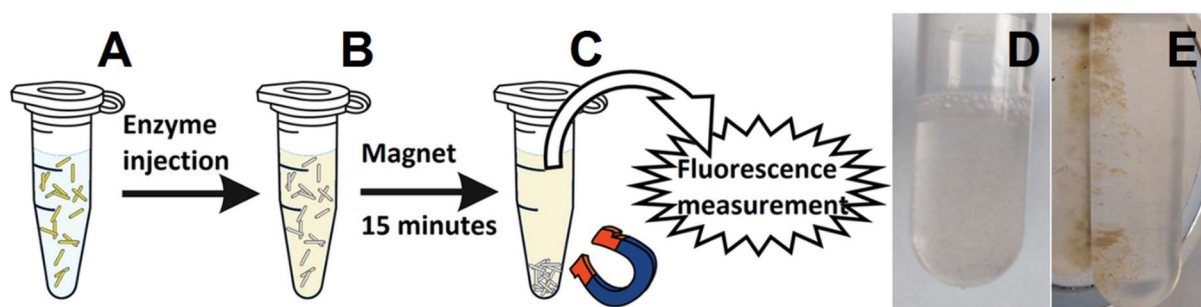


Figure 5.7. Visualization of proteolysis-based release of fluorescent component and manipulation of the sample with magnetic field. (A) represents nanotubes with load inside; (B) release of fluorophore into solution; (C) accelerated precipitation of nanotubes precipitate after release; (D) image of dispersed MAANTs(FITC-BSA) suspension and (E) attracted to the wall of the vial with N52 magnet.

Images of experimental setup for interaction experiment are shown in figure 5.7D-E, with MAANTs(FITC-BSA) in suspended form and precipitation with N52 magnet. After injection of the cathepsin B, the release of fluorescent protein fragments was followed with a spectrophotometer (fig. 5.8A). Initial sudden surge slowed down and reached steady state 4 hours after succeeding the injection of the enzyme. Although cathepsin B is considered moderately active enzyme, majority of reports finish kinetics curve measurement after 1 h. Taking into account high concentration of enzyme applied (220 nM) we suspect other effects like diffusion and steric hindrance to slow down observed release [49], [50].

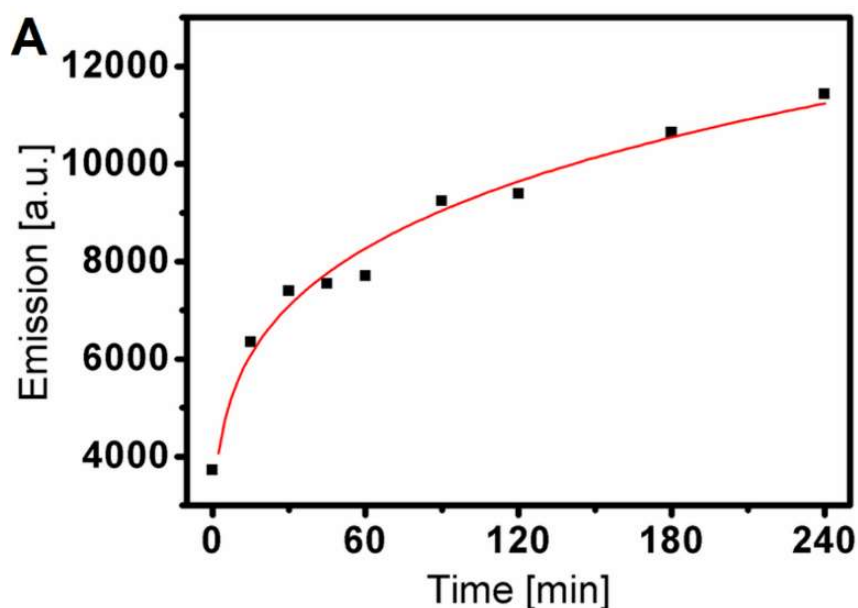
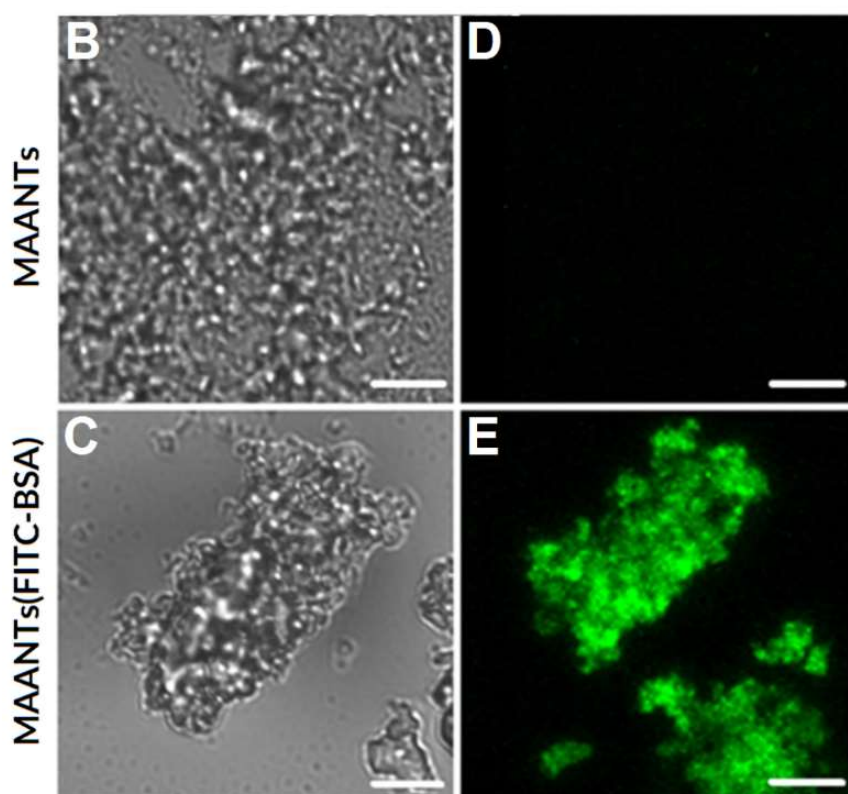


Figure 5.8. Experimental setup and measurements of fluorescent emission. (A) PL spectrum of fluorescent release driven by cathepsin B proteolysis of FITC-BSA, (B-C) white light, and (D-E) confocal microscope images of MAANTs and MAANTs(FITC-BSA). Scale bar 10 μm .



Nanotubes itself are too small to be structurally distinguished using confocal microscopy due to physical limitation of the method. Figure 5.8B-C presents images acquired with optical microscope that represent cluster of nanotubes. Nanotubes without FITC-BSA functionalization do not exhibit any fluorescent emission at given conditions. Magnetic AANTs(FITC-BSA) (fig. 5.8D-E), however, show intense emission in the green light region (515 – 530 nm detector) originated by the fluorescein presence [50].

5.5. Conclusions

Previous approaches enabled to establish technology that provides highly regular anodic alumina nanotubes through process of aluminum electrochemical etching [31], [45]. Low nanotoxicity of as-prepared material and high loading capacity has been demonstrated through interaction with biological systems – several cell lines and rodent species – laying foundation for future applications as a biomaterial and for drug delivery [32], [33], [51]. In this study we present the first work to our knowledge reporting anodic alumina nanotubes provided with magnetic responsivity and displaying potential to undergo selective, effective functionalization and stimuli-responsive release of their load. Successful self-assembly of maghemite nanoparticles-nanotube composite based on opposite surface charge was followed with ζ -potential measurements and observed under TEM. Moreover, it was possible to transfer the mobility of magnetic nanoparticles guided under magnetic field to the alumina nanotubes causing directional motion of the composite nanotubes. Proper design of magnetic high-aspect ratio material enables to combine maneuverability and controlled release – valuable for drug delivery – as demonstrated by Fizir et al [52]. In our report, magnetic responsivity has been employed to ease course of proteolysis experiment. Functionalization and successful attachment of albumin protein was demonstrated with FTIR with appearance of bond-specific signal attributed to formation of specific covalent bonds. Protein functionalization has been carried out utilizing similar approach to previously presented by Tabrizi et al. for aptasensors fabrication previously [53]. In this work PAA formed through pulse anodization is employed, which enables to yield selective inner-wall functionalization prior to dividing structure into nanotubes. Effectivity of the system to respond with the presence of cathepsin B was demonstrated with photoemission experiment. Initially, the concentration of released fluorescent compound increases rapidly reflecting the quick response to the presence of the enzyme, and stabilizes after 4 hours. This study demonstrates the great potential of the MAANTs for developing magnetically guided sensors aimed at the detection of biomolecules or drug release vehicles for localized treatments. Taking into account novelty of magnetic nanoporous anodic alumina nanotubes, our finding provide alternative to commonly used nanoprobe systems. Further efforts to optimize the process, aiming at enhanced colloidal stability and robustness of the structure, are under way so that MAANTs can become more accessible in various environmental conditions.

5.6. References

- [1] R. Jin, C. Zeng, M. Zhou, Y. Chen. Atomically Precise Colloidal Metal Nanoclusters and Nanoparticles: Fundamentals and Opportunities. *Chem. Rev.* **2016**, 116, 10346-10413, doi: 10.1021/acs.chemrev.5b00703.
- [2] V. S. Guruprasad, V. Maheshwari. Magnetic nano-nets for capture of microbes in solution based on physical contact. *J. Colloid Interface Sci.* **2019**, 535, 33-40, doi: 10.1016/j.cis.2018.09.079.
- [3] M. Zhang, W. Wang, F. Wu, P. Yuan, C. Chi, N. Zhou. Magnetic and fluorescent carbon nanotubes for dual modal imaging and photothermal and chemo-therapy of cancer cells in living mice. *Carbon* **2017**, 123, 70-83, doi: 10.1016/j.carbon.2017.07.032.
- [4] V. P. Torchilin. Multifunctional, stimuli-sensitive nanoparticulate systems for drug delivery. *Nat. Rev. Drug Discov.* **2014**, 13, 813-827, doi: 10.1038/nrd4333.
- [5] A. N. Morozovska, E. A. Eliseev, Y. M. Fomichov, Y. M. Vysochanskii, V. Y. Reshetnyak, D. R. Evans. Controlling the domain structure of ferroelectric nanoparticles using tunable shells. *Acta Mater.* **2019**, 183, 36-50, doi: 10.1016/j.actamat.2019.11.012.
- [6] I. A. Kinloch, J. Suhr, J. Lou, R. J. Young, P. M. Ajayan. Composites with carbon nanotubes and graphene: An outlook. *Science* **2018**, 362, 547-553, doi: 10.1126/science.aat7439.
- [7] J. Xu, Z. Cao, Y. Zhang, Z. Yuan, Z. Lou, X. Xu, X. Wang. A review of functionalized carbon nanotubes and graphene for heavy metal adsorption from water: Preparation, application, and mechanism. *Chemosphere* **2018**, 195, 351-364, doi: 10.1016/j.chemosphere.2017.12.061.
- [8] H. Sun, Y. Gao, N. Hu, Y. Zhang, C. Guo, G. Gao, Z. Ma, K. I. Ivanovich, Y. Qiu. Electronic coupling between molybdenum disulfide and gold nanoparticles to enhance the peroxidase activity for the colorimetric immunoassays of hydrogen peroxide and cancer cells. *J. Colloid Interface Sci.* **2020**, 578, 366-378, doi: 10.1016/j.jcis.2020.06.001.
- [9] G. Lazzara, G. Cavallaro, A. Panchal, R. Fakhrullin, A. Stavitskaya, V. Vinokurov, Y. Lvov. An assembly of organic-inorganic composites using halloysite clay nanotubes. *Curr. Opin. Colloid Interface Sci.* **2018**, 35, 42-50, doi: 10.1016/j.cocis.2018.01.002.
- [10] Y. Wan, P. Liu, Z. Yang, S. R. Raman, G. Xiong, H. Luo. Scalable synthesis of three-dimensional interconnected mesoporous TiO₂ nanotubes with ultra-large surface area. *Acta Mater.* **2015**, 93, 138-143, doi: 10.1016/j.actamat.2015.03.059.
- [11] D. Hill, A. R. Barron, S. Alexander. Comparison of hydrophobicity and durability of functionalized aluminum oxide nanoparticle coating with magnetite nanoparticles-links between morphology and wettability. *J. Colloid Interface Sci.* **2019**, 555, 323-330, doi: 10.1016/j.cis.2019.07.080.
- [12] N. Bertrand, J. Wu, X. Xu, N. Kamaly, O. C. Farokhzad. Cancer nanotechnology: The impact of passive and active targeting in the era of modern cancer biology. *Adv. Drug Deliv. Rev.* **2014**, 66, 2-25, doi: 10.1016/j.addr.2013.11.009.
- [13] A. Baeza, M. Colilla, M. Vallet-Regí. Advances in mesoporous silica nanoparticles for targeted stimuli-responsive drug delivery. *Expert Opin. Drug Deliv.* **2015**, 12, 415-439, doi: 10.1080/17425247.2019.1598375.
- [14] E. A. Sykes, J. Chen, G. Zheng, W. C. W. Chan. Investigating the impact of nanoparticle size on active and passive tumor targeting efficiency. *ACS Nano* **2014**, 8, 5696-5706, doi: 10.1021/nn500299p.

- [15] V. M. Andrade, R. J. Caraballo Vivas, S. S. Pedro, J. C. G. Tedesco, A. L. Rossi, A. A. Coelho, D. L. Rocco, M. S. Reis. Magnetic and magnetocaloric properties of La_{0.6}Ca_{0.4}MnO₃ tunable by particle size and dimensionality. *Acta Mater.* **2016**, 102, 49-55, doi: 10.1016/j.actamat.2015.08.080.
- [16] W. Lu, J. Li, Y. Sheng, X. Zhang, J. You, L. Chen. One-pot synthesis of magnetic iron oxide nanoparticle-multiwalled carbon nanotube composites for enhanced removal of Cr(VI) from aqueous solution. *J. Colloid Interface Sci.* **2017**, 505, 1134-1146, doi: 10.1016/j.jcis.2017.07.013.
- [17] X. Wan, Y. Zhan, Z. Long, G. Zeng, Y. He. Core@double-shell structured magnetic halloysite nanotube nano-hybrid as efficient recyclable adsorbent for methylene blue removal. *Chem. Eng. J.* **2017**, 330, 491-504, doi: 10.1016/j.cej.2017.07.178.
- [18] Y. He, S. Yang, H. Liu, Q. Shao, Q. Chen, L. Chang, J. Yuanli, L. Chuntai, G. Zhanhu. Reinforced carbon fiber laminates with oriented carbon nanotube epoxy nanocomposites: Magnetic field assisted alignment and cryogenic temperature mechanical properties. *J. Colloid Interface Sci.* **2018**, 517, 40-51, doi: 10.1016/j.jcis.2018.01.087.
- [19] M. M. Lu, M. S. Cao, Y. H. Chen, W. Q. Cao, J. Liu, H. L. Shi, D. Q. Zhang, W. Z. Wang, J. Yuan. Multiscale Assembly of Grape-Like Ferroferric Oxide and Carbon Nanotubes: A Smart Absorber Prototype Varying Temperature to Tune Intensities. *ACS Appl. Mater. Interfaces* **2015**, 7, 19408, doi: 10.1021/acsami.5b05595.
- [20] A. Fernández-Pacheco, R. Streubel, O. Fruchart, R. Hertel, P. Fischer, R. P. Cowburn. Three-dimensional nanomagnetism. *Nat. Commun.* **2017**, 8, 15756, doi: 10.1038/ncomms15756.
- [21] W. Hu, G. Z. Lum, M. Mastrangeli, M. Sitti. Small-scale soft-bodied robot with multimodal locomotion. *Nature* **2018**, 554, 81-85, doi: 10.1038/nature25443.
- [22] H. Masuda, H. Yamada, M. Satoh, H. Asoh, M. Nakao, T. Tamamura. Highly ordered nanochannel-array architecture in anodic alumina. *Appl. Phys. Lett.* **1997**, 71, 2770, doi: 10.1063/1.120128.
- [23] A. Santos, L. Vojkuvka, J. Pallarés, J. Ferré-Borrull, L. F. Marsal. In situ electrochemical dissolution of the oxide barrier layer of porous anodic alumina fabricated by hard anodization. *J. Electroanal. Chem.* **2009**, 632, 139-142, doi: 10.1016/j.jelechem.2009.04.008.
- [24] C. Eckstein, L. K. Acosta, L. Pol, E. Xifre-Perez, J. Pallares, J. Ferre-Borrull, L. F. Marsal. Nanoporous Anodic Alumina Surface Modification by Electrostatic, Covalent, and Immune Complexation Binding Investigated by Capillary Filling. *ACS Appl. Mater. Interfaces* **2018**, 10, 10571-10579, doi: 10.1021/acsami.8b00572.
- [25] A. Santos, V. S. Balderrama, M. Alba, P. Formentin, J. Ferre-Borrull, J. Pallares, L. F. Marsal. Nanoporous anodic alumina barcodes: Toward smart optical biosensors. *Adv. Mater.* **2012**, 24, 1050-1054, doi: 10.1002/adma.201104490.
- [26] L. K. Acosta, F. Bertó-Roselló, E. Xifre-Perez, A. Santos, J. Ferré-Borrull, L. F. Marsal. Stacked Nanoporous Anodic Alumina Gradient-Index Filters with Tunable Multispectral Photonic Stopbands as Sensing Platforms. *ACS Appl. Mater. Interfaces* **2019**, 11, 3360-3371, doi: 10.1021/acsami.8b19411.
- [27] A. Santos, J. Ferré-Borrull, J. Pallarès, L. F. Marsal. Hierarchical nanoporous anodic alumina templates by assymetric two-step anodization. *Phys. Status Solidi Appl. Mater. Sci.* **2010**, 208, 668-674, doi: 10.1002/pssa.201026435.
- [28] A. Santos, L. Vojkuvka, Maria Alba, V. S. Balderrama, J. Ferre-Borrull, J. Pallares, L. F. Marsal. Understanding and morphology control of pore modulations in nanoporous anodic

- alumina by discontinuous anodization. *Phys. Status Solidi Appl. Mater. Sci.* **2012**, 209, 2045-2048, doi: 10.1002/pssa.201228150.
- [29] L. Yi, L. Zhiyuan, H. Xing, L. Yisen, C. Yi. Investigation of intrinsic mechanisms of aluminium anodization processes by analyzing the current density. *RSC Adv.* **2012**, 2, 5164-5171, doi: 10.1039/C2RA01050J.
- [30] W. Lee, K. Schwirn, M. Steinhart, E. Pippel, R. Scholz, U. Gösele. Structural engineering of nanoporous anodic aluminium oxide by pulse anodization of aluminium. *Nat. Nanotechnol.* **2008**, 3, 234-239, doi: 10.1038/nnano.2008.54.
- [31] Y. Wang, A. Santos, A. Evdokiou, D. Losic. Rational design of ultra-short anodic alumina nanotubes by short-time pulse anodization. *Electrochim. Acta* **2015**, 154, 379-386, doi: 10.1016/j.electacta.2014.12.056.
- [32] Y. Wang, A. Santos, G. Kaur, A. Evdokiou, D. Losic. Structurally engineered anodic alumina nanotubes as nano-carriers for delivery of anticancer therapeutics. *Biomaterials* **2014**, 35, 5517-5526, doi: 10.1016/j.biomaterials.2014.03.059.
- [33] Y. Wang, G. Kaur, A. Zysk, V Liapis, S. Hay, A. Santos, D. Losic, A. Evdokiou. Systematic invitro nanotoxicity study on anodic alumina nanotubes with engineered aspect ratio: Understanding nanotoxicity by a nanomaterial model. *Biomaterials* **2015**, 46, 117-130, doi: 10.1016/j.biomaterials.2014.12.008.
- [34] S. Bhattacharjee. DLS and zeta potential - What they are and what they are not? *J. Control. Release* **2016**, 235, 337-351, DOI: 10.1016/j.jconrel.2016.06.017.
- [35] Y. Joo, Y. Jeon, S. U. Lee, J. H. Sim, J. Ryu, S. Lee, H. Lee, D. Sohn. Aggregation and stabilization of carboxylic acid functionalized halloysite nanotubes (HNT-COOH). *J. Phys. Chem. C* **2012**, 116, 18230-18235, doi: 10.1021/jp3038945.
- [36] M. Zhu, L. Liu, Z. Wang. Mesoporous silica via self-assembly of nano zinc amino-tris-(methylenephosphonate) exhibiting reduced fire hazards and improved impact toughness in epoxy resin. *J. Hazard. Mater.* **2020**, 392, 122343, doi: 10.1016/j.jhazmat.2020.122343.
- [37] M. Karimi, A. Ghasemi, P. S. Zangabad, R. Rahighi, S. M. Moosavi Basri, H. Mirshekari, M. Amiri, Z. Shafaei Pishabad, A. Aslani, M. Bozorgomid, D. Ghosh, A. Beyzavi, A. Vaseghi, A. R. Aref, L. Haghani, S. Bahrami, M. R. Hamblin. Smart micro/nanoparticles in stimulus-responsive drug/gene delivery systems. *Royal Society of Chemistry* **2016**, 45, 1457-1501, doi: 10.1039/C5CS00798D.
- [38] N. Song and Y. W. Yang. Molecular and supramolecular switches on mesoporous silica nanoparticles. *Chem. Soc. Rev.* **2015**, 44, 3474-3504, doi: 10.1039/C5CS00243E.
- [39] V. Georgakilas, J. N. Tiwari, K. C. Kemp, J. A. Perman, A. B. Bourlinos, K. S. Kim, R. Zboril. Noncovalent Functionalization of Graphene and Graphene Oxide for Energy Materials, Biosensing, Catalytic, and Biomedical Applications. *Chem. Rev.* **2016**, 116, 5464-5519, doi: 10.1021/acs.chemrev.5b00620.
- [40] M. Hiraoui, M. Guendouz, N. Lorrain, A. Moadhen, L. Haji, M. Oueslati. Spectroscopy studies of functionalized oxidized porous silicon surface for biosensing applications. *Mater. Chem. Phys.* **2011**, 128, 151-156, doi: 10.1016/j.matchemphys.2011.02.052.
- [41] M. Amouzadeh Tabrizi, J. Ferré-Borrull, L. F. Marsal. Highly sensitive IRS based biosensor for the determination of cytochrome c as a cancer marker by using nanoporous anodic alumina modified with trypsin. *Biosens. Bioelectron.* **2020**, 149, 111828, doi: 10.1016/j.bios.2019.111828.
- [42] R. Edelman, Y. G. Assaraf, I. Levitzky, T. Shahar, Y. D. Livney. Hyaluronic acid-serum albumin conjugate-based nanoparticles for targeted cancer therapy. *Oncotarget* **2017**, 8, 24337-24353, doi: 10.18632/oncotarget.15363.

- [43] G. C. Wood. A Model for the Incorporation of Electrolyte Species into Anodic Alumina. *J. Electrochem. Soc.* **1996**, 143, 74, doi: 10.1149/1.1836389.
- [44] J.T. Domagalski, E. Xifre-Perez, A. Santos, J. Ferre-Borrull, L.F. Marsal. Tailor-engineered structural and physico-chemical properties of anodic alumina nanotubes by pulse anodization: A step forward. *Microporous Mesoporous Mater.* **2020**, 303, 110264, doi:10.1016/j.micromeso.2020.110264
- [45] R. Ozao, H. Yoshida, T. Inada, M. Ochiai. Sulfur concentration in nanoporous alumina membrane. Studied by TA and XPS. *J. Therm. Anal. Calorim.* **2003**, 72, 113-118, doi: 10.1023/A:1023959401129.
- [46] E. Vidak, U. Javoršek, M. Vizovišek, B. Turk. Cysteine Cathepsins and their Extracellular Roles: Shaping the Microenvironment. *Cells* **2019**, 8, 264, doi: 10.3390/cells8030264.
- [47] X. F. Zhao, J. X. Wang, F. X. Li, S. Sueda, H. Kondo. Analysis of substrate specificity and endopeptidyl activities of the cathepsin B-like proteinase from *Helicoverpa armigera*. *Protein J.* **2005**, 24, 219-225, doi: 10.1007/s10930-005-6714-3.
- [48] L. Z. Swisher, A. M. Prior, S. Shishido, T. A. Nguyen, D. H. Hua, J. Li. Quantitative electrochemical detection of cathepsin B activity in complex tissue lysates using enhanced AC voltammetry at carbon nanofiber nanoelectrode arrays. *Biosens. Bioelectron.* **2014**, 56, 129-136, doi: 10.1016/j.bios.2014.01.002.
- [49] Y. Song, H. Fan, M. J. Anderson, J. G. Wright, D. H. Hua, J. Koehne, M. Meyyappan, J. Li. Electrochemical activity assay for protease analysis using carbon nanofiber nanoelectrode arrays. *Anal. Chem.* **2019**, 91, 3971-3979, doi: 10.1021/acs.analchem.8b05189.
- [50] G. Hungerford, J. Benesch, J. F. Mano, R. L. Reis. Effect of the labelling ratio on the photophysics of fluorescein isothiocyanate (FITC) conjugated to bovine serum albumin. *Photochem. Photobiol. Sci.* **2007**, 6, 152-158, doi: 10.1039/b612870j.
- [51] Y. Wang, I. Zinonos, A. Zysk, V. Panagopoulos, G. Kaur, A. Santos, D. Losic, A. Evdokiou. In vivo toxicological assessment of electrochemically engineered anodic alumina nanotubes: a study of biodistribution, subcutaneous implantation and intravenous injection. *J. Mater. Chem. B* **2015**, 5, 2511-2523, doi: 10.1039/C7TB00222J.
- [52] M. Fizir, P. Dramou, K. Zhang, C. Sun, C. Pham-Huy. Polymer grafted-magnetic halloysite nanotube for controlled and sustained release of cationic drug. *J. Colloid Interface Sci.* **2017**, 505, 476-488, doi: 10.1016/j.jcis.2017.04.011.
- [53] M. A. Tabrizi, J. Ferré-Borrull, L. F. Marsal. An optical biosensor for the determination of cathepsin B as a cancer-associated enzyme using nanoporous anodic alumina modified with human serum albumin-thionine. *Microchim. Acta* **2020**, 187, 230, doi: 10.1007/s00604-020-4188-9.

Chapter 6. Discussion and Conclusions

In the course of this PhD thesis, pulse anodization interlacing high and low density current pulses was investigated. Specific combination of the process conditions enables to yield structure with weaker connection between the cells that can be selectively divided into nanotubes made of anodic alumina. Mechanism of the electrochemical process was analyzed. Furthermore, nanotubes obtained in the process were evaluated. Additionally, attempts to functionalize these nanotubes were carried out.

First, the pulse anodization process was examined in detail, which enabled to understand the process better, facilitating tailor-engineering of these structures:

- i) Analysis of electrochemical parameters of the pulse anodization was carried out and the anodization profile evolution during the process was divided into distinct sections. Geometrical features and surface properties of nanotubes were attributed and quantified with regards to the process conditions: current density and pulse duration during high density pulses.
- ii) Increase of current density during high current pulses resulted in formation of longer and more narrow nanotubes. Furthermore, measured ζ -potential of nanotubes' decreased when higher current was applied, and suspensions ζ -potential varied between 25 and 8 mV for pulses of 290 to 390 mA/cm².
- iii) Pulse duration was demonstrated to serve as the most convenient mean to alter nanotubes' length without affecting other properties: dependence of obtained length and pulse duration was almost linear (268 ± 3 nm/s), while diameter and surface charge of nanotubes remain virtually unaffected.
- iv) Adjustments of the process enabled to obtain the shortest nanotubes reported in the literature ($424 \text{ nm} \pm 92 \text{ nm}$ avg. length) with the method.

Second, the fabrication process of anodic alumina nanotubes was refined and possibilities to modify the material investigated, allowing to reach higher separation rates and unveiling alternative methods to modify the nanotubes:

- i) Extended sonication time was demonstrated to improve separation rate and decrease aggregates fraction: peak of average size measured by DLS became more narrow and was shifted towards smaller sizes, while aggregates fraction substantially decreased. However, longer sonication may result in gradual degradation of nanotubes.

- ii) Temperature of sonication turned out to be a significant factor as well. The process carried out at lower temperatures resulted in significantly lower aggregates fraction and high amount of properly separated nanotubes. Furthermore, sonication at lower temperatures can mitigate degradation observed when sonicating at ambient and higher temperatures
- iii) Higher temperatures (above 30°C) accelerate degradation resulting in significant changes to morphology while standard duration (1 h) is conducted. Sonication at temperature of 65°C resulted in complete decay of the nanotube structure after standard sonication time.
- iv) Annealing of nanotubes templates (prior to separation) was effectively employed to modify the crystalline structure of nanotubes. XRD analysis revealed gradual increase of crystalline forms presence: initial formation of γ -Al₂O₃ and its transition into α -Al₂O₃ upon annealing at 1200°C. However, transition into α -Al₂O₃ results in decline of tubular morphology – hollow inside cannot be observed anymore.
- v) Annealed structure exhibited different surface properties as compared to native nanotubes: increased annealing temperature resulted in decrease of ζ -potential. Furthermore, ζ -potential of structure annealed at 1200°C was negative.
- vi) Annealing changes composition of the structure: with temperature increase, amount of sulfur in the structure decrease as well as oxygen to aluminum rate. When annealed at 1200°C, presence of sulfur cannot be detected.

Third, functionalization possibilities of anodic alumina nanotubes were investigated:

- i) Electrostatic decoration of anodic alumina nanotubes with maghemite was conducted. Different solutions (pH, presence of buffer) were examined. Interaction was observed as long as both type of nanoparticles (nanotubes and maghemite nanospheres) were of opposite surface charge.
- ii) Formation of composite improved dispersion of the composite – measured size distribution was lower as compared with native nanotubes.
- iii) Obtained composite featured responsiveness to the magnetic field reflected in magnet-controlled motion of the colloid observable with a naked eye.
- iv) Prior to separation into nanotubes, modification of the structure with FITC-BSA was conducted with aim to functionalize inner walls selectively. Further, separation into nanotubes was possible despite conducted modification with APTES.
- v) MAANTs(FITC-BSA) were demonstrated as effective material to detect presence of cathepsin B in the solution. In order to measure only the fluorophore released to the solution, nanotubes were forced to precipitate with a magnet.

It is believed that results obtained in this thesis will promote further experiments with anodic alumina nanotubes. These structures are a valuable material so far demonstrated mostly as a biomaterial/drug carrier, but with promising properties in different fields as well.

Fabrication of anodic alumina nanotubes through the pulse anodization is relatively modern anodization technique at the intermediate stage of development. To increase importance of the method, investigation was conducted to provide better understanding of the technique. Moreover, methods to modify the material properties and functionalization techniques were developed. From now on, it is suggested to design various combination of functionalities available with already accessible tools. Composition of inner functionality, with modification of the outer surface may serve in many applications: drug delivery, composites, sensors. Another valuable feature would be to increase stability of nanotubes suspension that could greatly elevate its versatility. Further, increased biocompatibility could be beneficial as well – studies *in vitro* and *in vivo* conducted so far demonstrate low but observable impact of their presence of living cells that could be further improved, for example by providing coating of commonly known chemicals such as PEG.

